Magnetic Phase Transitions in Driven-Dissipative Atomic Ensembles Interacting with Quantum Light

Inaugural-Dissertation

zur

Erlangung des Doktorgrades

der Mathematisch-Naturwissenschaftlichen Fakultät

der Universität zu Köln

vorgelegt von

Jan Gelhausen

aus Waldbröl

Köln 2018

Berichterstatter: Prof. Dr. Achim Rosch
Prof. Dr. Sebastian Diehl

Tag der mündlichen Prüfung: 27. Juli 2018

Contents

Summary

Present-day experiments have started to couple traditional simulations of ultracold atom experiments with quantum light-fields in cavities. This has provided a wealth of opportunities to enlarge the number of interaction potentials: cavity mediated long-range interactions compete with kinetic energies, longitudinal fields, short-ranged collisional or magnetic spin-spin interactions. The intracavity many-body lattice models often have to be maintained far from equilibrium through the presence of external driving lasers that help to boost and engineer the various interaction potentials. The steady influx of energy is compensated by a steady stream of energy out of the atom-cavity system for example by photon losses or atomic spontaneous emission. Several experiments have demonstrated that such environments can give rise to new competing quantum phases.

But this long-standing ambition to push for models with tailorable interaction potentials can bring with it also considerable challenges in their theoretical description, since spontaneous symmetry breaking transitions in many body lattice systems coupled to dynamical light-fields with single-photon character occur in the presence of drive and dissipation for the photonic force carriers. This clearly calls for model systems where the above mentioned interplay of interactions, drive, dissipation and cooperative many-body behaviour can be theoretically studied to provide simple, experimentally verifiable predictions.

The Dicke model is, through its simplicity (an exactly solved ferromagnet with infinite range atom-atom interactions mediated by a single cavity mode), an exceptionally well-suited candidate. As the generic model for atom-light interactions, it has been experimentally realized in a variety of modern quantum optical systems, highlighting its relevance for present-day research. The Dicke model is also highly versatile itself. It has been extended into the dissipative realm, was promoted to account for multiple optical light modes and was used to describe multiple, coupled single-mode cavity structures. It was adapted to treat spin-selective coupling to a cavity to describe superradiance phase transitions in multi-level atomic systems. Moreover, it was realised in electronic circuits where the dipole coupling of real atoms to single mode fields is replaced by a capacitive coupling of artificial atoms to a resonator mode. This illustrates that the Dicke model and its extended variants are 'future-proof' and continue to be of relevance for fundamental light-matter interactions and for driven-dissipative phase transitions.

In this thesis, we investigate magnetic phase transitions in driven-dissipative atomic ensembles interacting with quantum light. We present three research projects on variants of cooperative radiation of an ensemble of laser driven two-level atoms in a single mode optical cavity, as described by the Dicke model.

Throughout the chapters 2,3 and 4 that contain the main body of research of this thesis, we investigate phase transitions between non-equilibrium stationary states in engineered quantum-optical systems each of which extends the conventional Dicke model physics. As a starting point, we map the quantum equations of motion onto a set of semiclassical nonlinear stochastic equations and analyse their stationary states and instabilities with

master equations for atomic spin and photon mean-field amplitudes. These are used to obtain experimentally relevant parameters such as critical atom-light couplings for phase transitions, phase diagrams and properties of stationary non-equilibrium states in addition to cavity output spectra that identify the imprint of magnetic correlations in the light-field.

In chapter 2, we help resolve a discrepancy between earlier experimental investigations of the critical atom-light coupling strength for the superradiance transition in the Dicke model: higher external pumping strengths than theoretically predicted were needed to observe a coherent, superradiant state of the light field in an optical cavity. By including incoherent spontaneous emission of atomic excitations, we extend the dissipative Dicke model to a two loss channel variant containing both photon leakage and atomic decay that reproduces the experimentally observed critical atom-light coupling.

Recent experiments have started to interface quantum many body lattice models with coherent cavity fields, thereby allowing to realize new quantum phases through competing atom-cavity and atom-atom interactions. In chapter 3, we consider a simplified model for such a set-up where a single quantized mode of the light-field interacts with an ensemble of Rydberg-dressed atoms inside a high finesse optical cavity. This model provides a base case for further studies of quantum magnets in optical cavities. At the heart of this model is a competition of short- (dipolar atom-atom) and long-range (atom-light) interactions at the Hamiltonian level in the presence of both spontaneous emission and photon leakage through the cavity mirrors. We show that different magnetic phases can coexist with coherent atomic radiation and provide clear experimental signatures to identify the magnetic structure and intra-cavity dynamics. We suggest an experimental level-scheme for a quantum optical implementation of our model.

In chapter 4 we consider a generic, collective decay for many-body excitations in the paradigmatic Dicke model. This extension drastically enriches the dynamics as it induces a bicritical point and a bistable regime dominated by true non-equilibrium fluctuations that induce a dissipative first-order phase transition that can only be resolved by including finite fluctuation corrections with the help of stochastic Langevin equations. We investigate the hysteretic response to time-dependent ramps of the atom-light coupling. Discontinuous first-order phase transitions where metastable states coexist in a hysteresis domain have been investigated in recent dissipative quantum-optical experiments. We review noise-activation far from thermal equilibrium in chapter 5.

Deutsche Zusammenfassung

Moderne Experimente haben begonnen, ultrakalte atomare Gase mit Quanten-Lichtfeldern in optischen Hohlraumresonatoren wechselwirken zu lassen. Dies bietet eine Fülle von Möglichkeiten, die Anzahl der Wechselwirkungspotentiale zu erweitern: Langreichweitige atomare Wechselwirkungen konkurrieren mit kinetischen Prozessen wie z.B. kurzreichweitigen Streuprozessen, Magnetfeldern und magnetischen Spin-Spin Wechselwirkungen. In solch quantenoptischen Experimenten werden oft externe Treiblaser eingesetzt um die verschiedenen Wechselwirkungspotentiale zum einen überhaupt zu ermöglichen und zum anderen diese auch aufeinander abzustimmen. Solche Systeme erreichen stationäre Zustände nur wenn ein Fließgleichgewicht zwischen Energiegewinn (durch die Treiblaser) und Energieverlusten (spontaner Zerfall von atomaren Anreungen oder Verluste von Photonen) herrscht. Mehrere Experimente in diesen Regimes haben gezeigt, dass es so zu konkurrierenden Quantenphasen kommen kann.

Zugleich erwachsen aber auch erhebliche Herausforderungen in der theoretischen Beschreibung solcher Systeme: Spontane Symmetriebrechung in Vielteilchensystemen die an dynamische Lichtfelder mit quantencharakter koppeln treten zusammen mit Verlustprozessen auf. Dies erfordert Modellsysteme, in denen das oben erwähnte Zusammenspiel von Wechselwirkungen, Treibtermen, Verlustprozessen und kooperativem Verhalten theoretisch untersucht werden kann, mit dem Ziel einfache und experimentell überprüfbare Vorhersagen zu machen.

Das Dicke-Modell ist durch seine Einfachheit (ein exakt lösbarer Ferromagnet mit unendlich langreichweitigen Wechselwirkungen zwischen Atomen, vermittelt durch ein optisches Lichtfeld) ein hervorragend geeigneter Kandidat. Als generisches Modell für Atom-Licht-Wechselwirkungen wurde es experimentell in einer Vielzahl moderner quantenoptischer Systeme realisiert, was seine Relevanz für die heutige Forschung unterstreicht. Das Dicke-Modell ist auch selbst sehr anpassbar und vielseitig. Es kann zum Beispiel leicht in den dissipativen Bereich erweitert werden, oder in seiner Beschreibung mehrere optische Moden in einem Resonator, oder auch gekoppelte Resonatoren umfassen. Es wurde verwendet um Superradianzphasenübergänge in atomaren System mit vielschichtiger Levelstruktur, zum Beispiel realisiert durch spin-selektive Kopplung an das Lichtfeld, zu untersuchen. Es wurde zudem als effektives Modell in elektrischen Schaltkreisen realisiert wo die elektrische dipolare Kopplung von Atomen ans Lichtfeld durch eine kapazitive Kopplung von künstlichen Atomen an einen Resonator ersetzt worden ist. Dies verdeutlicht, dass das Dicke-Modell, nicht zuletzt durch seine zahlreichen Erweiterungen, auch zukünftig vorallem für die Beschreibung von fundamentalen Wechselwirkungen von Atomen mit Licht und für getrieben-dissipative Phasenübergänge von Relevanz für zukünftige Forschung sein wird.

In dieser Arbeit untersuchen wir magnetische Phasenübergänge in getrieben-dissipativen atomaren Ensembles, die mit einer einzelnen quanten-optischen Lichtmode wechselwirken. Diese Arbeit enthält drei publizierte Forschungsprojekte. In den Kapiteln 2, 3 und 4, die den Hauptteil der Forschung dieser Arbeit enthalten, untersuchen wir Phasenübergänge zwischen Nichtgleichgewichtszuständen in quantenoptischen Systemen, von denen jedes das konventionelle Dicke Modell entscheidend erweitert. Wir beschreiben Experimentelle Signaturen die zum Nachweis dieser Phasen dienen können. Den Ausgangspunkt unserer Untersuchungen bilden die quantenmechanischen Heisenberg-Langevin Gleichungen die wir auf einen Satz semiklassischer, nichtlinearer stochastischer Bewegungsgleichungen abbilden. Wir analysieren dessen stationäre Zustände und Instabilitäten mit Mastergleichungen für die Freiheitsgrade der atomaren Teilchen und des Lichtfeldes auch auf einem 'mean-field' level. Diese werden verwendet, um experimentell relevante Parameter wie kritische Atom-Lichstärken für Phasenübergänge, Phasendiagramme und Eigenschaften von stationären Nichtgleichgewichtszuständen, Lichtspektren zur Bestimmung von magnetischen Korrelationen im Lichtfeld oder 'Noise' Aktivierungsraten zu erhalten.

In Kapitel 2 helfen wir eine Diskrepanz zwischen früheren experimentellen Untersuchungen für die kritische Atom-Licht Kopplungsstärke für den Superradianzübergang des Dicke Modells aufzulösen: höhere externe Pumpstärken als theoretisch vorhergesagt waren nötig, um einen kohärenten, superradianten Zustand des Lichtfeldes in einem optischen Hohlraumresonator zu beobachten. Durch die Einbeziehung inkohärenter spontaner Emission von atomaren Anregungen erweitern wir das dissipative Dicke-Modell auf eine Variante mit zwei Verlustkanälen, die sowohl Verluste der Photonen durch die hocheffizienz Spiegel als auch Zerfälle atomarer Anregung enthält und die experimentell beobachtete kritische Atom-Lichtkopplung reproduziert.

Neuere Experimente haben begonnen, Gittermodelle von ultrakalten Quantenvielteilchensystemem mit kohärenten Hohlraumfeldern zu verbinden, wodurch neue Quantenphasen durch konkurrierende Atom-Licht- und Atom-Atom-Wechselwirkungen realisiert werden können. Im dritten Kapitel betrachten wir ein simplifiziertes Modell eines solchen Aufbaus, bei dem eine einzelne quantisierte Mode des Lichtfeldes mit einem Ensemble von Rydberg-Atomen wechselwirkt. Dies bietet einen kontrollierten Einstiegspunkt für weitere Forschung im Bereich von Quantenmagneten die in Wechselwirkung mit Lichtfeldern stehen. Das Hauptaugenmerk dieses Modells liegt auf einem Wettbewerb zwischen kurz- (dipolare Atom-Atom) und langreichweitigen (Atom-Licht) Wechselwirkungen auf Hamiltonischer Ebene in Gegenwart von spontaner Emission atomarer Anregungen und Verluste von Photonen durch die Spiegel des Hohlraumresonators. Wir zeigen, dass verschiedene magnetische Phasen von Atomen mit kohärenter, superradianter Strahlung koexistieren können und liefern klare experimentelle Signaturen um die magnetische Struktur und die Dynamik innerhalb des Hohlraumresonators zu identifizieren. Wir schlagen ein experimentelles Level-Schema für eine quantenoptische Umsetzung unseres Modells vor.

Im vierten Kapitel betrachten wir einen generischen, kollektiven Zerfall für Vielteilchenanregungen im paradigmatischen Dicke-Modell. Diese Erweiterung bereichert die Dynamik drastisch, da sie einen bikritischen Punkt und ein bistabiles Regime induziert, das von echten Nichtgleichgewichtsfluktuationen dominiert wird, die einen dissipativen Phasenübergang erster Ordnung induzieren, der nur durch endliche Fluktuationskorrekturen mittels stochastischer Langevin Gleichungen aufgelöst werden kann. Wir untersuchen die hysteretische Reaktion auf zeitabhängige Veränderung der Atom-Licht-Kopplung. Diskontinuierliche Phasenübergänge erster Ordnung, bei denen metastabile Zustände in einem Hysteresebereich nebeneinander existieren, wurden kürzlich in dissipativen quantenoptischen Experimenten untersucht.

Introduction

To kick off with a dramatic start: let us mention that life on Earth and Earth itself are fundamentally out-of-equilibrium [1]. The dynamics of weather, oceanic currents and movement of the Earth's crust are all driven by an influx of energy, e.g. in the form of heat from the earth's core or from the sun driving dynamics in the atmosphere. Biological systems that sustain metabolisms are dependent on an uptake of energy to power irreversible molecular reactions in fluctuating chemical environments. Non-equilibrium phenomena therefore permeate every aspect of life and are thus ubiquitous in nature. In fact, a report in 2007 compiled for the Office of Science of the Department of Energy (USA) [2] raised the task to identify and present to the scientific community five of the most urgent scientific questions and technological challenges we face today and in the future. One of the five grand challenges that was communicated among and identified by the scientific community [3, 4] was 'How do we characterize and control matter away - especially very far away - from equilibrium?'.

However, 'non-equilibrium' encompasses a great variety of phenomena and typically one can categorize according to two criteria: Firstly, it can refer to a general time-evolution of a many-body system and their relaxation to both equilibrium and non-equilibrium states. For example, the relaxation dynamics after a quantum quench in experiments with ultracold atoms allows one to track and identify universal time-evolution stages that precede the long time limit state. These stages are typically represented by prethermal states associated to quasiparticle formation and by a local equilibrium through quasiparticle scattering before the system finally relaxes to a global equilibrium state, see Refs. [5, 6, 7]. The second aspect of 'non-equilibrium' does not refer to relaxation dynamics but to properties of stationary states. A non-equilibrium stationary state is maintained by a compensation of fluxes (heat, energy, particles,. . .) triggered by external driving and dissipation which is why they are also referred to as flux equilibria. They are distinct from an equilibrium stationary state because the external driving often breaks detailed balance for the microscopic equations of motion. This can allow for a greater variety of stationary states, since they are in principle not restricted to Gibbs or Boltzmann distributions. If a non-equilibrium system is isolated from its environment, for example by switching off the explicit drive, it will undergo time-dependent relaxation dynamics as there is no flux compensation any more and the steady-state cannot be maintained. This is in contrast to a system in thermal equilibrium. If isolated from its environment, the state variables that describe it (temperature, pressure, particle number, . . .) remain unchanged. In this thesis we will be concerned with stationary non-equilibrium states only.

Far from equilibrium scenarios exclude linearised approximations to an equilibrium reference state because strong non-equilibrium conditions are not small perturbative corrections to coherent Hamiltonian dynamics. The separation of reversible and irreversible processes is deeply engrained in a thermodynamical framework of equilibrium systems [8]. For instance, in the thermodynamic limit, the second law of thermodynamics states that irreversible processes increase the entropy of the system until it is maximised. The state of maximum entropy is the equilibrium state and is characterized by a set of time-independent state variables (temperature, chemical potential, ...) that, per definition of the equilibrium state, only undergo reversible dynamics. This is a consequence of detailed balance and the time reversibility of the microscopic equations of motion. An external driving laser typically breaks this time reversibility. For a system in a flux equilibrium state, reversible Hamiltonian dynamics and irreversible driving and damping far from equilibrium generally have to be considered on an equal footing [9, 10, 11]. We review a more detailed explanation of this last statement in chapter 5.

Driving a system far from equilibrium, however still allows for pattern formation and structure instead of chaos and turbulence [12]. The description of systems in thermodynamic equilibrium benefits tremendously from extremum principles such as maximization of the system's entropy or, equivalently, the minimization of the free energy as the system's thermodynamic potential. What makes nonequilibrium systems challenging to understand is that thermodynamic extremization principles are not applicable. Meaning that there is a lack of an overarching guiding principle that determines the stationary probability distribution far from equilibrium, whereas in thermal equilibrium it is easily found as the Boltzmann or Gibbs distribution but not easily computed.

Non-equilibrium systems and transitions between different non-equilibrium states have not yet been unified and classified in an all encompassing theoretical framework and it is not clear to what degree universality emerges far from equilibrium.

A powerful method to describe non-equilibrium phenomena is the Keldysh functional integral formalism [13] where the quantum many-body master equation formulated in an operator representation is directly translated into an associated Keldysh action in a functional integral representation [14]. On the level of the action, the presence or absence of an equilibrium symmetry (related to energy conservation) works as an indication for non equilibrium conditions [15, 16]. In a system in thermodynamic equilibrium, reversible and irreversible dynamics are not independent from one another. In contrast, in driven quantum optics system where coherent dynamics are set by a Hamiltonian and dissipation is encoded with Lindblad operators, the sources of coherent and driven-dissipative dynamics become distinct and are not tied together by a symmetry [14, 17]. This allows for equilibrium and driven-open systems to be in different universality classes [18, 19].

In the '70s and '80s, in particular classical nonequilibrium systems have been treated in the context of Langevin equations with non-gradient drift fields to understand for instance non-thermal noise activation and rare fluctuations. Considerable effort has been invested in finding a generalized thermodynamic framework for flux equilibria far from equilibrium in particular for systems whose dynamical equations are classical nonlinear stochastic equations [20, 21]. The starting point is generally a dynamical description of fluctuations in a path-integral or an equivalent Fokker-Planck equation, see [21, 11] and references therein. Let us mention that in chapter 4 of this work, we derive a set of classical nonlinear stochastic equations that describe a genuine non-equilibrium system that fits in this framework which we detail and analyse in chapter 5. However non-equilibrium systems are not inherently classical. It is true that dissipation and damping can be detrimental to the build-up of quantum properties such as coherence or entanglement but engineered dissipation can drive the system in the long-time limit into states protected from noise (dark states). This was shown in [22] where reservoir engineering lead to a Bose-Einstein condensate as the stationary dark state of the system.

More recently, non-equilibrium states of matter and their phase transitions have garnered a lot of momentum since they are ubiquitous in damped-driven open quantum systems

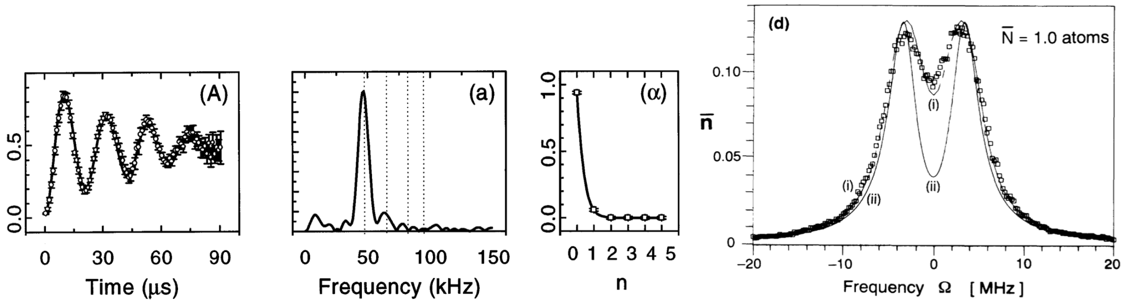

(a)

(b)

Figure I.1.: (a) Rabi Oscillations according to the transfer rate from the excited state e to the ground state g as given by $P_{eg}(t)$. Points are experimental measurements, solid line is a theoretical fit with, in comparison to Eq. (I.2), damped sinusoidals. (A) for an empty cavity with average thermal photon population $\bar{n}_{\text{therm}}(T = 0.8K) \sim 0.06$. '(a)' Fourier decomposition of time signal from a fit with $n = (0 - 5)$ photons at frequencies $\nu_0 = 47kHz, \nu = \sqrt{2}\nu_0, \nu = \sqrt{3}\nu_0, \ldots$. ($\alpha$) measured, vacuum photon distribution P_n. Figure taken from [31] (minor adaptions). (b) Experimentally observed normal mode splitting of the first excited state of a single atom interacting with a cavity mode. Shown is the transmission spectrum normalised to the average photon number $\bar{n}$ in the cavity in response to a weak laser drive with frequency Ω that probes the eigenmodes of the atom-cavity system. The spectrum shows the predicted frequency doublet splitting of $\Delta E = E_+ - E_- = 2g$, see Eq. (I.1). Figure taken from [32] (minor adaptions).

characterised by the presence of both coherent dynamics and controlled dissipation. The new impetus came from advances in experiments that have begun to merge quantum many-body lattice models as realised in ultracold atomic systems [23] with driven cavity setups [24, 25] that had been investigating fundamental light-matter interaction at the quantum level. This combines a high degree of experimental control with the driven-dissipative character of quantum optical experiments, promising an insight into non-equilibrium behaviour that is often prohibited in other systems by the shear complexity and vast number of interaction channels that occur e.g. in financial markets or biological systems.

In these new and inherently non-equilibrium scenarios, phase transitions occur when the continuous tuning of an external parameter leads to a transition between two non-equilibrium stationary states. What is more, it is possible to measure non-destructively phase transitions in real-time in quantum many-body systems using a dissipation channel that outcouples information to the external environment. For example, in a driven-nonlinear cavity, spectral properties of photons that leak from the cavity mirror can be related back to the dynamics of the intra cavity photon field, to detect for instance diverging correlations of fluctuations or the structure of hybridised atom-cavity modes [26, 27, 28]. This makes them ideal model systems to monitor dynamics close to dissipative first-order phase transitions where far from thermal noise-activation and fluctuations are crucial drivers for the system dynamics in phase space [29, 30].

Cavity quantum electrodynamics (CQED) [34] describes the field of research that investigates light matter interaction at the quantum level. As the name suggests, it dispenses with a classical description of electromagnetic radiation and instead operates in the few, or single photon regime. Cavities are indispensable tools to realise enhanced light-matter interactions which ultimately allows us to observe the coherent interaction of single atoms with single photons, providing an ideal testbed for the quantum theory of light-matter interaction. We review why this the case. In free-space, the probability for a laser photon

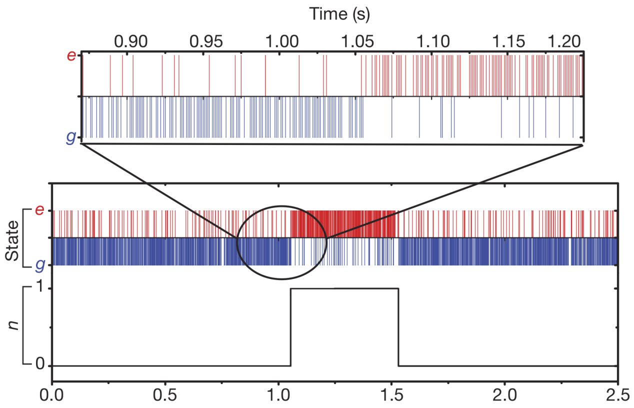

Figure I.2.: Non-destructive experimental measurement of intracavity photon number n due to vacuum fluctuations [33] as measured by the final state of a stream of atomic two-level systems $\{|g\rangle, |e\rangle\}$ passing through the cavity. Every line corresponds to a readout of a single atomic state. Experimental imperfections lead to false readouts as clearly visible in the measurement sequence. At $t = 1s$, a vacuum fluctuation leads to the appearance of a cavity photon which is seen by a great number of consecutive atoms. It finally decays at $t = 1.5s$. See text for details. Figure taken from [33]with minor adaptions only.

to interact with an atom is proportional to the cooperativity $C_{\text{free}} = \sigma/A$ which is the ratio of the laser beam width A and the scattering cross section σ. If light is trapped in a box, as realised by two high quality mirrors, photons bounce back and forth between them before they are eventually lost. In this case, the cooperativity is enhanced by the number of roundtrips F of the photon, $C_{\text{cav}} = FC_{\text{free}}$. An additional enhancement is obtained when the cavity contains an ensemble of N atoms which boosts the cooperativity a second time to $C_{\text{cav}} = NFC_{\text{free}}$. Through the strongly enhanced and repeated interaction of cavity photons with an atomic ensemble, the standing wave optical light field in a cavity becomes dynamical, meaning that the atomic motion exerts a backreaction on the cavity field and vice versa. Cavities are thus the perfect environment to study strong light-matter interactions.

Therefore, many modern experimental set-ups in quantum optics investigate atom-light interactions in cavity systems. All three major research projects of this thesis also belong to the research field of CQED. We therefore briefly review recent trends that are directly relevant to this thesis and give a brief and highly selective historical overview of experiments that have been important milestones for the research of atom-light interactions.

With growing experimental control and technical advances, it has been a trend to build scalable atom-cavity systems. For example by scaling up the number of photon modes M supported by the cavity and the number of atoms N participating in the atom-light interactions. We identify three regimes:

- $(\boldsymbol{a})$ Single-mode cavities ($M = 1$) interacting with few or single atoms ($N = 1$)
- $(\boldsymbol{b})$ Many-body radiation ($N \gg 1$) in single-mode ($M = 1$) dissipative cavities with atom-atom interactions
- $(\boldsymbol{c})$ Variable range atom-atom interactions in a many-body regime ($N \gg 1$) mediated by multiple cavity modes ($M \gg 1$)

We will briefly describe pioneering experiments in regimes $(\boldsymbol{a})$, $(\boldsymbol{b})$, and $(\boldsymbol{c})$ and indicate relations to the current work in this thesis.

(*a*) Single-mode cavities ($M = 1$) interacting with few or single atoms ($N = 1$)

We start by briefly recapitulating the pioneering work of many research scientists that paved the way for modern day experiments in cavity quantum electrodynamics. In the early days, experiments concentrated on exploring the quantum interaction between light and matter at the most fundamental level, i.e. they were trying to make one atom interact with a single or few photons at a time.

To experimentally resolve coherent exchange of excitations between atoms and photons, it is necessary to reach a strong coupling regime ($g \gg \kappa, \gamma$), where the timescale associated to coherent atom-light interactions (g) is much shorter than the timescale associated to decay of atomic excitations (γ) or to the decay of cavity modes (κ). This was first achieved in the early 1990s by Kimble, Thompson, Rempe, Haroche and collaborators [32, 35, 31, 36]. The main aim of their experiments was to observe smoking gun features for the discreteness of energy of the radiation field stored in a cavity and thus proving the quantum nature of the atom-cavity system. In a first experiment, this prove was obtained by observing a normal-mode splitting in a transmission intensity of a cavity that contained a single atom, see Fig. I.1b. We now explain the nature of this splitting. When atoms and photons interact, they form joined eigenstates, so called polaritons. The eigenenergies of the hybridised atom-photon modes is comprised of discrete levels whose spacing depends nonlinearly $E_{\mathrm{atom-light}}(n) \sim \sqrt{n+1}$ on the discrete number of photons n. This level splitting was predicted initially by Jaynes and Cummings [37] and Tavis and Cummings [38] in the '60s. For an empty cavity that contains no photons, the transmission intensity has a single peak resonance, corresponding to the vacuum mode ($n = 0$) of the cavity. If however there is a single atom inside the cavity, the first excited state of the atom-cavity system is split by a characteristic width $\Delta E = E_+ - E_- = 2g$ associated to the hybridised atom-cavity eigenmodes

$$E_\pm = \hbar\omega_z \pm \hbar g, \quad |\pm\rangle = \frac{1}{\sqrt{2}}\left(|e,0\rangle \pm |g,1\rangle\right). \tag{I.1}$$

The level splitting is a consequence of an absorption and emission cycle of the cavity photon by the atom that oscillates with the so-called vacuum Rabi frequency g and ω_z is the resonance frequency of the cavity as well as of the atom.

A second smoking gun feature for quantised atom-light interactions were direct experimental observations of Rabi-oscillations [31], the coherent exchange of excitations of a single atom and a single photon trapped between two high finesse optical mirrors. The time-evolution of the quantum state of the atom and the photon undergoes oscillations that transfers population of the excited state e to the ground state g and back again. The probability to find an atom that was initially in the excited state e after a time t in the ground state g is given by [31]

$$P_{eg}(t) = \sum_n P_n \sin^2\left(g\sqrt{n+1}t\right), \tag{I.2}$$

where P_n is the probability distribution for the photon number of the light field. For example it can be poissonian distributed for a coherent light source, and exponentially distributed for an incoherent light source such as thermal radiation. For a weak intracavity field, as realised by thermal population of the cavity mode at room temperature $n_{\mathrm{thermal}} \ll 1$, Eq. (I.2) predicts Rabi oscillations with a frequency set by g which is related to the dipole coupling strength of the light field to the atomic two-level system. The experimentally detected Rabi oscillations are depicted in Fig. I.1a.

These early endeavours [39, 40] were honoured with the Nobel Prize in Physics 2012 that was awarded jointly to Serge Haroche and David J. Wineland 'for ground-breaking

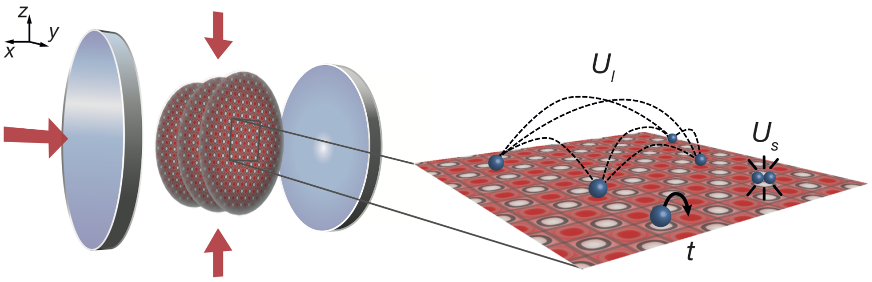

Figure I.3.: Sketch of an experimental realization [24] of competing short and long-range atom-atom interactions in a cavity. The cavity mode mediates infinite range atom-atom interaction of strength U_I that competes with on-site collisional interactions U_s and kinetic energies t of a lattice Bose-Hubbard model. The competition of these three energy scales leads to the emergence of new quantum phases, such as a state characterised by a regular density pattern of atoms, as favoured by the cavity whilst retaining the phase coherence of the Bose-Einstein condensate (supersolid phase). Figure taken from [24] with minimal adaptions only.

experimental methods that enable measuring and manipulation of individual quantum systems' [41]. In particular, in 2007 Haroche and his group [33] trapped photons in a box that would keep them alive long enough to perform non-destructive measurements on the number of photons in the cavity [42]. Their main idea was to read out phase shifts on initial and final atomic states that depend on the presence or absence of cavity photons

$$|\text{initial}\rangle = \frac{1}{\sqrt{2}}\left(|g\rangle + |e\rangle\right) \rightarrow |\text{final}\rangle = \frac{1}{\sqrt{2}}\left(e^{i\phi(n,\delta)}\,|g\rangle + |e\rangle\right). \tag{I.3}$$

A stream of Rydberg atoms in a coherent superposition of some ground and excited state manifold $\{|e\rangle, |g\rangle\}$ is sent through a cavity that is kept at a low temperature such that its average photon number due to thermal population is $\bar{n}_{thermal} \ll 1$. Depending on the presence or absence of a thermal cavity photon, the atoms exit the cavity with a phase shift $\phi(n, \delta)$ which in turn depends on the frequency detuning of the atom and cavity resonance δ. Through the application of a laser pulse, the terminal state of the atom is forced into $|g\rangle$ if $n = 0$ and $|e\rangle$ if $n = 1$. This experiment allowed the non-destructive observation of the birth, lifetime and decay of a cavity photon, see Fig. I.2.

(*b*) Many-body radiation ($N \gg 1$) in single-mode ($M = 1$) dissipative cavities with atom-atom interactions

For the next generation of experiments it was possible to significantly scale up the number of atoms in a cavity that could interact with a single mode of the optical light field. This was made possible also by the advancements of laser cooling an ensemble of atoms into ultracold quantum gases which could then be interfaced with intracavity optical lattices to trap the atoms spatially [43]. In particular, the paradigmatic Dicke model has been turned into experimental reality [44]. It describes the interaction of a laser-driven ensemble of two-level atoms with a quantised light-field in a cavity. Due to its special importance for this thesis, there is a detailed section (1.1) on its experimental realisation. Modern experiments are not restricted to simulate condensed matter systems but have made a significant steps towards engineering and controlling quantum optical systems in the presence of drive and dissipation that allows for the emergence of new quantum phases. This is evidenced for

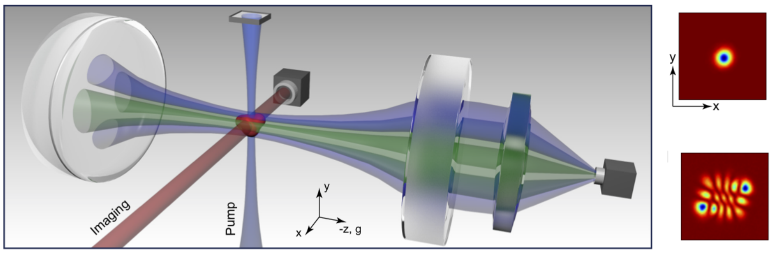

Figure I.4.: Experimental setup of a cavity that supports a set of nearly degenerate modes. On the right, one can see superradiant emission from a single mode cavity (top) and superradiant emission from a multimode cavity (bottom), as realised in the experiments at Stanford [45]. Figure taken from [45] (adapted, [48]).

instance by the most recent experimental progress (2015) at the ETH in Zurich [24] and in Hamburg [25] that interfaced a lattice bosonic Hubbard model with a cavity field leading to a Dicke-Hubbard model that features a competition of both short- and long-range interactions in a quantum optical system, see Fig. I.3. The Dicke-Hubbard model combines the well-studied superfluid to Mott insulator transition with a spatial self-organisation phase of the atoms in the cavity. This allows for a quantum phase that inherits phase coherence from the superfluid state and an atomic density wave with the periodicity of the cavity wavevector which was dubbed a supersolid phase. In chapter 3, we consider a quantum optical model that realises short and long-range atom-atom interactions in a cavity where the motional degrees of freedom have been frozen out by a deep optical lattice which can be considered as a simple base case to investigate magnetic phase transitions in coexistence with coherent cavity fields.

(*c*) Variable range atom-atom interactions in a many-body regime ($N \gg 1$) mediated by multiple cavity modes ($M \gg 1$)

The next experimental achievement was to increase the number of cavity modes from a single to multiple modes which is then interfaced with an atomic Bose-Einstein condensate placed in a cavity, see also Fig. I.4. This research was pioneered in Stanford in 2017 [45]. The atom-light coupling to multiple modes realises a rich structure of interactions of atoms at position ℓ and m with interaction strength $J_{\ell m}$ and can help not only to engineer a great variety of phases in stationary non-equilibrium states [46] but also to investigate possibly exotic collective phenomena and non-equilibrium fluctuations [47] in real time [27]. The multimode structure is realised by an adjustable-length cavity that can then support nearly frequency degenerate modes with different spatial mode profiles. When the system is driven from the side by a far off-resonant laser, the atoms can not only scatter the pump photons into a single cavity mode but into a superposition of many modes. Since the modes have spatially varying profiles, their relative weight changes with the position of the atom. Above a critical pumping strength, the atoms self-organise in a distinct density pattern and maximise scattering into the cavity, thereby realising a superradiance in the cavity. For a single-mode cavity this is one of two possible checkerboard configurations where the atoms are pinned at the even or odd antinodes of the dynamical cavity lattice. Superradiance of single and multiple modes in a cavity is shown in Fig. I.4.

Outline of the thesis

At the heart of this thesis are the chapters 2, 3 and 4, which are based on research projects that are published in peer-reviewed journals. Each of these projects is built around the Dicke model, the generic model for the interaction of a single quantized bosonic light mode with a laser-driven ensemble of atoms. In this thesis, we contribute to the previously mentioned regime ***(b)*** of many-body radiation in dissipative single-mode cavities with atom-atom interactions.

In chapter 1, the introductory chapter, we review essential theoretical aspects of open quantum systems that are relevant for the three major research projects contained in this thesis. We review the derivation of Heisenberg-Langevin equations that take into account the coupling of a system to an external bath which leads to the presence of damping and noise terms in addition to the coherent, Hamiltonian dynamics. We review the derivation of generalised Einstein rules that connect fluctuations and dissipations which is essential, for instance, to preserve quantum commutation relations over time. We also review the derivation of non-unitary time-evolution with Lindblad superoperators and point out crucial differences to temporal dynamics in closed Hamiltonian systems. We then recapitulate briefly the history of the Dicke model, its importance in modelling generic atom-light interactions and a few selected experimental realisations.

In chapter 2, we extend previous work on the dissipative Dicke model by considering the influence of incoherent, spontaneous emission of atomic excitations into free space, away from the cavity axis, thereby introducing a second decay channel in addition to photonic losses from the cavity mirror. This investigation is motivated by recent (2014, [49]) experimental work on a quantum optical realization of the Dicke model where a discrepancy between theoretical predictions and experimental data for the onset of the superradiance transition was found. Subsequent experimental measurements and new rounds of data taking from a group in Singapore (2018, [44]) show that the experimentally observed critical coupling for the superradiance transition is adequately described by taking into account an effective spontaneous atomic emission which is consistent with our theoretical prediction. The research presented in this chapter is published as

- *Many-body quantum optics with decaying atomic spin states:* (γ, κ) *Dicke model*
  J. Gelhausen and M. Buchhold and P. Strack
  Phys. Rev. A **95**, 063824, (2017)

In chapter 3, we consider a set-up where a single quantized mode of the light-field interacts with an ensemble of Rydberg-dressed atoms inside a high finesse optical cavity. At the heart of this model is a competition of short- (dipole-dipole) and long-range (atom-light) interactions at the Hamiltonian level in the presence of both incoherent spontaneous emission of atomic excitations and photon leakage through the cavity mirrors. Recent experimental progress on the realisation and control of optical intra-cavity lattices and Rydberg-dressed atoms featuring dipole-dipole interactions has put our model within experimental reach [50]. We calculate the non-equilibrium steady-state phase diagrams using mean-field theory and observe phase transitions between different magnetic phases of atoms that coexist with coherent atomic radiation. We suggest an experimental scheme for a quantum optical implementation of our model that is based on cavity-assisted Raman transitions in a hyperfine-split groundstate manifold of Rydberg atoms. Additionally, we calculate and identify clear experimental signatures in the form of cavity spectra for the variety of magnetic phases in the stationary states of the system. We have published our research.

- *Quantum-optical magnets with competing short- and long-range interactions: Rydberg-dressed spin lattice in an optical cavity*
  J. Gelhausen and M. Buchhold and A. Rosch and P. Strack
  SciPost Phys. **1**, 004 (2016)

In chapter 5, we consider the Dicke model with a generic, collective decay mechanism for many-body excitations. This extension drastically enriches the dynamics as strong collective decay can change the continuous superradiance transition at a bicritical point into a discontinuous transition. The dynamics of the system can generally not be resolved on a mean-field level as they predict bistability in the thermodynamic limit of large number of atoms N. It is therefore necessary to include finite fluctuations to resolve the dissipative first-order transition. The fluctuations are derived from a generalised Einstein theorem and are manifestly non-thermal as they depend on the state of the system. We analyse non-thermal noise activation and transitions between metastable mean-field states numerically. Additionally, we investigate hysteresis in the bistable regime that results from a response to a time-dependent ramp of the atom-light coupling. Moreover, we show that in a narrow region around the bicritical point there emerges an effective thermal description for the phase transitions. Part of this research is published.

- *Dissipative Dicke model with collective atomic decay: Bistability, noise-driven activation, and the nonthermal first-order superradiance transition*
  J. Gelhausen and M. Buchhold
  Phys. Rev. A **97**, 023807 (2018)

Chapter 5 contains a review of a path integral description of classical multicomponent Langevin equations. We derive the classical action associated to the stochastic optical Bloch equations that describe the non-equilibrium dynamics of the Dicke model investigated in chapter 4. This allows for a general understanding of noise activation rates in a weak-noise limit in and also far from equilibrium in the context of a well-studied 'rare-events' theory.

In an outlook section, we present possible future research directions to realise macroscopic steady states with a circulating probability current in an externally driven three-level system. Such a scenario is unique to non-equilibrium systems and prohibited by detailed balance in an equilibrium framework. Furthermore, we present some preliminary calculations on an antiferromagnetic phase transition in the presence of cavity-mediated fluctuations.

Chapter 1

Theoretical Background and Methods

In this chapter we introduce the Dicke model and its modern experimental realisations in Sec.1.1. In the next section, we review the time-evolution equation of the density matrix (Liouville equation) in an open-system environment and point out differences to unitary time-evolution in Sec. 1.2. We close with a review of fluctuation dissipation relations for quantum Heisenberg-Langevin equations in Sec. 1.3.

1.1. The Dicke model and its experimental realizations in cavity quantum electrodynamics

The Dicke model is the generic model for atom-light interactions. It allows the investigation of collective radiation of an ensemble of atoms (superradiance) in a very simple and yet experimentally relevant scenario. Originally introduced in 1954 by Robert Dicke [51] it bears now thousands of citations and has sparked intensive theoretical investigations and diverse research efforts into collective radiative phenomena for decades. For a review from 2011 on recent developments of the Dicke model in quantum optics, see [52] and for a review on superradiance in the Dicke model up to the 1980s, see [53]. A historical overview and a detailed description of the progress and evolution of describing atom-light interactions in terms of the Dicke model can be found in the PhD thesis [54]. Here we restrict our review to a minimum of essential features associated with the Dicke Hamiltonian. We follow in particular the modern reviews [52, 54, 55, 56, 53] .

The phase transition in the Dicke model is referred to as a superradiane transition. The term super in superradiance[1] refers to two phenomena. The first refers to a transient phenomena of cooperative spontaneous decay of an atomic ensemble that is initially coherently excited with a laser pulse. The second instance of superradiance occurs when the atomic ensemble interacts with a single mode of the light-field in a laser-driven cavity and is a phenomenon of a stationary state in a driven-dissipative system. We will briefly touch upon the first interpretation that was originally considered by Dicke [51] in the next subsection. We briefly review recent experiments, that refer to the second interpretation of superradiance in the last section.

Superradiance as a transient phenomena

First, we briefly touch upon the transient phenomena of superradiance that occurs when N initially excited atoms radiate in phase. For an ensemble of N atoms that radiates

---

[1] The article, *The Super of Superradiance* [55], goes into more detail.

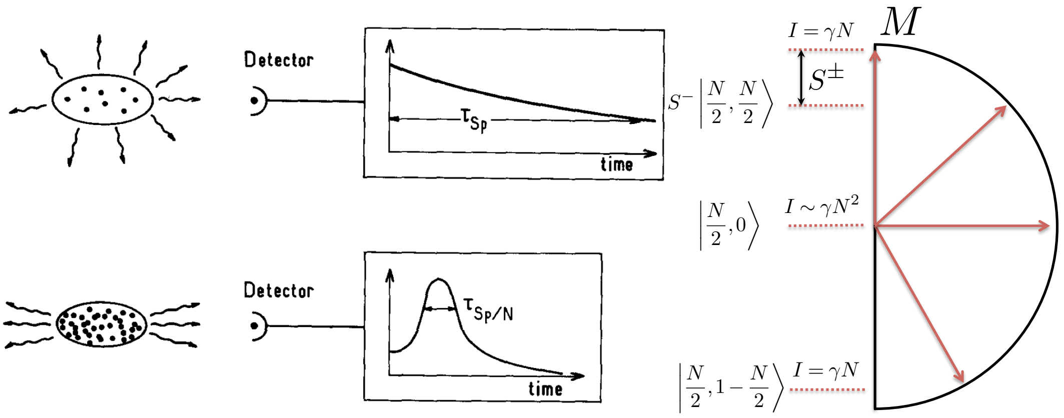

(a) (b)

Figure 1.1.: (a) Illustration of incoherent emission of radiation with exponentially decaying intensity (top) from an atomic cloud given by Eq. (1.1) and of coherent emission with a short burst of radiation (bottom) from an atomic cloud, given by Eq. (1.2). Figure taken from [53] with very minor adaptions only. (b) Superradiant decay channels for an atomic ensemble in symmetric Dicke states $|S, M\rangle$. There are $N + 1$ symmetric states with a decay rate $I = \gamma(S + M)(S - M + 1)$. Application of the collective spin lowering operator induces the depicted ladder transition in the sector with fixed $S = N/2$.

incoherently such as a thermally excited cloud of atoms, the radiation intensity is

$$\mathcal{I}_{\text{incoherent}} \sim N\hbar\omega_z\gamma \sim N\gamma, \tag{1.1}$$

where γ is the decay rate for a single atom and ω_z is the transition energy of some atomic level involved in the decay. If the atoms however radiate together, there can be an enhanced decay rate such that $\gamma_{\text{coherent}} = N\gamma$. The intensity then behaves as

$$\mathcal{I}_{\text{coherent}} \sim N\hbar\omega_z\gamma_{\text{coherent}} \sim N^2\gamma. \tag{1.2}$$

That is, a coherent atomic sample can radiate at an intensity that is N times stronger than that of an incoherent atomic sample. This also means that they radiate their energy N times faster $\tau \sim 1/\gamma_{\text{coherent}} \sim 1/(N\gamma)$ in a flash of energy, see Fig. 1.1a. Classically this is explained in the picture of having N antennae radiate in phase where the electric fields of all atoms add up such that their intensity is proportional to the electric field squared [53, 55].

From a quantum mechanical point of view, the enhancement of radiation can be explained when considering an atomic ensemble that collectively shares excitations. Consider a cloud of atoms whose extension (R) is much smaller than the wavelength (λ_z) of radiation $R \ll \lambda_z$. If initially the ensemble is in its ground-state $|\downarrow, \downarrow, \dots\rangle$ and one photon is absorbed by the atomic cloud, it is not possible to tell which atom is actually excited. Consequently, the state of the atomic sample is expressed as a coherent superposition of all states with a single excitation. For single-photon absorption this state is

$$|N/2, N/2 - 1\rangle = S^+ |\downarrow, \downarrow, \downarrow, \dots\rangle = \mathcal{N} \left(|\uparrow, \downarrow, \downarrow, \dots\rangle + |\downarrow, \uparrow, \downarrow, \dots\rangle + |\downarrow, \downarrow, \uparrow, \dots\rangle + \dots \right), \tag{1.3}$$

and the associated radiation rate is $I(N/2, N/2 - 1) \sim \gamma N$. That is, the decay rate of a single atomic excitation is enhanced by a factor N in comparison to the case of storing a single excitation in a single atom. This phenomenon is known as single-photon superradiance [55, 57].

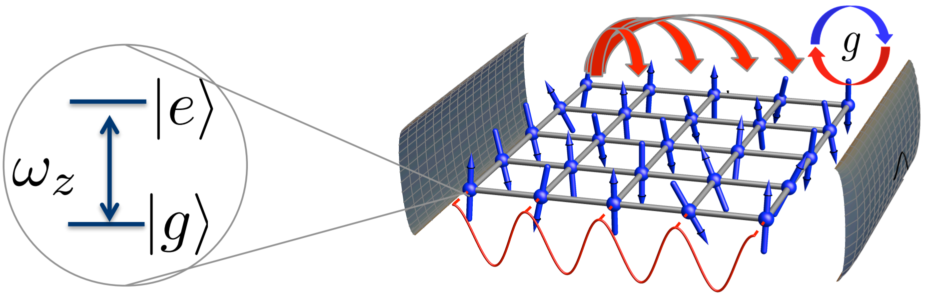

Figure 1.2.: Possible experimental setup for a realisation of the Dicke model. An ensemble of two level atoms (illustrated as spins) interact with a single quantised mode of the radiation field (red line) in a cavity with an atom-light coupling strength g. The excited state e and ground-state g are separated by an energy splitting of ω_z. Red arrows indicate the infinite-range atom-atom interaction mediated by the photons. The cavity mode function is commensurate with the intracavity lattice.

More generally, Dicke states are symmetrised collective angular momentum states $|S,M\rangle$ that are highly entangled [58]. For example, for two atoms, the symmetrised Dicke states correspond to the three spin $S=1$ triplet states $\{|\uparrow\uparrow\rangle, |\uparrow\downarrow\rangle + |\downarrow\uparrow\rangle, |\downarrow\downarrow\rangle\}$. Focusing on the maximum spin angular momentum state with cooperation number $S = N/2$, with N even, and taking the z-direction as the spin quantisation axis, M is constrained to the values $M \in \{-N/2, -N/2+1 \ldots, 0, \ldots, N/2\}$. M then measures the difference of atoms in the excited and the ground-state. Symmetric Dicke states can be constructed by successive application of the collective spin lowering operator S^- as

$$S^z |S,M\rangle = M |S,M\rangle, \tag{1.4}$$

$$S^2 |S,M\rangle = S(S+1) |S,M\rangle, \tag{1.5}$$

$$S^- |S,M\rangle = \sqrt{S(S+1) - M(M-1)}\, |S, M-1\rangle. \tag{1.6}$$

It can then be understood that the radiation is channelled to the $(N+1)$ collective states instead of the 2^N states for an incoherent ensemble of two-level atoms. In general, the rate of emission for the symmetric Dicke state is (see e.g. [56])

$$I(S,M) = |\langle S, M-1| S^- |S,M\rangle|^2 \gamma = \gamma(S+M)(S-M+1). \tag{1.7}$$

An illustration of the superradiant decay channels is given in Fig. 1.1b. From Eq. (1.7) it can be seen that for $|N/2, 0\rangle$ the radiation rate is close to its maximum and given as

$$I(N/2,0) = \gamma \left(N^2/4 + N/2\right) \sim \gamma N^2. \tag{1.8}$$

Superradiance as a thermodynamic phase transition

Here, we discuss the second instance of superradiance that is concerned with understanding cooperative atomic radiation as a property of a stationary non-equilibrium state. The Dicke model considers the coupling of an ensemble of N atoms with a single quantised mode of the light-field. It therefore extended the prototypical interaction of a single mode of the light-field with a single atom to the many atom case to take into account cooperative radiation of a many-body system. The Dicke Hamiltonian is

$$H = \omega_0 a^\dagger a + \omega_z S^z + \frac{g}{\sqrt{N}}(a + a^\dagger)(S^+ + S^-), \tag{1.9}$$

where ω_0 is the frequency of the single-mode cavity with cavity photon creation operator $a^\dagger$. Here, ω_z is the level splitting of the two-level atoms and g is the single photon atom-light coupling strength

$$g = \omega_z d_{eg} \sqrt{\frac{2\pi\hbar}{\omega_0}} \sqrt{\frac{N}{V}} \tag{1.10}$$

related to the dipole element d_{eg} of the two atomic levels. The collective spin operators are

$$S^+ = \sum_{\ell=1}^{N} \sigma_\ell^+ = \sum_{\ell=1}^{N} |e\rangle_\ell \langle g| \,, \quad S^- = \left(S^+\right)^\dagger \,, \quad S_\ell^z = \frac{1}{2} \sum_{\ell=1}^{N} \sigma_\ell^z = \frac{1}{2} \left(|e\rangle_\ell \langle e| - |g\rangle_\ell \langle g|\right) \tag{1.11}$$

and e, g is the excited and the ground-state of a two-level atom, respectively. The spin-photon coupling strength is typically phase dependent as $g(\boldsymbol{r}_\ell) = \psi(\boldsymbol{r}_\ell) g$, where $\psi(\boldsymbol{r}_\ell)$ is the cavity mode function. When the intracavity lattice is commensurate with the cavity mode function, all atoms experience the same coupling strength such that $g(\boldsymbol{r}_\ell) = const.$. An illustration is seen in Fig. 1.2. V is the quantization volume for the modes of the electric field, which is the cavity volume. The Dicke Hamiltonian commutes with the collective spin operator S^2 and therefore, its eigenvalues S, see Eq. (1.5). All dynamics takes place in a subspace associated to a fixed value S which is typically taken to be at its maximum $S = N/2$.

We consider the Dicke model in its thermodynamic limit $N \to \infty, V \to \infty$ with a fixed atomic density of the atoms $N/V = const.$ In this sense, the atom-light coupling is fixed in an experimental setup by the density of atoms, see Eq. (1.10).

In the form of Eq. (1.9) the Dicke Hamiltonian supports an inversion symmetry

$$(a, a^\dagger, S^+, S^-) \to (-a, -a^\dagger, -S^+, -S^-) \tag{1.12}$$

that is spontaneously broken at the superradiance transition. The Dicke model supports two different phases for $g \ll (\omega_0, \omega_z)$ and for $g \gg (\omega_0, \omega_z)$. We will now review their well-known properties of these phases. A similar discussion can e.g. be found in [54]. The phase transition can be described in a semiclassical description, where the collective angular momentum spin operators are replaced with their expectation values.

$$a \to \langle a \rangle \sqrt{N}, \quad S^z \to \frac{N}{2} \langle S^z \rangle \,, \quad S^\pm \to N \langle S^\pm \rangle \,. \tag{1.13}$$

In this sense, it is now understood that the atom-light coupling in Eq. (1.9) needs to be rescaled with a factor of $1/\sqrt{N}$, such that all terms correctly scale with N in the thermodynamic limit. The order parameter of the transition is the macroscopic expectation value of the cavity mode $\langle a \rangle$ and, equivalently the macroscopic polarization of the spins $\langle S^x \rangle = \langle S^+ \rangle + \langle S^- \rangle$.

For $g = 0$, eigenstates of the Dicke Hamiltonian are the simultaneous eigenstates of S^z and S^2 which are denoted as $|S, M\rangle$. The state with minimum energy for $\omega_z > 0$ is given by the state where all spins are in the ground state and the state of the photon field is the vacuum, such that $\langle a \rangle = \langle a^\dagger \rangle = \langle a^\dagger a \rangle = 0$. The atom-cavity state is then the product state of the spin and the zero-photon Fock-state

$$|\text{empty}\rangle = |\downarrow\downarrow\downarrow, \ldots\rangle \, |0\rangle \,, \quad \langle a \rangle = 0, \quad \langle S^z \rangle = -1, \quad \langle S^\pm \rangle = 0. \tag{1.14}$$

Please note that we have rescaled the macroscopic expectation values as in Eq. (1.13) to make the scaling with N explicit. In this case, the atom-cavity system is devoid of excitations and is referred to as the empty atom-cavity state. For non-zero atom-light coupling strengths $g \ll (\omega_z, \omega_0)$, the coupling of the spins to the vacuum mode of the cavity with $\sim \frac{g}{\sqrt{N}}(a + a^\dagger)(S^+ + S^-)$ will trigger transitions in the spin-sector associated to S^2 as $S^\pm |S, M\rangle \sim |S, M \pm 1\rangle$ and the states of the atom and of the cavity hybridise to form joined eigenstates, so called polariton modes.

For $g \gg (\omega_z, \omega_0)$, eigenstates in the spin-sector of the Hamiltonian are eigenstates to the spin-operator $(S^+ + S^-) = S^x$. The total spin quantum number S is still conserved. The cavity is in a displaced harmonic oscillator state [59] with

$$\langle a \rangle \neq 0, \quad \langle S^z \rangle = 0, \quad \langle S^x \rangle = \pm 1, \tag{1.15}$$

where the spin ensemble is thus in a state with macroscopic polarization in the spin x-direction that breaks the inversion symmetry in Eq. (1.12). This state is known as the superradiant state.

In this sense, the Dicke phase transition resembles a quantum phase transition separating a paramagnetic state for $g \ll g_c$ from a ferromagnetic state for $g \gg g_c$ with polarization in the x-direction. The description of the predicted phase transition in a semiclassical, meanfield framework is exact in the thermodynamic limit of a large number of atom-cavity emitters, since the model is understood as an infinite-range ferromagnet. The infinite-range atom-atom interaction is mediated by the cavity photons.

The equilibrium statistical mechanics of a thermal ensemble of atoms that interacts with a quantized radiation field with both co- $(S^+ a + h.c.)$ and counterrotating $(S^+ a^\dagger + h.c.)$ terms present was described by Hepp and Lieb [60], Hioe [61] and Carmichael, Walls and Gardiner [62]. They predicted a classical phase transition in a thermal ensemble at

$$g_c(T) = \frac{1}{2}\sqrt{\omega_0 \omega_z}\sqrt{\frac{1}{\tanh\left(\frac{\omega_z/2}{k_b T}\right)}}, \quad (\hbar = 1). \tag{1.16}$$

It can be seen that the critical spin-photon coupling g_c is on the order of the optical frequencies (ω_z, ω_0) in the system. However, it cannot become infinitely large since the dipole element of the excited and groundstate is related to the frequency splitting of the two-level atom via a sum-rule. It was shown later [63] that this sum-rule prohibits the spin-photon coupling from becoming large enough to realize the superradiance condition given in Eq. (1.16). This became known as the no-go theorem.

It was later realised that the no-go theorem can be circumvented in a driven system [26]. A driving scheme that makes the coupling strength g tunable by an external laser with Rabi-frequency Ω as $g^{\text{eff}}(\Omega)$ is not subject to a sum-rule that applies for the bare Hamiltonian parameters. The superradiance transition is therefore restored in a driven system. In a cavity that is driven from the outside and where photon modes can escape the cavity mirrors with a rate κ, the critical coupling for the superradiance transition changes to [26]

$$g_c = \frac{1}{2}\sqrt{\frac{\omega_z(\kappa^2 + \omega_0^2)}{\omega_0}}, \tag{1.17}$$

which shows that in comparison to the zero-temperature limit of the thermal transition $g_c(T \to 0) = 1/2\sqrt{\omega_0 \omega_z}$, the critical coupling is shifted to higher values to compensate for the losses. In chapter 2 and chapter 4, we will show how this coupling changes in a driven-dissipative setting when atomic excitations can spontaneously decay as well.

The no-go-theorem for the superradiance transition in cavity quantum electrodynamics

The no-go theorem states that the classical and the quantum Dicke superradiance transition for an ensemble of real atoms coupled to a single bosonic lightmode, see Eq. (1.9), is prohibited from occuring for real atoms that couple to the light field with their electric dipole moment. This was realised for the first time in 1975 in [63] where the authors prove that the phase transition is an artefact of neglecting a diamagnetic term $\sim \boldsymbol{A}^2$ in the light-matter Hamiltonian from which the Dicke Hamiltonian is derived, where $\boldsymbol{A}$ is the vector potential of the electromagnetic field. We briefly summarize their arguments. Keeping the diamagnetic contribution, adds an extra term $\sim \epsilon$ [63] to the Dicke Hamiltonian

$$H = \omega_0 a^\dagger a + \omega_z S^z + \frac{g}{\sqrt{N}}(a + a^\dagger)(S^+ + S^-) + \epsilon(a + a^\dagger)(a + a^\dagger). \tag{1.18}$$

This now shifts the critical coupling strength for the superradiance transition, which upon rewriting the atom-light coupling g with Eq. (1.10), is written as [63]

$$d_{eg}^2 \omega_z > \frac{e^2 \hbar}{2m}. \tag{1.19}$$

However, the relative strength of the electric dipole element d_{eg} and the frequency of the level splitting of the atoms ω_z are not independent from another. It can be shown from elementary quantum mechanical calculations that the dipole coupling strength is restricted by a sum-rule known also as the Thomas-Reiche-Kuhn sum rule. This restriction can be written in the form (see e.g. [56])

$$d_{eg}^2 \omega_z < \frac{e^2 \hbar}{2m}. \tag{1.20}$$

which exactly contradicts the condition for a superradiant state given in Eq. (1.19).

The diamagnetic term can typically safely be neglected when predicting general interaction features of matter-light couplings below the critical coupling strength. Its contribution can be estimated by comparing its strength with the photon frequency, [56]. This is also evidenced by the twenty-years worth of experiments and comparisons with predictions from the Dicke model for the non superradiant regime.

As mentioned above, the no-go theorem is overcome by 'synthetic cavity quantum electrodynamics' that is by realising an experimentally tunable coupling strength $g \to g^{\text{eff}}(\Omega)$, that depends on an external driving strength Ω [26]. More recently, it was shown that it is also possible to construct electronic circuit systems whose dynamics can be mapped onto the Dicke model. In the field of circuit quantum electrodynamics (circuit-qed) a collection of N Cooper pair boxes with an atom-like energy structure function as artificial atoms. In comparison to real atoms that couple with their electric dipole moment to the light field, the artifical atoms are coupled capacitively to a resonator. For a circuit-qed system, it was proven [64] that a quantum critical point for the spontaneous decay of the vacuum into the superradiant state exists as the coupling parameters are not restricted by an oscillator strength sum rule, meaning that there is no 'no-go-theorem' in circuit qed. Furthermore, in contrast to synthetic cavity qed where time-dependent pump-lasers dress the system and the Dicke Hamiltonian is realised only in a rotating-frame, circuit-based Hamiltonians are inherently time-independent.

In the next section we briefly present successful experimental engineering and observations of the superradiance transition in cavity qed systems.

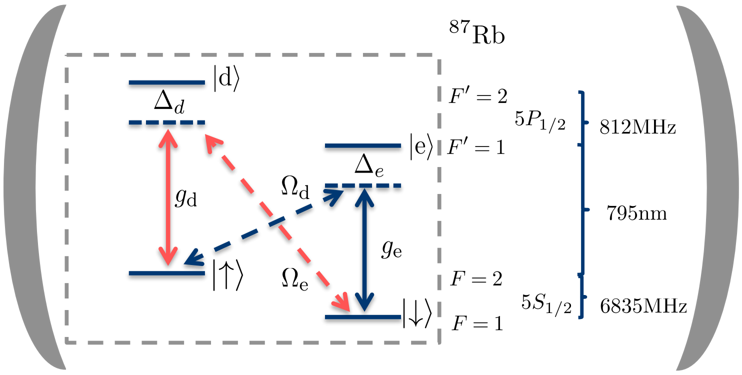

Figure 1.3.: Proposed level scheme [26] for a 'synthetic cavity QED' to circumvent the no-go theorem. The two-level states are modelled by the ground-states of a hyperfine structure $\{F, F'\}$ of ^{87}Rb that are coupled off-resonantly (Δ_e, Δ_d) to higher-lying states $|d\rangle$ and $|e\rangle$ with two lasers of Rabi-frequency Ω_d and Ω_e. A single mode cavity couples these states with an atom-light strength of g_s and g_e. The cavity assisted Raman transitions lead to an effective atom-light coupling of the ground-states $\{|\uparrow\rangle, |\downarrow\rangle\}$ with $g^{\text{eff}} = \frac{g_{\text{d,e}}\Omega_{d,e}}{2\Delta_{\text{d,e}}}$ that can be experimentally tuned by the laser Rabi-frequency and is thus not limited by the Thomas-Reiche-Kuhn sum rule. Red arrows generate terms $g^{\text{eff}}(\Omega_e)/\sqrt{N}(aS^- + a^\dagger S^+)$, blue arrows generate contributions of $g^{\text{eff}}(\Omega_d)/\sqrt{N}(a^\dagger S^- + aS^-)$. These terms describe light-scattering between the laser and the cavity mode. Figure redrawn from [26] with adaptions.

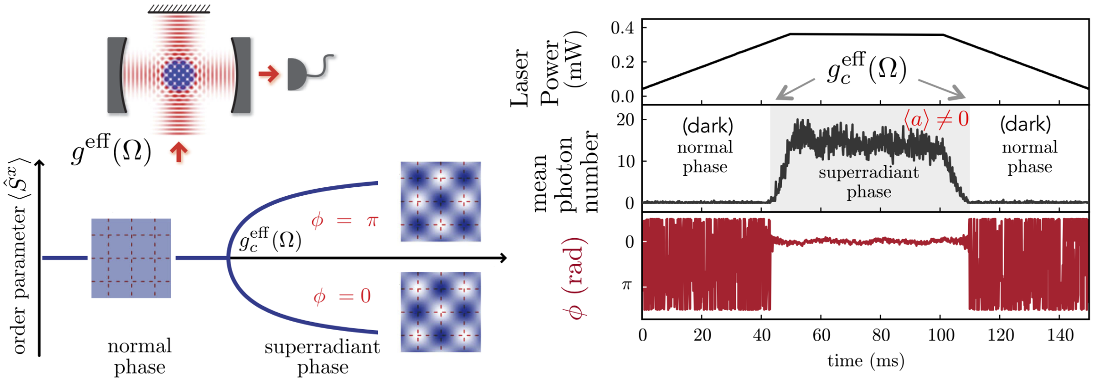

(a) (b)

Figure 1.4.: Experimental investigation [65] of symmetry breaking at the Dicke superradiance phase transition. (a) (top, figure taken from [65] (adapted)) Typical experimental setup of a Bose-Einstein-Condensate in a laser-driven cavity. (bottom, Figure taken from [28] (adapted with annotations)). The cavity-output can be monitored experimentally. Superradiance transition corresponds to a spatial self-organisation of the atoms (see text). (b) At the critical threshold coupling for the superradiance transition, $g^{\text{eff}} = g_c^{\text{eff}}$, the cavity mode is macroscopically occupied and light starts leaking through the cavity mirrors. The cavity phase and the phase of the laser are locked together in the superradiant regime. Figure taken from [28] (minor adaptions).

Modern Experimental Realisations of the Dicke superradiance transition

An ingenious scheme to engineer tunable and strong atom-light coupling strengths was proposed in 2007 by Dimer *et al.* [26] to circumvent the no-go theorem. They proposed a two-photon driving scheme containing four atomic levels that are coupled by a single cavity mode and two external driving fields of a laser. Adiabatically eliminating two of these four states, leaves a ground-state manifold of two states $\{|\uparrow\rangle, |\downarrow\rangle\}$ that are strongly coupled by two independent Raman processes involving the cavity mode and an external driving laser to realise both co- and counter-rotating terms of the atom-light coupling as

$$H_{\text{atom-light}} = \frac{g^{\text{eff}}(\Omega_e)}{\sqrt{N}}(aS^- + a^\dagger S^+) + \frac{g^{\text{eff}}(\Omega_d)}{\sqrt{N}}(a^\dagger S^- + aS^-), \tag{1.21}$$

where $g^{\text{eff}}_{e,d}(\Omega_{e,d})$ is an effective and tunable atom-light strength and $\Omega_{e,d}$ is the Rabi-frequency of the pump-laser. A detailed description of the level scheme is given in Fig. 1.3. In Sec. 3.4.4 of this thesis we will modify Dimer's original pumping scheme to allow for an an additional effective atom-atom interaction of the states $|\uparrow\rangle_i$ at site i and the state $|\uparrow\rangle_j$ at site j.

The first experimental realization of the superradiance transition was achieved in 2010 by coupling a motional degree of freedom of a Bose-Einstein condensate to a cavity [65]. More specifically they mapped the the four atomic levels depicted in Fig. 1.3 to finite momentum modes $|p_x, p_z\rangle = \{|0,0\rangle, |\pm\hbar k, \pm\hbar k\rangle\}$ of a Bose-Einstein condensate that is placed in a transversely driven cavity. In this effective model, the superradiance transition manifests itself as spatial self-organisation of the atoms in a density pattern characterised by the cavity wavevector k_c, see Fig. 1.4a. This breaks the homogeneous gas density and corresponds to the inversion symmetry breaking of the Dicke model.

We briefly describe now the experimental setup [65] depicted in Fig. 1.4. For $g^{\text{eff}}(\Omega) < g^{\text{eff}}_c(\Omega)$ the cavity typically is in its vacuum state, only negligibly occupied by thermal photons $n_{thermal} \ll 1$. The atoms are subject to an intracavity lattice $V_{\text{pump}}(z)$ in the $z-$direction that is created by the pump laser far off the atomic resonance. With increasing driving strength, the atoms scatter more pump photons into the cavity. This builds up a cavity field which itself induces an optical lattice $V \sim \cos^2(k_c x)$ in x-direction that exerts a dipole force on the atoms that influences the atomic motion. This rearrangement of the atomic distribution amplifies scattering into the cavity, and at a critical driving strength $g^{\text{eff}} = g^{\text{eff}}_c$ the scattering into the cavity is maximised which leads to a two-dimensional intracavity optical lattice that consists of the interference of the potential from the laser light V_{pump} and a coherent cavity field V_{sl} as $V(x,z) = V_{\text{sl}}(x,z) + V_{\text{pump}}(z)$. $V(x,z)$ pins the atoms spatially in one of two checkerboard patterns, as depicted in Fig. 1.4a (see experiments in [66, 67] with thermal atoms and experiment [65] with a BEC and theory prediction [68]). Experimentally, this can be observed since light starts to leak out from the cavity mirrors as seen in Fig. 1.4b. In the superradiant phase, we denote $\langle a\rangle = \alpha = |\alpha|e^{i\phi}$, with ϕ as the phase of the cavity photons and α as the coherent classical state of the cavity light field. The intracavity lattice is then given as [28]

$$V_{\text{sl}}(x,z) = U_0|\alpha|^2\cos^2(k_c x) + g^{\text{eff}}(\alpha+\alpha^*)\cos(\Delta\phi)\cos(k_c x)\cos(k_c z), \tag{1.22}$$

$$V_{\text{pump}}(z) = V_0\cos(k_c z)^2, \tag{1.23}$$

where $V_0 = \hbar\Omega_p/\Delta$ is the potential depth of the retro-reflected standing-wave pump laser with Rabi frequency of the pump Ω_p and $U_0 = g_0^2/\Delta$ is the potential depth created by a far off-resonant laser beam, where g_0 is the bare atom-light coupling strength and Δ is the frequency difference of the pump laser and the atomic two-level splitting. The relative phase $\Delta\phi$ between the pump-laser and the cavity field is locked to either $\Delta\phi = 0$ or to $\Delta\phi = \pi$, see [65] and Fig. 1.4b, and is associated to one of the two atomic checkerboard patterns, reflecting the inversion symmetry breaking of the superradiance transition. A dynamical switching between the two density patterns was investigated in [28].

In 2018 the Dicke superradiance transition was finally realised [44] in an optical cavity with an ensemble of Rydberg atoms and an atomic level structure as seen in Fig. 1.3. Here, the atoms are initially trapped in an intracavity lattice to strongly suppress atomic motion and to maximise the atom-light coupling as the optical lattice is chosen commensurate with the supported cavity modefunction. There is however an important difference between the superradiance transition with momentum states of a BEC and the superradiance transition with a real atomic level structure. While momentum states of a Bose-Einstein condensate are stable, atomic levels are subject to atomic dissipation such as spontaneous emission. This is why the superradiance transition in Eq. (1.17) correctly describes the critical coupling strength for the stable momentum states, whereas corrections need to be taken into account in the case of the atomic level structure. In Chapter 2 we take into account these effects and find (among other things) that the critical superradiance threshold is shifted to higher pump strengths to compensate for losses.

1.2. Time evolution in open quantum optical systems

In section 1.2.1 we review the derivation of a Lindblad master equation for an ensemble of atoms in a cavity that are coupled to the external modes of radiation under the rotating wave, Born and Markov approximations. Crucially, we derive the strength of a collective emission channel that becomes important when the system is in the superradiant state. Our approach is equivalent to an earlier investigation in a wavefunction picture [69]. We will investigate its consequences in detail in chapter 4. In Sec. 1.2.2 we briefly compare equilibrium with driven-dissipative phase transitions. We discuss signatures of phase transitions in quantum optical systems.

1.2.1. Lindblad master equation with coherent and incoherent emission of excitations

[2] Here, we will review the derivation of a Lindblad master equation for an open quantum optics system. A Lindblad equation is the most general, time-local time evolution equation for the density matrix of an open, dissipative system. Specifically, we consider the interaction of an ensemble of atoms in a cavity with the external vacuum modes of the electromagnetic field that function as a bath for the system, as displayed in Fig. 1.5. The system-bath interaction will result in relaxation of atomic excitations into the environment. The atoms can decay individually and incoherently, or they can decay collectively. In general, this leads to a time evolution equation for the density matrix with non-local couplings of the atoms, see Eq. (1.34). Collective decay contributions that add to the single atom decay rates have been derived in the context of single photon sub- and superradiant states [69] in a wave-function formalism. Here, we carry these considerations over to a density matrix formalism and show that a description in terms of Lindblad operators reproduces the results obtained from the wave function picture. The collective loss contribution emerges by allowing all spins to interact with one shared bath. The derivation of a Lindblad master equation with local decay processes can be found in most books in

---

[2] This section (1.2.1) appeared as part of the publication J. Gelhausen and M. Buchhold, Phys. Rev. A **97**, 023807 (2018). Here, we provide significantly more details for the derivation of the Lindblad equation with a non-local decay channel.

quantum optics (see e.g. [70]). Here, we detail how a collective decay contribution can emerge in an optical cavity. This sets the basis for our investigations in chapter 4.

Let us mention that for undriven systems it is generally not expected that the dynamics can be described with a Lindblad equation. The set of approximations and justifications for Lindblad dynamics given below in $\boldsymbol{(a-c)}$ are not generic for condensed matter systems but are adequate for driven two-level systems in quantum optical setups. The time-dependence of the laser drive is sometimes 'hidden' by changing into a frame rotating at the laser frequencies. For example in the case of the driven Dicke model, the atom-light interaction g is dressed by an external pumping laser such that it becomes tunable as $g \to g(\Omega)$, where Ω is the laser Rabi-frequency. The time-dependence of the drive is eliminated in a rotating frame.

The starting point for the Lindblad master equation is the von-Neumann equation in the interaction picture for the density matrix ρ_t that takes into account the degrees of freedom for the system and the degrees of freedom for the bath

$$\partial_t \rho_t = -i[H_t^{BS}, \rho_t], \quad (\hbar = 1). \tag{1.24}$$

The Hamiltonian H_t^{BS} specifies the system bath interaction. We assume a linear coupling of bath to system operators and perform a rotating wave approximation where we drop terms $\sim \sigma_\ell^+ b_k^+, \sim \sigma_\ell^- b_k$. We comment on the approximation in $\boldsymbol{(a)}$, see below. In the interaction picture, the system-bath interaction is cast into the form

$$H_t^{BS} = \sum_k \sum_{\ell=1}^{N} \left(\varepsilon_{k,\ell} \sigma_\ell^+ b_k e^{i(\omega_z - \nu_k)t} + \varepsilon_{k,\ell}^* b_k^\dagger \sigma_\ell^- e^{-i(\omega_z - \nu_k)t} \right). \tag{1.25}$$

We have performed the unitary transformation

$$H_t^{BS} = U_t^\dagger H_{\mathrm{BS}} U_t, \quad U_t = \exp\left(-i\left(H^S + H^B\right)t\right), \tag{1.26}$$

where the bath Hamiltonian $H^B = \sum_k \nu_k b_k^\dagger b_k$ consists of harmonic oscillators with mode frequency ν_k and mode index k. The non-interacting system Hamiltonian $H^S = \frac{\omega_z}{2} \sum_{\ell=1}^{N} \sigma_\ell^z$ contains only the frequency splitting of the two-level system as ω_z. Here, the coupling strength to the bath is given as $\varepsilon_{k,\ell} = \varepsilon_k e^{-i\boldsymbol{k}\boldsymbol{r}_\ell}$, with ε_k taking into account the frequency dependence of the kth radiation mode that is given by $\nu_k = ck$. Typically it is a good approximation (see later) to assume $\epsilon_k \sim \sqrt{\gamma/2\pi}$, where γ is the spontaneous decay rate of an atom.

In the following we invoke three key approximations, mentioned in $\boldsymbol{(a)}, \boldsymbol{(b)}$, and $\boldsymbol{(c)}$ for the time-evolution of the density matrix that are typically carried out in quantum optical systems. These are described in great detail in [71] by Daley. Here, we follow his justifications:

- $\boldsymbol{(a)}$ Rotating wave approximation (RWA) on system-bath interactions corresponds to neglecting co-rotating terms $\sim \sigma_\ell^+ b_k^+, \sim \sigma_\ell^- b_k$ in Eq. (1.25). By performing this approximation, one defines explicitly a slow $(1/(\omega_z - \omega_B))$ and a fast $(1/(\omega_z + \omega_B))$ timescale, where ω_B is a typical bath timescale. One is interested in coarse graining the dynamics to the slow timescale and blurring out what happens on fast timescales because their effects will, through the fast oscillations, average to zero. The perturbation theory is then carried out on timesteps associated to the coarse-grained slow dynamics.
- $\boldsymbol{(b)}$ The Born approximation. This approximation assumes that there are no strong correlations between the bath and the system, which allows to decouple the system and

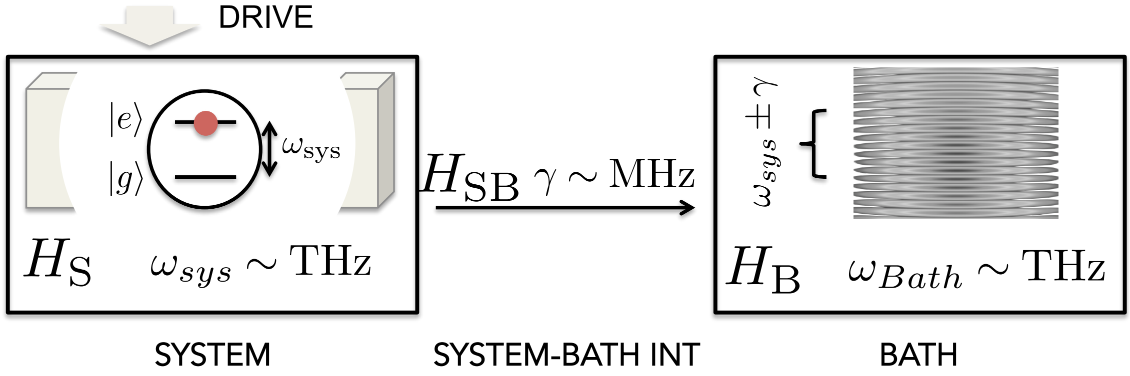

Figure 1.5.: Illustration of system, bath and system-bath coupling. The system we consider consists of an ensemble of atoms in a cavity, described by H_S. A typical frequency scale of the system is given by $\omega_{sys} = \omega_z$ which is the frequency splitting of the two-level atom which are typically in the THz regimes for optical systems. A lifetime of an optical excitation is associated to a much smaller frequency scale $\gamma \sim$ MHz and represents the timescales generated by the system and environment interaction. The system frequency ω_{sys} can dominate all other frequency scales and sets the frequency at which the system modes couple to the bath modes spread by a narrow window given by γ.

reservoir density matrix as $\rho_t = \rho_t^S \otimes \rho_t^B$. This is justified as $\gamma \ll \omega_{\rm z}, \omega_B$. Meaning that the frequency scales relevant for the system and bath dynamics $(\omega_B, \omega_{\rm z})$ are much larger than the dynamics induced by the system-environment interaction (γ). This is important because the system will couple strongly to the bath only in a narrow frequency window of width γ centered around system frequency, see Fig. 1.5.

(c) The Markov approximation consists of two parts. In the first step, one assumes that the bath density matrix stays time-independent $\rho_t^B = \rho_{t=0}^B$, which follows from $\gamma \ll \omega_{\rm B}$ meaning that relaxation timescales of the system $1/\gamma$ are much larger than any timescale associated to correlation functions in the bath. Meaning that the bath will have relaxed back to its equilibrium state on a much faster timescale than given by $(1/\gamma)$ induced by system-reservoir interactions. The second part is an assumption on the system density matrix. Namely that the dynamics of the system stays unaffected by its interaction with the reservoir at earlier times. Practically, an emitted photon from a decaying atom will never return to interact with the system again and the system irreversibly dissipates energy into the environment. As mentioned earlier, the bath correlation functions decay rapidly in time. The system and bath coupling is then assumed frequency independent on these short time scales, as $\epsilon_k \to \sqrt{\gamma/2\pi}$, meaning that the system couples strongly to the bath only on the frequency scales associated with the system.

We review how Eq. (1.24) is generally solved by taking into account second-order perturbations of the system-reservoir coupling H_t^{BS}. Formally, one can write its solution

$$\rho_t = \rho_0 - i\int_0^t dt'[H_{t'}^{BS}, \rho_{t'}], \tag{1.27}$$

which can be re-inserted back into the von-Neumann equation (1.24) to obtain

$$\partial_t \rho_t = -i[H_t^{BS}, \rho_0 - i\int_0^t dt'[H_{t'}^{BS}, \rho_{t'}]]. \tag{1.28}$$

At this stage, one typically invokes the Born-approximation ***(b)*** that assumes small system reservoir correlations, forbidding large system-reservoir entanglement. We assume therefore a factorization, see ***(b)***, as

$$\rho_t = \rho_t^S \otimes \rho_{,0}^B, \tag{1.29}$$

where we assume the bath to be stationary as $\rho_{,t}^B \approx \rho_{,0}^B$, see ***(c)***, meaning that the reservoir is large and relaxes back to its initial state much faster than any dynamics induced by the system-reservoir interaction. Tracing out the bath degrees of freedom, one obtains

$$\mathrm{Tr}_B[\rho_t] = \mathrm{Tr}_B[\rho_t^S \otimes \rho_{,0}^B] = \rho_S, \tag{1.30}$$

where $\mathrm{Tr}_B[\rho_B] = 1$. We assume further that, at the initial time $t = 0$ the system density matrix commutes with $\mathrm{Tr}\{[H_t^{BS}, \rho_0]\} = 0$ [71]. We assume in the next step the Markov approximation, stating that the density matrix of the system is memoryless, $\rho_{t'}^S = \rho_t^S$, see ***(c)***. The time-evolution equation (1.28) is now written as

$$\begin{aligned}\partial_t \rho_t^S &= -\mathrm{Tr}_B\{[H_t^{BS}, \int_0^t dt' [H_{t'}^{BS}, \rho_t]]\} \\ &= \int_0^t dt'\ \mathrm{Tr}_B \left[\left(H_t^{BS} \rho_t H_{t'}^{BS} + H_{t'}^{BS} \rho_t H_t^{BS} \right) - H_t^{BS} H_{t'}^{BS} \rho_t - \rho_t H_{t'}^{BS} H_t^{BS} \right]\end{aligned} \tag{1.31}$$

To evaluate the trace over the bath degrees of freedom, we note that the Hamiltonian H^{BS} always appears quadratically in Eq. (1.31). Consistent with the RWA ***(a)***, we drop terms $\sim \sigma_\ell^+ b_k^+$ and $\sim \sigma_\ell^- b_k$ on the system-reservoir interaction. Additionally, the average single particle population of the reservoir modes k is given as $\bar{n}_k \equiv \bar{n}(\nu_k) = 1/\left(e^{\beta\hbar\nu_k} - 1\right)$. Cavity quantum optics typically operates also in the optical frequency regime which is in the few hundreds of 10^2 THz regime whereas the radiation modes at room temperature are typically only few THz. There is thus a separation of two orders of magnitude which means that $\hbar\omega_z/k_bT \gg 1$ and consequently we will treat the reservoir as a zero-temperature reservoir since $\bar{n}(\omega_z) = 0$ and

$$\mathrm{Tr}_B[b_k b_{k'}^\dagger \rho_B] = \delta_{kk'}(1 + \bar{n}_k) \sim \delta_{kk'}, \tag{1.32}$$

$$\mathrm{Tr}_B[b_k^\dagger b_{k'} \rho_B] = \delta_{k,k'} \bar{n}_k \sim 0. \tag{1.33}$$

With these approximations, the time evolution for the system from Eq. (1.31) is found to be

$$\partial_t \rho_t^S = \int_0^t dt' \sum_{k,\ell,\ell'} |\varepsilon_k|^2 e^{-i(\boldsymbol{k}-\boldsymbol{k}_0)(\boldsymbol{r}_{\ell'}-\boldsymbol{r}_\ell)} \left[\sigma_{\ell'}^- \rho_t \sigma_\ell^+ \left(\zeta_k + \zeta_k^*\right) - \rho_t \sigma_{\ell'}^+ \sigma_\ell^- \zeta_k^* - \sigma_{\ell'}^+ \sigma_\ell^- \rho_t \zeta_k \right], \tag{1.34}$$

where we have made explicit that in the Dicke model all momenta are expressed with respect to the cavity wave vector $\boldsymbol{k}_0$ and we have collected temporal phase factors as

$$\zeta_k(t' - t) = \exp\left(-i(\omega_z - \nu_k)(t' - t)\right). \tag{1.35}$$

For a large number of atoms, the sum over all atoms and momenta is only non-vanishing for two different contributions. Either for $\ell = \ell'$, which describes the uncorrelated, single atom decay. Or for $|\boldsymbol{k} - \boldsymbol{k}_0| \approx 0$, which describes correlated decay into modes near the cavity wave vector. We note that contributions with $\ell \neq \ell'$ are generally suppressed by the volume factor $\propto 1/V$, which is implicit in the atom-light coupling constant ε_k. We single out the uncorrelated single atom loss, which has been treated in many previous works (e.g.

see [72]) and find

$$
\begin{aligned}
\partial_t \rho^S(t) =& \gamma \sum_{\ell=1}^{N} \left(\sigma_\ell^- \rho_t \sigma_\ell^+ - \frac{1}{2}\{\sigma_\ell^+ \sigma_\ell^-, \rho_t\} \right) \\
&+ \int_0^t dt' \sum_{k,\ell' \neq \ell} e^{-i(\boldsymbol{k}-\boldsymbol{k}_0)(\boldsymbol{r}_{\ell'}-\boldsymbol{r}_\ell)} |\varepsilon_k|^2 \left(\sigma_{\ell'}^- \rho_t \sigma_\ell^+ (\zeta_k + \zeta_k^*) - \rho_t \sigma_{\ell'}^+ \sigma_\ell^- \zeta_k^* - \sigma_{\ell'}^+ \sigma_\ell^- \rho_t \zeta_k \right)
\end{aligned}
\tag{1.36}
$$

For the second contribution to Eq. (1.36), we focus only on the collective part that arises from wave vectors $|\boldsymbol{k}-\boldsymbol{k}_0| \approx 0$. We proceed by calculating the weight of the associated delta function

$$
\int_0^t dt' \sum_k |\varepsilon_k|^2 e^{-i(\boldsymbol{k}-\boldsymbol{k}_0)(\boldsymbol{r}_{\ell'}-\boldsymbol{r}_\ell)} \zeta_k \approx \int_0^t dt' \sum_k |\varepsilon_k|^2 \frac{(2\pi)^3}{V} \delta(\boldsymbol{k}-\boldsymbol{k}_0) \zeta_k \tag{1.37}
$$

We assume that the bath modes lie dense and work in the continuum limit to use the replacements

$$
\delta(\boldsymbol{k}-\boldsymbol{k}_0) = \frac{1}{2\pi} \int_{-R}^{R} e^{i(k-k_0)r} \delta(\theta_k - \theta_{k_0}) \delta(\phi_k - \phi_{k_0}) dr \frac{1}{k^2 \sin(\theta_k)} \tag{1.38}
$$

$$
\sum_k \to \frac{V}{(2\pi)^3} \int_0^\infty dk k^2 \int_0^\pi \sin(\theta_k) d\theta_k \int_0^{2\pi} d\phi_k. \tag{1.39}
$$

which leads to the integral

$$
\int_0^t dt' \sum_k |\varepsilon_k|^2 e^{-i(\boldsymbol{k}-\boldsymbol{k}_0)(\boldsymbol{r}_{\ell'}-\boldsymbol{r}_\ell)} \zeta_k \tag{1.40}
$$

$$
\begin{aligned}
&\approx \int_0^t dt' \int_0^\infty dk |\varepsilon_k|^2 \left[\frac{1}{2\pi} \int_{-R}^{R} e^{-i(k-k_0)r} dr \right] e^{i(ck-\omega_z)(t-t')} \\
&= \int_0^t dt' \int_0^\infty dk |\varepsilon_k|^2 \frac{1}{2\pi} \int_{-R}^{R} \exp\left[ic(k-k_0)(t-t'-r/c) + ic(k_0-k_z)(t-t') \right] dr \\
&= |\varepsilon_{k_0}|^2 \int_0^t dt' \int_{-R}^{R} dr \frac{1}{2\pi} \frac{2\pi}{c} \delta(t-t'-r/c) \exp\left[ic(k_0-k_z)(t-t') \right] \\
&= |\varepsilon_{k_0}|^2 \int_{-R}^{R} dr \frac{1}{2c} \frac{R}{c} |\varepsilon_{k_0}|^2 \exp\left[ic(k_0-k_z)r/c \right] \\
&= |\varepsilon_{k_0}|^2 \frac{\sin\left((k_0-k_z)R\right)}{c(k_0-k_z)}
\end{aligned}
\tag{1.41}
$$

Here R is the radius of the atomic cloud in the cavity which is much larger than the cavity wavelength. In the last line we have used that $|\varepsilon_k|^2$ does not vary significantly around $k \sim k_0$ and pull it out of the integral

$$
\int_0^\infty dk |\varepsilon_k|^2 \exp\left[ic(k-k_0)(t-t'-r/c) \right] = \frac{2\pi}{c} \delta(t-t'-r/c) |\varepsilon_{k_0}|^2. \tag{1.42}
$$

As a result, one obtains

$$
\int_0^t dt' \sum_k |\varepsilon_k|^2 e^{i(\boldsymbol{k}-\boldsymbol{k}_0)(\boldsymbol{r}_\ell-\boldsymbol{r}_{\ell'})} \zeta_k = \frac{\sin\left((k_0-k_z)R\right)}{c(k_0-k_z)} |\varepsilon_{k_0}|^2 = \frac{2\pi D(k_z)}{2\pi D(k_z)} \frac{\sin\left((k_0-k_z)R\right)}{c(k_0-k_z)} \frac{|\varepsilon_{k_0}|^2}{|\varepsilon_{k_z}|^2} |\varepsilon_{k_z}|^2
$$

$$
= \gamma \frac{\sin\left((k_0-k_z)R\right)}{c(k_0-k_z)} \frac{|\varepsilon_{k_0}|^2}{2\pi D(k_z) |\varepsilon_{k_z}|^2} \tag{1.43}
$$

$$
= \gamma \frac{3}{8\pi} \left(\frac{\lambda_z^2}{4\pi R^3} \right) \frac{|\varepsilon_{k_0}|^2}{|\varepsilon_{k_z}|^2} \frac{\sin\left((k_0-k_z)R\right)}{(k_0-k_z)} \equiv \gamma\alpha \tag{1.44}
$$

here, the volume of the atomic sample is taken to be $V = 4/3\pi R^3$ and the density of states $D(k_z) = Vk_z^2/\pi^2 c$ and $\gamma = 2\pi|\varepsilon_{k_z}|^2 D(k_z)$. If the difference between the two wavenumbers k_0 and k_z is small, one can expand the sin function to first order to reproduce the result for the strength of the collective decay in [69] obtained from a wavefunction picture, i.e.

$$\lim_{k_z \to k_0} \alpha = \frac{3}{8\pi}\left(\frac{\lambda_0^2}{4\pi R^2}\right). \tag{1.45}$$

Here, Eq. (1.44) determines the strength of collective losses in a large sample limit $R \gg \lambda_0$. Therefore, the strength of the collective contribution is bounded by $0 \leq \alpha \leq 1$. Using Eq. (1.44) in Eq. (1.36) leads to the non-local density matrix equation

$$\partial_t \rho_t^S = \mathcal{L}_\gamma[\rho] = \gamma \sum_{\ell=1}^{N}\left(\sigma_\ell^- \rho_t \sigma_\ell^+ - \frac{1}{2}\{\sigma_\ell^+ \sigma_\ell^-, \rho_t\}\right) + \gamma\alpha \sum_{\ell' \neq \ell}\left(\sigma_{\ell'}^- \rho_t \sigma_\ell^+ - \frac{1}{2}\{\sigma_{\ell'}^+ \sigma_\ell^-, \rho_t\}\right). \tag{1.46}$$

This derivation for the non-local contribution to the spontaneous decay is equivalent to an earlier calculation performed in a wavefunction picture [69] for a large-sample limit. The established decay rates for a single excitation are reproduced by $\mathcal{L}_\gamma$ [69], i.e. one finds the single atom decay rate γ, the decay rate of a superradiant state of N atoms to be $\gamma(1+\alpha(N-1))$ and the decay rate of a subradiant state (see e.g. [69]) to be $\gamma(1-\alpha)$. We will provide a more detailed interpretation of the terms after the next subsection. First, we estimate the typical strength of the collective decay for modern experiments trapping atoms in intracavity lattices.

Estimation of collective decay contribution for lattice based cavity experiments

[3] It is possible to roughly estimate the order of magnitude of the geometric factor α that determines the collective loss rates. For the intracavity lattices investigated in chapter 2 and chapter 3 we find that collective loss contributions are negligible and we can restrict the analysis to effects of incoherent spontaneous emission in these chapters.

For the estimation of the geometric coupling strength, we take the cavity parameters from the Singapore setup as detailed in [73] and in [49] with Eq. (1.45)

$$\alpha \sim \frac{3}{32\pi^2}\left(\frac{39}{50000}/(1/10)\right)^2 \sim 6 \times 10^{-7}. \tag{1.47}$$

In order to define a sensible thermodynamic limit $N \to \infty$, both the average energy and loss rate per particle have to remain finite. The collective loss rate in Eq. (1.46), however, scales as αN and thus we define $\alpha = \beta/N$ where $\lim_{N\to\infty}\beta = const.$ has to remain constant in the thermodynamic limit. This leads to the Lindblad superoperator $\mathcal{L}_\gamma$ as given in chapter 4 in Eq. (4.4). In an experimental setup, β is then determined by the cavity geometry factor α and the experimentally relevant number of atoms $N = N_{\text{exp}}$.

The collective emission rates appearing in the mean-field equations throughout chapter 4 are enhanced by the number of atoms loaded into the lattice which we take as $N \sim 10^4$ [73, 49] which would leave us with a conservative estimate of

$$\beta = \alpha N \sim 10^{-3}. \tag{1.48}$$

---

[3] This subsection was part of the publications: J. Gelhausen and M. Buchhold and P. Strack Phys. Rev. A **95**, 063824, (2017) and J. Gelhausen and M. Buchhold Phys. Rev. A **97**, 023807 (2018) and we have used some paragraphs verbatim.

We can set this into perspective by comparing it to the relevant system frequencies. Below we quote the experimental values for the parameter set

$$(\omega_0, \omega_z, \kappa, \gamma) = (100(5), 77(2), 100, 0.075 - 0.3)kHz \tag{1.49}$$

as obtained for a quantum optical realisation of the Dicke model, see [74] for details. Here κ is the half-width-half-maximum linewidth of the cavity, γ is the effective rate of spontaneous emission per atom, ω_0 is an effective frequency for cavity photons and ω_z is an effective frequency for the level splitting of the atoms. In this experiment, the typical number of atoms N loaded into the trap was around $N \sim 10^5$, which leads to

$$\gamma\beta = \gamma\alpha N \sim (0.0045 - 0.018)kHz. \tag{1.50}$$

For the collective loss rate to be relevant for the system dynamics, $\gamma\beta$ has to be comparable to typical system frequencies. However, we find that $\gamma\beta \ll \omega_0$ which means that the collective decay contribution can be neglected for the lattice based cavity experiments treated in chapter 2 and chapter 3.

In chapter 4 we consider strong collective decays such there is a competition between the effective atom-atom coupling strength J mediated by the cavity and the dissipatively induced nonlinearities $\sim \gamma\beta$, meaning that $\gamma\beta \sim J \sim \omega_0$. Future experiments into the dissipative Dicke model might be able to access the regime where $\gamma\beta \sim J$ that is necessary to experimentally measure the bistability regime and the fluctuation induced dynamics we find in chapter 4.

We mention briefly that it might also be possible to engineer a strong collective loss channel by coupling the atoms to a second single-mode cavity that operates in the bad cavity limit of strong losses.

Sub- and superradiant transition rates

[4] One can check that the dissipators in Eq. (1.46) can be mapped exactly to the wave-function approach that was derived previously in [69] and correctly reproduces sub- and superradiant decay rates. As an example, we calculate the decay rates of the single photon sub- and superradiant states

$$|-\rangle \equiv |S = N/2 - 1, M = -N/2 + 1\rangle, \tag{1.51}$$

$$|+\rangle \equiv |S = N/2, M = -N/2 + 1\rangle, \tag{1.52}$$

respectively. Both states are defined as

$$|+\rangle = \frac{1}{\sqrt{N}} \sum_{\ell=1}^{N} |j\rangle, \tag{1.53}$$

$$|-\rangle = \frac{1}{\sqrt{N}} \left[\sum_{j=1}^{N/2} |j\rangle - \sum_{j'=1}^{N/2} |j' + N/2\rangle \right] \tag{1.54}$$

where $|j\rangle = |\downarrow, \ldots, \downarrow, \uparrow_j, \downarrow \ldots, \downarrow\rangle$ labels the position of the one-atom excitation, S is the total spin component and $M = (N_\uparrow - N_\downarrow)/2$. We make use of Eq. (1.46) for the time-evolution of the sub- and superradiant states as

$$\begin{aligned} \partial_t \left(|\pm\rangle \langle\pm| \right) = \gamma(1-\alpha) \Big[\sum_{\ell=1}^{N} \Big(\sigma_\ell^+ |\pm\rangle \langle\pm| \sigma_\ell^- \Big) - |\pm\rangle \langle\pm| \Big] \\ + \gamma\alpha \Big[S^+ |\pm\rangle \langle\pm| S^- - \frac{1}{2} 2(S(S+1) - M(M-1)) |\pm\rangle \langle\pm| \Big]. \end{aligned} \tag{1.55}$$

---

[4] This section was published as a supplementary material in J. Gelhausen and M. Buchhold and P. Strack Phys. Rev. A **95**, 063824, (2017)

The rate of emission for the super (I_+) and subradiant rates (I_-) is extracted from Eq. (1.55) as

$$\begin{aligned} I_{S,M} &= \gamma\Big[1-\alpha+\alpha(S(S+1)-M(M-1))\Big] && (1.56)\\ I_+ &= \gamma\,(1+(N-1)\alpha) && (1.57)\\ I_- &= \gamma\,(1-\alpha) && (1.58) \end{aligned}$$

It can be seen that the decay rate of the superradiant state is collectively enhanced, while the subradiant state has a lower decay rate than a single atomic excitation $I_{\text{single}} = \gamma$. The strength of the collective contribution is bounded by $0 \leq \alpha \leq 1$. Super and sub-radiant states have been observed experimentally for two trapped ions [75] and in the context of a superradiance experiment for two artificial atoms in a cavity with high decay rate [76].

Unitary and non-unitary time-evolution

> We briefly point out well-known structural differences in unitary and non-unitary time-evolution. In particular we will review the derivation of the adjoined master equation for a system operator in a Lindblad picture, see Eq. (1.72) that we use throughout this thesis.

The unitary time-evolution of the density matrix is obtained from the von-Neumann equation

$$\partial_t \rho_t = -i[H, \rho_t], \quad \rho_t = U_t \rho_0 U_t^\dagger, \quad U_t = e^{-iHt}. \tag{1.59}$$

The equation of motion for the system operators in the Heisenberg picture then follow from

$$\partial_t \langle O_t \rangle = \mathrm{Tr}[\dot{O}_t \rho_0] = \mathrm{Tr}[O_0 \dot{\rho}_t] = -i\mathrm{Tr}[O_0[H, \rho_t]] = -i\mathrm{Tr}[[O_0, H], \rho_t] = \mathrm{Tr}[-i[O_t, H]\rho_0]. \tag{1.60}$$

It can be read off as

$$\partial_t O_t = i[H, O_t], \quad O_t = U_t^\dagger O_0 U_t \tag{1.61}$$

The unitary time evolution also guarantees that products of operators evolve identically to the time evolution of the product of the time-evolved operators.

$$(OP)_t = U_t^\dagger O P U_t = U_t^\dagger O U_t U_t^\dagger P U_t = O_t P_t \tag{1.62}$$

In driven-dissipative systems, the von-Neumann equation is replaced with the Liouville equation

$$\begin{aligned} \partial_t \rho_t &= \mathcal{L}[\rho_t], && (1.63)\\ \mathcal{L}[\rho_t] &= -i[H, \rho_t] + \sum_\ell \left(L_\ell \rho L_\ell^\dagger - \frac{1}{2}\{L_\ell^\dagger L_\ell, \rho_t\} \right), && (1.64) \end{aligned}$$

where the Lindblad jump operators are given by L_ℓ with a local index ℓ, e.g. $L_\ell = \sigma_\ell^-$, describing atomic spontaneous emission. The formal solution of the Lindblad equation is now given in terms of

$$\rho_t = e^{\mathcal{L}t} \rho_0. \tag{1.65}$$

The exponential of the superoperator is defined via a Taylor series expansion. The adjoined Liouvillian $\mathcal{L}^\dagger$ is defined via the operation

$$\mathrm{Tr}[O\mathcal{L}[P]] = \mathrm{Tr}[\mathcal{L}^\dagger[O]P]. \tag{1.66}$$

As a consequence, the time-dependent expectation value of an operator can be expressed as

$$\langle O_t\rangle = \mathrm{Tr}[O_0\rho_t] = \mathrm{Tr}[O_0 e^{\mathcal{L}t}[\rho_0]] = \mathrm{Tr}[e^{\mathcal{L}^\dagger t}[O_0]\rho_0] = \mathrm{Tr}[O_t\rho_0], \tag{1.67}$$

and consequently

$$\partial_t \langle O\rangle_t = \mathrm{Tr}[\dot{O}_t\rho_0] = \mathrm{Tr}[O_0\dot{\rho}_t] = \mathrm{Tr}[O_0\mathcal{L}[\rho_t]] = \mathrm{Tr}[O_0\mathcal{L}[e^{\mathcal{L}t}\rho_0]] \tag{1.68}$$

$$= \mathrm{Tr}[\mathcal{L}^\dagger[e^{\mathcal{L}^\dagger t}O]\rho_0] = \mathrm{Tr}[\mathcal{L}^\dagger[O_t]\rho_0], \tag{1.69}$$

which leads to the identification of the adjoined master equation for the time evolution of operators as

$$\partial_t O_t = \mathcal{L}^\dagger[O_t], \quad O_t = e^{\mathcal{L}^\dagger t}O_0 \tag{1.70}$$

$$\mathcal{L}^\dagger[O_t] = i[H, O_t] + \sum_\ell \left(L_\ell^\dagger O_t L_\ell - \frac{1}{2}\{L_\ell^\dagger L_\ell, O_t\}\right). \tag{1.71}$$

We will frequently make use of Eq. (1.70) throughout this thesis. The form of $\mathcal{L}^\dagger$ is verified under the cyclic property of the trace as

$$\begin{aligned}\partial_t \langle O_t\rangle &= \mathrm{Tr}[O_o\dot{\rho}_t] = \mathrm{Tr}[\left(O_0 L\rho_t L^\dagger - \frac{1}{2}O_0\{L^\dagger L, \rho_t\}\right)] = \mathrm{Tr}[\left(L^\dagger O_0 L\rho_t - \frac{1}{2}\{L^\dagger L, O_0\}\right)\rho_t] \\ &= \mathrm{Tr}[\mathcal{L}^\dagger[O_0]\rho_t] = \mathrm{Tr}[\mathcal{L}^\dagger[e^{\mathcal{L}^\dagger t}O_0]\rho_0] \\ &= \mathrm{Tr}[\mathcal{L}^\dagger[O_t]\rho_0].\end{aligned} \tag{1.72}$$

The adjoined master equation (1.72) has the order of operators reversed in the first term $\mathcal{L}^\dagger[.] = \left(L^\dagger.L + \dots\right)$ in comparison to the regular Liouville $\mathcal{L}[.] = \left(L.L^\dagger + \dots\right)$. The time evolution operator for a driven-dissipative system is not hermitian itself $\mathcal{L} \neq \mathcal{L}^\dagger$ but it preserves hermiticity for every density matrix. In non-unitary time-evolution, the evolution of products of operators is not distributed to the individual operators as is the case for unitary time-evolution

$$(OP)_t = e^{\mathcal{L}^\dagger t}(OP) \neq \left(e^{\mathcal{L}^\dagger t}O\right)\left(e^{\mathcal{L}^\dagger t}P\right) = O_t P_t. \tag{1.73}$$

An important example for a damped cavity is discussed in Eq. (1.125), where $\langle a_t\rangle \langle a_t^\dagger\rangle \neq \langle (aa^\dagger)_t\rangle$. In the next section, we briefly discuss driven-dissipative phase transitions and their signatures.

1.2.2. Equilibrium and non-equilibrium phase transitions

Driven-dissipative phase transitions occur far from equilibrium. Since the definition of 'non-equilibrium' hinges on the absence of thermodynamic equilibrium we mention briefly common concepts and definitions of equilibrium thermodynamics. We give a non-exhaustive and brief overview of thermal phase transitions (TPT) and quantum phase transitions (QPT) to contrast and compare them with driven-dissipative phase transitions (DPT) far from equilibrium. Where possible we make connections to the work presented in this thesis.

Equilibrium phase transitions

Phase transitions generally refer to a macroscopic change in the properties of a system in response to a change of an external control parameter, e.g. a structural change in a liquid-solid transition. We present a brief and incomplete review. Equilibrium phase transitions are treated in every book on statistical mechanics, see e.g. [77]. For a system in equilibrium with an external reservoir at fixed temperature T, a phase transition separates an ordered, low symmetry phase at low temperature $T < T_c$ from a disordered, high symmetry phase at high temperatures $T > T_c$. The different symmetry properties distinguish one phase from another. In general, an increase in the temperature from a low temperature phase $(T < T_c)$ will also increase thermal fluctuations ($\sim k_b T$) which start to compete with interactions in the system. At $T = T_c$ long-wavelength thermal fluctuations destroy the long-range correlations such that the ordered state is replaced by a disordered state. The divergence of fluctuations at the critical point guarantees that the two phases with different symmetry can be matched and are sharply divided from another at the critical point.

The macroscopic change in the properties of the system are typically tracked by a phenomenological order parameter ϕ that is zero in the high-temperature $\phi(T > T_c) = 0$ and finite in the low-temperature phase $\phi(T < T_c) \neq 0$. One of the achievements of equilibrium statistical mechanics is to describe thermal phase transitions with the help of thermodynamic potentials that depend on few macroscopic thermodynamic variables (temperature, particle density, ...). Close to a continuous phase transition, near $T = T_c$ where the order parameter is small, the free energy can typically be expanded in a power series of the order parameter as $F(\phi, T) = \sum_n \alpha_n \phi^n$, see e.g. [78]. The set of expansion coefficients $\{\alpha_n\}$ depend on external parameters and temperature and the power series expansion respects the symmetries of the model. For a spatially uniform systems with an inversion symmetry $\phi \to -\phi$, the Free-energy can typically be expanded in even powers of the order parameter

$$F(T, \phi) - F_0 = a(T)\phi^2 + b(T)\phi^4 + O(\phi^6) + const, \tag{1.74}$$

where $b > 0$ due to stability requirements of the thermodynamic potential and the sign change of the coefficient $a(T) \sim T - T_c$, marks an instability in the system, leading to a phase transition. Minimizing the Free-energy with respect to the order parameter for a fixed temperature T as

$$\partial_\phi F(\phi, T) = 0 \tag{1.75}$$

yields the thermodynamic state of the system as parametrised by ϕ. For example, a continuous phase transition from a paramagnet to a ferromagnet in the two-dimensional Ising model corresponds to a spontaneously broken inversion symmetry and can be described with a power series expansion of an order parameter as in Eq. (1.74). In equilibrium statistical mechanics, the tendency of a system to maximise entropy (minimize free energy) in the stationary state is an overarching concept formulated as the second law of thermodynamics. One of the most important theoretical achievements in the field of equilibrium phase transitions is their categorization in terms of universality classes [79], meaning that critical power law behaviour of e.g. order parameters close to the critical point become independent of the microscopic details of the Hamiltonian. The universality class depends then on the dimensionality of the system and on the symmetries that are present in the model. Universality is ensured by the diverging correlation length ξ of fluctuations

$$\xi \sim |T - T_c|^{-\nu}, \tag{1.76}$$

where ν is the correlation length exponent.

A system that is coupled with a thermal reservoir at a constant temperature T, treated in the language of the canonical ensemble, will, in the long-time limit, be fully characterised by its equilibrium probability distribution $P_{\mathrm{eq}}(\boldsymbol{s})$, for a configuration $\boldsymbol{s}$ build from a set of microstates $\boldsymbol{s} = \{s_1, s_2, s_3, \dots, s_N\}$, where N is the number of system constituents and s_i labels an internal state. The internal energy of a configuration is measured by a Hamiltonian $H(\boldsymbol{s}) = E_{\boldsymbol{s}}$. Explicitly, the probability to occupy a configuration $\boldsymbol{s}$ is given by the Boltzmann distribution as

$$P_{eq}(\boldsymbol{s}) = \frac{1}{Z} e^{-E_s/T}, \quad Z(\beta) = \sum_{\{E_s\}} e^{-\beta E_s}, \tag{1.77}$$

where $Z(\beta)$ is the thermodynamic partition sum over the set of all configurations $\{\boldsymbol{s}\}$. The Boltzmann weights P_{eq} are a central result of statistical physics of equilibrium systems. For a two-dimensional Ising model, a configuration $\boldsymbol{s} = \{\sigma_1, \sigma_2, \sigma_3, \dots, \sigma_N\}$ would be a particular pattern of spin up and down ($\sigma_i = \pm 1$) of the entire lattice that has associated with it the energy $E_{\boldsymbol{s}}$ calculated from the Ising-Hamiltonian $H(\boldsymbol{s}) = -J \sum_{\boldsymbol{s}} \sigma_i \sigma_j$. Thermodynamic expectation values then emerge as averages over all sets of microstates, weighed appropriately by the equilibrium distribution $\langle . \rangle = \sum_{\{\boldsymbol{s}\}} (.) P_{eq}(\{\boldsymbol{s}\})$. An equilibrium state is thus, in a sense fully characterized by the Boltzmann probability distribution P_{eq}. The stationary probability distribution emerges as the long-time limit of a dynamical evolution, $\lim_{t\to\infty} P(\boldsymbol{s}, t) \equiv P_{eq}(\boldsymbol{s})$, where $P(\boldsymbol{s}, t)$ is the probability to find the configuration $\boldsymbol{s}$ at time t. The dynamical equation is assumed to obey a classical rate equation ($P(\boldsymbol{s}_i) = P_i, \boldsymbol{s}_i \in \{\boldsymbol{s}\}$) for the occupation probabilities

$$\frac{dP_i}{dt} = \sum_j (P_j \gamma_{ji} - P_i \gamma_{ij}) = \sum_j J_{ji}, \tag{1.78}$$

where γ_{ij} is the transition rate from configuration $\boldsymbol{s}_i$ to configuration $\boldsymbol{s}_j$. If the transition rates are ergodic, i.e that every configuration $\boldsymbol{s}_i$ can be reached from any other set of configurations $\boldsymbol{s}_j$, the stationary state of the system uniquely follows from the master equation. The master equation (1.78) states the conservation of probability, as $\sum_i P_i = 1$ and $\sum_i \partial_t P_i = \sum_i \sum_j J_{ji} = 0$. In general, the stationary distribution that results from this equation depends on the set of transition rates such that $P_i^{eq} = P_i^{eq}(\{\gamma_{ij}\})$. However, if the system satisfies time-reversal symmetry for the microscopic transition rates, there is no net current between any two pairs of configurations in the stationary state

$$J_{ji}^{eq} = P_j^{eq} \gamma_{ji} - P_i^{eq} \gamma_{ij} = 0, \tag{1.79}$$

where $\lim_{t\to\infty} J_{ij}(t) \equiv J_{ij}^{eq} = 0$. This detailed balance condition is used in numerical simulations of systems in thermal equilibrium to generate artificial dynamics that samples configurations $\boldsymbol{s}_i$ according to their Boltzmann weight

$$\frac{P_j^{eq}}{P_i^{eq}} = \frac{\gamma_{ji}}{\gamma_{ij}} = e^{-\beta(E_j - E_i)}. \tag{1.80}$$

In this sense, Eq. (1.80) guarantees, independent on initial conditions, that the stationary probability distribution is the Boltzmann distribution, see Eq. (1.77). However, the detailed balance condition leaves some freedom, since two different sets of transition rates $\{\gamma_{ij}\}$ and $\{\gamma'_{ij}\}$ generate the same stationary distribution when $\gamma_{ij}/\gamma_{ji} = \gamma'_{ij}/\gamma'_{ji}$. For example, Glauber and Metropolis transition rates generate the same equilibrium probability distribution for the Ising model in Monte Carlo simulations, see e.g. [80]. We will contrast that to the stationary state of a non-equilibrium system in the next section.

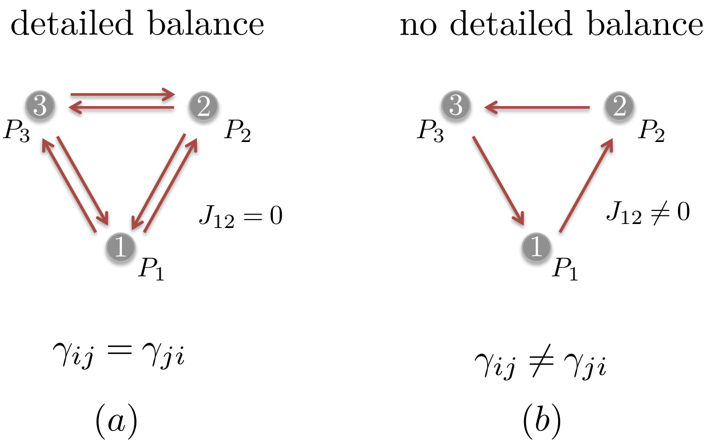

Figure 1.6.: Stationary state configurations with and without detailed balance as obtained from a master equation (1.78). In both cases we have $P_1 = P_2 = P_3 = 1/3$ in (a) we chose $\gamma_{ij} = \gamma$ resulting in the absence of currents $J_{ij} = 0$ and in an equilibrium scenario. In (b) we have $\gamma_{32} = \gamma_{21} = \gamma_{13} = 0$ and $\gamma_{12} = \gamma_{23} = \gamma_{31} = \gamma$ which results in non-vanishing currents $|J_{ij}| = \gamma/3$ which thus defines a non-equilibrium stationary state.

Non-equilibrium steady states

A non-equilibrium system typically has, per definition, all or almost all of the above outlined concepts missing. We will review, on the basis of a classical master equation, that the dynamics in a non-equilibrium stationary state can face much less restrictions than a stationary state in equilibrium because of the possible absence of detailed balance.

An equilibrium stationary state is entirely pre-determined by a thermal density matrix resulting in a Boltzmann probability distribution for the occupation of microstates and the absence of currents $J_{ij} = 0$, due to detailed balance, i.e. it is defined by the set $\{P^{eq}, J_{ij} = 0\}$. On the level of master equations, a non-equilibrium stationary state (NESS) is a priori not restricted by detailed balance and enjoys more freedom, leading to a rich variety of stationary states P_i that are sustained by persistent currents between the set of system configurations $\boldsymbol{s}_i$ and $\boldsymbol{s}_j$. Therefore, a truly non-equilibrium stationary state is distinct from a stationary state in equilibrium through the presence of non-vanishing probability currents in the system. On the level of the master equation (1.78), not only the probability distribution becomes time-independent in the long-time ($\lim_{t\to\infty} P(\boldsymbol{s}_i, t) \equiv P_i^*$) limit but also the currents become stationary in the NESS ($\lim_{t\to\infty} J(\boldsymbol{s}_i, \boldsymbol{s}_j, t) \equiv J_{ij}^*$) and satisfy a Kirchhoff-like rule where the sum of incoming and outgoing currents for a configuration i vanish

$$\sum_j J_{ij}^* = \sum_j P_j^* \gamma_{ji} - P_i^* \gamma_{ij} = 0, \tag{1.81}$$

allowing however for non-vanishing currents $J_{ij}^* \neq 0$ (heat, energy, mass, ...) that explicitly violate the detailed balance condition in Eq. (1.79). For this reason, a NESS is sustained by a compensation of fluxes. Consequently, a stationary probability distribution is entirely determined by the set of transition rates $P^*(\{\gamma_{ij}\})$ and slight changes in the rates lead to different distributions that likely do not obey the Boltzmann distribution because of the absence of a coupling to a thermal reservoir. Therefore, suggestions have been put forward to characterize a NESS by both its stationary probability distribution and the set of non-vanishing currents as the set $\{P^*(\{\gamma_{ij}\}), J_{ij}^*\}$ between pairs i and j of microstates that define the flux equilibrium [81, 82]. A brief illustration of detailed balance and non-vanishing currents is given in Fig. 1.6.

Dissipative phase transitions : closing of the Liouvillian gap

Moving now from a classical description to a framework that encompasses also a possible quantum nature of a non-equilibrium problem, we consider the Liouvillian $\mathcal{L}$ as the dynamical operator for a driven-dissipative many-body system. Unlike for closed systems, where the generator of time-evolution is the hermitian Hamiltonian $H = H^\dagger$, the Liouvillian is not hermitian $\mathcal{L} \neq \mathcal{L}^\dagger$ but hermiticity preserving. The Liouvillian defines the time-evolution of the system density matrix

$$\dot{\rho} = \mathcal{L}[\rho]. \tag{1.82}$$

Its solution can be written in terms of the right eigenvectors ρ_n of the Liouvillian

$$\rho_t = e^{\mathcal{L}t}\rho_{t=0} = \sum_n \alpha_n \rho_n e^{\lambda_n t} = \rho_{ss} + \sum_{n\geq 1} \alpha_n \rho_n e^{\lambda_n t}, \tag{1.83}$$

where the stationary density matrix is defined through

$$\mathcal{L}\rho_{\text{ss}} = 0 \tag{1.84}$$

and corresponds to the zero eigenvalue of the Liouvillian (see e.g. [83] for a detailed analysis on eigenvalues, eigenvectors, symmetries and conserved quantities in Lindblad master equations). This is similar to the classical master equation in Eq. (1.78) that can be rewritten with a matrix M as $\frac{d}{dt}\boldsymbol{P} = M\boldsymbol{P}$, where $\boldsymbol{P}_i = P_i$. The stationary distribution $\boldsymbol{P}^*$ is then the zero-mode of M. This does not fix all matrix elements of M and reflects the fact that the dynamics to reach the same stationary state can be different as long as both sets of transition rates obey detailed balance (see discussion below Eq. (1.80)). Since the density matrix obeys $\text{Tr}[\rho_t] = 1$ at all times, it follows that $\text{Tr}[\rho_{n>0}] = 0$. However, linear combinations of density matrices $\rho_{n>0}$ can be correctly normalised density matrices. In general, the eigenvalue structure $\{\lambda_n\} \in \mathbb{C}$ of the right eigenvectors ρ_n to the Liovillian $\mathcal{L}$ is associated to the (complex) excitation spectrum of the system as

$$\mathcal{L}\rho_n = \lambda_n \rho_n. \tag{1.85}$$

It can be seen from Eq. (1.83) that real parts of the eigenvalues define relaxation rates and it can be proven that, $\text{Re}[\lambda_n] < 0 \ \forall n$ (see e.g. [84]). The longest relaxation time to the stationary state is given by the timescale associated to the inverse of the Liouvillian gap,

$$\bar{\lambda} = \max[\text{Re}[\lambda_n]], \tag{1.86}$$

that is the eigenvalue with the closest real part to zero. This eigenvalue defines a complex Liouvillian gap. Suppose now that there is an external control parameter g that induces a phase transition at a critical value $g = g_c$. For a sudden change of the stationary density matrix $\rho_{ss}(g)$ and therefore of system observables in the stationary state, it is a necessary condition that this gap must vanish asymptotically as $\lim_{g\to g_c} \bar{\lambda} = 0$, see [85]. In the vicinity of the critical point, the Liouvillian gap becomes strongly suppressed and the relaxation time to the stationary state increases, leading to a critical slowing down of the dynamics. Likewise, the behaviour of the Liouvillian gap close to a critical point in dissipative first order phase transitions has sparked intense research recently in driven-dissipative systems in quantum optics [29, 86, 85].

Similarly, we investigate the low-frequency dynamics of a collective polariton mode (excitation gap and damping rate) in a dissipative phase transition in Sec. 3.4.2 which can be seen in Fig. 3.4b, that parallels the behaviour of the Liouvillian gap. An illustration of the pole structure of a polariton mode and the eigenvalue structure of the Liouvillian close to the phase transition point is given in Fig. 1.7. A brief comparison of equilibrium, non-equilibrium and driven-dissipative phase transitions is given in Tab. 1.2.2.

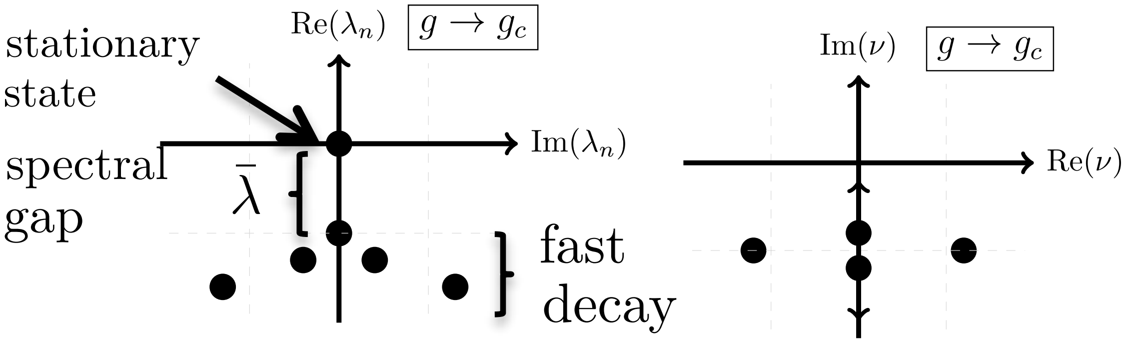

(a) (b)

Figure 1.7.: (a) Illustration of Liouvillian spectrum of complex (excitation and damping) eigenvalues. The stationary state sits at $\lambda_0 = 0$. The spectral gap $\bar{\lambda}$ separates fast decaying modes from the stationary state. A system instability and a possible nonanalytic change of system observables in the stationary state occurs when the gap vanishes $\lim_{g\to g_c} \bar{\lambda} = 0$. (b) Illustration of a low-energy pole structure of a Green's function G_R for hybridised atom-cavity modes of the dissipative Dicke phase transition, see e.g. [87]. Real and imaginary parts encode excitation energies and damping rates, respectively. Close to the critical transition $g < g_c$, the poles become purely imaginary with a magnitude set by the rate of dissipation. At the phase transition $\lim_{g\to g_c} \nu \to 0$, i.e. one pole vanishes, indicating a system instability. For detailed explanations, see [87, 85] and Sec. 3.4.2.

Dissipative phase transitions described by nonlinear differential equations

Detecting phase transitions in the eigenvalue structure of a Liouvillian can be impractical since it typically grows exponentially in size with the number of system constituents, making it hard to achieve a numerical diagonalization of $\mathcal{L}$ in many cases. In this thesis, we will detect driven-dissipative phase transitions as stability changes in fixed points of non-linear differential equations. In some classical limit of a non-equilibrium system, it is typically described in its macroscopic behaviour by a set of nonlinear differential equations that can be derived from the adjoined Lindblad master equation (1.72)

$$\partial_t \boldsymbol{\sigma} = \boldsymbol{D}(\boldsymbol{\sigma}) + \boldsymbol{\xi}(\boldsymbol{\sigma}). \tag{1.87}$$

In these classical Langevin equations there can appear a noise function $\boldsymbol{\xi}(\boldsymbol{\sigma})$ that can depend on the degrees of freedom of the system as parametrised by $\boldsymbol{\sigma}$. It can thus have a non-thermal, i.e. non-constant noise intensity. Here the set of $\boldsymbol{\sigma} = (\sigma^x, \sigma^y, \sigma^z)$ parametrises macroscopic quantities of the system which could contain a phenomenological order parameter. Symmetries of the system are incorporated in the generator of dynamics, e.g. $D(\sigma^x, \sigma^y, \sigma^z) = D(-\sigma^x, -\sigma^y, \sigma^z)$ for a model with an Ising-like inversion symmetry $(\sigma^x, \sigma^y) \to (-\sigma^x, -\sigma^y)$. Stationary states of the system, $\lim_{t\to\infty} \boldsymbol{\sigma_t} = \boldsymbol{\sigma}_0$ represent (typically) a unique and stable fixed point of the dynamics. They exist as a consequence of a balance of external drive and dissipation. At a critical threshold value of the external drive $g = g_c$, this fixed point becomes unstable and the long time-limit behaviour of the system changes dramatically as typically a new stable fixed point emerges. Stability changes for dynamical systems are classified in bifurcation theory, see e.g. [12] (see next section). The bifurcation analysis does not take into account fluctuations and is therefore the mean-field equivalent of analysing phase transitions in thermal equilibrium. The change in the fixpoint landscape could bring with it a spontaneously broken symmetry from a state, where $\sigma^x(g < g_c) = 0$ to $\sigma^x(g > g_c) \neq 0$. In that sense one can still have spontaneous symmetry breaking and phase transitions also in the absence of a free-energy or a free-energy functional equivalent.

We briefly review linear stability analysis in Sec. 1.2.2. If the drive parameter is tuned close to the transition point $g = g_c$ the systems behaviour is entirely determined by the type of instability or bifurcation. In this sense, it is possible that a variety of different non-equilibrium systems can show universal behaviour close to an instability.

However, close to a critical point, it might be possible to map the dynamics, as given by Eq. (1.87), onto an effective mode ϕ that allows then for a power expansion of the generator of dynamics as

$$\partial_t \phi = -\frac{\partial \mathcal{H}}{\partial \phi} + \xi(\phi). \tag{1.88}$$

Here, the generator of both dissipative and deterministic dynamics is the Hamiltonian that, for a one-component system with no spatial dependence can always be written in a potential form with a power expansion

$$\mathcal{H} = a_g \phi^2 + b_g \phi^4 + c_g \phi^6 + O(\phi^8), \tag{1.89}$$

$$\langle \xi(\phi)_t \xi(\phi)_{t'} \rangle = \left(T_{\text{eff}} + \tilde{a}_g \phi^2 + \tilde{b}_g \phi^4 + \tilde{c}_g \phi^6 + O(\phi^8) \right) \delta(t - t'), \tag{1.90}$$

where the set $(a_g \tilde{a}_g, b_g, \tilde{b_g}, c_g, \tilde{c}_g)$ depend on the external drive g and

$$T_{\text{eff}} = \lim_{\phi \to 0} \langle \xi_t \xi_{t'}(\phi) \rangle \, \delta(t - t') \tag{1.91}$$

is an effective temperature that typically depends on the strength of dissipation as a constant noise intensity. In this sense, close to the critical point of a dissipative phase transition ($\phi \sim 0$), the system can undergo a thermal phase transition with, in this case, the thermal universality class of the Ising model and a stationary probability distribution

$$P(\phi) \sim \exp\left(-\mathcal{H} / T_{\text{eff}} \right), \tag{1.92}$$

that results as the stationary solution of the Fokker-Planck equation, associated to the Langevin equation. The emergence of a thermodynamic universality class close to a critical point has been observed for a variety of models, see [88, 89, 90] and references therein. It was shown that also for the superradiance transition of the photon field in the presence of photon losses with rate κ there emerges a constant noise intensity, $T_{\text{eff}} \sim \kappa$, at the transition point, see [91]. In this thesis we identify a potential description given by Eq. (1.89) for an open variant of the Dicke model at a bicritical point in Sec. 4.3.2 and show that the fluctuations at the critical point have a constant noise intensity, see Sec. 5.4.

The ground-state of the closed Dicke model for the coupling to a $T = 0$ bath environment undergoes a quantum phase transition from a vacuum to a superradiant state. In an open Dicke model, where the atoms are coupled to lossy photons, the phase transition is analysed as a change in the stationary state properties of the system. Nagy *et al.* [47] asked the question how criticality in the stationary non-equilibrium state is related to the critical behaviour at the quantum phase transition of the ground state in the closed system. They found that the occupation of the photon mode close to the superradiance transition in the presence of photon loss diverges with a different critical exponent than in the corresponding closed Dicke system, [47, 27]. The presence of loss modified the static critical exponents in comparison to the quantum phase transition in a closed system.

Classification of linearised instabilities

In this thesis, we will frequently analyse stability of fixed points and their bifurcations. To predict instabilities one typically linearises the (noise-free $\langle \boldsymbol{\xi} \rangle = 0$) set of differential

	TPT	QPT	DPT
System operator	Hamiltonian $H = H^\dagger$	Hamiltonian $H = H^\dagger$	Liouvillian $\mathcal{L}^\dagger \neq \mathcal{L}$
Relevant quantity	Free Energy $F(\rho) = \langle H \rangle_\rho - T \langle S \rangle_\rho$	Energy eigenvalues $E_\Psi : H \lvert \Psi \rangle = E_\Psi \lvert \Psi \rangle$	'Complex energy' eigenvalues $\lambda_\rho : \mathcal{L}\rho = \lambda_\rho \rho$
State	Gibbs state $\rho_T = \underset{\rho \geq 0, \mathrm{Tr}(\rho)=1}{\operatorname{argmin}} [F(\rho)]$ $\rho_T \propto \exp[-H/k_b T]$	Ground State $\lvert \Psi_0 \rangle = \min_{\lvert\lvert \lvert \Psi \rangle \rvert\rvert = 1} [\langle \Psi \rvert H \lvert \Psi \rangle]$ $[H - E_{\Psi_0}] \lvert \Psi \rangle_0 = 0$	Steady state $\rho_0 = \underset{\lvert\lvert \rho_{tr} \rvert\rvert=1}{\operatorname{argmin}} [\lvert\lvert \mathcal{L}\rho \rvert\rvert_{tr}]$ $\mathcal{L}\rho_0 = 0$
Phase transition	Nonanalyticity in $F(\rho_T)$	$\Delta = E_{\Psi_1} - E_{\Psi_0}$ vanishes	ADR=max[Re(λ_ρ)] vanishes

Table 1.1.: Brief comparison of thermal phase transition (TPT) quantum phase transition (QPT) and dissipative phase transition (DPT). Here $\lvert\lvert \cdot \rvert\rvert_{\mathrm{tr}}$ denotes the trace norm and S the entropy and ADR is the asymptotic decay rate. This table is taken from [85].

equations Eq. (1.87) around the fixed point as $\boldsymbol{\sigma}_t \to \boldsymbol{\sigma}_0 + \delta\boldsymbol{\sigma}_t$ and investigate whether the perturbations $\delta\boldsymbol{\sigma}_t$ grow (unstable) or decay (stable) in time. Here we assume a three component field as $\boldsymbol{\sigma} = (\boldsymbol{\sigma^x}, \boldsymbol{\sigma^y}, \boldsymbol{\sigma^z})$. We expand the set of equations (1.87) around the stationary state to linear order and linearise

$$\partial_t (\boldsymbol{\sigma_0} + \delta\boldsymbol{\sigma}) = \boldsymbol{D}(\boldsymbol{\sigma}_0) + \boldsymbol{J}[\boldsymbol{f}(\boldsymbol{\sigma})]|_{\boldsymbol{\sigma}=\langle\sigma\rangle_0} \cdot \delta\boldsymbol{\sigma} + \mathcal{O}(\delta\boldsymbol{\sigma}^2) \tag{1.93}$$

$$\partial_t(\delta\boldsymbol{\sigma}) = \boldsymbol{J}[\boldsymbol{f}(\boldsymbol{\sigma})]|_{\boldsymbol{\sigma}=\sigma_0} \cdot \delta\boldsymbol{\sigma} + \mathcal{O}(\delta\boldsymbol{\sigma}^2) \tag{1.94}$$

Here $\boldsymbol{J}[\boldsymbol{f}(\boldsymbol{\sigma})]|_{\boldsymbol{\sigma}=\boldsymbol{\sigma_0}}$ is the Jacobian matrix evaluated at the fixed points that satisfy $\boldsymbol{D}(\boldsymbol{\sigma_0}) = \boldsymbol{0}$. It's eigenvalues λ_i determine the stability of the fixed points. The general solution is then cast into the form

$$\delta\boldsymbol{\sigma}_t = \sum_i \alpha_i e^{\lambda_i t} \boldsymbol{v}_i. \tag{1.95}$$

The eigenvalues are in general complex

$$\lambda_i = \nu + i\mu, \tag{1.96}$$

with $(\nu, \mu) \in \mathbb{R}$ and define the behaviour of the system when it is weakly perturbed from the stationary state. From the decomposition it can easily be seen that the real part ν defines the damping rate and the imaginary part μ defines oscillations. A fixed point is stable if $\nu < 0 \ \forall i$. Fixed points and their stability changes (bifurcations) are categorized according to the behaviour of the set (ν, μ) as the transition is approached, see e.g. [12].

For a stability change of a fixed point it is clear that some $\nu_j \to 0$ as $g \to g_c$. For example, analysing the Dicke phase transition in the presence of photon loss with a semiclassical set of nonlinear differential equations, shows that the transition from the empty atom-cavity system (paramagnet) to the superradiant state (ferromagnet) is associated with a supercritical pitchfork bifurcation where a single fixed point is replaced by three fixed points and the qualitative structure of phase space changes substantially. In this case for $g < g_c$ there is only one fixed point, which is the empty state that becomes unstable at $g = g_c$. For $g > g_c$ there are three fixed points. Two superradiant fixed points associated to the inversion symmetry of the model and the remaining fixed point is the empty state which is unstable. This bifurcation can also be seen in Fig. 1.4a. Generally one can ask the question if the bifurcation analysis of a (semi)classical system can reveal features of the associated phase transition of the groundstates in the quantum model. In the case of the Dicke model it was conjectured [92] and shown [93] that the stability loss of the classical fixed point in a pitch fork bifurcation is associated to entanglement in the stationary state of the corresponding quantum system that peaks at the phase transition.

1.3. Dissipation and fluctuations in open quantum optical systems

In this section we review and point out the importance of fluctuation-dissipation relations in classical and quantum setups. We start in a classical setup by reviewing Brownian motion to show that the average kinetic energy of a macroscopic particle immersed in a fluid (thermal bath) is correctly predicted only when the bath degree of freedom, modelled in terms of noise functions, are taken into account. Next, we consider a quantum mechanical setting, a single mode cavity coupled to the vacuum radiation modes. We review that the vacuum noise is important for the preservation of commutation relations for the cavity operators. In the next section, we show that quantum Langevin equations always fulfil generalized Einstein relations that relate fluctuations with dissipations. We make use of these relations in chapter 2 and chapter 4.

1.3.1. Classical Langevin equation

The dynamics of a macroscopic particle (that we will refer to as bead in this section) with mass m immersed in a fluid can be described by a stochastic generalization of Newton's equation which is called classical Langevin equation [94]. This is a standard procedure and in this section, we follow [95]. The particles in the fluid will collide with the macroscopic bead and provide a source of random forces acting on the bead. As it is an impossible task to track individual collisions, these will be modelled with a stochastic force function ξ_t that is fed back phenomenologically into the equation of motion for the bead. Additionally, there appears also a phenomenologically added friction coefficient γ, specific to each fluid. In the absence of external forces ($F_{\text{ext}} = 0$), the one-dimensional Langevin equation reads

$$m\frac{d}{dt}v_t = -m\gamma v_t + \xi_t. \tag{1.97}$$

The stochastic force ξ_t is modelled as a short ranged, correlated Gaussian random variable characterised by their first and second moment,

$$\langle \xi_t \rangle = 0, \quad \langle \xi_t \xi_{t'} \rangle = A\delta(t - t'), \tag{1.98}$$

where $A > 0$ is a constant, describing the variance of the force and $\langle . \rangle$ is a statistical average over the reservoir degrees of freedom. The Langevin equation is based on a separation of timescales in 'fast', associated with the bath and 'slow' associated with the dynamics of the macroscopic bead. If we average over the forces of the bath first, one effectively neglects the random noise, as $\langle \xi_t \rangle = 0$. Then Eq. (1.97) is solved with

$$\langle v_t \rangle = e^{-\gamma t} \langle v_0 \rangle, \tag{1.99}$$

such that in the long time limit, the average velocity of the particle vanishes. However, a particle in equilibrium with a thermal reservoir is expected to have characteristic fluctuations in accordance with its thermal energy provided by the bath. For a one-dimensional system, the equipartition theorem states that the average kinetic energy of the macroscopic bead is the same as the thermal energy of the bath. However, we see that if we neglect the random force of the bath, this theorem is violated

$$\lim_{t\to\infty} \langle v_t^2 \rangle = \lim_{t\to\infty} e^{-2\gamma t} \langle v_0^2 \rangle \to 0 \neq \frac{k_b T}{m}. \tag{1.100}$$

Thus, Newton's equation correctly predicts a vanishing average velocity for long times, but it cannot correctly predict the time evolution of the fluctuations.

In the next step, we thus keep the noise term ξ_t and solve the Langevin equation formally

$$v_t = e^{-\gamma t} v_0 + \int_0^t ds\ e^{-\gamma(t-s)} \tilde{\xi}_s, \quad \tilde{\xi}_t = \xi_t/m. \tag{1.101}$$

The average kinetic energy of the macroscopic bead in the stationary equilibrium state is constant, which means that

$$\frac{d}{dt} \langle v_t^2 \rangle = 2 \langle \dot{v}_t v_t \rangle = 2 \left(-\gamma \langle v_t^2 \rangle + \langle \tilde{\xi}_t v_t \rangle \right) = 0. \tag{1.102}$$

with

$$\langle \tilde{\xi}_t v_t \rangle = \langle v_0 e^{-\gamma t} \tilde{\xi}_t + \int_0^t ds \quad e^{-\gamma(t-s)} \tilde{\xi}_s \tilde{\xi}_t \rangle = \int_0^t ds \quad e^{-\gamma(t-s)} \langle \tilde{\xi}_s \tilde{\xi}_t \rangle = \frac{A}{2m^2}. \tag{1.103}$$

The set of equations (1.102) and (1.103) define the strength of the noise completely. The relation between the strength of fluctuations A and dissipations γ is thus

$$\langle v_t^2 \rangle = \frac{1}{\gamma} \langle \tilde{\xi}_t v_t \rangle = \frac{A}{2\gamma m^2} = \frac{k_b T}{m}. \tag{1.104}$$

one can readily identify fluctuation-dissipation relation or classical Einstein relation as

$$A = 2 m k_b T \gamma. \tag{1.105}$$

Here k_b is the Boltzmann constant. The variance of the fluctuating forces is connected to the strength of dissipation, as it should be since both forces have the same origin. This example shows the importance of taking into account the fluctuating forces of the bath when it comes to calculating the time evolution of fluctuations for the macroscopic variables of the system.

This is equally true in the theory of quantum damping described in terms of Heisenberg-Langevin equations for open quantum systems which we consider in the next section.

1.3.2. Quantum Heisenberg Langevin equations

> In the following we review the derivation of the equation of motion for a single mode cavity coupled to the external reservoir of radiation modes (1.117). This allows to understand how damping and fluctuations carry over from a classical to a quantum setting. This is a standard example, that is found in most books on quantum optics. In this section we follow [96] and [70].

We consider the example of a single quantised light-mode supported by a cavity that is coupled to an external reservoir of radiation modes. This system is fundamentally open as the cavity mirrors are imperfect such that photons can leave the cavity system and there is a steady rate of energy transfer through the mirrors. This damping mechanism is accounted for by the coupling to the quantised radiation modes outside the cavity. Also the external radiation modes will feed back into the equation of motion for the cavity mode, leading to fluctuations. The damping and noise terms account for dissipation and fluctuations. We start the derivation of the quantum Langevin equations by starting from the conventional Heisenberg equations with the set of Hamiltonians

$$H = H_0 + H_{SR}, \quad H_0 \ = \hbar\omega_0 a^\dagger a + \sum_k \hbar\omega_k b_k^\dagger b_k, \quad H_{SR} = \hbar \sum_k g_k (b_k^\dagger a + a^\dagger b_k), \tag{1.106}$$

where H_0 models the harmonic oscillators with annihilation operators for the cavity mode a and for the bath modes b_k and ω_k is the energy dispersion of the bath oscillators in free space. Furthermore, H_{SR} is the system reservoir interaction in a rotating-wave approximation that retains only energy-conserving contributions $\sim b_k^\dagger a$ and $\sim a^\dagger b_k$. The coupling strength of the cavity modes to bath mode k is given by g_k. The radiation modes have to be quantised in free space and the single-mode approximation of the cavity is not applicable in free space, leading to a continuum of modes where the subscript k indicates the mode index. The external modes are densely spaced and in a continuum limit for the mode description one replaces

$$\sum_k |g_k|^2 \to \int_0^\infty \frac{d\omega}{2\pi}\ 2\kappa(\omega), \quad \sum_k \to \int_{-\infty}^\infty d\omega, \quad g_k \to \sqrt{\frac{2\kappa(\omega)}{2\pi}}. \tag{1.107}$$

where the factor of 2 in front of the frequency dependent rate $\kappa(\omega)$ appears for convenience. Momentarily however, we stick to a discrete mode picture for ease of notation and for evaluations of mode summations we bear in mind the above quoted replacement rule for the frequency integrals. The equation of motion for both bath and cavity operators is obtained from the Heisenberg equation of motion ($\hbar = 1$)

$$\dot{a}_t = i[H, a_t] = -i\omega_0 a_t - i\sum_k g_k b_{k,t}, \tag{1.108}$$

$$\dot{b}_{k,t} = i[H, b_{k,t}] = -i\omega_{k,t} b_{k,t} - i g_k a_t. \tag{1.109}$$

Since we would like to track the evolution of the system operators, we formally integrate the equation for the bath modes from a past time $t_0 = 0$ to the current time t

$$b_{k,t} = b_{k,0} e^{-i\omega_k t} - i g_k \int_0^t dt' a_{t'} e^{-i\omega_k (t-t')}. \tag{1.110}$$

The formal solution is plugged into Eq. (1.108) for the system operator

$$\dot{a}_t = -i\omega_0 a_t - \sum_k g_k^2 \int_0^t dt' a_{t'} e^{-i\omega_k(t-t')} - i\sum_k g_k b_{k,0} e^{-i\omega_k t}. \tag{1.111}$$

In order to continue, we make use of the fact that the frequency dependence of the bath modes varies slowly in the frequency window centred around the cavity frequency broadened by the cavity decay rate. This approximation is known as the Markov-approximation, see Sec. 1.2, and amounts to the replacement

$$\kappa(\omega) \approx \kappa(\omega_0) = const., \tag{1.112}$$

with the replacement conventions in Eq. (1.107), the first sum is evaluated as

$$\sum_k g_k^2 \int_0^t dt' a_{t'} e^{-i\omega_k(t-t')} = 2\kappa \int_0^t dt' a_{t'} \delta(t-t') = \kappa a_t \tag{1.113}$$

where the delta function contributes only with factor 1/2 since the upper integration boundary coincides with the argument of the delta function such that it is split in 'half'. The second summation is evaluated as

$$-i\sum_k g_k b_{k,0} e^{-i\omega_k t} = -\sqrt{2\kappa}\frac{i}{\sqrt{2\pi}}\sum_k b_{k,0} e^{-i\omega_k t} = \sqrt{2\kappa}\xi_t^a \tag{1.114}$$

where we have defined the input noise function

$$\xi_t^a = -\frac{i}{\sqrt{2\pi}}\sum_k b_{k,0} e^{-i\omega_k t} \tag{1.115}$$

that feeds back in the equation of motion for the cavity mode. In this sense, the cavity mode evolves in response to the action of the bath fields from an earlier time $t > t_0 = 0$. Here the noise operator depends on the initial state of the bath via $b_{k,0}$. The term 'noise' for the input fields can make sense if the initial state is an incoherent state such as a thermal state and if initially the bath and system states factorize. However, $b_{k,0}$ could also be a coherent input field such as a laser and the term noise would not be appropriate. Here we shall however be concerned with the former case only.

Plugging the two contributions from Eq. (1.115) and Eq. (1.113) into Eq. (1.111) results in a damping term $\sim \kappa$ describing the decay of photons through the cavity mirrors into the external vacuum modes and fluctuations in the form of an input noise-operator ξ_t^a explicitly containing the reference to the bath operators at some previous time. The only non-vanishing noise-correlation function for a $T = 0$ external bath is given as

$$\langle \xi_t^a \xi_{t'}^{a\dagger} \rangle = \delta(t - t'). \tag{1.116}$$

Together these equations result in the quantum Heisenberg-Langevin equation (QHLE)

$$\dot{a}_t = -i\omega_0 a_t - \kappa a_t + \sqrt{2\kappa}\xi_t^a \tag{1.117}$$

This equation represents the quantum analogue to the classical Langevin equation discussed in Sec. 1.3.1.

Importance of noise for multioperator expectation values

> Taking the example of the damped cavity, we now show that when we average over the reservoir degrees of freedom before solving the Heisenberg-Langevin equation, we can correctly predict single-operator expectation values in the long-time limit but acquire wrong results for multioperator expectation values. This is in complete analogy to the classical Brownian motion where we have seen that we correctly obtain a vanishing velocity $\lim_{t\to\infty} \langle v_t \rangle = 0$ if we first average over the noise but in violation of the fluctuation dissipation theorem have obtained $\lim_{\to\infty} \langle v_t^2 \rangle \to 0$.

We start by simplifying the notation for the QHLE (1.117) by changing into a frame rotating at the cavity frequency ω_0. Formally we define a slowly varying envelope by replacing $a_t = \tilde{a}_t e^{i\omega_0 t}$. In the following, we will however label $\tilde{a}_t$ as a_t with the agreement that we make the distinction explicit only if we need to switch back between pictures. We can then rewrite Eq. (1.117) as

$$\dot{a}_t = -\kappa a_t + \xi_t^a, \tag{1.118}$$

which is formally solved with

$$a_t = a_{t=0} e^{-\kappa t} + \int \quad dt' \xi_{t'}^a e^{-\kappa(t-t')}, \quad \xi_t^a = -i \sum_k g_k b_k(0) e^{-i(\omega_0 - \omega_k)t}. \tag{1.119}$$

Averaging the cavity equation of motion over the reservoir degrees of freedom with

$$\langle . \rangle_R = \mathrm{Tr}[.\rho_R], \quad \rho_R = 1/Z e^{-H_R/T}, \tag{1.120}$$

where ρ_R is the thermal density matrix of the bath, correctly predicts an exponential damping of the cavity mode

$$\langle a_t \rangle_{\mathrm{R}} = \langle a_{t=0} \rangle_{\mathrm{R}} \, e^{-\kappa t}. \tag{1.121}$$

However, the dissipative dynamics alone does not preserve the commutation relations.

$$[\langle a_t \rangle_{\mathrm{R}}, \langle a_t^\dagger \rangle_{\mathrm{R}}] = e^{-2\kappa t} \neq 1. \tag{1.122}$$

Solving the Langevin equation before we average over the reservoir, restores the commutation relations

$$[a_t, a_t^\dagger] = [a_{t=0}, a_{t=0}^\dagger] e^{-2\kappa t} + \int_0^t \int_0^t dt' dt'' \ \ [\xi_t^a, \xi_t^{a^\dagger}] e^{-2\kappa(t-t')} e^{-2\kappa(t-t'')} = 1 \tag{1.123}$$

This is the first important result. We have seen through Eq. (1.123) that it is the task of the noise to preserve the commutation relations for the system operators. We have used $\sim [a_0, \xi_{in,t}^{a^\dagger}] = 0$ as a consequence of causality. The cavity modes at $t_0 = 0$ cannot be influenced by the noise functions at some later time $t > t_0$. More importantly, we have made use of the noise commutation relations

$$[\xi_t^a, \xi_{t'}^{a^\dagger}] = \sum_{k,k'} g_k g_{k'} e^{-i(\omega_0 - \omega_k)t} e^{-i(\omega_0 - \omega_{k'})t'} [b_k, b_{k'}^\dagger] = \sum_k g_k^2 e^{-i(\omega_0-\omega_k)(t-t')} = 2\kappa \delta(t-t'), \tag{1.124}$$

where we used the bosonic commutation relation $[b_k, b_{k'}^\dagger] = 1$.

Apart from conservation of commutation relations, the noise ensures also the correct evolution of multioperator expectation values such as the thermal population of the cavity mode in the stationary state $\lim_{t\to\infty} \langle a_t^\dagger a_t \rangle = \bar{n}(\omega_0)$. It obeys the differential equation

$$\begin{aligned} \frac{d}{dt} \langle a_t^\dagger a_t \rangle_R &= \langle \dot{a}_t^\dagger a_t \rangle_R + \langle a_t^\dagger \dot{a}_t \rangle_R \\ &= -2\kappa \left\langle a_t^\dagger a_t \right\rangle_R + \left\langle \xi_t^{a^\dagger} a_t \right\rangle_R + \left\langle a_t^\dagger \xi_t^a \right\rangle_R \\ &= -2\kappa \left\langle a_t^\dagger a_t \right\rangle_R + 2\kappa \bar{n}(\omega_0), \end{aligned} \tag{1.125}$$

In the stationary state we now correctly obtain the average thermal cavity population

$$\lim_{t\to\infty} \left\langle a_t^\dagger a_t \right\rangle_R = \bar{n}(\omega_0). \tag{1.126}$$

Here, we have imposed the generalised Einstein relation that connects fluctuations and dissipations

$$\left\langle \xi_t^{a^\dagger} a_t \right\rangle_R + \left\langle a_t^\dagger \xi_t^a \right\rangle_R = \left\langle \xi_t^{a^\dagger} \xi_t^a \right\rangle_R = 2\kappa \bar{n}(\omega_0) \tag{1.127}$$

to obtain a solution consistent with our expectations. This is the second important result of this section. We point out the formal similarity with classical Brownian motion in Eq. (1.104).

General properties of the noise operators

The Einstein relation in Eq. (1.127) can also formally be derived. We show this here, together with some general properties of noise functions. We consider the external vacuum to be a thermal reservoir at a Temperature T. Averaging over the reservoir degrees of freedom leads to the following set of non-vanishing expectation values

$$\left\langle b_{k,0} b_{k',0}^\dagger \right\rangle_R = \delta_{k,k'} (\bar{n}_k + 1), \tag{1.128}$$

$$\left\langle b_{k',0}^\dagger b_{k,0} \right\rangle_R = \delta_{k,k'} \bar{n}_k, \tag{1.129}$$

We can obtain further relations

$$\langle \xi_t^a \rangle_R = \left\langle \xi_t^{a^\dagger} \right\rangle_R = 0 \tag{1.130}$$

$$\begin{aligned}
\left\langle \xi_t^a \xi_{t'}^{a^\dagger} \right\rangle_R &= \sum_{k,k'} g_k g_{k'} e^{-i(\omega_0-\omega_k)t} e^{-i(\omega_0-\omega_k)t'} \left\langle b_k b_{k'}^\dagger \right\rangle_R \\
&= \sum_k g_k^2 (\bar{n}_k + 1) e^{-i(\omega_0-\omega_k)(t-t')} = 2\kappa(\bar{n}_k+1)\delta(t-t') \qquad (1.131)
\end{aligned}$$

$$\left\langle \xi_t^{a^\dagger} \xi_{t'}^a \right\rangle_R = 2\kappa \bar{n}_k \delta(t-t') \tag{1.132}$$

and $\bar{n}_k = 1/\left(e^{\beta\hbar\omega_k} - 1\right)$ is the average thermal occupation in mode k. The correlations of the noise-operators with the system variables are given as

$$\left\langle \xi_t^{a^\dagger} a_t \right\rangle_R = e^{-\kappa t} \left\langle a_0 \xi_t^{a^\dagger} \right\rangle_R + \int_0^t dt' \quad e^{-\kappa(t-t')} \left\langle \xi_t^{a^\dagger} \xi_t^a \right\rangle_R = \kappa \bar{n}_k \tag{1.133}$$

$$\left\langle a_t^\dagger \xi_t^a \right\rangle_R = \kappa \bar{n}_k, \tag{1.134}$$

where we have used Eq. (1.130) and the fact that the bath and the system operators are statistically independent, such that $\left\langle a_0 \xi_t^{a^\dagger} \right\rangle_R = a_0 \left\langle \xi_t^{a^\dagger} \right\rangle_R = 0$. Here we remark that the Einstein relation (1.127) now directly follows from Eq. (1.133) and Eq. (1.134). Again we mention the structural similarity to the classical Einstein relations in Eq. (1.103).

1.3.3. Generalised Einstein relations to connect fluctuations with dissipation

> The Heisenberg-Langevin equations (HLE) explicitly contain the influence of the environment for the system through the presence of noise-operators ξ_i^O. For the case of a damped cavity, we have calculated explicitly the relations of noise and damping. Here, we review generalised Einstein relations as presented in [97] that connect fluctuations with dissipation. They are derived from the general form of a HLE as presented in Eq. (1.135).

Quantum Langevin or Heisenberg-Langevin equations are always in the form

$$\frac{d}{dt} O_\alpha = D_\alpha[\boldsymbol{O}] + \xi_\alpha, \tag{1.135}$$

where D_α specifies the deterministic or drift forces of the dynamics and depends only on the system and not the reservoir variables. It captures both unitary and damping dynamics as

$$D_i[\boldsymbol{O}] = -i[O_i, H] + \mathcal{L}^\dagger[O_i]. \tag{1.136}$$

Here $\mathcal{L}^\dagger$ is the conjugate Lindblad operator as shown in Eq. (1.70). ξ_α is the noise operator for the system operator O_α and will in general depend on the bath and on the system operators. The noise itself is assumed to be Gaussian with a vanishing reservoir expectation value $\langle \xi_\alpha \rangle = 0$. The two-time correlation function of the noise operators is assumed to be of the form

$$\langle \xi_{\alpha,t}^\dagger \xi_{\beta,t'} \rangle = 2\mathcal{D}_{\alpha\beta} \delta(t-t'), \tag{1.137}$$

where $\mathcal{D}_{\alpha\beta}$ measures the strength of the noise-intensity.

The generalised Einstein equations now relate the deterministic forces to the diffusion coefficients of the system by the equation

$$\frac{d}{dt} \langle O_{\alpha,t}^\dagger O_{\beta,t} \rangle - \langle D_\alpha^\dagger O_{\beta,t} + O_{\alpha,t}^\dagger D_\beta \rangle \equiv 2\mathcal{D}_{\alpha\beta} = \langle \xi_{\alpha,t}^\dagger \xi_{\beta,t} \rangle \tag{1.138}$$

This relation is useful if it is possible to calculate the equation of motion for $\langle O_\alpha^\dagger O_\beta \rangle$ independently from the single operator equations of motion. This becomes possible for instance if the system operators $O_\alpha^\dagger$ and O_β satisfy some commutation algebra where the operators reproduce themselves. Such as is the case for spins $\sigma^i\sigma^j = i\epsilon_{ijk}\sigma^k$. We will briefly outline why the Einstein relation holds. We begin by spelling out the time-derivative

$$\frac{d}{dt}\langle O_\alpha^\dagger O_\beta \rangle = \langle \dot{O}_\alpha^\dagger O_\beta + O_\alpha^\dagger \dot{O}_\beta \rangle = \langle D_\alpha^\dagger O_\beta + O_\alpha^\dagger D_\beta + \xi_\alpha^\dagger O_\beta + O_\alpha^\dagger \xi_\beta \rangle \tag{1.139}$$

We thus need to show that the correlations of the force operator with the system operator are given by the autocorrelations of the forces. This will be a consequence of causality considerations which state that a system operator cannot be related to future effects of the force operator.

To make use of this statement we employ the relation

$$O_{\beta,t} - O_{\beta,t-\Delta t} = \int_{t-\Delta t}^{t} dt' \dot{O}_{\beta,t'}, \tag{1.140}$$

to evaluate the fluctuation of the noise operators with the system variables

$$\langle \xi_{\alpha,t}^\dagger O_{\beta,t} \rangle = \underbrace{\langle \xi_{\alpha,t}^\dagger O_{\beta,t-\Delta t} \rangle}_{=0,\text{causality}} + \langle \int_{t-\Delta t}^{t} \underbrace{\xi_{\alpha,t}^\dagger D_{\beta,t'}}_{=0,\,\forall t<t',\text{causality}} + \xi_{\alpha,t}^\dagger \xi_{\beta,t'} dt' \rangle \tag{1.141}$$

$$\approx \langle \int_{t-\Delta t}^{t} \xi_{\alpha,t}^\dagger \xi_{\beta,t'} \rangle \, dt' = \frac{1}{2} \langle \int_{-\infty}^{\infty} d\tau \xi_{\alpha,0}^\dagger \xi_{\beta,\tau} \rangle \equiv \mathcal{D}_{\alpha\beta} \tag{1.142}$$

In the last line we have used that the noise correlations are stationary and that the time interval Δt is considered much longer than the autocorrelation time of the forces so that we can extend the integration boundaries. The calculations are similar for $\langle O_{\alpha,t}^\dagger \xi_{\beta,t} \rangle$. Putting the pieces together, we obtain

$$\langle O_{\alpha,t}^\dagger \xi_{\beta,t} \rangle + \langle \xi_{\alpha,t}^\dagger O_{\beta,t} \rangle = 2\mathcal{D}_{\alpha\beta} = \langle \xi_{\alpha,t}^\dagger \xi_{\beta,t} \rangle \,, \tag{1.143}$$

which concludes the derivation of the Einstein relations given in Eq. (1.138). We have already seen an example of Eq. (1.143) for the case of a damped cavity, see Eq. (1.138). We consider further examples for the usefulness of the generalized Einstein relations for spin systems. We will use the following relations in chapter 2 and partly in chapter 4.

Application example I:

We consider the derivation of the noise-intensity for a single spin that is linearly coupled to a bath of harmonic oscillators that model the external vacuum modes. Here we show the necessity for fine-tuned fluctuation-dissipation relations. For instance, the Pauli operators that appear in a quantum mechanical description of the spins have to satisfy, $(\sigma^\alpha)^2 = 1$, where $\alpha = (x, y, z)$. The task of the noise is now to to ensure that this relation is preserved over time as

$$\frac{d}{dt}\langle (\sigma^x)^2 \rangle = \langle D^\dagger \sigma^x \rangle + \langle \sigma^x D \rangle + \langle \xi^x \xi^x \rangle = 0. \tag{1.144}$$

This equation can be seen as a definition for the noise strength experienced by a single, damped spin. The strength of the noise is in that sense fine-tuned and for the spin system depends on the state of the system itself. This is in contrast to an entirely thermal system where the noise-intensity is set by some external parameter such as the temperature.

Application example II: Noise correlations for single spins

We will illustrate the above procedure of deriving diffusion coefficients by considering the Heisenberg-Langevin equations of a two-level spin $H = \sigma^z \omega_z/2$ coupled to the external vacuum radiation modes, such that γ is the atomic spontaneous emission rate. The HLE are

$$\partial_t \sigma_t^x = -\omega_z \sigma_t^y - \frac{\gamma}{2}\sigma_t^x + \xi_t^x \tag{1.145}$$

$$\partial_t \sigma_t^y = \omega_z \sigma_t^x - \frac{\gamma}{2}\sigma_t^y + \xi_t^y \tag{1.146}$$

$$\partial_t \sigma_t^z = -(1+\sigma_t^z)\gamma + \xi_t^z \tag{1.147}$$

This set of equations now determines the correlations for the noise operators. We illustrate the procedure for the x, z components. According to the Einstein Relations of Eq. (1.138) and using the spin algebra $\sigma^i \sigma^j = i\epsilon_{ijk}\sigma^k$ we obtain

$$\begin{aligned}\langle \xi_t^x \xi_t^z \rangle = 2\mathcal{D}_{xz} &= \partial_t \langle \sigma_t^x \sigma_t^z \rangle - \langle D_x \sigma_t^z + \sigma_t^x D_z \rangle \\ &= \gamma \langle \sigma_t^x - i\sigma_t^y \rangle \, . \end{aligned} \tag{1.148}$$

Repeating this procedure for all possible components leads to the correlation matrix of the noise as

$$\langle \xi_{t'}^\alpha \xi_t^\beta \rangle = \gamma \delta(t-t')\chi^{\alpha\beta}, \tag{1.149}$$

$$\chi^{\alpha\beta} = \begin{pmatrix} 1 & -i & (\sigma^x - i\sigma^y) \\ i & 1 & i(\sigma^x - i\sigma^y) \\ (\sigma^x + i\sigma^y) & -i(\sigma^x + i\sigma^y) & 2(1+\sigma^z) \end{pmatrix}_{\alpha\beta} \tag{1.150}$$

This is an operator valued covariance matrix for the noise functions of the Heisenberg Langevin Equation. The matrix $\chi^{\alpha\beta}$ specifies noise correlations of the spins that depend on the state of the system and are therefore different from a constant, thermal noise intensity. We use the noise matrix χ to define the strength of the noise for numerical simulations of stochastic nonlinear equations in chapter 4.

Chapter 2

Decaying Atomic Spin States: (γ, κ) Dicke Model

The Dicke model can explain cooperative radiation of an ensemble of laser driven atoms that interact with a single quantised mode of the light field in an optical cavity. A quantum optical system that realises the Dicke superradiance phase transition is necessarily a driven-open system and has to take into account loss processes of excitations into the external environment. We extend previous Dicke model investigations concerned with photon losses with rate κ through cavity mirrors [26] by considering a second decay channel that focuses on internal atomic spin states that are subject to spontaneous emission with rate γ that is composed of individual, incoherent atomic emission and of a collective emission channel. We compute a modified critical atom-light coupling for the cooperative radiative phase transition in the cavity that takes into account the strength of both loss channels (κ, γ). We determine the mean-field non-equilibrium steady states for spin and photon observables as well as the cavity spectra in the long-time limit, $t \to \infty$. A recent (2018) experimental realization of the superradiance phase transitions using internal atomic states with atoms in optical lattices [44] has shown clear signatures of atomic spontaneous emission and shows good agreement with our theoretical predictions.

- This research is published as:
  Many-body quantum optics with decaying atomic spin states:(γ, κ) *Dicke model*,
  J. Gelhausen and M. Buchhold and P. Strack, Phys. Rev. A **95**, 063824 (2016)
- In comparison to the publication we have made several modifications. We have amended the summary of results presented in the beginning of this chapter. Moreover we changed the Introduction 2.1 and have updated Sec. 2.3.2 where we compare our theoretical analysis (2016) with the latest experimental rounds of data taking (2018, Singapore [44]). The derivation of a collective decay channel for the atoms and an estimation of its strength have been moved to chapter 1 where it was embedded in an introductory discussion on general time-evolution in open quantum systems. Minor rephrasings and changes have been made throughout the chapter for instance to mention and cite the most recent experiments relevant to this work and to cross reference and comment on other chapters in this thesis. Some paragraphs have been rearranged and one paragraph has been left out entirely and is only found in the online publication. We have also added an additional figure 2.3c.
- All other sections can be found identically (with minor adaptions) in the above mentioned publication.

2.1. Introduction

Cavity quantum electrodynamics provides a fundamental testbed for atom-light interactions at the quantum level. Modern day experiments have invested significant research efforts towards scaling up the minimal building block of one atomic qubit coupled to a single photon towards an ensemble of N ultracold atomic qubits trapped within tunable optical lattices between two cavity mirrors hosting photons with optical wavelengths [98, 24, 99]. These set-ups allow controllable loading of large numbers of ultracold atoms into optical resonators by overlaying cavity mode functions with lattice potentials to achieve a 'single-site resolution' for atom-cavity systems such that every atom couples with the same strength to the cavity photon.

Making the lattice potentials sufficiently deep, one can now access a regime in which the atomic motion is suppressed completely and the dynamics of internal spin excitations play the lead role. The ensuing collective behaviour from the coupling of light and matter is captured by the Dicke Hamiltonian an infinite-ranged, exactly solvable [100, 101] model predicted to describe a quantum phase transition where the vacuum ground state of the cavity changes into a twice degenerate state consisting of a macroscopic atomic polarization (ferromagnet) and a coherent electromagnetic field in the cavity, the so-called superradiant state. Reaching the quantum critical point requires the fundamental atom-light coupling (g) to be on the order of the atomic transition (ω_z) and cavity (ω_0) frequencies. However, it was shown that the atomic electric dipole elements are bounded by an oscillator sum-rule, prohibiting the superradiance transition from occurring for real atoms. A detailed discussion is given in Sec. 1.1. Driven-dissipative systems circumvent this no-go-theorem by boosting the atom-light coupling with an external pumping scheme [26] to reach a strong-coupling regime for the effective spin-photon coupling, $g > (\omega_0, \omega_z)$, needed to achieve the Dicke transition.

Experimental realizations of the Dicke model have been achieved with thermal or condensed Bose-Einstein condensates [102, 65], for internal spin states in external pumping schemes with ultracold, trapped atoms [49] and for artificial atoms (superconducting qubits) coupled to microwave photons [76] .

A basic physical difference to the earlier realizations of the Dicke model using momentum states of a Bose gas is the increased fragility of internal spin states to dissipative processes such as atomic spontaneous emission. The decay rate of collective momentum modes γ_{mom} of an atomic gas is small ($\gamma_{\text{mom}} \ll \kappa \lesssim g$) and limited mostly by thermal effects and collisions [103, 104, 105, 106, 107]. By contrast, single-site atomic spontaneous emission with rate γ tends to deplete the system of excitations and drives each spin into the $|\downarrow\rangle$ state. There is no analogue of this dissipative process for momentum states and therefore its basic physical effects have not been explored much in this context. Moreover, the experiments by Baden *et al.* [49] (2014, Singapore) were not entirely able to compare their data to a theory for the open Dicke model with spontaneous emission, clearly identifying a gap in the current literature.

The objective of the research presented in this chapter is to reveal the interplay of spontaneous emission with the collective interactions induced by the resonator. We extend previous works of the open Dicke model [26], which were restricted to photon losses, to the full two loss channels (γ, κ) variant. The atomic spontaneous emission consists of single-site atomic decay and a collective atomic contribution [69] whose strength is controlled by the cavity geometry in a large sample limit. We have explicitly derived a non-local contribution to the emission channel in Sec. 1.2.1. For the lattice based experiments considered in this work, the collective atomic decay is much smaller than all other typical scales, which we have demonstrated in Sec. 1.2.1.We therefore restrict the present analysis to the limit of weak collective decay and consider strong collective losses in chapter 4.

Meanwhile, new rounds of data taking by Zhiqiang *et al.* [44] (2018, Singapore) have confirmed that a decay channel for the atoms cannot be neglected and needs to be treated on the same footing as cavity photon loss. Their measurements show clear signatures of atomic spontaneous emission confirming our theoretical calculations.

Summary of results and outline of the chapter

We derive a formula for the critical coupling $g_c(\kappa,\gamma)$ for the onset of superradiance in Sec. 2.3.1 in the presence of both single-site and collective atomic spontaneous emission. This addresses an observed discrepancy between early experimental measurements of $g_c(\kappa)$ (2014, Singapore[49]) that observed higher pump strengths than predicted when only the dissipative channel of the photons was taken into account. We compare our predictions for $g_c(\kappa,\gamma)$ with most recent (2018, Singapore [44]) experimental measurements of the Dicke superradiance transition in Sec. 2.3.2 and find good agreement.

In the presence of spontaneous emission, we calculate an effective temperature at the superradiance transition for the photon modes, see Sec. 2.3.6 and identify clear signatures of atomic spontaneous emission in the cavity output spectrum Sec. 2.3.5 that can experimentally be verified. Based on the mean-field master equations derived in Sec. 4.3, we compute the values of non-equilibrium steady states and pin down effects of atomic spontaneous emission.

Based on experimental parameters and the specific setup considered in [44], we have shown in Sec. 1.2 that a collective loss channel for atomic excitations for the current lattice based experiments is negligible. Its strengths is determined from the cavity geometry and cavity parameters such as the ratio of the cavity wavelength to the size of the trapped atomic cloud, see Sec. 1.2.1. We will therefore mainly focus on incoherent atomic emission and consider strong collective losses in Chapter 4.

2.2. (γ,κ) Dicke model

In this section, we begin by explaining the model Dicke Hamiltonian and the Liouvillians for the two decay processes: photon loss and atomic spontaneous emission. Then, we connect this model to a recent quantum optics experiment, wherein the spin states in the Dicke Hamiltonian were realized via two atomic hyperfine-split levels. We finally present the Heisenberg-Langevin and the mean-field master equations within the Markov approximation.

2.2.1. Hamiltonian and Liouvillians

The core of the set-up is an array of N atomic spins at fixed positions in space that interact with a single cavity mode, as described by the Dicke-Hamiltonian

$$H = \omega_0 a^\dagger a + \left(\frac{U}{2N}\sum_{\ell=1}^{N}\sigma_\ell^z\right) a^\dagger a + \frac{\omega_z}{2}\sum_{\ell=1}^{N}\sigma_\ell^z + \frac{g}{\sqrt{N}}(a+a^\dagger)\sum_{\ell=1}^{N}(\sigma_\ell^+ + \sigma_\ell^-)\,. \tag{2.1}$$

Here the photon energy is ω_0, and ω_z denotes the atomic transition frequency. For the atomic degrees of freedom we use the notation $\sigma_i^+ = |e\rangle_i\langle g|\,, \sigma_i^z = |e\rangle_i\langle e| - |g\rangle_i\langle g|$ and

$S^{\pm} = \sum_{\ell=1}^{N} \sigma_{\ell}^{\pm}$. Here (e, g) refers to the excited and ground state of a two-level atom, respectively and a labels the annihilation operator for a cavity photon. There appears also an additional dynamical frequency shift of the photons due to a coupling U to the collective spin z-component which arises for the quantum-optical implementation of the model we discuss below.

The second class of processes introduce decoherence and are irreversible decay processes of both, photonic (rate κ) and atomic excitations (rate γ) into the reservoir modes of the electromagnetic vacuum surrounding the cavity. The photons decay through the imperfect mirrors and the atoms directly decay into the reservoir modes via the solid angle not covered by the mirrors, as shown in Fig. 3.1. Their effect can be captured by introducing the Lindblad operators, which act on the system density matrix ρ in the following way:

$$\begin{aligned} \mathcal{L}_{\gamma}[\rho] =& \gamma(1-\alpha) \sum_{\ell=1}^{N} \left(\sigma_{\ell}^{-} \rho \sigma_{\ell}^{+} - \frac{1}{2} \{ \sigma_{\ell}^{+} \sigma_{\ell}^{-}, \rho \} \right) \qquad (2.2) \\ &+ \gamma\alpha \left(S^{-} \rho S^{+} - \frac{1}{2} \{ S^{+} S^{-}, \rho \} \right), \\ \mathcal{L}_{\kappa}[\rho] =& \kappa \Big[2a\rho a^{\dagger} - \{ a^{\dagger} a, \rho \} \Big] \; . \qquad (2.3) \end{aligned}$$

Here, the atomic spontaneous emission consists of two contributions. The first is the single atom decay rate γ for a single atom at site ℓ (2.2). The second contribution is a collective decay contribution expressed with the collective atomic operators $S^{\pm} = \sum_{\ell=1}^{N} \sigma_{\ell}^{\pm}$ (2.3). The prefactor controls the strength of the collective decay and depends on the cavity geometry. While a detailed derivation of the atomic Lindblad operator can be found in Sec. 1.2.1, we want to stress here that the lattice setups under consideration generally correspond to $\alpha \ll 1$, as estimated in Sec.1.2.1. It can be seen that in such a description the single atom loss term scales linearly in the atom number whereas the collective loss term scales quadratically with the atom number. Since every experimental system is necessarily finite with a well-defined atom-number N_0, so is the collective loss rate. In order to define a sensible thermodynamic limit, for which both the average energy and loss rate per particle remain constant, the geometric coupling term is rewritten as $\gamma\alpha \to \gamma\alpha N/N = \beta/N$. The thermodynamic limit is now understood as taking $N \to \infty$ and $V \to \infty$ with $N/V = const.$ and $\beta = \alpha N_0 = const.$, where N_0 is the experimentally relevant number of atoms and therefore fixes the collective loss rate. This is analogous to the thermodynamic limit of the Dicke Hamiltonian, for which the coupling of the light field to an individual atom is finite and fixed in any experimental set-up. However, the correct description of the system in the thermodynamic limit necessitates that the coupling is written as $\sim \frac{g}{\sqrt{N}} \sum_{\ell=1}^{N} \sigma_{\ell}^{x} (a + a^{\dagger})$ such that in the thermodynamic limit g is constant and fixed.

The interplay and competition between unitary and irreversible dynamics can be studied with a Master equation for the density matrix

$$\dot{\rho} = -i[H, \rho] + \mathcal{L}_{\kappa}[\rho] + \mathcal{L}_{\gamma}[\rho] \; . \qquad (2.4)$$

As the Hamiltonian in Eq. (2.1) does not conserve the total number of excitations $\mathcal{N} = a^{\dagger}a + \frac{1}{2} \sum_{\ell=1}^{N} \sigma_{\ell}^{z} + \frac{N}{2}$ the Hamiltonian will counteract the depletion processes of the Lindblad terms. This is in contrast to a Hamiltonian where the counter-rotating terms are dropped in a rotating-wave-approximation and for which there would be no other steady-state than the empty dark state.

Symmetries

Eq. (2.4) is invariant under a combined, discrete $\mathbb{Z}_2$ symmetry transformation

$$\mathbb{Z}_2 : [a + a^\dagger, \sigma_\ell^x, \sigma_\ell^y] \to [-(a + a^\dagger), (-\sigma_\ell^x, -\sigma_\ell^y)], \tag{2.5}$$

which corresponds to a unitary transformation

$$U_\pi = \exp\left(i\pi\left[a^\dagger a + \sum_{\ell=1}^{N} \sigma_\ell^z\right]\right). \tag{2.6}$$

This symmetry is spontaneously broken at the Dicke superradiance transition.

Additionally, the spin sector of the Hamiltonian in Eq. (2.1) is invariant under a combination of time reversal and rotation in spin-space around the y-axis with angle $\theta = \pi$. In the absence of a loss channel in the spin sector, this means that the steady-state must be invariant under this transformation as well, which enforces $\langle \sigma^y \rangle = 0$. This symmetry is broken in the presence of Liouvillian $\mathcal{L}_\gamma$ in the spin sector and therefore steady states with non-zero $\langle \sigma^y \rangle \neq 0$ are accessible in the dynamics. In the photon sector, the corresponding symmetry is broken as well due to the presence of $\mathcal{L}_\kappa$, which leads to complex expectation values $\langle a \rangle \in \mathbb{C}$.

We mention here that the Hamiltonian dynamics together with the Lindblad contribution $\mathcal{L}_\kappa$ conserves the pseudo-angular momentum $\langle \boldsymbol{S}_t \rangle^2$ but this conservation is explicitly broken by $\mathcal{L}_\gamma$. Using semi-classical steady states defined below, one finds

$$\partial_t \langle \boldsymbol{S}_t \rangle^2 = 2 \langle \boldsymbol{S}_t \rangle \cdot \partial_t \langle \boldsymbol{S}_t \rangle = -\gamma \left(\langle \boldsymbol{S}_t \rangle^2 + 2 \langle \sigma_t^z \rangle \left(1 + \frac{\langle \sigma_t^z \rangle}{2} \right) \right), \tag{2.7}$$

such that the steady-state value requires $\lim_{t\to\infty} \langle \boldsymbol{S}_t \rangle^2 = -2 \langle \sigma^z \rangle \left(1 + \frac{\langle \sigma^z \rangle}{2}\right)$ to hold.

Experimental context in cavity QED

The Hamiltonian in Eq. (2.1) describes a laser-driven atomic ensemble in an optical cavity where atoms are trapped in an intracavity lattice such that they couple with the same strength to the optical light field of a cavity resonator, see Fig. 1.3 as recently realized experimentally (2018, Singapore [44]). The Hamiltonian is time-independent only in a frame rotating at the frequencies of the driving laser, see [26, 44]. Moreover, some form of Raman-transition assisted pumping scheme as originally suggested in [26] and displayed in Fig. 1.3 is required to boost the spin-photon coupling g to the strong-coupling regime ($g > (\omega_z, \omega_0) \gg (\kappa, \gamma)$) needed to achieve the Dicke transition. In the driven scheme, the coupling is externally tunable as it depends on the Rabi-frequencies of the driving laser Ω as $g(\Omega)$. There atomic levels realize an effective spin system $\{|\uparrow\rangle, |\downarrow\rangle\}$ that can be the hyperfine-structure manifold of the ground states of ^{87}Rb. Typically this is the $5^2\mathrm{S}_{1/2}$ manifold. The cavity-assisted Raman transitions are achieved by coupling to the states of the first excited state manifold $5^2\mathrm{P}_{1/2}$ or $5^2\mathrm{P}_{3/2}$. As the laser frequencies are coupled off-resonantly, there appears an additional dispersive shift of the cavity frequency with strength U, see Eq. (2.1). For a more detailed description of the laser-dressing scheme, see Sec. 1.1.

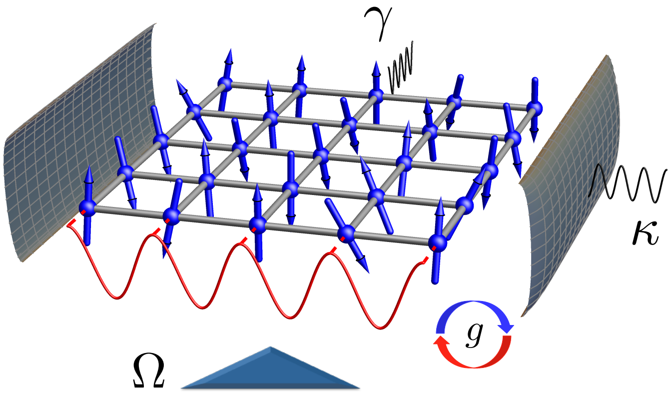

Figure 2.1.: Sketch of the system setup. The optical lattice inside the cavity is commensurate with the single light mode of the cavity that couples all atoms with strength g to the light-field. The atoms can directly spontaneously decay with rate γ into the reservoir of electromagnetic modes via the solid angle not covered by the cavity mirrors. These losses are uncorrelated single-site losses and collective emissions into a shared external reservoir once the system is in the superradiant state. The collective contribution to the decay is estimated in Sec. 1.2.1 and found to be negligibly small for the current setup. Photons can leave the system through the cavity mirrors with rate κ. The system is driven from the side with a laser of Rabi frequency Ω to stabilize the excitation number.

2.2.2. Heisenberg-Langevin and mean-field master equations

The Heisenberg equation of motion for an arbitrary system operator O is calculated according to the adjoined master equations, see Sec. 1.2

$$\partial_t O = -\, i[H, O] + \mathcal{L}_\gamma^\dagger[O] + \mathcal{L}_\kappa^\dagger[O] + \xi_t^O \,, \tag{2.8}$$

where the Hamiltonian is given by Eq. (2.1) and (κ, γ) refer to the cavity damping and the rate of spontaneous emission, respectively and $\mathcal{L}^\dagger[O] = \sum_\ell L_\ell^\dagger O L_\ell - 1/2\{L_\ell^\dagger L_\ell, O\}$ and $L_\ell = \{a, \sigma_\ell^-, \sum_{\ell=1}^N \sigma_\ell^-\}$ being the set of jump operators for cavity decay for incoherent atomic spontaneous emission and collective atomic emission, respectively. The Heisenberg-Langevin equations (2.8) for these variables are:

$$\partial_t a_t = -\left[\kappa + i\left(\omega_0 + \frac{U}{2N}\sum_{\ell=1}^N \sigma_{\ell,t}^z\right)\right] a_t - i\frac{g}{\sqrt{N}}\sum_{\ell=1}^N \left(\sigma_{\ell,t}^- + \sigma_{\ell,t}^+\right) + \sqrt{2\kappa}a_{\mathrm{in,t}} \tag{2.9}$$

$$\partial_t \sigma_{i,t}^+ = i\left(\omega_z + \frac{U}{N}a_t^\dagger a_t\right)\sigma_{i,t}^+ - i\frac{g}{\sqrt{N}}\sigma_{i,t}^z\left(a_t + a_t^\dagger\right) - \frac{\gamma}{2}\sigma_{i,t}^+ + \frac{\gamma\alpha}{2}\sum_{\ell\neq i}\sigma_{\ell,t}^+\sigma_{i,t}^z + \xi_{i,t}^+ \tag{2.10}$$

$$\partial_t \sigma_{i,t}^z = 2\frac{g}{\sqrt{N}}\left(a_t + a_t^\dagger\right)\left(\sigma_{i,t}^- - \sigma_{i,t}^+\right) i - (1 + \sigma_{i,t}^z)\gamma - \gamma\alpha\sum_{\ell\neq i}\left(\sigma_{i,t}^+\sigma_{\ell,t}^- + cc.\right) + \xi_{i,t}^z \tag{2.11}$$

It can be seen that the incoherent atomic loss $(\sim \gamma)$ induces linear dissipative terms, whereas the collective loss $(\sim \gamma\alpha)$ introduces non-local and non-linear couplings of the spins. Here, $\left(a_{\mathrm{in,t}}, \xi_{i,t}^z, \xi_{i,t}^+\right)$ are the fluctuating quantum mechanical noise operators with zero mean. They result from integrating out the bath of electromagnetic modes outside the cavity in the Born-Markov approximations, we have embedded an explicit derivation in Sec. 4.4.

We will proceed to analyze the Heisenberg-Langevin equations in a mean-field framework where we apply a site-decoupling for the many-atom states. The mean-field state cannot keep track of the behaviour of atoms on different sites. Therefore, taking the expectation values $\langle . \rangle = \mathrm{Tr}[.\otimes_{n=1}^{N} \rho_n]$,where the density matrix is site decoupled as $\rho = \otimes_{i=1}^{N} \rho_i$, leads to the mean-field equation for N two-level atoms

$$\partial_t \langle a_t \rangle = -\left[\kappa + i\left(\omega_0 + \frac{U}{2}\langle \sigma_t^z \rangle\right)\right]\langle a_t \rangle - ig(\langle \sigma_t^- \rangle + \langle \sigma_t^+ \rangle)\ , \tag{2.12}$$

$$\partial_t \langle \sigma_t^+ \rangle = \left[i\left(\omega_z + U\langle a_t^\dagger \rangle \langle a \rangle_t\right) - \frac{\gamma}{2}(1 - \beta\langle \sigma_t^z \rangle)\right]\langle \sigma_t^+ \rangle - ig\langle \sigma_t^z \rangle(\langle a_t \rangle + \langle a_t^\dagger \rangle)\ , \tag{2.13}$$

$$\partial_t \langle \sigma_t^z \rangle = -\gamma\left[(1 + \langle \sigma_t^z \rangle) + 2\beta\langle \sigma_t^- \rangle\langle \sigma_t^+ \rangle\right] + 2ig(\langle a_t \rangle + \langle a_t^\dagger \rangle)(\langle \sigma_t^- \rangle - \langle \sigma_t^+ \rangle)\ . \tag{2.14}$$

Here we have set $\beta = \alpha(N-1)$ which fixes the strength of the collective decay as discussed in Sec. 2.2.1. Expectation values of the noise operators vanish $\langle \xi_t^z \rangle = \langle \xi_t^+ \rangle = \langle a_{in,t} \rangle = 0$. In the remainder of the chapter, we provide an analysis of these equations on a mean-field level and calculate the corresponding non-equilibrium steady-states and connect our theoretical results to the recent quantum optical realization of the Dicke phase transition with cavity-assisted Raman transitions [49, 44] to address the observed discrepancy between critical pump strengths and calculations restricted to photon loss only [26]. As pointed out above, we restrict our analysis to the case of weak collective decay contributions, with $0 \leq \beta \ll 1$ which is an appropriate approximation for the present large sample limit, where the extensions of the cavity and the atomic sample are much bigger than the optical wavelength of the cavity modes. A conservative approximation of the geometric contribution α is given in Sec. 1.2.1. We reserve an analysis of strong collective decay contributions for chapter 4 (see also Refs. [69]).

2.3. Results

In this section, we first compute an analytic formula for the critical coupling for the onset of Dicke superradiance in the presence of both correlated and uncorrelated atomic spontaneous emission. We then use this formula to determine an effective atomic loss rate for the experiment in Ref. [49]. We also compare this effective decay rate to other atomic loss channels such as the collective polariton lifetime. We close by searching for signatures of the additional loss channel γ in the cavity output spectrum and by computing the effective temperature of the system at the superradiance transition.

2.3.1. Critical coupling for onset of superradiance $g_c(\kappa, \gamma)$

We first transform Eqs. (2.9-2.11) into frequency space by the following relation:

$$\mathcal{O}_t = \frac{1}{2\pi}\int_{-\infty}^{\infty} e^{-i\nu t}\mathcal{O}(\nu)d\nu, \quad \mathcal{O}_t^\dagger = \frac{1}{2\pi}\int_{-\infty}^{\infty} e^{-i\nu t}\mathcal{O}^\dagger(-\nu)d\nu\ , \tag{2.15}$$

where the operator $\mathcal{O}_t$ is either of $\left(a_t, \sigma_{i,t}^+, \sigma_{i,t}^z, a_{\mathrm{in,t}}, \xi_{i,t}^+, \xi_{i,t}^z\right)$ and $\mathcal{O}_t^\dagger$ refers to either of $\left(a_t^\dagger, \sigma_{i,t}^-, a_{\mathrm{in,t}}^\dagger\right)$. We then specifically make a distinction between the semi-classical steady states and the amplitude fluctuations around these values by linearising Eqs. (2.9-2.11). We define the fluctuation operators in frequency space by the relation

$$\sigma^+(\nu) = 2\pi\langle \sigma^+ \rangle\delta(\nu) + \delta\sigma^+(\nu), \tag{2.16}$$

$$\sigma^z(\nu) = 2\pi\langle \sigma^z \rangle\delta(\nu) + \delta\sigma^z(\nu), \tag{2.17}$$

$$a(\nu) = 2\pi\sqrt{N}\langle a \rangle\delta(\nu) + \delta a(\nu)\ . \tag{2.18}$$

Where the set of steady-states $\langle\sigma^+\rangle$ and $\langle\sigma^z\rangle$ and $\langle a\rangle$ are solutions to Eqs. (2.12-2.14) in the long-time limit. Here, $\delta\sigma^+(\nu), \delta\sigma^z(\nu)$ and $\delta a(\nu)$ describe fluctuations about the semi-classical steady-state and $\delta(\nu)$ denotes a delta function in frequency space. The equations for the amplitude fluctuations are generated by inserting Eqs. (2.16-2.18) into the Fourier transformed set of Eqs. (2.9-2.11). At long times, we may neglect second-order terms in the fluctuations by assuming that the steady-state values are large compared to the associated fluctuations in the thermodynamic limit $N \to \infty$. The linearized equations can be cast in matrix form

$$\boldsymbol{\xi}(\nu) = \delta(\nu) f(\boldsymbol{\sigma}) + \boldsymbol{G}_R^{-1}(\nu) \cdot \boldsymbol{\delta\sigma}(\nu), \tag{2.19}$$

where the fluctuation (noise) operators are collected in the vectors $\delta\boldsymbol{\sigma}(\nu)$ ($\boldsymbol{\xi}(\nu)$):

$$\delta\boldsymbol{\sigma}^T(\nu) = \left(\delta a(\nu), \delta a^\dagger(-\nu), \delta\sigma^+(\nu), \delta\sigma^-(-\nu), \delta\sigma^z(\nu)\right), \tag{2.20}$$

$$\boldsymbol{\xi}^T(\nu) = \left(\sqrt{2\kappa} a_{\text{in}}(\nu), \sqrt{2\kappa} a_{\text{in}}^\dagger(-\nu), \xi^+(\nu), \xi^-(-\nu), \xi^z(\nu)\right). \tag{2.21}$$

The inverse response function (retarded Green's function) then reads as

$$\boldsymbol{G}_{\boldsymbol{R}}^{-1}(\nu) =$$

$$\begin{pmatrix} \frac{1}{2} iU\langle\sigma^z\rangle + \kappa - i\nu + i\omega_0 & 0 & ig & ig & i\frac{U}{2}\langle a\rangle \\ 0 & -\frac{1}{2} iU\langle\sigma^z\rangle + \kappa - i\nu - i\omega_0 & -ig & -ig & -i\frac{U}{2}\langle a^\dagger\rangle \\ ig\langle\sigma^z\rangle - iU\langle a^\dagger\rangle\langle\sigma^+\rangle & ig\langle\sigma^z\rangle - iU\langle a\rangle\langle\sigma^+\rangle & -iU\langle a\rangle\langle a^\dagger\rangle + \frac{\gamma}{2}(1-\beta\langle\sigma^z\rangle) - i\omega_z - i\nu & 0 & ig(\langle a\rangle + \langle a\rangle^\dagger) \\ iU\langle a^\dagger\rangle\langle\sigma^-\rangle - ig\langle\sigma^z\rangle & -ig\langle\sigma^z\rangle + iU\langle a\rangle\langle\sigma^-\rangle & 0 & iU\langle a\rangle\langle a^\dagger\rangle + \frac{\gamma}{2}(1-\beta\langle\sigma^z\rangle) + i\omega_z - i\nu & -ig(\langle a\rangle + \langle a\rangle^\dagger) \\ 2ig(\langle\sigma^+\rangle - \langle\sigma^-\rangle) & 2ig(\langle\sigma^+\rangle - \langle\sigma^-\rangle) & 2ig(\langle a\rangle + \langle a\rangle^\dagger) + 2\beta\gamma\langle\sigma^-\rangle & -2ig(\langle a\rangle + \langle a\rangle^\dagger) + 2\beta\gamma\langle\sigma^+\rangle & \gamma - i\nu \end{pmatrix} \tag{2.22}$$

The notation in Eq. (2.19) indicates that the responses of the system $\boldsymbol{\delta\sigma}(\nu)$ to the "driving force" $\boldsymbol{\xi}(\nu)$ is indeed described by the function $\boldsymbol{G}_R(\nu)$. The steady state contribution is encoded in $f(\boldsymbol{\sigma})$ which is left unspecified as it just gives a peak at zero-frequency in the cavity spectrum. We approach the phase transition from the normal phase, for which $\langle a\rangle = \langle\sigma^+\rangle = 0$ and assume the atoms to be fully polarized $\langle\sigma^z\rangle = -1$. Evaluating the condition for super radiance,

$$\lim_{\nu \to 0} \det[\boldsymbol{G}_{\boldsymbol{R}}^{-1}(\nu)] = 0, \tag{2.23}$$

which is appropriate as long as $\beta < \sqrt{1 + \left(\frac{\omega_z}{\gamma/2}\right)^2}$, we find the critical coupling

$$g_c(\gamma, \kappa, U, \beta) = \frac{\sqrt{\frac{\gamma^2}{4}(1+\beta)^2 + \omega_z^2}\sqrt{\kappa^2 + \left(\omega_0 - \frac{U}{2}\right)^2}}{2\sqrt{\omega_z\left(\omega_0 - \frac{U}{2}\right)}}. \tag{2.24}$$

This formula recovers the known expression [26] in the limit $(U, \gamma) \to 0$ and the critical coupling known from [108] in the limit $\gamma \to 0$. It can be seen that the spontaneous emission γ shifts the atomic energy scale ω_z and the photon loss rate κ shifts the cavity frequency ω_0. As expected, the addition of spontaneous atomic emission leads to an increased value for the critical coupling g_c to compensate for the losses. In the limit $\beta \to 0$, $g_c(\kappa, \gamma)$ has meanwhile been reproduced by a calculation in a fermionic path-integral [109] (after our article was avilable online).

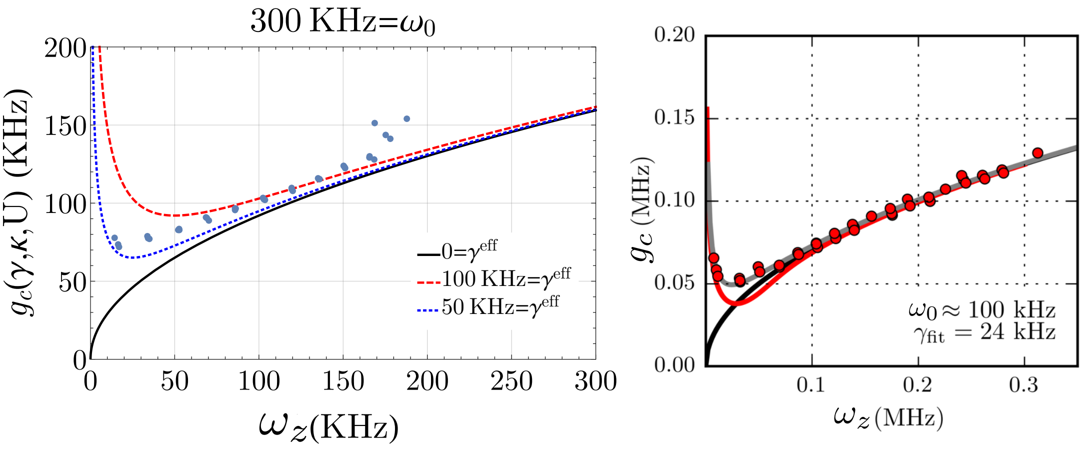

(a)

(b)

Figure 2.2.: Experiment and theory comparison for the critical coupling strength $g_c(\kappa, \gamma, U, \beta = 0)$ from Eq. (2.24) for the onset of superradiance. The experimental data is fitted with an effective decay rate $\gamma^{\rm eff}$ as modelled by the Lindblad $\mathcal{L}_\gamma$ in Eq. 2.2.(a) Comparison with the experimental data obtained in (2014, Singapore [49]). We give an estimate for a lower (dotted) and upper (dashed) effective decay rate $\gamma^{\rm eff}$ of the effective atomic dipole and compare it to the theory curve for $\gamma^{\rm eff} = 0$ (solid). We have used the experimentally determined values $U = -12.4$ KHz and $\kappa = 100$ KHz. In the regime $|\omega_0| \gg |U|$ the effects of the frequency shift U for the critical coupling are negligible. For small longitudinal fields ω_z, the theory curves show a clear upswing in the critical coupling, see text for details. (b) New rounds of data taking (2018, Singapore, [44])(dots) have accessed the upswing at small effective frequencies of ω_z more carefully and have fitted an effective decay rate $\gamma_{\rm eff}$ to the superradiance threshold (gray curve). This was compared with a curve taking into account other sources of noise (see text) (red curve). It can be seen that the gray curve adequately predicts the superradiance threshold (see text for details). Figure (b) taken from (2018, Singapore [44]) with adapted labelling.

2.3.2. Comparison with experimental results

Here, we compare the superradiance threshold value $g_c(\kappa, \gamma, U), \beta = 0$ with experimental data from the two Dicke model simulations (2014, Singapore [49]) and (2018, Singapore [44]). In both experiments, the Dicke model was realized using cavity-assisted Raman transitions [49]. A sudden increase in the number of detected cavity photons upon ramping up the drive strength of an external laser has been associated with the threshold for Dicke superradiance. They compared the experimentally observed threshold couplings to the conventional theory value without spontaneous emission ($g_c(\kappa)$) [26, 108] and found a discrepancy: higher pump strengths than predicted were necessary to observe an increase in photon numbers.

We find it useful to use a single effective atomic decay γ_{eff}, captured by the Lindblad operator of Eq. (2.2), to enable an experiment-theory comparison by fitting the superradiance threshold with γ_{eff}. The latest experimental data also took into account other sources of noise such as the effect of thermal motion which introduces decoherence by collisions and Doppler broadening in addition to a spontaneous emission contribution from the scattering of pump photons. However, these contributions were estimated as much smaller than the fitted decay rates and only Doppler shifts become non-vanishingly small at small longitudinal field detuning [44]. However, other sources of noise (noise in the trapping potential, loss of atoms from the trap, dissipative dephasing, noise in the driving laser) could also be modelled and included to account. Therefore γ^{eff} should be regarded as an effective spin decay rate after eliminating the far- detuned excited state, possibly other decay channels, and other experimental imperfections.

Using the computed value for the critical coupling in Eq. (2.24), in the limit $\beta \to 0$, the effective decay rate $\gamma = \gamma^{\text{eff}}$ is fitted to experimental data from (2014, Singapore [49]) to reduce the discrepancy between experiment [49] and theory. As mentioned before, the collective atomic decay channel is irrelevant for the present setup, justifying the restriction of the following analysis to the case $\beta = 0$. The results of the fitting procedure are shown in Fig. 2.2a.

An additional interesting regime to pin down the effects of γ^{eff} is the critical region for small longitudinal spin detuning ω_z. From the critical coupling Eq. (2.24), we observe that $g_c(\gamma^{\text{eff}}, \kappa, U)$ becomes large for small ω_z provided γ^{eff} is finite. By contrast in the strict $\gamma^{\text{eff}} \to 0$ limit $g_c(\gamma^{\text{eff}} = 0, \kappa, U)$ decreases for small ω_z. New rounds of data-taking (2018, Singapore [44]) have accessed this regime and reproduce this clear upswing for small longitudinal fields, consistent with non-negligible atomic spontaneous emission, see Fig. 2.2b.

To this end, one may wonder whether the experimentally observed γ^{eff} can be explained by the decay rate that the $|\uparrow\rangle = |F = 2, m_F = 2\rangle$ state in the $5^2\text{S}_{1/2}$ manifold inherits from the excited state in the $5^2\text{P}_{3/2}$ manifold to which the cavity couples. This inherited decay rate can be estimated as

$$\gamma_{\text{inherited}} = \chi \left(\Omega_r/\Delta_r\right)^2 \gamma_{\text{exc}} = \chi g^2/(NC\kappa) \; , \tag{2.25}$$

where the proportionality constant χ is fixed by the transition strengths between the involved atomic levels. $C = g_{\text{cav}}^2/(\kappa\gamma_{\text{exc}})$ is the single atom cooperativity and $(g_{\text{cav}}, \kappa, \gamma_{\text{exc}}) = 2\pi \times (1.1, 0.1, 3)$ MHz. κ is the cavity decay rate and $2g_{\text{cav}}$ is the single photon Rabi frequency for the transition of $|F = 2, m_F = 2\rangle$ to $|F' = 3, m_F' = 3\rangle$, γ_{exc} is the fundamental atomic decay rate of the excited state level coupling to the cavity. Ω_r and Δ_r are the Rabi frequency and the detuning of the driving laser, respectively, that couples the $|\uparrow\rangle$ state to the aforementioned excited state of the $5^2\text{P}_{3/2}$ manifold. We have set the Raman coupling strength $g = \sqrt{N} g_{\text{cav}} \frac{\Omega_r}{\Delta_r}$ in Eq. (2.25) with N a fixed number of atoms in the ground-state manifold.

γ_{exc}	$\gamma^{\text{eff}}(g=g_c)$	$\gamma_{\text{Polariton}}(g=g_c)$	$\gamma_{\text{inherited}}(g=g_c)$
3000 KHz	(50 – 100)KHz	(72 – 103) KHz	0.02 KHz

Table 2.1.: Overview of various decay rates and their KHz values for the experimental setup in [49]. The range for $\gamma^{\text{eff}}(g=g_c)$ is estimated in Fig. 2.2. $\gamma_{\text{Polariton}}$ is calculated from Eq. (2.27) with the set of parameters $(\omega_0, \kappa, \omega_z, \gamma^{\text{eff}})$=(300, 100, 150, (50; 100))KHz. $\gamma_{\text{inherited}}$ is determined by the model parameters and expressed as $\gamma_{\text{inherited}}(g=g_c) = 24g_c^2/(NC\kappa)$, where N is the number of atoms in the trap, $C = g_{\text{cav}}^2/(\kappa, \gamma_{exc})$ is the single atom cooperativity, κ is the cavity decay rate and $2g_{\text{cav}}$ is the single photon Rabi frequency for the transition of $|F=2, m_F=2\rangle$ to $|F'=3, m'_F=3\rangle$. The value for $\gamma_{\text{inherited}}$ was calculated for $(N, C, g_c, \kappa) = (5\cdot 10^4, 4, 120\text{KHz}, 100\text{KHz})$ where the number of atoms represents a typical order of magnitude for the experiment in [49].

As we show and discuss in Table 2.1, $\gamma_{\text{eff}} \gg \gamma_{\text{inherited}}$, such that $\gamma_{\text{inherited}}$ alone is not sufficient to explain the experimental data.

2.3.3. Polariton decay rates

For non-zero atom-light coupling, the atomic and photonic excitations of the system start to hybridize and are commonly referred to as polaritons. The decay of the polaritons describes a correlated decay mechanism with rate $\gamma_{\text{polariton}}$, which involves many atoms and photons. The corresponding decay rate is a function of the bare decay rates of the individual atoms γ, the bare decay rate of the individual photons κ, the energies of the bare atoms ω_z and of the photons ω_0 as well as the atom photon coupling g. The rates can be read off from the imaginary part of the resonance frequencies ν for the linearized system dynamics, that can be determined from

$$\lim_{(\beta,U)\to 0} \det[\boldsymbol{G}_{\text{R}}^{-1}(\nu)] = 0, \quad \gamma_{\text{Polariton}} = |\text{Im}(\nu)| \tag{2.26}$$

In Fig. 2.3 we plot the effective decay rates $\gamma_{\text{polariton}}$ as a function of the atom-light coupling g as they are also shown in [26] for the κ only case.

As such $\gamma_{\text{Polariton}}$ sets the width of the resonance peaks in the cavity-spectrum. We explore certain limits for the collective decay rates. For $g \to 0$, the resonances calculated from Eq. (2.26) are located at $\nu_{\text{atom}} = \pm\omega_z - i\frac{\gamma}{2}$, at $\nu_{\text{photon}} = \pm\omega_0 - i\kappa$ and the σ_z-resonance is at $\nu = -i\gamma$, see Fig. 2.3a. Corresponding to resonances located at the characteristic atom and photon frequencies with a line-shape of a Lorentz-curve with a width determined from the microscopic decay rates. At $g = g_c$ the decay rate of the critical pole with finite imaginary part (see Fig. 2.3b, solid, blue line) is given as

$$\gamma_{\text{Polariton}}(g=g_c) = \frac{2\left(\gamma^2\kappa + 2\gamma\left(\kappa^2+\omega_0^2\right) + 4\omega_z^2\kappa\right)}{\gamma^2 + 8\gamma\kappa + 4\left(\omega_z^2+\kappa^2+\omega_0^2\right)} \tag{2.27}$$

$$\lim_{\gamma\to 0}\gamma_{\text{Polariton}}(g=g_c) = \kappa\frac{2\omega_z^2}{\omega_z^2+\kappa^2+\omega_0^2}, \tag{2.28}$$

The behaviour of $\gamma_{\text{Polariton}}$ as a function of the atom-light coupling is shown in Fig. 2.3.

2.3.4. Non-equilibrium steady states for spins and photons

In this section, we discuss the steady-state operator expectation values $\langle a\rangle, \langle\sigma^+\rangle, \langle\sigma^z\rangle$, where $\langle a\rangle$ is the complex field amplitude that accounts for a coherent photon conden-

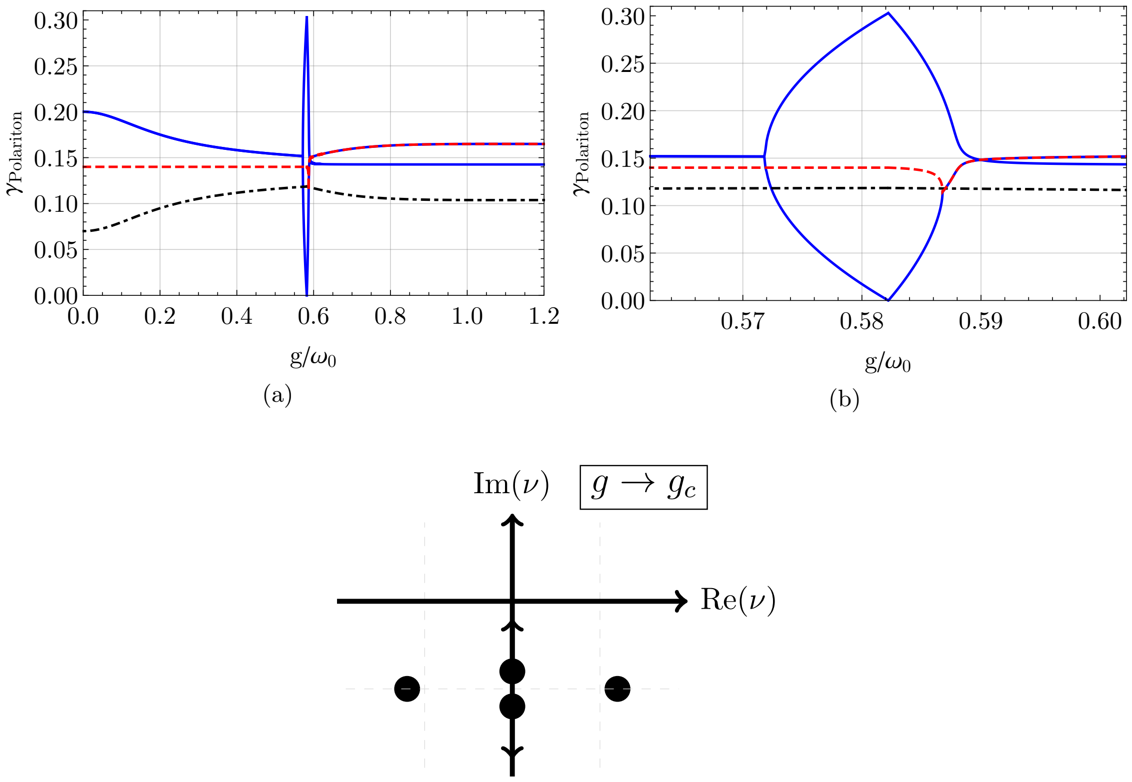

(a)

(b)

(c)

Figure 2.3.: Decay rates ($\gamma_{\text{Polariton}}$) of (in general) hybridized atom-photon modes for varying atom-light coupling strength g/ω_0 obtained from solving Eq. (2.26) for the set $\omega_z/\omega_0 = 1.3, \kappa/\omega_0 = 0.2, \gamma/\omega_0 = 0.14$. (a) For $g \to 0$, the lifetimes are given by the microscopic cavity decay rate $\kappa/\omega_0 = 0.2$ (solid) and the single atom decay rate $\gamma/(2\omega_0) = 0.07$ for the atomic polarisations (dot-dashed) and the decay rate associated to the density of excitations $\gamma/\omega_0 = 0.14$ (dashed). (b) Close-up around the critical atom-light coupling strength $g = g_c \approx 0.582\omega_0$. In the regime $g < g_c$ there is a splitting of a polariton branch into a mode with finite and vanishing lifetime at the phase transition point $g = g_c$. This is depicted in (c). The splitting occurs when the real-part of the excitation frequencies ν vanishes (not shown). (c) Two low-energy poles of $\boldsymbol{G}_R^{-1}(\nu)$ for $g \to g_c$ become entirely imaginary and of one of the two poles vanishes at $g = g_c$ and destabilizes the empty state. The other pole retains a finite imaginary part (spectator pole). The behaviour of the low-energy poles for the full two loss channel analysis (κ, γ) is identical to the case where only photon losses are considered, see [87].

sate, $\langle\sigma^+\rangle$ is the complex atomic polarization amplitude and $\langle\sigma^z\rangle$ measures the atomic population imbalance. The dynamics of the expectation values is given by the mean-field equations Eqs. (2.12-2.14). In the semi-classical picture for a spin-1/2 system we construct the expectation value of the spin-vector $\langle \boldsymbol{S}_t\rangle = (\langle\sigma^x(t)\rangle, \langle\sigma^y(t)\rangle, \langle\sigma^z_t\rangle)^T$. It defines the orientation of the averaged atomic Bloch vector. The non-equilibrium Bloch dynamics of the collective angular momentum without spontaneous emission was studied in Ref. [108].

An analytical solution for the semi classical steady-states $(\partial_t\langle\sigma^\alpha_t\rangle) = 0$ and $\partial_t\langle a_t\rangle = 0$ is accessible by setting $U = 0$ and $\beta = 0$. However, we show the effect of the collective decay contribution for the steady-state of the $\langle\sigma^x\rangle$ order parameter in Fig. 2.4b. Analysis of effective Dicke Hamiltonians with non-zero U in the $\gamma \to 0$ regime have been investigated in detail [110, 108, 111] such that we focus on consequences of non-vanishing radiative decay. We mention that in an experimental realization with cavity-assisted Raman transitions $U = 0$ is achieved by having equal amplitudes for co- and counter-rotating terms of the effective Dicke-Hamiltonian [26]. Slight experimental mismatches of the amplitudes lead to vanishingly small $|U| \ll (|\omega_0|, |\omega_z|, \kappa, \gamma)$ such that the resulting nonlinearities in the equation of motion can safely be neglected. We solve the system of non-linear equations for the fixed points to obtain the steady-states. For $g < g_c$ the only steady-state is $\langle a\rangle = \langle\sigma^+\rangle = 0$ and $\langle\sigma^z\rangle = -1$. This is the empty atom-cavity system as the spontaneous atomic decay and photon loss depletes the system of all excitations. The mean-field expectation values for the fields in the superradiant phase $g > g_c$ are:

$$\langle a\rangle = \pm\frac{\sqrt{\frac{\kappa^2+\omega_0^2}{\omega_0}}\sqrt{\omega_z\left(1-\frac{J_c}{J}\right)}}{\sqrt{2}(-\omega_0+i\kappa)}, \tag{2.29}$$

$$\langle\sigma^x\rangle = \Big(\langle\sigma^+\rangle + \langle\sigma^-\rangle\Big) = \pm\frac{\sqrt{2\omega_z(J-J_c)}}{J}, \tag{2.30}$$

$$\langle\sigma^y\rangle = -i\Big(\langle\sigma^+\rangle - \langle\sigma^-\rangle\Big) = \mp\gamma\frac{\sqrt{\frac{\omega_z}{2}(J-J_c)}}{\omega_z J}, \tag{2.31}$$

$$\langle\sigma^z\rangle = -(J_c/J). \tag{2.32}$$

Here the different signs for the steady-state solutions reflect the $\mathbb{Z}_2$ symmetry which is spontaneously broken by the choice of a specific state, see Eq. (2.5), and we have abbreviated the notation by defining

$$J = \frac{4g^2\omega_0}{\kappa^2+\omega_0^2}, \quad J_c = \frac{\left(\frac{\gamma}{2}\right)^2+\omega_z^2}{\omega_z}. \tag{2.33}$$

A plot of Eqs. (2.29-2.32) is given in Fig. 2.4a. The critical coupling strength g_c for the superradiant phase transition (see Eq. (2.24) in the $(\beta, U) \to 0$ limit) can also be obtained by equating the two expressions in Eq. (2.33).

Note that the solutions for the mean-field expectation values do not recover the solutions that are obtained by taking the $\gamma \to 0$ limit from the outset in Eqs. (2.12-2.14). This is because the present steady-state is usually approached with a rate $\propto 1/\gamma$ which diverges in the $\gamma \to 0$ limit. However, we mention that the steady state expectation value of $\langle\sigma^y\rangle$ in Eq. (2.2) is induced by the atomic dissipation ($\sim \gamma$). Since the presence of the Liouvillian $\mathcal{L}_\gamma$ in Eq. (2.31) breaks time-reversal symmetry in the atomic sector that protected the expectation value from acquiring non-vanishing values.

2.3.5. Cavity output spectrum

The internal dynamics of the atom-cavity system can be probed by analyzing the light that leaks from the cavity mirrors. We employ standard input-output theory for the

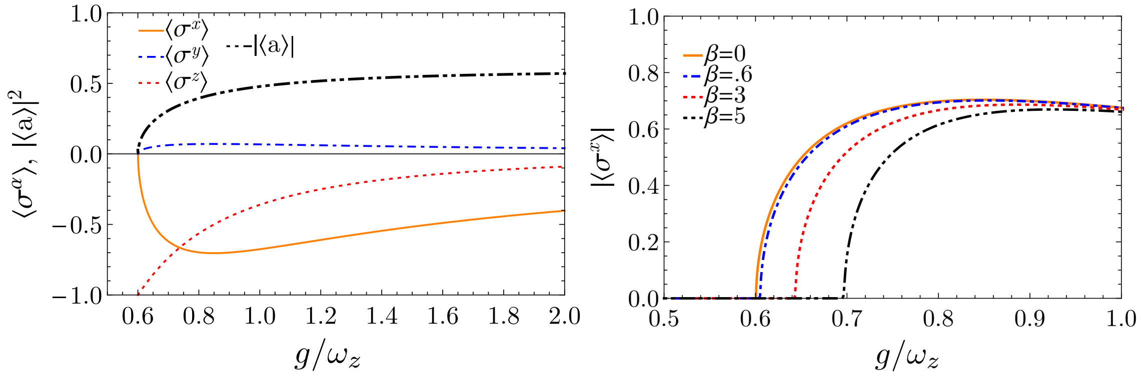

(a) (b)

Figure 2.4.: Stable steady-state field amplitudes in the superradiant phase for the set of parameters $\gamma = \kappa = 0.2|\omega_z|, \omega_0 = 1.4|\omega_z|$. The critical coupling g_c is given by Eq. (2.24) which is valid as long as $\beta < \sqrt{1 + \left(\frac{\omega_z}{\gamma/2}\right)^2} \approx 10$. (a) Amplitudes $|\langle a\rangle|$ and $(\langle\sigma^x\rangle, \langle\sigma^y\rangle, \langle\sigma^z\rangle)$ without a collective decay contribution, i.e. $\beta = 0$. The critical coupling evaluates to $g_c(\beta = 0)/\omega_z \approx 0.6$. (b) Influence of collective decay processes of strength $\beta = \alpha(N - 1)$ for steady-state field amplitude $|\langle\sigma^x\rangle|$.

quantum Langevin equations [112, 113, 26], to calculate the cavity spectrum in the limit $(U, \beta) \to 0$, to focus on the effect of single-site atomic spontaneous emission. The input-fields are related to the output fields by the boundary relation [112, 113]

$$a_{\text{out}}(\nu) = \sqrt{2\kappa}a(\nu) - a_{\text{in}}(\nu), \tag{2.34}$$

$$a^\dagger_{\text{out}}(-\nu) = \sqrt{2\kappa}a^\dagger(-\nu) - a^\dagger_{\text{in}}(-\nu). \tag{2.35}$$

The annihilation operators $(a_{\text{out}}(\nu), a_{\text{in}}(\nu), a(\nu))$ correspond to the output field, the input field, and the intra cavity field, respectively. If we take the bath to be in the vacuum state at zero-temperature, the noise-correlations for the atomic degrees of freedom can be expressed in the basis $(i, j) \in (+, -, z)$ by

$$\langle\xi^i_{\ell',t'}\xi^j_{\ell,t}\rangle = \gamma\delta(t - t')\Big[\delta_{\ell,\ell'} + (1 - \delta_{\ell,\ell'})\alpha\Big]M^{ij}_{\ell'\ell} \tag{2.36}$$

$$M^{ij}_{\ell'\ell} = 2\begin{pmatrix} 0 & 0 & 0 \\ \frac{1}{2}\sigma^z_{\ell',t}\sigma^z_{\ell,t'} & 0 & -\sigma^z_{\ell',t}\sigma^-_{\ell,t'} \\ -\sigma^+_{\ell',t'}\sigma^z_{\ell,t} & 0 & 2\sigma^+_{\ell',t'}\sigma^-_{\ell,t} \end{pmatrix}_{ij} \tag{2.37}$$

where the indices $(i, j) \in (+, -, z)$ refers to the atomic variables. The expectation value averages over the bath degrees of freedom. Consequently, entries of the correlation matrix are still operator-valued. For contributions $\ell = \ell'$ the local operator algebra can be used to simplify correlations. We remark that this matrix does not need to be hermitian, since the external bath is described by the vacuum and only terms $\propto b_k(0)b^\dagger_k(0)$ contribute. Here b_k is an annihilation operator for a bath mode. Correlations of the form $\langle\xi^+(t)\ldots\rangle = 0$ and $\langle\ldots\xi^-(t)\rangle = 0$ vanish. An explicit derivation of noise correlations is found in Sec. 4.4. The relevant noise correlations $(\alpha = 0)$ are

$$\langle a_{\text{in}}(\nu')a^\dagger_{\text{in}}(-\nu)\rangle = \delta(\nu + \nu')\ , \tag{2.38}$$

$$\langle\xi^-(-\nu')\xi^+(\nu)\rangle = \gamma\delta(\nu + \nu')\ , \tag{2.39}$$

$$\langle\xi^z(\nu)\xi^z(\nu')\rangle = 2\gamma(1 + \langle\sigma^z\rangle)\delta(\nu + \nu')\ , \tag{2.40}$$

$$\langle\xi^z(\nu)\xi^+(\nu')\rangle = 2\gamma\langle\sigma^+\rangle\delta(\nu + \nu'). \tag{2.41}$$

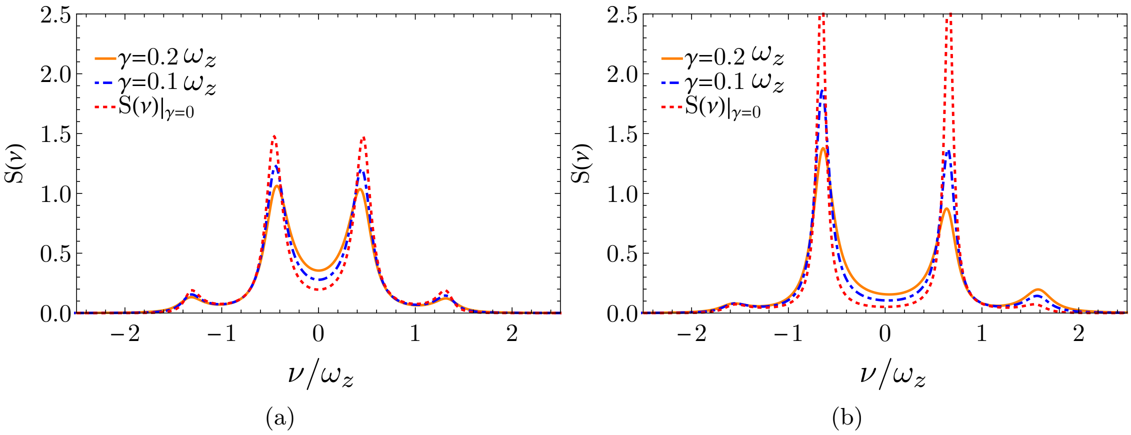

(a) (b)

Figure 2.5.: Cavity spectra in the vacuum phase with spontaneous emission and a broken frequency symmetry $S(\nu) \neq S(-\nu)$. We have normalized the spectra such that $\int S(\nu) d\nu = 1$. When there is no atomic spontaneous emission ($S(\nu)|_{\gamma=0}$), the frequency symmetry of the cavity spectrum is restored. All parameters are in units of $|\omega_z|$: $\kappa = 0.2|\omega_z|, g = 0.4|\omega_z| < g_c$. The figure (a) shows the on-resonance spectrum: $\omega_0 = 1.0|\omega_z|$, the figure (b) shows the off-resonance spectrum at $\omega_0 = 1.4|\omega_z|$.

Similarly the noise-operators coupling to the photons are delta correlated in time

$$\langle a_{\mathrm{in,t}} a^\dagger_{\mathrm{in,t'}} \rangle = \delta(t - t') \; . \tag{2.42}$$

We solve Eq. (2.19) for the fluctuations around the photon condensate and omit the coherent contribution coming from the zero-frequency components specified by $f(\boldsymbol{\sigma})$. Making use of Eqs. (2.34-2.35), the cavity fluorescence spectrum $S(\nu)$ (for a vacuum input field) accounting for the fluctuations around the steady state is

$$S(\nu) = \langle a^\dagger_{\mathrm{out}}(\nu) a_{\mathrm{out}}(\nu) \rangle = 2\kappa \langle \delta a^\dagger(\nu) \delta a(\nu) \rangle = 2\kappa \int_{-\infty}^{\infty} e^{-i\nu\tau} \langle \delta a^\dagger(0) \delta a(\tau) \rangle \, d\tau. \tag{2.43}$$

The cavity spectrum in the $g < g_c$ case for the steady-states $\langle \sigma^+ \rangle = \langle \sigma^- \rangle = 0$ and $\langle \sigma^z \rangle = -1$ becomes

$$S(\nu) = 8g^2\kappa \frac{s(\nu)}{|\Omega(\nu)|^2}, \tag{2.44}$$

$$s(\nu) = \left(\gamma \left(\gamma^2 + 4(\omega_z - \nu)^2 \right) \left(\kappa^2 + (\nu + \omega_0 \right)^2 + 32\omega_z^2 g^2 \kappa \right) \tag{2.45}$$

$$\begin{aligned} \Omega(\nu) =& (\kappa - i\nu)^2 \left(4\omega_z^2 + (\gamma - 2i\nu)^2 \right) \\ &+ \omega_0^2 \left(4\omega_z^2 + (\gamma - 2i\nu)^2 \right) - 16\omega_z g^2 \omega_0. \end{aligned} \tag{2.46}$$

The poles in $\Omega(\nu)$ in Eq. (2.44) correspond to the hybridized atom-cavity eigenmodes of the system. They are given by the solutions to the equation $\det[\boldsymbol{G}_{\boldsymbol{R}}^{-1}(\nu)] = 0$ where $\boldsymbol{G}_{\boldsymbol{R}}^{-1}(\nu)$ is defined in Eq. (2.22).

The output spectrum in the presence of spontaneous atomic decay is no longer symmetric under inversion on the frequency axis $S(\nu) \neq S(-\nu)$, see Fig. 2.5. This is due to the fact that in the presence of atomic decay, cavity photons can exit the cavity in two different ways. Either directly via the cavity decay channel $\sim \kappa$ or indirectly via exciting an atom and subsequently decaying via spontaneous emission $\sim \gamma$. The latter process of

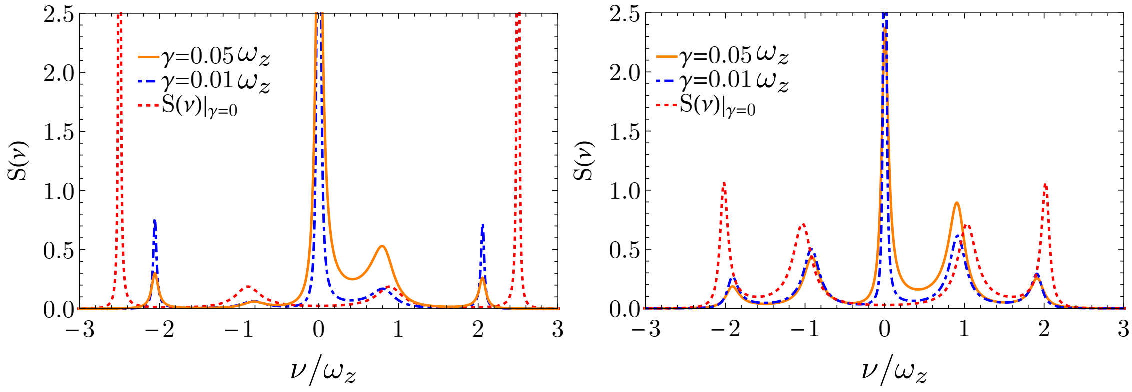

(a) (b)

Figure 2.6.: Cavity spectra in the superradiant regime with spontaneous emission and a broken frequency symmetry $S(\nu) \neq S(-\nu)$. We have normalized the spectra such that $\int S(\nu) d\nu = 1$. All parameters are in units of $|\omega_z|$: $\kappa = 0.2|\omega_z|, g = 0.8|\omega_z| > g_c$. Here, $S(\nu)|_{\gamma=0}$ is understood as solving the Eqs. (4.8)-(4.11) on a mean-field level by setting $\gamma = 0$ from the outset and calculating $S(\nu)$ with Eq. (3.34), see [26]. In figure (a) the system is on resonance: $\omega_0 = |\omega_z|$, in figure (b) it is off resonance: $\omega_0 = 1.4|\omega_z|$.

combined excitation and decay prefers photon states with positive frequency. This leads to a reduction of $S(\nu)$ for positive frequencies and introduces the mentioned asymmetry in the photon output spectrum. In the limit of vanishing spontaneous emission, the cavity spectrum collapses to the familiar result [26] and the frequency symmetry is restored:

$$\lim_{\gamma \to 0} S(\nu) = \frac{16\omega_z^2 g^4 \kappa^2}{|\Omega'(\nu)|^2}, \tag{2.47}$$

$$\Omega'(\nu) = (\omega_z^2 - \nu^2)(\kappa - i\nu)^2 + \omega_0^2(\omega_z^2 - \nu^2) - 4\omega_z g^2 \omega_0. \tag{2.48}$$

A typical cavity output spectrum for the superradiant case $g > g_c$ is defined in Eq. (2.55) and can be seen in Fig. 2.6. Here $\gamma > 0$ leads to a broadening of the spectrum and a pronounced weight of $S(\nu)$ at positive frequencies $\nu > 0$ due to the dominant effect of stimulated emission and absorption over spontaneous decay effects. In Fig. 2.6 and Fig. 2.5 the expression $S(\nu)|_{\gamma=0}$ refers to the cavity spectrum that is obtained by setting $\gamma = 0$ in Eqs. (2.9)-(2.11) and by then following the same procedure as outlined above, see [26].

Cavity spectra in the superradiant regime

We detail the calculations performed in Sec.2.3.5 to obtain the cavity spectrum $S(\nu)$ that is defined in Eq. (2.43). The fluctuations $\delta a(\nu), \delta a^\dagger(\nu)$ around the photon condensate are given as

$$\begin{aligned} \delta a(\nu) = {} & a_{\text{in}}^\dagger(-\nu) f(\nu) + a_{\text{in}}(\nu) g(\nu) \\ & + \xi^-(-\nu) m(\nu) + \xi^+(\nu) h(\nu) + \xi^z(\nu) \ell(\nu) \end{aligned} \tag{2.49}$$

$$\begin{aligned} \delta a^\dagger(-\nu) = {} & a^+(-\nu)_{\text{in}} g^\dagger(-\nu) + a_{\text{in}}(\nu) f^\dagger(-\nu) \\ & + \xi^-(-\nu) h^\dagger(-\nu) + \xi^+(\nu) m^\dagger(-\nu) + \xi_z(\nu) \ell^\dagger(-\nu) \end{aligned} \tag{2.50}$$

By employing Eqs. (2.38-2.41) we can identify the cavity-spectrum as

$$\begin{aligned} S(\nu) = {} & f^\dagger(\nu) f(\nu) + \gamma h^\dagger(\nu) h(\nu) + 2\gamma(1 + \langle \sigma^z \rangle) \ell(\nu) \ell^\dagger(\nu) \\ & + 2\gamma \langle \sigma^- \rangle h^\dagger(\nu) \ell(\nu) + 2\gamma \langle \sigma^+ \rangle \ell^\dagger(\nu) h(\nu) \end{aligned} \tag{2.51}$$

Where the functions $\ell(\nu), h(\nu), f(\nu)$ are

$$\begin{aligned}&\Omega(\nu) = -i(\gamma - i\nu)\left(4\omega_z^2 + (\gamma - 2i\nu)^2\right)\left(\omega_0^2 + (\kappa - i\nu)^2\right)\\&+ 32\omega_z g^3\omega_0(\langle a^\dagger\rangle + \langle a\rangle)(\langle\sigma^-\rangle - \langle\sigma^+\rangle)\\&+ 8g^2\left(-(\langle a^\dagger\rangle + \langle a\rangle)^2(2\nu + i\gamma)(\kappa - i\nu)^2 - \omega_0^2(\langle a^\dagger\rangle + \langle a\rangle)^2(2\nu + i\gamma) - 2\omega_z\omega_0\langle\sigma^z\rangle(\nu + i\gamma)\right)\end{aligned}$$

with

$$\Omega(\nu)f(\nu) = -16i\omega_z g^2\kappa\left(2g(\langle a^\dagger\rangle + \langle a\rangle)(\langle\sigma^-\rangle - \langle\sigma^+\rangle) + \langle\sigma^z\rangle(-\nu - i\gamma)\right) \tag{2.52}$$

$$\Omega(\nu)h(\nu) = -2\sqrt{2\kappa}g(\kappa - i(\nu + \omega_0))\left(8g^2(\langle a^\dagger\rangle + \langle a\rangle)^2 + (\gamma - i\nu)(\gamma + 2i(\omega_z - \nu))\right) \tag{2.53}$$

$$\Omega(\nu)\ell(\nu) = -8\sqrt{2\kappa}\omega_z g^2(\langle a^\dagger\rangle + \langle a\rangle)(\kappa - i(\nu + \omega_0)) \tag{2.54}$$

The cavity spectrum for the superradiant case for $g > g_c$ is given by

$$S(\nu) = \frac{s(\nu)}{\Omega(\nu)\Omega^*(\nu)} \tag{2.55}$$

with

$$\begin{aligned}&\Omega(\nu) = -i(\gamma - i\nu)\left(4\omega_z^2 + (\gamma - 2i\nu)^2\right)\left(\omega_0^2 + (\kappa - i\nu)^2\right) + 32\omega_z g^3\omega_0(\langle a^\dagger\rangle + \langle a\rangle)(\langle\sigma^-\rangle - \langle\sigma^+\rangle)\\&- 8ig^2\left((\langle a^\dagger\rangle + \langle a\rangle)^2(\gamma - 2i\nu)(\kappa - i\nu)^2 + \omega_0^2(\langle a^\dagger\rangle + \langle a\rangle)^2(\gamma - 2i\nu) + 2\omega_z\omega_0\langle\sigma^z\rangle(\gamma - i\nu)\right)\end{aligned} \tag{2.56}$$

with

$$\begin{aligned}&s(\nu) = 8g^2\kappa\Big\{\gamma\left(\gamma^2 + \nu^2\right)\left[\gamma^2 + 4(\omega_z - \nu)^2\right]\left[\kappa^2 + (\nu + \omega_0)^2\right] + 64g^4(\langle a^\dagger\rangle + \langle a\rangle)^2\Big\{(\langle a\rangle + \langle a^\dagger\rangle)^2\gamma\\&\left[\kappa^2 + (\nu + \omega_0)^2\right] - 2\omega_z^2\kappa(\langle\sigma^-\rangle - \langle\sigma^+\rangle)^2\Big\} + 16g^2\Big\{(\langle a^\dagger\rangle + \langle a\rangle)^2\gamma\left[\gamma^2 + 2\left(\omega_z^2 + \omega_z\nu - \nu^2\right)\right]\\&\left[\kappa^2 + (\nu + \omega_0)^2\right] + 2\omega_z^2\kappa\langle\sigma^z\rangle^2\left(\gamma^2 + \nu^2\right) + 2\gamma\langle\sigma^z\rangle(\langle a^\dagger\rangle + \langle a\rangle)^2\omega_z^2\left[\kappa^2 + (\nu + \omega_0)^2\right]\Big\}\\&+64\gamma\omega_z g^3(\langle a^\dagger\rangle + \langle a\rangle)\left[(\langle a^\dagger\rangle + \langle a\rangle)^2(\langle\sigma^-\rangle + \langle\sigma^+\rangle)\left[\kappa^2 + (\nu + \omega_0)^2\right] + 2i\omega_z\kappa\langle\sigma^z\rangle(\langle\sigma^-\rangle - \langle\sigma^+\rangle)\right]\\&+ 8\gamma\omega_z g(\langle a^\dagger\rangle + \langle a\rangle)\left[\kappa^2 + (\nu + \omega_0)^2\right]\Big[\gamma^2(\langle\sigma^-\rangle + \langle\sigma^+\rangle) - i\gamma(2\omega_z - 3\nu)(\langle\sigma^-\rangle - \langle\sigma^+\rangle)\\&+2\nu(\omega_z - \nu)(\langle\sigma^-\rangle + \langle\sigma^+\rangle)\Big]\Big\}\end{aligned} \tag{2.57}$$

At the phase transition, there are two poles that become purely imaginary and describe the over-damped dynamics. The corresponding expressions are obtained by expanding $\det[\boldsymbol{G_R^{-1}}(\nu)] = 0$ up to second-order in the frequency with $(\beta, U) \to 0$. We refer to the solutions of the resulting quadratic equation by (ν_1, ν_2). The first pole vanishes linearly in $(g - g_c)$ and is given as:

$$\nu_1 = \frac{8i\omega_z\omega_0\left(\gamma^2 + 4\omega_z^2\right)(g - g_c)(g + g_c)}{\kappa\left(\gamma^2 + 4\omega_z^2\right)^2 + 32\gamma\omega_z g_c^2\omega_0} \tag{2.58}$$

The residual pole at $g = g_c$ is given by Eq. (2.27), with the limit

$$\lim_{\kappa\to 0}\nu_2 = -i\gamma\frac{\omega_0^2}{\frac{\gamma^2}{4} + \left(\omega_z^2 + \omega_0^2\right)}. \tag{2.59}$$

The pole structure is visualized in Fig. 2.3c.

2.3.6. Effective temperature

In Ref. [91], the authors outlined an approach to extract the effective temperature of open quantum-optical systems. The idea is to map the photon equation of motion to classical Langevin equations and read off the effective temperatures as a function of the noise correlation functions. Here, we generalize this analysis to include single-site atomic spontaneous emission γ and extract the corresponding effective temperature. To that end, we define the real part of the photon component $\delta x(\nu)$ and the corresponding noise operator $\xi_x(\nu)$:

$$\begin{aligned}
\delta x(\nu) =& \frac{1}{\sqrt{2\omega_0}} \left(\delta a(\nu) + \delta a^\dagger(-\nu)\right), \qquad (2.60)\\
\xi_x(\nu) =& \frac{1}{\sqrt{2\omega_0}} \Big[\xi_a(\nu) r(\nu) + \xi_{a^\dagger}(-\nu) r^*(-\nu) + \xi^+(\nu) p(\nu) + \xi^-(-\nu) p^*(-\nu)\Big].
\end{aligned}$$

Here, $\xi_a \equiv \sqrt{2\kappa} a_{\text{in}}$ and the fluctuation operators $\delta a(\nu), \delta a^\dagger(-\nu)$ are defined in terms of noise operators in Eqs. (2.49), (2.50).

In the δx-channel, the response of the fluctuations to the "driving force" $\xi_x(\nu)$ is described by the equation

$$\xi_x(\nu) = \left(\omega_0^2 - \frac{16\omega_z g^2}{4\omega_z^2 + (\gamma - 2i\nu)^2}\omega_0 + (\kappa - i\nu)^2\right) \delta x(\nu). \qquad (2.61)$$

At low frequencies, equation Eq. (2.61) resembles a Langevin equation for a classical particle subject to a harmonic potential with oscillation frequency

$$\alpha^2 = \left(\omega_0^2 - \frac{16\omega_z g^2}{\gamma^2 + 4\omega_z^2}\omega_0 + \kappa^2\right) \qquad (2.62)$$

and an effective damping constant

$$\tilde{\kappa} = 2\left(\kappa + \frac{32\gamma\omega_z g^2 \omega_0}{(\gamma^2 + 4\omega_z^2)^2}\right). \qquad (2.63)$$

This illustrates the fact that the photon can decay via two channels: directly via κ and by first converting it to an atomic excitation, which can then decay via γ.

The stochastic force operator satisfies the relation $\Big[\xi_x(-\nu)\Big]^\dagger = \xi_x(\nu)$ and obeys the commutation relation:

$$\begin{aligned}
&\frac{1}{2}\left\langle \xi_x(\nu)\xi_x(\nu') + \xi_x(\nu')\xi_x(\nu)\right\rangle = \\
&\delta(\nu + \nu')\left(\frac{2\kappa}{4\omega_0}\Big[r(\nu)r^\dagger(-\nu') + r(\nu')r^\dagger(-\nu)\Big]\frac{\gamma}{4\omega_0}\Big[p(\nu)p^\dagger(-\nu') + p(\nu')p^\dagger(-\nu)\Big]\right) \qquad (2.64)
\end{aligned}$$

Where $p(\nu)$ and $r(\nu)$ are given by Eq. (2.65) and by Eq. (2.66). The complex functions $r(\nu)$ and $p(\nu)$ are defined as

$$\begin{aligned}
r(\nu) &= (\kappa - i(\nu + \omega_0)), \qquad (2.65)\\
p(\nu) &= -\frac{4g(\gamma - 2i(\omega_z + \nu))}{3\omega_z^2 + (\gamma - 2i\nu)}\omega_0. \qquad (2.66)
\end{aligned}$$

At low frequencies the right-hand side of Eq. (2.61) evaluates to

$$\left(\omega_0^2 - \frac{16\omega_z g^2}{\gamma^2 + 4\omega_z^2}\omega_0 + \kappa^2\right) - 2i\nu\left(\kappa + \frac{32\gamma\omega_z g^2\omega_0}{(\gamma^2 + 4\omega_z^2)^2}\right) \qquad (2.67)$$

where we have dropped contributions $\mathcal{O}(\nu^2)$ and the commutation relation at $\nu' = -\nu$, see Eq. (2.64), evaluates to:

$$\frac{1}{2}\left\langle \xi_x(\nu)\xi_x(\nu') + \xi_x(\nu')\xi_x(\nu)\right\rangle \approx \frac{\kappa}{\omega_0}\left(\kappa^2+\omega_0^2\right) \\ + \frac{\gamma}{4\omega_0}\frac{32g^2}{\gamma^2+4\omega_z^2}\omega_0^2 + \mathcal{O}(\nu^2) \tag{2.68}$$

We evaluate them at the critical point, which is approached from the normal phase ($\langle a\rangle = \langle\sigma^+\rangle = 0$, $\langle\sigma^z\rangle = -1$).

We may now identify the effective temperature of the system at the critical point as

$$2\tilde{\kappa}T_{\text{eff}}^{\text{crit}} = \lim_{\nu\to 0}\frac{1}{2}\left\langle \xi_x(\nu)\xi_x(-\nu) + \xi_x(-\nu)\xi_x(\nu)\right\rangle\Big|_{g=g_c}, \tag{2.69}$$

$$T_{\text{eff}}^{\text{crit}} = \frac{\left(\gamma^2+4\omega_z^2\right)\left(\kappa^2+\omega_0^2\right)\left(\gamma\omega_0+2\omega_z\kappa\right)}{8\omega_z\omega_0\left(\gamma^2\kappa+2\gamma\left(\kappa^2+\omega_0^2\right)+4\omega_z^2\kappa\right)}. \tag{2.70}$$

In the presence of only a single photonic decay channel, we recover the known cases [91]

$$\lim_{\gamma\to 0} T_{\text{eff}}^{\text{crit}} = \frac{\kappa^2+\omega_0^2}{4\omega_0}, \tag{2.71}$$

$$\lim_{\kappa\to 0} T_{\text{eff}}^{\text{crit}} = \frac{\frac{\gamma^2}{4}+\omega_z^2}{4\omega_z}. \tag{2.72}$$

2.4. Conclusions and future directions

In this chapter we investigated the effect of atomic spontaneous emission on the non-equilibrium steady-states of the open Dicke model. By determining the critical coupling $g_c(\kappa, \gamma, U)$ for the onset of superradiance as an explicit function of the spontaneous emission rate γ, we were able to compare this result to experimental values for the onset of superradiance as measured by Baden *et al.* [49] (2014, Singapore) and for the new rounds of data taking [44] (2018, Singapore). We could show that the predicted superradiance threshold is accurately captured by $g_c(\kappa, \gamma, U)$. We have calculated effective temperatures for the superradiance transition and analysed signatures of spontaneous decay in the cavity output spectra.

In the next chapter, we will include additional short-range interactions between the atoms, for example by weakly dressing the spin-up level with a Rydberg state [50]. This interaction will now compete with cavity-mediated, long-range interactions and the various drive and decay processes.

Chapter 3

Rydberg-Dressed Spin Lattice in an Optical Cavity

Recent experiments start to blur the boundaries between cavity quantum electrodynamics and closed system simulations with ultracold quantum gases. Prominent examples include lattice quantum many-body systems that are interfaced with a dynamical, quantum light field in a cavity. The cavity field can act as a global range potential for atom-atom interactions that can compete with the short-ranged collisional interactions, longitudinal fields and kinetic energies of the underlying lattice dynamics, realizing new quantum phases [24, 25] in Dicke-Hubbard models. In a similar spirit, also quantum spin systems have been trapped in intracavity lattices where they interact with single-mode optical lightfields (2018, [114]). In these cases, it is desirable to freeze out the atomic motion with deep optical lattices such that only the internal spin-spin dynamics competes with spin-light interactions. A theoretical modelling of these systems faces complexity at the interface of: spontaneous symmetry-breaking and emergent phases of interacting many-body systems with a large number of atoms $N \to \infty$, a coupling to fluctuating quantum light fields, and non-equilibrium physics of driven, open quantum systems. In this chapter we propose what is possibly the simplest, quantum-optical magnet with competing short- and long-range interactions, in which all three elements can be analysed comprehensively: a Rydberg-dressed spin lattice [50] coherently coupled to a single photon mode. Solving a set of coupled even-odd sublattice master equations for atomic spin and photon mean-field amplitudes, we find three key results. (R1): Superradiance and a coherent photon field appears in combination with spontaneously broken magnetic translation symmetry. The latter is induced by the short-range nearest-neighbour interaction from weakly admixed Rydberg levels. (R2): This broken even-odd sublattice symmetry leaves its imprint in the light via a novel peak in the cavity spectrum. (R3): The combined effect of atomic spontaneous emission, drive, and interactions can lead to phases with dynamically oscillating cavity fields.

Most recent experiments at the ETH in Zürich (2018, [114]) have started to engineer spin-dependent couplings of a multi-level Bose Einstein condensate to a cavity photon field giving rise to the formation of a spin texture in the driven atom-cavity system. Meanwhile, also oscillating cavity fields have been experimentally observed in an open version of the spin-1 Dicke model (2017, [115]).

- The research presented in this chapter is published: J. Gelhausen, M. Buchhold, A. Rosch and P. Strack, Quantum-optical magnets with competing short- and long-range interactions: Rydberg-dressed spin lattice in an optical cavity, *SciPost Phys. 1, 004 (2016).*
- In comparison to the published research article we have made several changes to embed the research paper into the general framework of the thesis. We have rewritten

large parts of the introduction, the conclusion, have updated and rephrased the model section and the research summary at the beginning of this chapter, also to take into account the latest (as of 2018) experimental investigations relevant to this research. We have edited and rephrased Sec. 3.5.2 on beyond mean-field effects. Minor changes have been made throughout the rest of this chapter. This includes merging selected sections (results sections with their more detailed description), cutting out some smaller paragraphs entirely and rephrasings across the board. We have included cross-references to other chapters and sections of this thesis and have added citations to take into account new experimental achievements that have been published after our research article was published.

- Large parts of this chapter can be found almost identically and verbatim in the above mentioned publication.

3.1. Introduction

Experiments have started to combine atomic gases [23, 116] with optical cavities, bringing together tunable atomic interactions in optical lattices with driven open setups that interface the atoms with dynamical quantum light fields [25, 24]. Expressing the goal for quantum systems in lattice structures to realize possibly exotic magnetic phases with spin systems.

However, it provides an experimental challenge to gain control over and build large arrays of quantum spin systems with scalable interaction potentials. Especially the simulation of Hamiltonians that describe magnetic interactions are challenging to realise with short-range collisional or tunneling processes as they create only very small effective magnetic exchange couplings which in turn require a very-low temperature environment that push conventional cooling techniques close to their limit of few nanokelvins [117].

But it is also possible to directly engineer strong spin-spin interactions that overcome severe low-temperature limitations for example with dipolar molecules [118] and ions in Penning traps [119]. In particular, magnetic interactions between spin-systems have been engineered with laser-dressed Rydberg atoms [50] giving rise to strong angular dependent interaction potentials of atomic levels in ground-state manifolds [120], extending experimental control over interactions to both their geometric shape and their strength. The shape of interactions can also be controlled by manipulating the geometry of the underlying trapping lattice, clearing the way for exploration of frustrated spin systems [121]. Experimental setups have begun to use arrays of magnetic microtraps to build almost arbitrary lattice geometries with tunable intersite spacings of up to several μm [122] such that also effectively step-like potentials, mimicking nearest-neighbour interactions, are a possibility.

This paves the way to study non-equilibrium magnetic systems with clean interactions that can compete with energy scales induced by driving and decay processes of nonequilibrium systems [123, 124]. The magnetic systems can be made approximately disorder free since targeted atomic loading processes can achieve almost unity filling. Interfacing the self-interacting quantum spin models with dynamical light fields induces a competition of short-ranged atomic and cavity-induced long-range interactions in an open system environment which opens up the exploration of quantum magnets with possibly new quantum phases [24, 25]. The question of how quantum light interacts with a self-interacting set of qubits is of a broad relevance and includes for example cavity Rydberg polaritons [125, 126] and Rydberg-EIT setups [127, 128, 129].

With the research presented in this chapter and our paper, we want to initiate the study of quantum-optical magnets with competing short- and long-range interactions, under non-equilibrium conditions with dissipative processes for the photonic force carriers. The goal is to provide a "base case" or the simplest prototype of such a quantum-optical magnet. A natural experimental set-up consists of a photon box to trap the light field and a deep optical intracavity lattice with unit filling that allows step-like interaction potentials for the spin-dependent interaction potentials which at the same time freezes out any motional degrees of freedom for the atoms.

This raises the question how an atomic two-level system can couple to two competing potentials with different range and independently tunable magnitude. We propose to use an atomic "two dipoles in-one" unit (illustrated below in Fig. 3.11) that simultaneously couples two different force-mediating photon fields (described in Sec. 3.2) by using optical pumping schemes to realise boosted spin-photon couplings [26, 44] and laser-dressed atomic ground-states with weakly admixed dipolar Rydberg states [50].

We investigate the magnetic phase transitions in these driven-dissipative atomic arrays using coupled even-odd sublattice mean-field master equations for the spin and photon degrees of freedom in the thermodynamic limit and show clear signatures of the magnetic correlations in the light field leaving the cavity mirrors. These cavity spectra can be used to unambigously identify the different magentic phases and intracavity dynamics in an experimental setup.

Driven-dissipative lattice models based on effective spin-1/2 models similar to the one presented here have been in focus quite recently [123, 124, 130, 131]. We stress that a group at ETH in Zürich has recently observed (2018, [114]) the formation of a spin-texture in a quantum gas that was coupled to an optical cavity, setting the stage for future studies of competing spin-spin interactions with cavity-mediated long-range interactions.

3.2. Model: Rydberg-dressed spin lattice coupled to single-mode light field

Here, we suggest to couple a Rydberg-dressed spin lattice [50] as depicted in Fig. 3.1 to a single mode of an optical resonator. This amounts to supplementing the existing experimental set-ups of quantum many-body lattice models in optical cavities [24, 25] by weakly admixing a Rydberg-level to a ground-state manifold of a two-level system (we detail a suggestion for a quantum optical implementation in Sec. 3.4.4).

The Hamiltonian H consists of two contributions, the pure spin-part and the interaction of the spins with the optical light field as $H = H_{\text{spin}} + H_{\text{spin-light}}$. It is written as

$$H_{\text{spin}} = -\frac{\Delta}{2}\sum_{\ell=1}^{N}\sigma_\ell^z + \frac{V}{d}\sum_{\langle \ell m\rangle}\left(\frac{1+\sigma^z}{2}\right)_\ell\left(\frac{1+\sigma^z}{2}\right)_m , \tag{3.1}$$

where the sum $\sum_{\langle \ell m\rangle}$ goes over all nearest-neighbor pairs of the square lattice and $d = z/2$ is the dimension of the lattice with z the coordination number. In comparison to chapter 2 and chapter 4, we have denoted the two-level splitting of the spins with Δ instead of ω_z to make clear that it reflects an effective parameter that can externally be tuned both negative and positive by adjusting the detuning of a pump-laser. For a negative ($-\Delta < 0$) longitudinal field it is favorable for the spins to point up along the z-axis $|\uparrow\rangle$. Competing against this is the repulsive or antiferromagnetic "Rydberg-mediated" term, which minimizes energy by favouring spatially alternating configurations, such as Néel

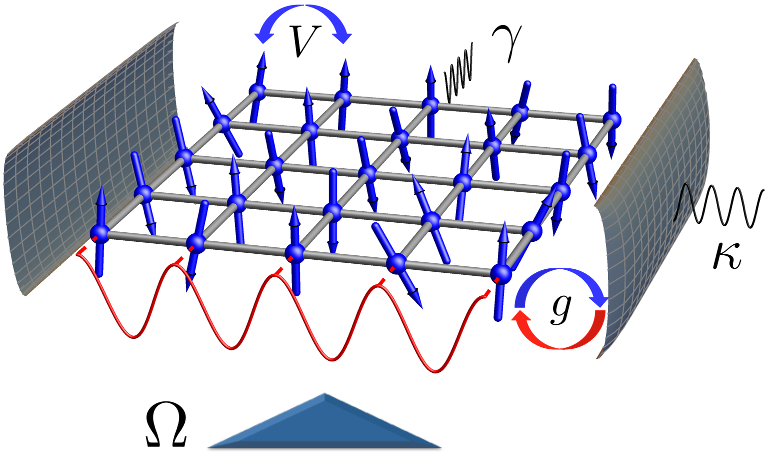

Figure 3.1.: Rydberg-dressed spin lattice coupled to single-mode optical light field. We take the atoms to be in a deep optical lattice (for example a Mott insulator at unit filling) such that no motion occurs and only internal spin excitations drive the dynamics. From weakly admixing a Rydberg level, an effective nearest-neighbor interaction (repulsive) V competes with an effectively infinite range interaction from the single light mode of the cavity that couples all atoms with strength g. The atoms can spontaneously decay with rate γ and photons can leave the system through the cavity mirrors with rate κ. The system is driven from the side with a laser of Rabi frequency Ω.

antiferromagnetic states, e. g. $|\uparrow\downarrow\uparrow\downarrow \ldots\rangle$. In contrast to a conventional Ising $\sim \sigma_\ell^z \sigma_m^z$ interaction term, the Rydberg interaction is conditioned on population in the upper state.

The spin-light coupling to a single mode of an optical cavity is expressed as

$$H_{\mathrm{spin-light}} = \frac{g}{\sqrt{N}}(a + a^\dagger) \sum_{\ell=1}^{N} (\sigma_\ell^+ + \sigma_\ell^-) + \omega_0 a^\dagger a \,, \tag{3.2}$$

where ω_0 is the effective cavity frequency in a rotating frame and N is the number of atoms; the rescaling of the effective spin-light coupling with $1/\sqrt{N}$ ensures a non-trivial thermodynamic limit as explained in detail in chapter 2. All coupling constants appearing here $\{\omega_0, \Delta, g, V\}$ are explicitly tunable experimentally in a quantum optical realisation of the model, see Sec. 3.4.4.

Within our mean-field treatment, the light-field in the cavity can either be the vacuum mode $\langle a \rangle = 0$ or it can be in a coherent state $\langle a \rangle \neq 0$. By cavity vacuum, we mean the Fock state with zero photon excitations. If there is a macroscopic occupation of the cavity mode, then $\langle a + a^\dagger \rangle \neq 0$ and the system is in a superradiant state where the spins experience a transverse field in x-direction $\sim g\left(\langle a \rangle + \langle a^\dagger \rangle\right) \sum_{\ell=1}^{N} \sigma_\ell^x$. Choosing the lattice and cavity modefunction commensurate as in Fig. 3.1 results in a homogeneous coupling g, that is, all the spins couple in the same way to the cavity.

The two dissipative processes are modelled by the Lindblad operators for photon losses through the mirrors with rate κ and spontaneous emission of the atoms with rate γ into the reservoir modes of the electromagnetic vacuum surrounding the cavity:

$$\mathcal{L}_\gamma[\rho] = \frac{\gamma}{2} \sum_{\ell=1}^{N} \left[2\sigma_\ell^- \rho \sigma_\ell^+ - \{\sigma_\ell^+ \sigma_\ell^-, \rho\} \right], \tag{3.3}$$

$$\mathcal{L}_\kappa[\rho] = \kappa \left[2a\rho a^\dagger - \{a^\dagger a, \rho\} \right] , \tag{3.4}$$

where ρ is the system density matrix. Here, we have not included a possible collective decay mechanism for the atomic ensemble as they are typically very weak for the lattice-based setup we consider here, as estimated in Sec.1.1. This justifies to restrict ourselves to the analysis of incoherent spontaneous emission only. Spatially modulated phases in the presence of coherent driving of lattice atoms have been discussed in an open, non-equilibrium setting in particular by Lee and collaborators [123, 124]; see also Ref. [132]. We extend such models by coupling the spin degrees of freedom to a quantum light field.

We proceed to analyse the system as described by Eqs. (3.1-3.4) using even-odd sublattice mean-field master equations and cavity spectra to detect experimental signatures of magnetic correlations in the quantum light in Sec. 3.4. In Sec. 3.4.4 we include a suggestion for a quantum optical implementation of our model. We discuss in detail the validity of our approach and especially discuss implications of beyond mean-field effects in Sec. 3.5. We close with a conclusion in Sec. 3.6.

3.3. Coupled sublattice mean-field master equations for atoms and photons

We now derive and solve the coupled mean-field master equations for both, the spin degrees of freedom and the photons in the thermodynamic limit of $N \to \infty$. We account for different spin expectation values on the even versus odd sublattice of the bipartite square lattice of Fig. 3.1. The goal is to allow for steady-states with spontaneously broken translational (even-odd interchange) symmetry. We have checked that the homogeneous solutions only ever become unstable against plain-wave perturbations with wavevector $(k_x, k_y) = (\pi, \pi)$, see Sec. 3.5.3, (lattice constant set to 1) justifying our sublattice Ansatz.

To this end, we now approximate the solution of the full master equation

$$\partial_t \rho = -i[H, \rho] + \mathcal{L}_\kappa[\rho] + \mathcal{L}_\gamma[\rho] \; , \tag{3.5}$$

by factorizing the spin part of density operator for all even sites as $\rho_e = \bigotimes_{\ell=1}^{N/2} \rho_{e,\ell}$ and analogously for the odd sites $\rho_o = \bigotimes_{\ell=1}^{N/2} \rho_{o,\ell}$.

We comment further on the prospects of capturing finite spatial correlations and fluctuations beyond mean-field in Sec. 3.5.2. We further define the spin expectation values on the even and odd sublattices, respectively: $\langle \sigma^\alpha_{e/o} \rangle = \mathrm{Tr}[\rho_{e/o} \sigma^\alpha_{e/o}]$ where α refers to (x, y, z). The first four equations read

$$\begin{aligned}
\partial_t \langle \sigma^x_e(t) \rangle &= \langle \sigma^y_e(t) \rangle \left[\Delta - 2V(\langle \sigma^z_o(t) \rangle + 1)\right] - \frac{\gamma}{2} \langle \sigma^x_e(t) \rangle & (3.6)\\
\partial_t \langle \sigma^y_e(t) \rangle &= \langle \sigma^x_e(t) \rangle \left[2V(\langle \sigma^z_o(t) \rangle + 1) - \Delta\right] - 2g[\langle a(t) \rangle + \langle a^\dagger(t) \rangle] \langle \sigma^z_e(t) \rangle - \frac{\gamma}{2} \langle \sigma^y_e(t) \rangle & (3.7)\\
\partial_t \langle \sigma^z_e(t) \rangle &= 2g[\langle a(t) \rangle + \langle a^\dagger(t) \rangle] \langle \sigma^y_e(t) \rangle - \gamma(1 + \langle \sigma^z_e(t) \rangle) & (3.8)\\
\partial_t \langle a(t) \rangle &= -(\kappa + i\omega_0) \langle a(t) \rangle - \frac{1}{2} ig(\langle \sigma^x_e(t) \rangle + \langle \sigma^x_o(t) \rangle) & (3.9)
\end{aligned}$$

The equations for the odd sublattice spin projections follow from Eqs. (3.6-3.8) by exchanging the sublattice index $e \leftrightarrow o$. The complex conjugate of Eq. (3.9) completes the set of eight coupled equations. Here, we rescaled the photonic variable with $a(t) \to \sqrt{N} \langle a(t) \rangle$ a steady-state is macroscopically occupied in the thermodynamic limit and one may also define $\langle \sigma^\alpha_{e,o} \rangle \equiv \frac{1}{(N/2)} \sum_{\ell \in even,odd}^{N} \sigma^\alpha_\ell$.

Phase	Broken Symmetry	Order Parameter
$\mathrm{SR}_{\mathrm{UNI}}$	Superradiance $\mathbb{Z}_2$	$\langle a \rangle \neq 0$
AFM	Lattice translations T_{lat}	$\langle \sigma_e^z \rangle - \langle \sigma_0^z \rangle \neq 0$
AFM+SR	$\mathbb{Z}_2$ *and* T_{lat}	$\langle \sigma_e^z \rangle - \langle \sigma_0^z \rangle \neq 0$, $\langle a \rangle \neq 0$
FP	None	None

Table 3.1.: Order parameters for the phases in Fig. 3.2. Whenever the photon parity is broken, the x-projections of the spins also attain a finite expectation value $\langle \sigma^x \rangle \neq 0$.

Mean field master equations are often a necessary first step to study driven-dissipative systems, see for example, Refs. [133, 123, 124, 134, 135, 136, 137] and Ref. [138] for a variety of contexts.

3.4. Key results and their derivation

3.4.1. Combination of superradiance and magnetic translation symmetry-breaking ($\kappa \neq 0, \gamma = 0$)

Our first key result is Fig. 3.2: the non-equilibrium steady-stase phase diagram of Eqs. (3.1-3.4) setting the atomic spontaneous emission $\gamma = 0$ for now.

This way of solving the problem implicitly takes first the thermodynamic limit $N \to \infty$ and subsequently the long-time limit $t \to \infty$. We keep κ finite to account for photon losses. In Sec. 3.5.1, we show how the somewhat unphysical limit $\kappa \to 0$ reproduces in fact the phase boundaries of a corresponding ground state $T = 0$ model.

Using cavity-assisted Raman transitions [26] to tune the atom-light coupling,the $\gamma = 0$ limit describes the limit of relatively far detuned excited states, where population in the decaying levels is suppressed such that the ground-state manifold froming the two-level system is relatively stable. These phase diagrams are computed from solving for steady states of mean-field master equations for the real-valued atomic variables $(\langle \sigma^x \rangle, \langle \sigma^y \rangle, \langle \sigma^z \rangle)$ and the complex-valued photon expectation values $(\langle a \rangle, \langle a^\dagger \rangle)$, see Eqs. (3.6-3.9).

The phases shown in Fig. 3.2 can be classified according to their “order parameters” in Table 3.1. Let us describe the phases in more detail. Upon increasing the coupling to the photons along the g-axis in Fig. 3.2, for $V/|\Delta| < 1/4$, a fully polarized phase ($\mathrm{FP}_\uparrow$, $|\uparrow\uparrow ...\rangle$) becomes superradiant crossing the Dicke transition, which has been studied in detail for both, the closed thermal and ground states as well as the open version including the full two loss channel variant in a (γ, κ) Dicke model including single-site atomic spontaneous emission, see chapter 2 and for an experimental realisation see [44] (2018, Singapore). Meanwhile, also an open version of the spin-1 Dicke model with both loss channels present has been experimentally realised [115]. The superradiance transition breaks a discrete symmetry

$$\mathbb{Z}_2 : [a + a^\dagger, \sigma_\ell^x, \sigma_\ell^y] \to [-(a + a^\dagger), -\sigma_\ell^x, -\sigma_\ell^y]. \tag{3.10}$$

The experimental signature is a jump of the photon number inside the resonator [24, 49, 44, 115, 28] and the cavity ’lights up’. Recall that here we have the atomic spins pinned in a deep optical lattice such that all motional degrees of freedom are frozen out and we consider the dynamics of internal spin states only. This is in contrast to the realizations of the Dicke model with momentum states of the atomic gas [142, 102, 65]; therein the onset of superradiance is accompanied by a spatial self-organisation of the atoms in a

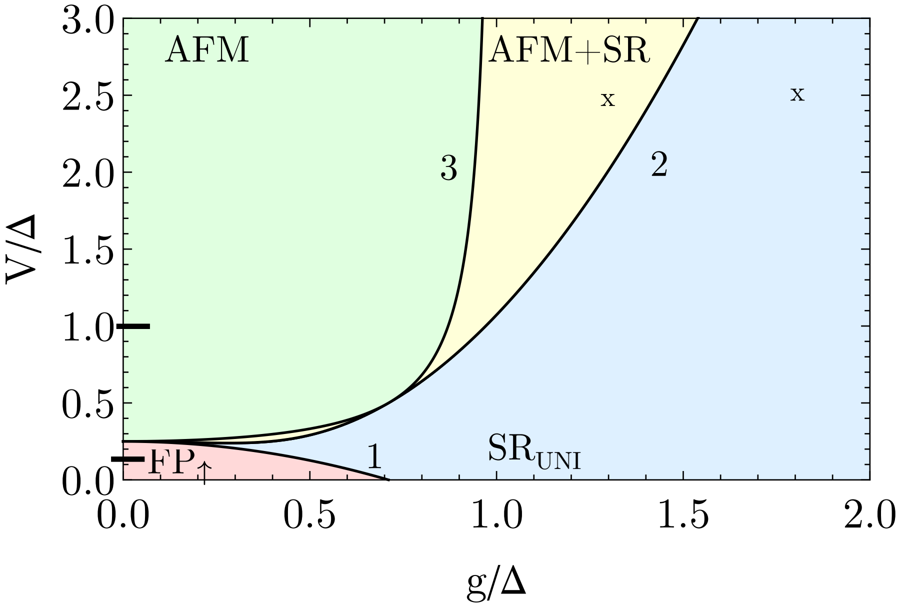

Figure 3.2.: Non-equilibrium mean-field phase diagram of a Rydberg-dressed spin lattice (with nearest neighbor interaction V) coupled to a single-mode optical light field with rate g. In units of the spin longitudinal field Δ for photon losses only ($\kappa \neq 0, \gamma = 0$). The key feature is the yellow strip, AFM+SR phase, in which spatially modulated magnetic moments occur together with a superradiant photon condensate, see Tab. 3.1. This phase may be regarded as the magnetic analogue of the (superradiant) supersolid of moving lattice bosons in an optical cavity [24, 139, 140, 141]. The yellow strip merges into the V-axis at a multi-critical point from which four different phases can be reached by infinitesimal variation of parameters. At the multi-critical point ($g/\Delta = 0, V/\Delta = 1/4$) the spins feel zero effective longitudinal field and any small coupling to a field can align them. $\mathrm{SR}_{\mathrm{UNI}}$ is a uniform superradiant phase. AFM stands for antiferromagnetic with differing magnetic moments on the even and the odd sublattice. $\mathrm{FP}_{\uparrow}$ is a fully polarized phase in which all spins point up. The magnetisations and the value of the photon condensate across the transitions are continuous. Cavity spectra at positions labeled with (x) are depicted in Fig. 3.5. Numerical parameters used: $\omega_0/\Delta = 2.0, \kappa/\Delta = 0.2$.

checkerboard pattern. Here, with the setup displayed in Fig. 3.1, the superradiance leads to uniform spin polarization in x-direction and the Rydberg-mediated repulsion competes with this and tends to break the even-odd lattice translation symmetry.

Up the V-axis, at $g = 0$ the magnetisations of the system can change discontinuously (at $V = \Delta/4$ in two dimensions) from a fully polarised state ($\mathrm{FP}_{\uparrow}$) to an antiferromagnetic excitation pattern (AFM). This AFM phase breaks a discrete even-odd translation symmetry

$$T_{\mathrm{lat}} : [\sigma^{\alpha}_{e,o}] \to [\sigma^{\alpha}_{o,e}] \,, \tag{3.11}$$

which can lead to different sublattice magnetisations as depicted in Fig. 3.2. Here, T_{lat} exchanges the even (e) and odd (o) sublattice index of the atomic variables σ^{α} with $\alpha = \{x, y, z\}$ in the Hamiltonians in Eqs. (3.1-3.2). As described further in the caption of Fig. 3.2, the AFM+SR phase has a curious feature, namely that it is split in two regions, that are delimited by a touching point of two second-order phase transition lines of the $\mathrm{SR}_{\mathrm{UNI}}$ and the plain AFM phase at $V/|\Delta| = 1/2$. For this special value, the effective magnetic field on one sublattice vanishes. At this point, however, the transition becomes discontinuous.

Phase boundaries and order parameters with photon losses ($\kappa \neq 0, \gamma = 0$)

Here, we provide a more detailed analysis of the above mentioned results for the case where the atoms do not decay spontaneously and the only loss-process is given by the Lindblad $\mathcal{L}_{\kappa}$, see Eq. (3.4). The Eqs. (3.6-3.9) with $\gamma = 0$ conserve in this case a pseudo-angular momentum

$$\langle \sigma^{x}_{e,o} \rangle^2 + \langle \sigma^{z}_{e,o} \rangle^2 = 1 \tag{3.12}$$

provided we start from an initial state such as $|\downarrow, \downarrow, \ldots\rangle$ that is devoid of all excitations which fulfills this condition. This would have to be realised with a preparation protocol to realise a low-entropy initial state, e.g. by first having the external lasers switched off and starting in a classical antiferromagnetic state where the atom-light coupling is gradually ramped up. Here (e, o) refers to the even and odd sub lattice respectively. Due to the presence of time-reversal symmetry in the atomic channel, the steady-state of the system constrains $\langle \sigma^{y}_{e,o} \rangle = 0$ (see the discussion above in Sec. 3.4.3).

The phase diagram in Fig. 3.2 is calculated, with photon losses, by numerically solving for the stationary states of Eqs. (3.6-3.9). We determine stability by inspecting the real parts of the eigenvalues from the corresponding stability matrix that is obtained by linearising Eqs. (3.6-3.9) to first oder in fluctuations around the steady-states, see Sec. 3.5.3.

Together with the constraint Eq. (3.12), the set of Eqs. (3.6-3.9) can be solved analytically. The homogeneous ($\langle \sigma^{x,z} \rangle \equiv \langle \sigma^{x,z}_{e} \rangle = \langle \sigma^{x,z}_{o} \rangle$) steady-state solutions, which describe the Dicke superradiance transition are

$$\langle a \rangle = \mp \frac{g \langle \sigma^x \rangle}{\omega_0 - i\kappa}, \tag{3.13}$$

$$\langle \sigma^x \rangle = \mp \frac{\sqrt{J - J_c}\sqrt{J + \Delta}}{\sqrt{2}\sqrt{J + 2V}}, \tag{3.14}$$

$$\langle \sigma^z \rangle = \frac{J_c + \Delta}{2J - J_c + \Delta}. \tag{3.15}$$

We have defined $J = \frac{4g^2\omega_0}{\kappa^2 + \omega_0^2}$ and $J_c = \Delta - 4V$. A plot of the Eqs. (3.13)-(3.15) is illustrated in Fig. 3.3. Starting in the antiferromagnetic phase and increasing the atom-light coupling

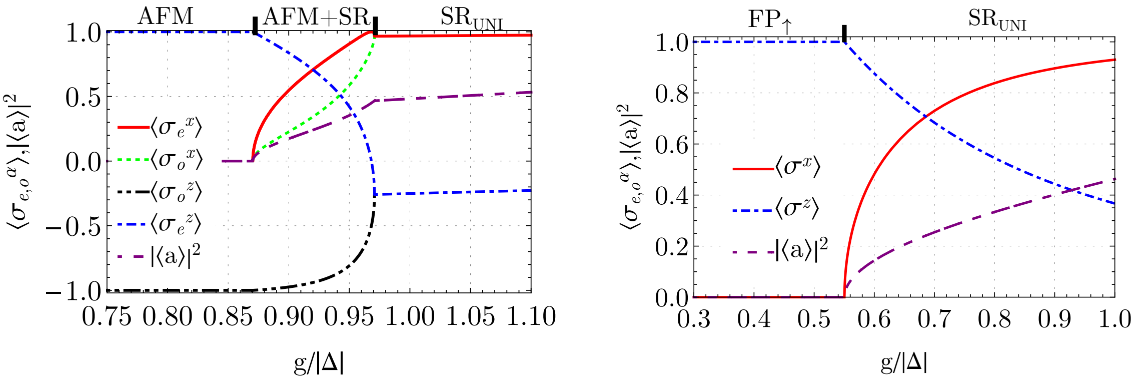

(a) (b)

Figure 3.3.: Steady-states for Eqs. (3.6-3.9) with $\gamma = 0$ for the parameters $\omega_0 = 2.0|\Delta|$, $\kappa = 0.2|\Delta|$ for the phases depicted in Fig. 3.2. (a) Behavior of the magnetisations and the coherent photon condensate in the plain antiferromagnet (AFM), in the regime where translational symmetry breaking and a superradiant photon condensate occur together (AFM+SR) and in the Dicke-phase (SR$_{\text{UNI}}$) as the atom-light coupling g is increased at a fixed value of $V = |\Delta|$. All transitions are continuous in the order-parameters. The plot in (b) shows the onset of superradiance as the atom-light coupling is increased, for a fixed value of $V = 0.1|\Delta|$.

g, a regime where superradiance ($\langle a\rangle \neq 0$) and a phase with different sub-lattice magnetisations occur together is predicted ($\langle\sigma_e^z\rangle - \langle\sigma_o^z\rangle \neq 0$) which, due to Eq. (3.12) implies $\langle\sigma_e^x\rangle - \langle\sigma_o^x\rangle \neq 0$. Due to the finite longitudinal field Δ, one sublattice is easier flipped than the other and the system realizes a "canted" antiferromagnet. If the atom-light coupling is increased even further, translational symmetry is restored and the system realises a Dicke superradiant phase. This can be seen by tracking the evolution of the magnetisation as g is increased in Fig. 3.3a.

We now derive analytical expressions for the phase-transition lines displayed as solid lines in Fig. 3.2.

First, we transform the mean-field equations (3.6-3.9) in frequency space via Fourier transformation

$$\mathcal{O}(t) = \frac{1}{\sqrt{2\pi}}\int_{-\infty}^{\infty} e^{-i\nu t}\mathcal{O}(\nu)d\nu, \quad \mathcal{O}^{\dagger}(t) = \frac{1}{\sqrt{2\pi}}\int_{-\infty}^{\infty} e^{-i\nu t}\mathcal{O}^{\dagger}(-\nu)d\nu. \tag{3.16}$$

In general, one should add Markovian quantum noise-operators with zero-mean to the photonic and atomic set of master equations that result from the interaction of the atom-cavity system with the vacuum modes outside of the cavity. These we denote $\xi_{e,o}^{\alpha}(\nu)$ as the atomic and $\xi^{a}(\nu)$ as the photonic noise-operators in frequency space.

Next, we add back fluctuations around the stationary states of Eqs. (3.6-3.9)

$$\langle\sigma_{e,o}^{\alpha}(\nu)\rangle \rightarrow \langle\sigma_{e,o}^{\alpha}\rangle\,\delta(\nu)\sqrt{2\pi} + \delta\sigma_{e,o}^{\alpha}(\nu) \tag{3.17}$$

$$\sqrt{N}\,\langle a(\nu)\rangle \rightarrow \sqrt{N}\,\langle a\rangle\,\delta(\nu)\sqrt{2\pi} + \delta a(\nu)\ , \tag{3.18}$$

where the steady-states are denoted as $\langle\sigma_{e,o}^{\alpha}\rangle$ with $\alpha = (x, y, z)$ and $\langle a\rangle$ is the expectation value for a coherent photon condensate. Here, $\delta\sigma_{e,o}^{\alpha}(\nu)$ and $\delta a(\nu)$ describe quantum fluctuations about the semi-classical steady-state and $\delta(\nu)$ denotes a delta function in frequency space. At long times, we may neglect second-order terms in the fluctuations by assuming that the steady-state values are large compared to the associated fluctuations in the thermodynamic limit $N \to \infty$.

The now linearized equations can be cast in matrix form.

$$\boldsymbol{\xi}(\nu) = \delta(\nu) f(\boldsymbol{\sigma}) + \boldsymbol{G}_R^{-1}(\nu) \cdot \boldsymbol{\delta\sigma}(\nu) \tag{3.19}$$

where the fluctuations around the steady state are collected in $\boldsymbol{\delta\sigma}(\nu)$ and the noise-operators are collected into $\boldsymbol{\xi}(\nu)$:

$$\delta\boldsymbol{\sigma}^T(\nu) = \Big(\delta\sigma_e^x(\nu), \delta\sigma_e^y(\nu), \delta\sigma_e^z(\nu), \delta a(\nu), \delta a^\dagger(-\nu), \delta\sigma_o^x(\nu), \delta\sigma_o^y(\nu), \delta\sigma_o^z(\nu)\Big) \tag{3.20}$$

$$\boldsymbol{\xi}^T(\nu) = \Big(\xi_e^x(\nu), \xi_e^y(\nu), \xi_e^z(\nu), \xi^a(\nu), \xi^{a^\dagger}(-\nu), \xi_o^x(\nu), \xi_o^y(\nu), \xi_o^z(\nu)\Big) \tag{3.21}$$

The function $f(\boldsymbol{\sigma})$ is associated with the coherent part of the steady-states and thus only leads to a zero-frequency peak in the cavity-spectrum. The responses of the fluctuations $\delta\boldsymbol{\sigma}$ to the noise or 'driving-forces' $\boldsymbol{\xi}$ is encoded by the retarded Green-function $\boldsymbol{G}_R(\nu)$, its inverse $\boldsymbol{G}_R^{-1}(\nu)$ is given as:

$$\begin{pmatrix}
\frac{1}{2}(\gamma - 2i\nu) & 2V(\langle\sigma_o^z\rangle + 1) - \Delta & 0 & 0 & 0 & 0 & 0 & 2V\langle\sigma_e^y\rangle \\
\Delta - 2V(\langle\sigma_o^z\rangle + 1) & \frac{1}{2}(\gamma - 2i\nu) & 2g(\langle a\rangle + \langle a^\dagger\rangle) & 2g\langle\sigma_e^z\rangle & 2g\langle\sigma_e^z\rangle & 0 & 0 & -2V\langle\sigma_e^x\rangle \\
0 & -2g(\langle a\rangle + \langle a^\dagger\rangle) & \gamma - i\nu & -2g\langle\sigma_e^y\rangle & -2g\langle\sigma_e^y\rangle & 0 & 0 & 0 \\
\frac{1}{2}ig & 0 & 0 & \kappa - i(\nu - \omega_0) & 0 & \frac{1}{2}ig & 0 & 0 \\
-\frac{1}{2}ig & 0 & 0 & 0 & \kappa - i(\nu + \omega_0) & -\frac{1}{2}ig & 0 & 0 \\
0 & 0 & 2V\langle\sigma_o^y\rangle & 0 & 0 & \frac{1}{2}(\gamma - 2i\nu) & 2V(\langle\sigma_e^z\rangle + 1) - \Delta & 0 \\
0 & 0 & -2V\langle\sigma_o^x\rangle & 2g\langle\sigma_o^z\rangle & 2g\langle\sigma_o^z\rangle & \Delta - 2V(\langle\sigma_e^z\rangle + 1) & \frac{1}{2}(\gamma - 2i\nu) & 2g(\langle a\rangle + \langle a^\dagger\rangle) \\
0 & 0 & 0 & -2g\langle\sigma_o^y\rangle & -2g\langle\sigma_o^y\rangle & 0 & -2g(\langle a\rangle + \langle a^\dagger\rangle) & \gamma - i\nu
\end{pmatrix} \tag{3.22}$$

The frequency-resolved spectrum of excitations governed by the fluctuations can be obtained from the characteristic equation

$$\mathrm{Det}[\boldsymbol{G}_{\mathrm{R}}^{-1}(\nu)] = 0. \tag{3.23}$$

All poles of the retarded Green function are located in the lower complex frequency plane. The damping rate of the excitations can be read off from the imaginary part of these poles, see for instance Reference [13]. In the case of second order transitions, the order-parameters $(\langle a\rangle, \langle\sigma_{e,o}^x\rangle, \langle\sigma_{e,o}^z\rangle)$ change continuously at the phase transitions. We obtain analytical expressions for the phase boundaries by solving

$$\lim_{\nu\to 0} \mathrm{Det}[\boldsymbol{G}_{\mathrm{R}}^{-1}(\nu)] = \alpha^2 = 0\ . \tag{3.24}$$

The zeroth-order frequency component refers to a possible gap α^2 of the system that will close continuously ($\lim_{g\to g_c} \alpha^2 \to 0$) when the phase transition is approached by increasing the atom-light coupling g. We arrive at the set of transition lines given by Eq. (3.26)-(3.29) that are depicted as black lines in Fig. 3.2 where they match the numerically calculated transitions based on a linear stability analysis. The open character of the system becomes manifest in the expressions for the phase boundaries as all transitions explicitly depend on the rate of photonic dissipation κ. Starting from the $\mathrm{FP}_\uparrow$ phase, the Dicke superradiance transition in presence of the Rydberg interaction sets in at the critical coupling strength:

$$g_{\mathrm{c},1} = \frac{\sqrt{\kappa^2 + \omega_0^2}\sqrt{\omega_0(\Delta - 4V)}}{2\omega_0}, \tag{3.25}$$

$$V_{\mathrm{c},1} = \frac{\Delta}{4} - \frac{g^2\omega_0}{\kappa^2 + \omega_0^2}. \tag{3.26}$$

The finite Rydberg-dressed interaction V modifies the effective longitudinal field experienced by the spins which shifts the position of the superradiant condensate in comparison to the $V = 0$ case. Eq. (3.25) collapses to the familiar Dicke superradiance transition in the case $V \to 0$ [26]. The crossover from the (AFM+SR) regime to the Dicke superradiant phase (SR) is given by:

$$\begin{aligned}
&V_{\mathrm{c},2} = \\
&\Bigg[4g^2\omega_0 \left(4g^2\omega_0 + \sqrt{\Delta^2\left(\kappa^2+\omega_0^2\right)^2 - 8\Delta g^2\omega_0\left(\kappa^2+\omega_0^2\right) + 80g^4\omega_0^2}\right) \\
&+ \Delta\left(\kappa^2+\omega_0^2\right)\sqrt{\Delta^2\left(\kappa^2+\omega_0^2\right)^2 - 8\Delta g^2\omega_0\left(\kappa^2+\omega_0^2\right) + 80g^4\omega_0^2} \\
&+ \Delta^2\left(\kappa^2+\omega_0^2\right)^2\Bigg] / 8\left(\kappa^2+\omega_0^2\right)\left(\Delta\left(\kappa^2+\omega_0^2\right)+2g^2\omega_0\right) \ . \qquad (3.27)
\end{aligned}$$

The transition line from the AFM phase to the AFM+SR regime is given by $(-\Delta < 0)$

$$g_{\mathrm{c},3} = \frac{\sqrt{\Delta}\sqrt{\kappa^2+\omega_0^2}\sqrt{4V-\Delta}}{2\sqrt{2}\sqrt{V}\sqrt{\omega_0}}, \qquad (3.28)$$

$$V_{\mathrm{c},3} = \frac{\Delta^2\left(\kappa^2+\omega_0^2\right)}{4\left(\Delta\left(\kappa^2+\omega_0^2\right)-2g^2\omega_0\right)} \ . \qquad (3.29)$$

We note that the line where AFM and SR order occur together diverges $V_{\mathrm{c},3} \to \infty$ as $\lim_{g\to g_\star}$ with $g_\star = \left(\sqrt{\Delta}\sqrt{\kappa^2+\omega_0^2}\right) / \left(\sqrt{2}\sqrt{\omega_0}\right)$. Moreover, on a mean-field level, there is a touching point g_t of two second-order phase transition lines that can be found by equating Eq. (3.27) and Eq. (3.29) which yields $g_t = \left(\sqrt{\Delta}\sqrt{\kappa^2+\omega_o^2}\right)\left(2\sqrt{\omega_o}\right)$ and $V_{\mathrm{c},3}(g_t) = \Delta/2$ marks the point where the effective longitudinal field on one of the sublattices vanishes. On a mean-field level, we find a multi-critical point, where all second-order phase transition lines meet on the $g = 0$-axis at $V = \Delta/4$.

3.4.2. Even-odd sublattice peak in cavity spectrum

Here we show that the translation-symmetry breaking induced by the nearest-neighbour Rydberg-dressed interaction V leads to a novel collective mode and peak in the spectrum. Figure 3.4 shows the cavity spectrum upon increasing g from the (AFM+SR) phase with broken T_{lat} symmetry into the $\mathrm{SR}_{\mathrm{UNI}}$ phase where translation symmetry is restored. Here, the 'even-odd' polariton mode vanishes in a specific way: Denoting the frequency of the polariton pole as ν, we observe that both, its real part (gap) and the imaginary part (damping rate) vanish with coupling constant (from the AFM+SR phase toward line 2 in Fig. 3.2) with

$$\mathrm{Re}[\nu] \propto \pm\sqrt{g_c - g}, \quad \mathrm{Im}[\nu] \propto -(g_c - g) \ , \qquad (3.30)$$

where g_c refers to the right boundary delimiting the AFM+SR phase. This is because the translational symmetry T_{lat} affects the atomic sector only which does not couple directly to the photonic rate of dissipation κ. This is in contrast to Dicke-type models whose dynamics becomes purely overdamped/imaginary at the transition [91], see Fig. 2.3c that is, the real part of the mode vanishes first.

Derivation of the cavity output spectrum ($\kappa \neq 0, \gamma = 0$)

Here we calculate the frequency-resolved cavity output spectrum for the light that leaks from the imperfect cavity mirrors within a standard input-output theory [112, 113, 26]

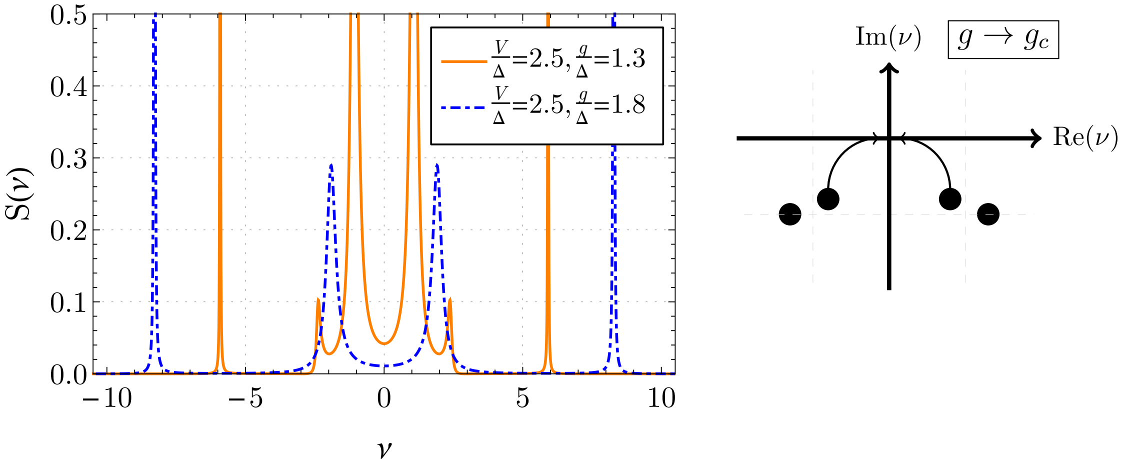

(a) (b)

Figure 3.4.: Even-odd sublattice peak in the cavity spectrum (peak close to zero frequency of the orange, solid line), which appears when the translational lattice symmetry T_{lat} is spontaneously broken by the Rydberg-dressed nearest-neighbor interaction V. The two cavity spectra are computed for the positions labeled by (x) in Fig. 3.2. The blue, dashed line has the two polariton peaks in the uniform SR_{UNI} phase with the photonic branch around the cavity frequency $\omega_0/\Delta = 2.0$. The orange, solid line is the spectrum in the AFM+SR regime with broken T_{lat}; it shows the prominent even-odd peak, which becomes soft toward the phase boundary (the right edge of the yellow strip in Fig. 3.2. (b) Low-energy pole structure of the even-odd sublattice peak, where both the real and the imaginary part of the poles vanish simultaneously as $g \to g_c$ according to Eq. (3.30).

and show how the ’even-odd’ polariton pole is identified. We find that every phase in Fig. 3.2 shows a characteristic cavity output spectrum making it possible to experimentally distinguish one phase from the other. The input fields are related to the output fields by the relation

$$a_{\text{out}}(\nu) = \sqrt{2\kappa}a(\nu) - a_{\text{in}}(\nu), \tag{3.31}$$

$$a^\dagger_{\text{out}}(-\nu) = \sqrt{2\kappa}a^\dagger(-\nu) - a^\dagger_{\text{in}}(-\nu). \tag{3.32}$$

The annihilation operators $(a_{\text{out}}(\nu), a_{\text{in}}(\nu), a(\nu))$ correspond to the output field, the vacuum input field, and the intra cavity field, respectively and we have used $\xi_a(\nu) = \sqrt{2\kappa}a_{\text{in}}(\nu)$. The Markovian quantum noise operators with zero mean are determined by their second-order correlation functions. For the photonic channel they read

$$\langle a_{\text{in}}(\nu')a^\dagger_{\text{in}}(-\nu)\rangle = \delta(\nu + \nu') \tag{3.33}$$

We solve Eq. (3.19) for $a_{\text{out}}(\nu)$ and $a^\dagger_{\text{out}}(-\nu)$ together with Eq. (3.33) to obtain the output spectrum for a vacuum input field

$$S(\nu) = \langle a^\dagger_{\text{out}}(\nu)a_{\text{out}}(\nu)\rangle = 2\kappa \langle \delta a^\dagger(\nu)\delta a(\nu)\rangle = 2\kappa \int_{-\infty}^{\infty} e^{-i\nu\tau} \langle \delta a^\dagger(0)\delta a(\tau)\rangle \, d\tau. \tag{3.34}$$

The unnormalized fluorescence spectrum $S(\nu)$ is proportional to finding a photon at frequency ν and thus displays the position and the spectral weight of the resonance energies of hybridized atom-cavity modes. We only depict cavity-spectra in the $\gamma = 0$ limit. We have investigated the effect of spontaneous emission on the cavity spectra in the $V \to 0$ limit in chapter 2 and found that it can induce a frequency asymmetry in the cavity spectrum since atomic excitations can leave the cavity directly by emission into free space.

The cavity spectra for $\kappa \neq 0, \gamma = 0$ can be obtained for every phase in Fig. 3.2. In the fully polarized phase ($\langle a \rangle = \langle \sigma^x \rangle = 0, \langle \sigma^z \rangle = 1$) for $g < g_{c,1}$ and $-\Delta < 0$, the cavity spectrum is obtained as

$$
\begin{aligned}
S_1(\nu) &= \frac{16\kappa^2 g^4 (\Delta - 4V)^2}{|\Omega_0|^2}, && (3.35)\\
|\Omega_1|^2 &= \Big|\Big((\kappa - i\nu)^2(-\Delta + \nu + 4V)(\Delta + \nu - 4V) + 4g^2\omega_0(\Delta - 4V)\\
&\quad +\omega_0^2(-\Delta + \nu + 4V)(\Delta + \nu - 4V)\Big)\Big|^2 && (3.36)
\end{aligned}
$$

and is depicted in Fig. 3.5c. In the limit $V \to 0$ it reduces to the familiar expression obtained in Ref. [26]. In the AFM phase ($\langle \sigma^z_e \rangle = -1, \langle \sigma^z_o \rangle = 1, \langle a \rangle = \langle \sigma^x \rangle = 0$), the spectrum is given by

$$
\begin{aligned}
S_3(\nu) =& \frac{64\kappa^2 g^4 V^2 \left(\Delta^2 - 4\Delta V + \omega^2\right)^2}{|\Omega_3|^2} && (3.37)\\
\Omega_3 =& \Big|(\omega - \Delta)(\Delta + \omega)(\kappa - i\omega)^2(-\Delta + 4V + \omega)(\Delta - 4V + \omega)\\
&+\omega_0^2(\omega - \Delta)(\Delta + \omega)(-\Delta + 4V + \omega)(\Delta - 4V + \omega) + 8g^2 V\omega_0\left(\Delta^2 - 4\Delta V + \omega^2\right)\Big|^2 && (3.38)
\end{aligned}
$$

and a typical spectrum can be seen in Fig. 3.5a. In the homogeneous phase we make use of Eqs. (3.13-3.15) and obtain the spectrum as

$$
S_4(\nu) = \frac{16\kappa^2 g^8 \omega_0^2 \left(\kappa^2 + \omega_0^2\right)^6 (\Delta - 2V)^4}{|\Omega_4|^2} \tag{3.39}
$$

depicted in Fig. 3.5d. We leave Ω_4 unspecified as it is too large to print. It contains the polariton resonances that can also be calculated from Eq. (3.23). We denote the cavity spectrum in the AFM+SR regime as $S_4(\nu)$. We solve Eqs. (3.6-3.9) numerically in the long-time limit and use Eq. (3.34) to determine the spectrum numerically, see Fig. 3.5b. Now we discuss the characteristic features and the behavior of the poles.

Discussion of cavity spectra and low-frequency pole structure for ($\kappa \neq 0, \gamma = 0$)

We describe and depict the characteristic features of the cavity spectra for each phase of the mean-field phase diagram in Fig. 3.2 below. We begin our discussion with an analysis of the cavity spectra $S(\nu)$ in each phase. The cavity spectra are shown in Fig. 3.5. In general there are either four or six poles in the cavity spectrum. In the former case these originate from two photon-branches and two atomic branches that are symmetrically arranged around the zero-frequency axis. We identify the branches by their $g \to 0$ limit in the fully polarised phase where the resonances settle at the bare frequencies given by $\nu_{\text{Atom}} = \pm\Delta$ and $\nu_{\text{Photon}} = \pm\omega_0 - i\kappa$. There are six poles when the translational symmetry in the atomic sector is broken. The additional poles reflect the even/odd imbalance of the system and are thus attributed to the Rydberg interaction, see Fig. 3.5a. This provides a clear feature to experimentally detect a phase with antiferromagnetic order.

The cavity spectra in Fig. 3.5c (fully polarized $\text{FP}_\uparrow$) and in Fig. 3.5d (superradiant phase) are well-known and derived in [26] in the $V \to 0$ limit. In the superradiant regime, an increasing Rydberg interaction V shifts the atomic poles to higher energies whereas the peaks associated to the photonic branch settle around the cavity resonance at $\text{Re}(\nu) = \pm\omega_0 = \pm 2.0|\Delta|$. In the AFM and the (AFM+SR) phase, the cavity spectra depicted in

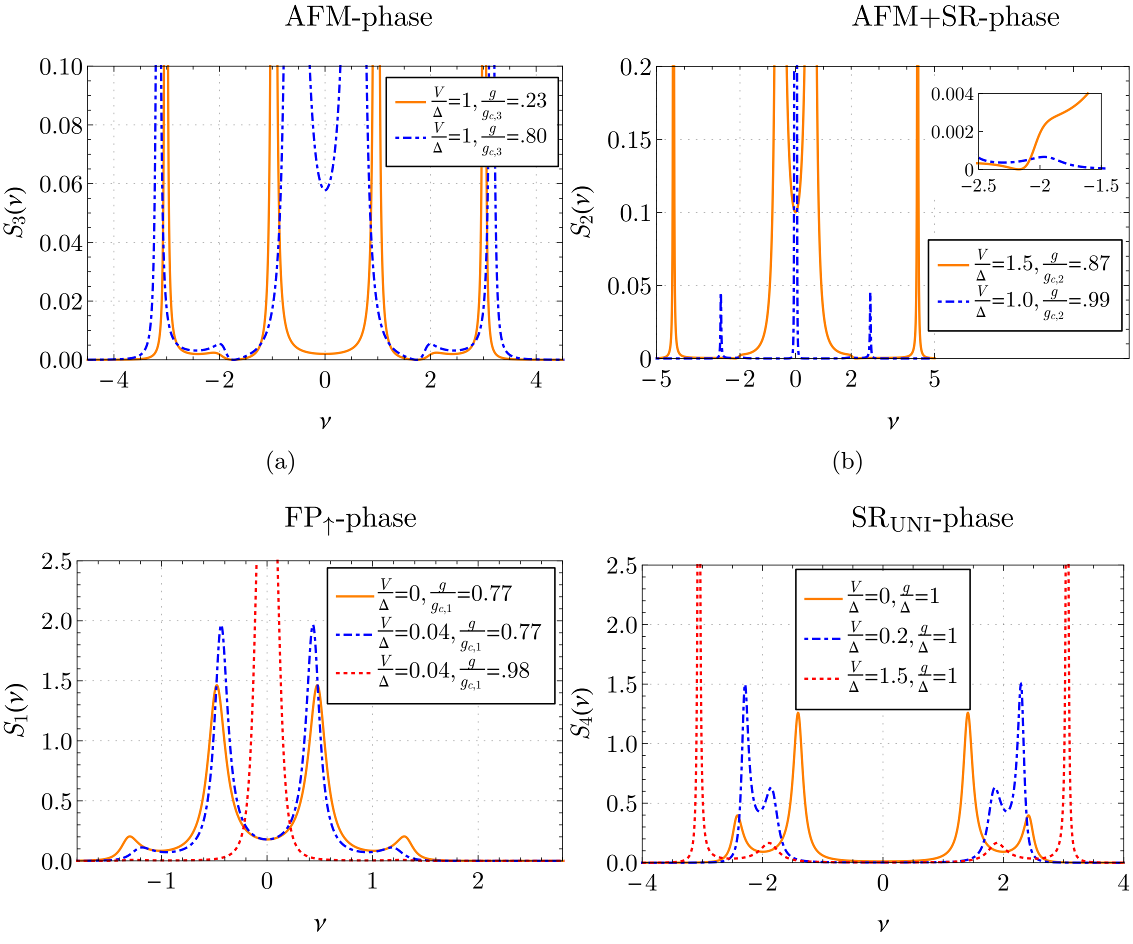

(a) (b)

(c) (d)

Figure 3.5.: Typical cavity spectra for each of the four phases depicted in Fig. 3.2. In general, the resonances show the hybridised atom-cavity eigenenergies that can be obtained from solving Eq. (3.23). There are four poles in the cavity spectrum when translational symmetry is intact as in (c,d) and there are six poles when translational symmetry is broken as (a,b). (a) Cavity spectrum in the plain antiferromagnetic phase. The broken translational symmetry is reflected in the appearance of an additional (Rydberg) resonance in the atomic-sector. (b) Cavity spectra in the regime of a broken $\mathbb{Z}_2$ and translational symmetry T. As $g \to g_{c,2}$, two of the six poles move towards $\nu = 0$ (dot-dashed line). At $g = g_{c,2}$ translational symmetry is restored and the additional Rydberg-induced even-odd peaks disappear. (Inset) Close to the frequency at $\nu = \omega_0/\Delta = \pm 2.0$ there are resonances with small but finite weight corresponding to the cavity resonance. (c) Cavity spectrum for the fully polarized phase FP$_\uparrow$ with no photonic excitations $\langle a \rangle = 0$. (d) Spectrum in the superradiant regime $\langle a \rangle \neq 0$ with translational symmetry T still intact.

Fig. 3.5a and Fig. 3.5b exhibit the aforementioned even/odd sublattice peak that reflects the broken translational symmetry in the atomic sector, so that there are six poles in total.

The frequency-resolved eigenenergies of the hybridized atom-cavity modes display a characteristic behaviour close to the phase transition as $g \to g_{c,1,2,3}$ in Fig. 3.2. On the real frequency axis, all phase transitions appear when at least one of the either four or six poles hits the zero $\nu = 0$. The low-frequency behaviour of the critical poles leading to the Dicke superradiance transition has already been established [143]. From the four poles, two (which we refer to as (ν_a, ν_b) in the following) approach the origin in the complex frequency plane. First, both poles become completely imaginary as $g \to g_{c,1}$. A single one of these poles vanishes at the phase-transition $|\nu_a| = 0$ while the other retains a finite imaginary part at $g = g_{c,1}$ set by the dissipation ($\nu_b(g = g_{c,1}) \sim -i\kappa$) emphasizing that the Dicke superradiance transition directly couples to the dissipation. The cavity spectrum in Fig. 3.5c exhibits a pole at zero frequency but with a finite, purely imaginary contribution as $g \to g_{c,1}$. The intensity under this finite-width peak diverges, which indicates a macroscopic occupation of the cavity-mode $\langle a \rangle \neq 0$. As the transition from the AFM into the (AFM+SR)-phase involves a superradiance transition, the same behaviour of the low-frequency poles can be observed as $g \to g_{\mathrm{c},3}$. When translational symmetry is broken, this transition mainly affects the atomic channel. As the photonic sector alone couples to a dissipative channel, we numerically observe that when translational symmetry is restored as one goes from the (AFM+SR) into the SR phase as $g \to g_{\mathrm{c},2}$, two of the six poles approach the origin on the complex frequency plane. In contrast to the Dicke superradiance transition both the real and imaginary part of the two low-frequency poles vanish together, see Fig. 3.4b for an illustration of the pole structure and Fig. 3.5b for the cavity spectra in the (AFM+SR) phase. At $g > g_{\mathrm{c},2}$ translational symmetry T_{lat} is restored and the spectrum is given by Fig. 3.5d.

3.4.3. Photon number oscillations ($\kappa \neq 0, \gamma \neq 0$)

We now account for a non-zero rate of atomic spontaneous emission $\gamma \neq 0$. Specific details of a given quantum-optical implementation (see Sec. 3.4.4) will determine which set of Lindblad operators and additional atomic levels need to be accounted for. In order to gain a first qualitative picture, we model an effective decay rate with $\mathcal{L}_\gamma[\rho]$ in Eq. (3.3) between the effective spin-up and spin-down states ($|1\rangle$ and $|0\rangle$ in Fig. 3.11. We expect γ to become larger once the detuning to the shorter lived excited states is decreased; it is generally true that the effective ground state levels inherit a finite lifetime from admixing a short-lived state. For a specific experimental set-up, one may also include other types of atomic losses or dephasing.

This at first sight innocuous change has interesting consequences. Even qualitative features of Fig. 3.2 are drastically changed. Allowing for a small γ, see Fig. 4.5, in particular wipes out the stable AFM phase and introduces a fully downward polarized state $\mathrm{FP}_\downarrow$ as well as a novel oscillatory phase (AFM+SR)-OSC. Here also the photon field amplitude oscillates which can be detected by time-resolved measurements of the intensity of the light leaving the cavity.

At the root of these effect is $\mathcal{L}_\gamma[\rho]$ in Eq. (3.3): it explicitly breaks the discrete symmetry G given by the product of time-reversal: $\mathcal{T}_\ell = -i\sigma^y_\ell K_\ell$, $t \to -t$ (for a spin $s = 1/2$) and spin rotation around the y-axis by π: $D^{1/2,\ell}_{y,\pi} = -i\sigma^y_\ell$. Here K_ℓ is the complex conjugation operator such that $\mathcal{G}_\ell = D^{1/2,\ell}_{y,\pi}\mathcal{T}_\ell = -K_\ell$. If we write $G = \Pi^N_{\ell=1}\mathcal{G}_\ell$ we have $GHG^{-1} = H$. In particular, this implies for steady states $\langle \sigma^y_{e,o} \rangle = \langle G\sigma^y_{e,o}G^{-1} \rangle = -\langle \sigma^y_{e,o} \rangle \overset{!}{=} 0$ if $\gamma = 0$. For $\gamma \neq 0$, the spins can start developing expectation values also in the y-direction. In a mean-field picture of a system in thermal equilibrium, the spin tries to align with the magnetic field generated by its neighbours. In the presence of decay with rate γ there is now a competition of the coherent mean-field dynamics and the dissipative Lindblad terms that try to push the spin into the spin-down $|\downarrow, \downarrow, \dots\rangle$ state. This offers new possibilities for the spin dynamics such as anomalous spin precession [124] not available in equilibrium.

We show the phases for a further range of parameters $(\Delta/\gamma, g/\gamma)$ space for a fixed strength V of the Rydberg interaction in two spatial dimensions in Fig. 3.7. In mean-field theory we distinguish five phases in the long time limit. Three are steady-states denoted as

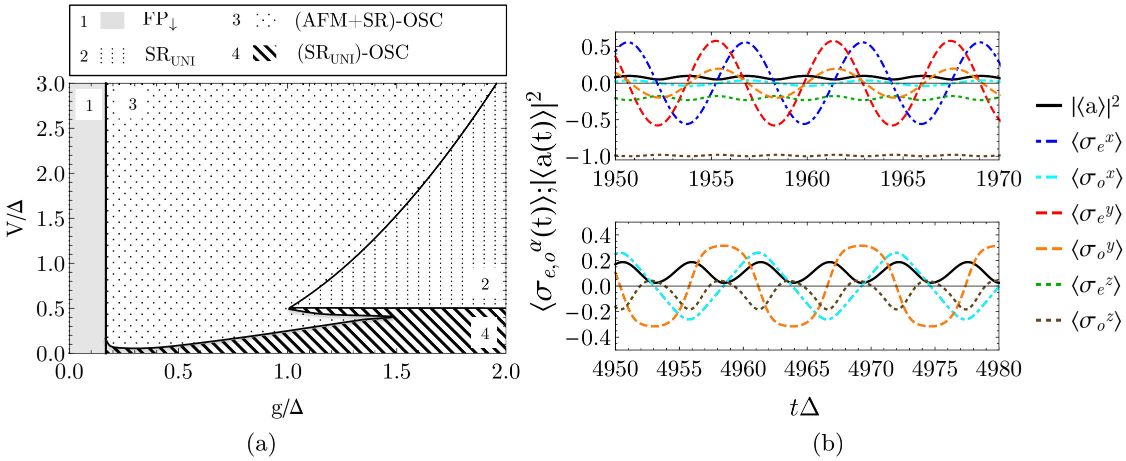

Figure 3.6.: (a) Supplementing the phase diagram Fig. 3.2 in the (V/Δ,g/Δ)-plane by a small amount of atomic dissipation $\gamma/\Delta = 0.01$ with $(\omega_0/\Delta = 2.0, \kappa/\Delta = 0.2)$ changes the steady-state landscape drastically. In comparison to the $\gamma/\Delta = 0.0$ case (compare Fig. 3.2), there are no stable steady-states with a broken lattice symmetry T_{lat} any more. Instead, the system can show persistent oscillations in time. (b) Depiction of the non-uniform (top, (AFM+SR)-OSC) oscillations and the uniform (bottom, $\mathrm{SR}_{\mathrm{UNI}}$-OSC) oscillations that characterize the long time limit behavior of Eqs. (3.6-3.9) with finite γ. Parameters for the upper plot are $(V/\Delta = g/\Delta = 0.5)$, the lower plot is obtained at $(V/\Delta = 0.3, g/\Delta = 1.2)$.

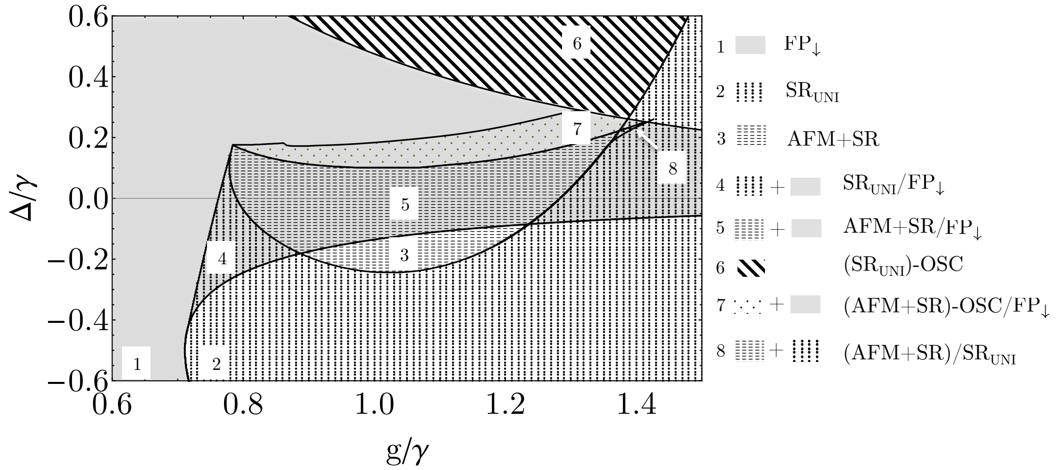

Figure 3.7.: Non-equilibrium steady-state phase diagram of Eqs. (3.1-3.4) with finite, atomic spontaneous emission $(\kappa/\gamma = 0.2, V/\gamma = 1.8, \omega_0/\gamma = 2.0)$. Apart from time-independent states, the dynamics also realises limit cycles where atomic and photon components show persistent oscillations in time. Oscillations can be uniform or different on the even/odd sublattice, see Fig. 3.8. Depending on the initial configuration, the system can reach different long-time fixpoints. Bistabilities occur whenever two phases overlap (see legend). Crystalline antiferromagentic order only occurs together with superradiance (AFM+SR).

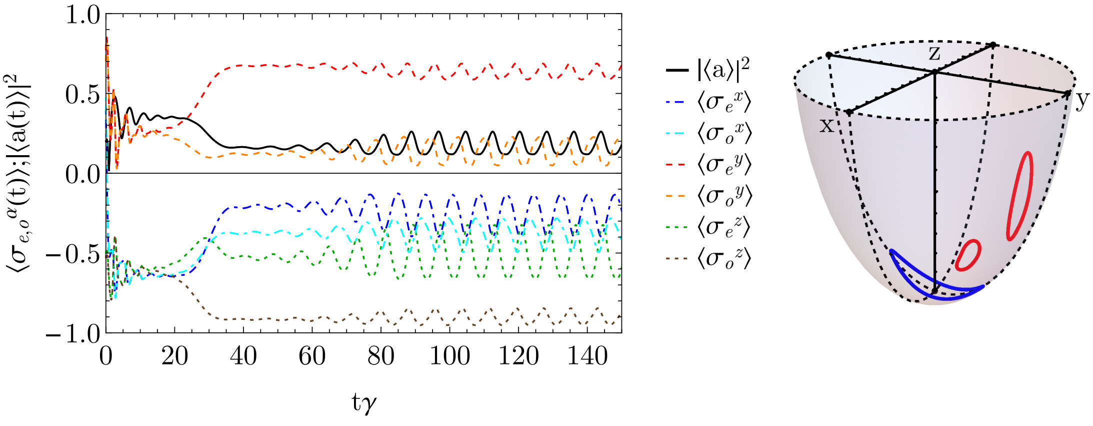

(a)

(b)

Figure 3.8.: (a): Persistent spin and photon-field oscillations appear in the (AFM+SR)-OSC phase for $\Delta > 0$ close to the (AFM+SR) stable region for the parameters used in Fig. 3.4.3 for $g/\gamma = 1.1, \Delta/\gamma = 0.15$. Note that between $t\gamma \approx 10 - 25$ the amplitudes display (quasi-) plateaus followed by a rapid in/decrease toward their final mean values; and only then the oscillations begin and persist. Let us mention that for moving atomic gases in a cavity, Ref. [144] found “pre-thermalized” plateaus in the time evolution for the order parameter by solving Fokker-Planck type kinetic equations. It is however not clear, if the mean-field master equation can at all capture or hint at such effects. (b): Illustration of the atomic components for the limit cycles on the lower part of the Bloch sphere. The two upper lineshapes (red) depict the lines traced by the oscillations on the even and the odd sublattice in the (AFM+SR)-OSC phase, as depicted in (a). The lower lineshape illustrates a limit cycle of uniform oscillations of the atomic components in the $\mathrm{SR_{UNI}}$ phase. We mention that oscillating cavity fields have been experimentally observed recently (2018) in the superradiant state of a spin-1 Dicke model [115].

($\mathrm{FP}_{\downarrow}$, $\mathrm{SR_{UNI}}$, AFM+SR, see also Tab. 3.1) and two are stable limit cycles. The Lindblad operators try to drive the system into an empty state without any excitations; consequently AFM order can only occur in the presence of a coherent drive, i.e. together with a photon condensate $\langle a\rangle$. In the latter phases, the system exhibits oscillations in both atomic and photonic components, since the atomic dynamics couples back to the photon sector through Eq. (3.13). The oscillations can be uniform in all components $(\mathrm{SR_{UNI}}) - \mathrm{OSC}$ or different on the sublattices $(\mathrm{AFM} + \mathrm{SR}) - \mathrm{OSC}$.

We observe bistabilities, meaning that the eventual fate of the system in the long-time limit depends on the initial conditions. However, we also find a small strip in the phase diagram where the system is bistable between $\mathrm{AFM} + \mathrm{SR}$ and a $\mathrm{SR_{UNI}}$ phase. We will discuss bistabilities below and in Sec. 3.5.2 in more detail. An explicit investigation of a bistable region that is subject to non-equilibrium fluctuation dynamcis is analysed in chapter 4.

Phase boundaries and order parameters with spontaneous emission ($\kappa \neq 0, \gamma \neq 0$)

As discussed in Sec. 3.4.3, allowing for spontaneous emission ($\gamma \neq 0$) in addition to photon leakage ($\kappa \neq 0$) has a dramatic influence on the phase diagram obtained from the behaviour of the mean-field master equations in the long-time limit. In comparison to the $\gamma = 0$ case, the phase diagram is enriched by the presence of oscillatory and bistable phases, see Fig. 4.5 and Fig. 3.7. We first turn our attention to the case where there is a small amount of dissipation in the atomic channel ($\gamma = 0.01|\Delta|$) to analyse its impact on the long-time limit behaviour of the steady-state phases depicted in Fig. 3.2. We observe (see Fig. 3.6) that allowing for a small amount of dissipation, there are no stable steady-states that involve a broken lattice symmetry T_{lat}. The only steady-states in the investigated $(V/\Delta$,$g/\Delta)$-plane is the empty atom-cavity system ($\text{FP}_{\downarrow}$) and a uniform superradiant phase (SR_{UNI}). The remaining long-time limit behavior is characterized by persistent oscillations that can be uniform ($\text{SR}_{\text{UNI}} - \text{OSC}$) or non-uniform ($(\text{AFM} + \text{SR}_{\text{UNI}}) - \text{OSC}$). As the Rydberg interaction is conditioned on population in the upper state, the phase boundary of the empty atom-cavity system is independent of V. Formally, we obtain its phase boundary by inspecting the eigenvalues of the stability matrix corresponding to the fixed point $(\langle a\rangle = \langle\sigma^x\rangle = \langle\sigma^y\rangle = 0, \langle\sigma^z\rangle = -1)$. The real part of at least one of the associated stability eigenvalues becomes positive when

$$\gamma\kappa\left((\gamma+2\kappa)^2+4\Delta^2\right)^2 - 32\Delta\lambda^2\omega_0(\gamma+2\kappa)^2 \tag{3.40}$$

$$+\,8\gamma\kappa\omega_0^2(\gamma-2\Delta+2\kappa)(\gamma+2(\Delta+\kappa)) + 16\gamma\kappa\omega_0^4 = 0. \tag{3.41}$$

Solving for g yields,

$$g_{(crit,FP_{\downarrow})} = \frac{\sqrt{\gamma\kappa}\sqrt{((\gamma+2\kappa)^2+4\Delta^2)^2+8\omega_0^2(\gamma-2\Delta+2\kappa)(\gamma+2(\Delta+\kappa))+16\omega_0^4}}{4\sqrt{2}\sqrt{\Delta\omega_0(\gamma+2\kappa)^2}}. \tag{3.42}$$

Here, we observe that at $g = g_{(crit,FP_{\downarrow})}$ the associated linearized stability matrix of Eqs. (3.6-3.9) obtains a pair of purely imaginary complex conjugated eigenvalues which signalizes that the system changes into a limit cycle via a Hopf bifurcation. Limit cycles in driven-dissipative models have been observed before e.g. in spin-1/2 systems [145, 146] and with Bose-Einstein condensates in optical cavities, see e.g. References [110, 147] and in driven QED-cavity arrays [148].

The transition into the stable SR_{UNI}-phase is discontinuous and we can solve Eqs. (3.6-3.9) in the long-time limit to obtain the photon condensate as

$$|\langle a\rangle|^2 = \frac{\pm\sqrt{J^4(\Delta+J)^2(\Delta-2V)^2}+J^2(\Delta+J)(2V-\Delta)}{4J\omega_0(J+2V)^2} + O(\gamma^2)\ , \tag{3.43}$$

where the coupling constant $J(\kappa,\omega_0)$ is given by Eq. (3.74). Here the ± sign indicates that there are two branches of which only one is stable. Stable solutions (SR_{UNI}) are depicted in Fig. 3.6a. In the limit of weak atomic noise, it can be seen from Eq. (3.43) that a stable solution to zeroth-order in γ must satisfy $V > \Delta/2$. The phase boundary between the two oscillating phases depicted in Fig. 3.6 is obtained by comparing the oscillation amplitudes (in Fig. 3.6b) on the even vs. the odd sublattices in the long-time limit that result from direct integration of Eqs. (3.6-3.9).

Next, we turn our attention to the features of the phase diagram depicted in Fig. 3.7 where losses in the atomic channel can be strong. We analyze the oscillations of both atomic and photonic components in the long-time limit by explicit integration of Eqs. (3.6-3.9). Numerically we find persistent oscillations close to the (AFM+SR) region that are different on the even/odd sublattice, see Fig. 3.8. We determine the phase boundary for the(AFM+SR)-OSC phase depicted in Fig. 3.7 by sampling initial conditions for the atomic components on the Bloch sphere and then integrating the set of Eqs. (3.6-3.9) directly. The phase boundary is set by the parameters $(\Delta/\gamma, g/\gamma)$ for which the long-time limit is determined by the empty atom-cavity system ($\text{FP}_{\downarrow}$) for all initial conditions.

In Fig. 3.9 we track the behaviour of the amplitude of the oscillations as a function of g/γ and observe that the amplitudes decay continuously as the (AMR+SR) phase

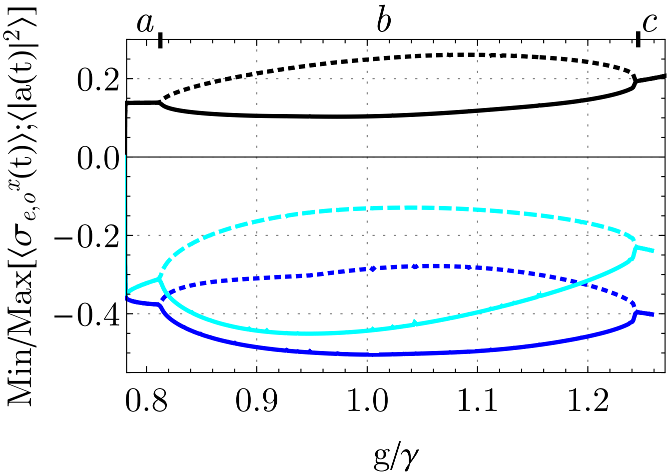

Figure 3.9.: Amplitudes of the oscillations in the (AFM+SR)-OSC phase. Dashed (solid) blue lines show max(min)[$\langle\sigma^x_{e,o}(t)\rangle$] and black lines show max(min)[$\langle|a(t)|^2\rangle$]. Data is obtained by extracting the minimum and maximum of the amplitudes of $\langle\sigma^x_{e,o}(t)\rangle$ and $\langle|a(t)|^2\rangle$ in a time interval chosen such that it contains several oscillations (if any are present) at long times. If the minimum and maximum coincide, the system settled into a steady state (a, c) corresponding to the (AFM+SR) phase, otherwise the system is in the (AFM+SR)-OSC limit cycle phase (b). Close to the (AFM+SR)-phase, the amplitudes decay continuously. Parameters: $(\omega_0/\gamma = 2.0, \Delta/\gamma = 0.15, \kappa/\gamma = 0.2, V/\gamma = 1.8)$

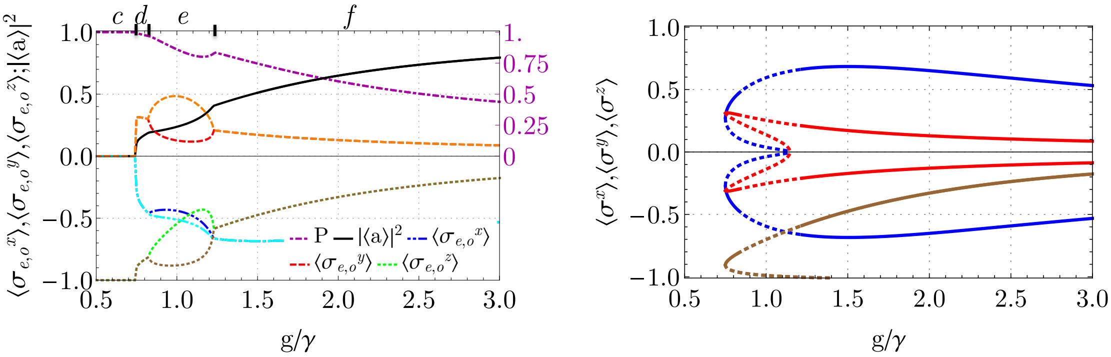

(a) (b)

Figure 3.10.: Non-monotonous behaviour of the order-parameters as the atom-light coupling g/γ is varied. The system changes discontinuously from the empty atom-cavity system (FP$_\downarrow$,c) into a homogeneous phase (SR$_{\text{UNI}}$,d) that becomes unstable towards an (AFM+SR,e) phase that disappears again in favor for an (SR$_{\text{UNI}}$,f) phase. On the right axis, the purity is shown that consistently decays, indicating the transition into a mixed state. (b) Stability analysis for homogeneous solutions as plotted in (a). (Unstable) stable, homogeneous solutions are plotted as (dotted) thick lines. The transition from the FP$_\downarrow$ state into the SR$_{\text{UNI}}$ state is discontinuous if $V/\gamma > 0$. Parameters: $(\omega_0/\gamma = 2.0, \Delta/\gamma = -0.1, \kappa/\gamma = 0.2, V/\gamma = 1.8)$

is approached. Numerically, we find no evidence that the (AFM+SR)-phase becomes unstable towards Hopf bifurcations meaning that stable limit cycles occur only outside the AFM+SR phase.

We continue our analysis by describing the behaviour of the magnetisations in the different domains of the phase diagram depicted in Fig. 3.7. In Fig. 3.10a we plot the magnetisation values in the steady-state for increasing the atom-light coupling g/γ. Starting in the empty atom-cavity, the system changes discontinuously into a $\mathrm{SR}_{\mathrm{UNI}}$ phase that soon after becomes unstable towards even/odd sublattice magnetisations (AFM+SR) that disappear again in favour for a re-entrance of the $\mathrm{SR}_{\mathrm{UNI}}$ phase. We depict the homogeneous solutions $\mathrm{SR}_{\mathrm{UNI}}$ and their stability in Fig. 3.10b. We find that for $V/\gamma > 0$ the transition into the Dicke superradiance state is discontinuous.

We note that with $\gamma \neq 0$ the length of the semi-classical Bloch vector $\langle \boldsymbol{S}_{e,o} \rangle = \left(\langle \sigma^x_{e,o} \rangle, \langle \sigma^y_{e,o} \rangle, \langle \sigma^z_{e,o} \rangle \right)$, is not conserved any more and can shrink for increasing g/γ values. In equilibrium systems, an increase in the coupling parameter should stabilize the order in the steady-state, here we instead observe a non-monotonous behaviour where the 'order parameters' decay again after having reached a maximum value. We illustrate this decay by plotting the purity $P = \mathrm{Tr}[(\rho_e \otimes \rho_o)^2] = \mathrm{Tr}[\rho_e^2]\mathrm{Tr}[\rho_o^2]$ of the density matrix alongside the magnetisations. Both quantities decay as g/γ is increased. In the case of the purity P this indicates the decay towards a purely mixed state.

The phase transitions in and out of the (AFM+SR) phases are continuous, whereas transitions from the empty atom-cavity system into the $\mathrm{SR}_{\mathrm{UNI}}$ phase are discontinuous for $V/\gamma > 0$, see Fig. 3.10. On a mean-field level we observe bistabilities in the phase diagram depicted in Fig. 3.7. These could be induced by the nonlinearities in the mean-field master equations or can hint at non-trivial behaviour induced by fluctuations where the system in the long-time limit switches between the two steady-states predicted on a mean-field level, see [149] and also chapter 4. Mostly, bistabilities occur with the empty atom-cavity system ($\mathrm{FP}_{\downarrow}$). The corresponding stability line can be calculated analytically from the stability matrix and we find that it is independent of V since the Rydberg-dressed interaction is conditioned on population in the excited state, see Eq. (3.41). The size of the (AFM+SR) region instead does depend on V.

3.4.4. Ideas for quantum-optical implementation of the model

> We seek a quantum optical implementation which realizes the Hamiltonian in Eqs. (3.1,3.2). At the core of our model is the "two dipoles in-one" unit depicted in Fig. 3.11. As described in the caption, Dipole 1 could be created by weakly admixing a relatively low quantum number Rydberg level ($n \sim 30$) to a set of long-lived hyperfine split states $|1\rangle$ and $|0\rangle$. Dipole 2 couples to the cavity via two far-detuned, excited states $|d\rangle, |e\rangle$. In this section, we present in how the (effective) set of parameters $\{\omega_0, \Delta, V, g\}$ can be expressed through the set of external laser parameters $\{\Delta_d, \Delta_e, g_d, g_e, \Omega_d, \Omega_e, \Omega_{Ryd}\}$ as presented in Fig. 3.11 and as such becomes entirely tunable, as shown in the main result of this section, see Eq. (3.63).

The atomic levels we consider to realize an effective spin system could be the hyperfine-structure manifold of the ground states of ^{87}Rb. Typically this is the $5^2S_{1/2}$ state split into the $F = 1$ and the $F = 2$ manifold such that $|0\rangle = |\downarrow\rangle = |F = 1, m_F = -1\rangle$ and $|1\rangle = |\uparrow\rangle = |F = 2, m_F = -2\rangle$. Here, cavity-assisted Raman transitions couple the $(|0\rangle, |1\rangle)$ ground-states via adiabatic elimination of the detuned excited states $(|d\rangle, |e\rangle)$ to the cavity [26, 49]. Then, the cavity is (indirectly) pumped with photons from the transversal pumping-laser that scatter off the atoms and populate the cavity mode. In that way, the pump is

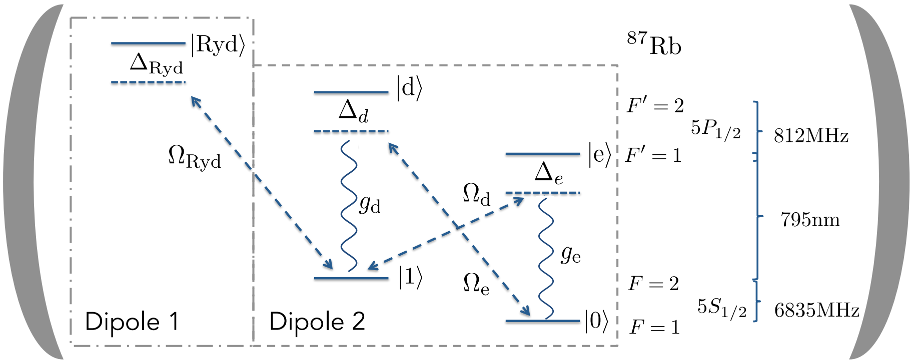

Figure 3.11.: Blueprint for a quantum optical implementation of two dipoles in one atomic qubit that allow engineering of the spin-spin interation V and the spin-light coupling g appearing in the Hamiltonians of Eqs. (3.1,3.2). The effective spin degree of freedom is encoded in the levels $|1\rangle$ and $|0\rangle$. The resonator mirrors (grey shades) stands symbollically for the mirrors of the cavity and the depicted level scheme corresponds to the ground state manifold $5S_{1/2}$ and the first excited state manifold $5P_{1/2}$ of ^{87}Rb including their typical frequency splittings. *Dipole 1*: A dressing laser can weakly admix a Rydberg level to a ground-state $|1\rangle \to |1\rangle + \frac{\Omega_{\mathrm{Ryd}}}{2\Delta_{\mathrm{Ryd}}}|\mathrm{Ryd}\rangle = |\tilde{1}\rangle$. We want the resulting effective potential $V^{\mathrm{eff}}_{\ell m}$ between $|\tilde{1}\rangle_\ell$ and $|\tilde{1}\rangle_m$ states to be predominantly nearest-neighbor in a square lattice spaced by an optical wavelength. Complex potentials including angle-dependencies can be realized [50, 120, 121]. *Dipole 2*: Cavity-assisted transitions with a double Raman scheme [26] have been explained in detail in Sec. 1.1, in essence they provide a tunable spin-light coupling g(Ω_e, Ω_d), where Ω_e, Ω_d are external Rabi frequencies of the driving laser. This provides the infinite-range coupling between all the spins.

"hidden" in the atom-photon coupling g as $g(\Omega)$ depends on the Rabi frequency of the external driving laser.

Dipole 1 in Fig. 3.11, consists of admixing a small part of a Rydberg state to the state $|1\rangle$ that is also coupled to the cavity.

To first-order in perturbation theory of the driving, the ground-state becomes dressed with a small fraction of the excited state $|\tilde{1}\rangle \approx |1\rangle + \frac{\Omega_{\mathrm{Ryd}}}{2\Delta_{\mathrm{Ryd}}}|\mathrm{Ryd}\rangle + \mathcal{O}\left(\frac{\Omega_{\mathrm{Ryd}}}{2\Delta_{\mathrm{Ryd}}}\right)^2$, where Ω_{Ryd} is the Rabi-frequency and Δ_{Ryd} is the detuning from the Rydberg level. Ground-states $\{|\tilde{1}\rangle_i, |\tilde{1}\rangle_j\}$ interact then with a dressed Rydberg interaction that can be controlled by changing $(\Omega_{\mathrm{Ryd}}, \Delta_{\mathrm{Ryd}})$ of the dressing laser [150, 151, 152, 153]. Dressing schemes for Rydberg atoms on optical lattices have recently been experimentally realised [50] and the effective Rydberg potential depends strongly on the chosen Rydberg states [120].

In a suitably chosen rotating frame of reference the parameters appearing in the Hamiltonian Eqs. (3.1,3.2), can be expressed as follows. For the spin longitudinal field Δ and the effective cavity frequency ω_0, we have

$$\Delta = -\Delta_1 + \frac{\Omega^2_{\mathrm{Ryd}}}{4\Delta_{\mathrm{Ryd}}}\,, \qquad \omega_0 = N\frac{g_e^2}{\Delta_e} + \omega_a\,, \tag{3.44}$$

with ω_a and Δ_1 defined in Eq. (3.59). The coherent coupling to the cavity can be tuned by the two external lasers $\Omega_{d,e}$ [26]:

$$g = \sqrt{N}\frac{g_{d,e}\Omega_{d,e}}{2\Delta_{d,e}}, \quad \frac{\Omega_d}{4\Delta_d} = \frac{\Omega_e}{4\Delta_e}, \quad \frac{g_d^2}{\Delta_d} = \frac{g_e^2}{\Delta_e}\,. \tag{3.45}$$

Finally, the Rydberg-mediated potential takes the general form [152]

$$V^{\mathrm{eff}}_{\ell m} = \left(\frac{\Omega_{\mathrm{Ryd}}}{2\Delta_{\mathrm{Ryd}}}\right)^4 \frac{C_6}{r^6_{\ell m} + R^6_c} \,, \tag{3.46}$$

and the V appearing in Eq. (3.1) evaluates Eq. (3.46) at a fixed $r_{\ell m}$ equal to the distance between neighboring lattice sites such that the tails of the interaction potential can be neglected and the interaction is effectively step-like. R_c is the critical radius defined by $2\Delta_{\mathrm{Ryd}} \equiv V(R_c)$ which yields $R_c = \left(\frac{C_6}{2\hbar|\Delta_{\mathrm{Ryd}}|}\right)^{1/6}$. At smaller distances $r_{\ell m} < R_c$, dressing to doubly excited states becomes ineffective because of the large detuning $|\Delta_{\mathrm{Ryd}}| + V_{\ell m}$. The soft-core potentials contain a number of additional resonances at $r_{ij} \ll R_c$, which are undesirable to realise clean interactions. To ensure the interacting atoms in an optical lattice interact via the clean van-der-Waals tail, it is more advantageous to address relatively low-lying Rydberg states with principal quantum numbers $n \sim 30$, as R_c can then also shrink down to optical wavelengths. Additionally, we comment that complementary to optical lattices, two-dimensional arrays of microtraps have already been used [154] to trap single ^{87}Rb atoms with lattice spacings $\sim \mu m$.

In Sec. 3.5.4, we present an overview of the relevant energy and time scales including a discussion on problematic Rydberg decays.

Transformation of fully time-dependent model into rotating frame

Here, we detail calculations where we derive how the parameters of the Hamiltonians $H_{\mathrm{spin-light}}$ given by Eq. (3.2) and H_{spin} given by Eq. (3.1) are related to tunable laser parameters that result from the optical implementation shown in Fig. 3.11. The Hamiltonian we consider is of the form

$$H = H_{\mathrm{cav}} + H_{\mathrm{atoms}} + H(t)_{\mathrm{pump}} + H_{\mathrm{atom-light}} + H_{\mathrm{atom-atom}} \tag{3.47}$$

$$H_{\mathrm{cav}} = \omega_0 a^\dagger a \tag{3.48}$$

$$H_{\mathrm{atoms}} = \sum_{\ell=1}^{N} \omega_d \left|d\right\rangle_\ell \left\langle d\right| + \omega_e \left|e\right\rangle_\ell \left\langle e\right| + \omega_{\mathrm{Ryd}} \left|\mathrm{Ryd}\right\rangle_\ell \left\langle \mathrm{Ryd}\right| + \omega_1 \left|1\right\rangle_\ell \left\langle 1\right| \tag{3.49}$$

$$H_{\mathrm{pump}}(t) = \sum_{\ell=1}^{N} \frac{\Omega_e}{2} e^{-i\omega_{\Delta e} t} \left|e\right\rangle_\ell \left\langle 1\right| + \frac{\Omega_d}{2} e^{-i\omega_{\Delta d} t} \left|d\right\rangle_\ell \left\langle 0\right| + \frac{\Omega_{\mathrm{Ryd}}}{2} e^{-i\omega_{\Delta r} t} \left|\mathrm{Ryd}\right\rangle_\ell \left\langle 1\right| + \mathrm{h.c.} \tag{3.50}$$

$$H_{\mathrm{atom-light}} = \sum_{\ell=1}^{N} \left(g_d \left|d\right\rangle_\ell \left\langle 1\right| + g_e \left|e\right\rangle_\ell \left\langle 0\right|\right) a + \mathrm{h.c.} \tag{3.51}$$

$$H_{\mathrm{atom-atom}} = \sum_{\langle \ell m\rangle} V_{\ell m} \left(\left|\mathrm{Ryd}\right\rangle_\ell \left\langle \mathrm{Ryd}\right|\right) \left(\left|\mathrm{Ryd}\right\rangle_m \left\langle \mathrm{Ryd}\right|\right) \tag{3.52}$$

The frequencies $(\omega_d, \omega_e, \omega_{\mathrm{Ryd}}, \omega_1)$ refer to the atomic levels labelled by the sequence $(d, e, \mathrm{Ryd}, 1)$ and are measured relative to the atomic level $|0\rangle$. Correspondingly, the frequencies $(\omega_{\Delta d}, \omega_{\Delta e}, \omega_{\Delta \mathrm{r}})$ refer to the laser frequencies of the pump-terms. Here, ω_0 denotes the bare cavity resonance. We have assumed homogeneous pumping of the atoms from the side $\Omega_{(d,e);\ell} \approx \Omega_{(d,e)}$ and a homogeneous coupling of the light field to the atoms $g_{(d,e);\ell} \approx g_{(d,e)}$ which is ensured by engineering the intracavity lattice commensurate with the cavity mode function as shown in Fig. 3.1. We eliminate the explicit time-dependence by switching into a rotating frame such that the new Hamiltonian reads

$$\tilde{H} = U^\dagger H U - U^\dagger i\partial t U, \quad U(t) = \exp\left(-iH_0 t\right) \tag{3.53}$$

$$\tag{3.54}$$

where the Hamiltonian H_0 is given as

$$\begin{aligned}
H_0 = &\left(\omega_{\Delta d} - \omega_1'\right) a^\dagger a \\
&+ \sum_{\ell=1}^{N} \Big[\left(\omega_{\Delta e} + \omega_1'\right) |e\rangle_\ell \langle e| + \omega_{\Delta d} |d\rangle_\ell \langle d| + \omega_1' |1\rangle_\ell \langle 1| + \left(\omega_{\text{Ryd}} + \omega_1'\right) |\text{Ryd}\rangle_\ell \langle \text{Ryd}| \Big]
\end{aligned} \tag{3.55}$$

Cross coupling lasers need to be tuned such that they are strongly detuned from the levels $(|d\rangle, |e\rangle)$ which can then be eliminated adiabatically. Under the condition $|\Delta_{d,e}| \gg (\kappa, \gamma, \Omega_{d,e})$, the dynamics of the system are now described by an effective Hamiltonian $\tilde{H} = \tilde{H}_{\text{Ryd}} + \tilde{H}_{10} + \tilde{H}_{\text{L}}$:

$$\tilde{H}_L = \sum_{\ell=1}^{N} \frac{\Omega_{\text{Ryd}}}{2} \left(|\text{Ryd}\rangle_\ell \langle 1| + |1\rangle_\ell \langle \text{Ryd}|\right) \tag{3.56}$$

$$\tilde{H}_{\text{Ryd}} = - \Delta_{\text{Ryd}} \sum_{\ell=1}^{N} |\text{Ryd}\rangle_\ell \langle \text{Ryd}| + \sum_{\langle \ell m \rangle} V_{\ell m} \left(|\text{Ryd}\rangle_\ell \langle \text{Ryd}|\right) \left(|\text{Ryd}\rangle_m \langle \text{Ryd}|\right) \tag{3.57}$$

$$\begin{aligned}
\tilde{H}_{10} = &\omega_a a^\dagger a + \sum_{\ell=1}^{N} \Bigg[\left(\Delta_1 + \frac{\Omega_e^2}{4\Delta_e}\right) |1\rangle_\ell \langle 1| + \frac{\Omega_d}{4\Delta_d} |0\rangle_\ell \langle 0| \\
&+ \frac{1}{2} \left(\frac{g_e \Omega_e}{\Delta_e} |0\rangle_\ell \langle 1| a^\dagger + \frac{g_d \Omega_d}{\Delta_d} |1\rangle_\ell \langle 0| a^\dagger + \text{h.c.} \right) + \left(\frac{g_e^2}{\Delta_e} |0\rangle_\ell \langle 0| + \frac{g_d^2}{\Delta_d} |1\rangle_\ell \langle 1| \right) a^\dagger a \Bigg]
\end{aligned} \tag{3.58}$$

where we have used the following frequencies

$$\begin{aligned}
\omega_a &= \omega_0 - \left(\omega_{\Delta d} - \omega_1'\right), \\
\Delta_{\text{Ryd}} &= -[\omega_{\text{Ryd}} - \left(\omega_{\Delta r} + \omega_1'\right)] \\
\Delta_1 &= \omega_1 - \omega_1', \\
2\omega_1' &= \omega_{\Delta d} - \omega_{\Delta e} \, .
\end{aligned} \tag{3.59}$$

In a next step, high-lying Rydberg states are admixed to the ground-states $|1\rangle_\ell$ to realise a Rydberg-dressed interaction between the states $|\tilde{1}\rangle = |1\rangle + \frac{\Omega_{\text{Ryd}}}{2\Delta_{\text{Ryd}}} |\text{Ryd}\rangle + \mathcal{O}\left(\frac{\Omega_{\text{Ryd}}}{2\Delta_{\text{Ryd}}}\right)$. Typically, two-body Born-Oppenheimer potentials as a function of the distance r_{ij} between two Rydberg levels are obtained by diagonalising Hamiltonians of the form $H_L + H_{\text{Ryd}}$ in a two-atom basis [153]. A detailed calculation that includes coupling to the complicated level structure is thus highly non-trivial. Focusing on the weak-dressing regime $\Omega_{\text{Ryd}}/\Delta_{\text{Ryd}} \ll 1$ and red-detuning of the dressing laser we follow the many-body perturbation expansion performed in Ref. [152] to obtain the effective Hamiltonian for the Rydberg part to leading order in the corrections

$$\begin{aligned}
\tilde{H}_{\text{Ryd}} &= -\frac{\Omega_{\text{Ryd}}^2}{4\Delta_{\text{Ryd}}} \sum_{\ell=1}^{N} |\tilde{1}\rangle_\ell \langle \tilde{1}| + \frac{1}{2} \left(\frac{\Omega_{\text{Ryd}}}{2\Delta_{\text{Ryd}}}\right)^4 \sum_{i \neq j} \frac{C_6}{r_{ij} + R_c^6} \left(|\tilde{1}\rangle_i \langle \tilde{1}|\right) \left(|\tilde{1}\rangle_j \langle \tilde{1}|\right) \\
&= -\frac{\Omega_{\text{Ryd}}^2}{4\Delta_{\text{Ryd}}} \sum_{\ell=1}^{N} |\tilde{1}\rangle_\ell \langle \tilde{1}| + \frac{1}{2} \sum_{i \neq j} V_{\text{ij}}^{\text{eff}} \left(|\tilde{1}\rangle_i \langle \tilde{1}|\right) \left(|\tilde{1}\rangle_j \langle \tilde{1}|\right)
\end{aligned} \tag{3.60}$$

It can be seen that the dressed states $|\tilde{1}\rangle$ acquire additional light-shifts $\sim \Omega_{\text{Ryd}}^2/(4\Delta_{\text{Ryd}})$ and the Rydberg potential is tunable by changing $(\Omega_{\text{Ryd}}, \Delta_{\text{Ryd}})$. Here, V_{ij}^{eff} and R_c are defined in Eq. (3.46). We now replace $|1\rangle$ with the dressed Rydberg state $|\tilde{1}\rangle$ everywhere in Eq. (3.58). With

$$\sum_{\ell=1}^{N} |1\rangle_\ell \langle 1| = \frac{1}{2}\sum_{\ell=1}^{N} \left(|1\rangle_\ell \langle 1| - |0\rangle_\ell \langle 0| + N\right) = \frac{1}{2}\sum_{\ell=1}^{N} \sigma_\ell^z + \frac{N}{2} \tag{3.61}$$

$$\sum_{\ell=1}^{N} |0\rangle_\ell \langle 0| = -\frac{1}{2}\sum_{\ell=1}^{N} \left(|1\rangle_\ell \langle 1| - |0\rangle_\ell \langle 0| - N\right) = -\frac{1}{2}\sum_{\ell=1}^{N} \sigma_\ell^z + \frac{N}{2} \tag{3.62}$$

the Hamiltonian is now cast into the form:

$$\begin{aligned}
\tilde{H} =& a^\dagger a \left[\frac{N}{2}\left(\frac{g_e^2}{\Delta_e} + \frac{g_d^2}{\Delta_d}\right) + \omega_a\right] \\
&+ \sum_{\ell=1}^{N} \sigma_\ell^z \frac{1}{2}\left[\left(\frac{\Omega_d^2}{4\Delta_d} - \frac{\Omega_e^2}{4\Delta_e}\right) + \Delta_1 - \frac{\Omega_{\mathrm{Ryd}}^2}{4\Delta_{\mathrm{Ryd}}} + \frac{1}{2}\sum_{m(m\neq\ell)}^{N} V_{m\ell}^{\mathrm{eff}}\right] \\
&+ \sum_{\ell=1}^{N} \sigma_\ell^z \frac{1}{2}\frac{1}{N}\left(\frac{g_d^2}{\Delta_d} - \frac{g_e^2}{\Delta_e}\right) a^\dagger a + \sum_{\ell=1}^{N}\left[\frac{\lambda_d}{\sqrt{N}}\left(\sigma_\ell^+ a^\dagger + \sigma_\ell^- a\right) + \frac{\lambda_e}{\sqrt{N}}\left(\sigma_\ell^+ a + \sigma_\ell^- a^\dagger\right)\right] \\
&+ \frac{1}{2}\sum_{i\neq j} V_{\mathrm{ij}}^{\mathrm{eff}} \frac{\sigma_i^z}{2}\frac{\sigma_j^z}{2} ,
\end{aligned} \tag{3.63}$$

with effective spin-photon couplings (set equal and denoted by g in Eq. (3.45))

$$\lambda_{d,e} = \sqrt{N}\frac{g_{d,e}\Omega_{d,e}}{2\Delta_{d,e}} . \tag{3.64}$$

To generate AFM ordering it is advantageous for the effective longitudinal field corresponding to the second term in the first line in Eq. (3.63) to be negative.

We analyse typical orders of magnitudes. The hyperfine structure splitting in the ground state manifold is $\omega_1 = 2\pi \times 6.835\mathrm{GHz}$. Typically the cavity-assisted Raman transitions are achieved by coupling to the first excited state manifold that is split into a fine-structure $5^2P_{1/2}$ with $F' = 2$ and $F' = 1$ that for this choice is on the order of 812MHz. The external driving lasers are separated by approximately twice the ground-state hyperfine splitting $\omega_{1'} = \frac{1}{2}\left(\omega_{\Delta d} - \omega_{\Delta e}\right) \sim \omega_1$ such that $\Delta_1 = \omega_1 - \omega_{1'} \sim$MHz. For weakly admixing the Rydberg state to the groundstate manifold $|\uparrow\rangle$ the detuning from the Rydberg state Δ_{Ryd} must satisfy $\Omega_{\mathrm{Ryd}} \ll \Delta_{\mathrm{Ryd}}$. Typical Rabi frequencies for the drive to the Rydberg level are $\Omega_{\mathrm{Ryd}} \sim$MHz. The detuning from the Rydberg level now has a frequency component $\omega_{1'}$ from the Raman-scheme: $\Delta_{\mathrm{Ryd}} = -[\omega_r - (\omega_{\Delta r} + \omega_{1'})]$. This can take the usual detuning Δ_{Ryd} far above the MHz regime which makes $\Delta_{\mathrm{Ryd}} \ggg \Omega_{\mathrm{Ryd}}$. The longitudinal field $\left(\Delta_1 - \frac{\Omega_{\mathrm{Ryd}}^2}{4\Delta_{\mathrm{Ryd}}}\right)$ for $\Omega_d = \Omega_e$ and $\Delta_d = \Delta_e$ is in the MHz range and can in principle be tuned positive and negative.

3.5. Discussion of results

3.5.1. Comparison with a $T = 0$ equilibrium spin mean-field solution

Here we analyze a $T = 0$ equilibrium spin model with the same phases as Fig. 3.2 upon identifying one spin interaction constant with cavity parameters. Specifically, we analyze Hamiltonians $H_{\mathrm{spin-light}}$ Eq. (3.2) and H_{spin} Eq. (3.1) within a (standard) equilibrium mean-field theory for spins. We explain why the equilibrium and non-equilibrium phase diagram can be mapped onto each other in this specific case. Adiabatically eliminating the cavity photons typically results in a coherent and a dissipative term for the atomic sector. However, here only the coherent part (infinite range atom-atom interaction) survives and the dissipative contribution is exactly cancelled due to the presence of both co- and counter-rotating terms $\sim (a + a^\dagger)(\sigma^+ + \sigma^-)$ in the atom-light interaction. Dynamics and statistics remain different in the non-equilibrium case, however.

First, we integrate out the quadratic photon terms which yields an effective Hamiltonian that features a ferromagnetic all-to-all atom-atom coupling J. The connection to the non-equilibrium system is then made explicit by letting J depend on κ as pointed out below. The Hamiltonian we consider is written as

$$\tilde{H} = -\frac{J}{N}\sum_{ij}\sigma_i^x\sigma_j^x - \frac{\Delta}{2}\sum_i \sigma_i^z + \frac{1}{2}V\sum_{\langle \ell m\rangle}^{N}\sigma_\ell^{ee}\sigma_m^{ee} \tag{3.65}$$

Where the 1/2 in front of the Rydberg interaction avoids overcounting. We cast the last terms into a spin-language with the replacement $\sigma_\ell^{ee} = 1/2(1+\sigma_\ell^z)$. We decouple the interaction terms in mean-field theory by expanding the operators around their mean-value to linear order in fluctuations. We neglect all second-order fluctuation terms and write the effective spin-Hamiltonian in a form that resembles the interaction of the spin-variables with an effective, local magnetic field that needs to be determined self-consistently and represents the mean field from the neighbouring spins. Ignoring constant energy shifts, the full mean-field Hamiltonian assuming $d = 2$-spatial dimensions is given as

$$\tilde{H}^{\mathrm{MF}} = -V\frac{N}{2}\langle\sigma^z_{\mathrm{even}}\rangle\langle\sigma^z_{\mathrm{odd}}\rangle + NJ\langle\sigma^x\rangle^2 + \sum_{i\in even}\boldsymbol{B}^{\mathrm{even}}\boldsymbol{\sigma}_i + \sum_{j\in odd}\boldsymbol{B}^{\mathrm{odd}}\boldsymbol{\sigma}_j \tag{3.66}$$

Here, we have already accounted for an *even/odd* sub-lattice asymmetry in the $z-$components. We use the vector of Pauli matrices as $\boldsymbol{\sigma} = (\sigma^x, \sigma^y, \sigma^z)^T$ and define the local magnetic fields as

$$\boldsymbol{B}^{\mathrm{even/odd}} = \left(\left[\langle\sigma^z_{\mathrm{odd/even}}\rangle V + (V - \Delta/2)\right]\hat{\boldsymbol{z}} + 2J\langle\sigma^x\rangle\hat{\boldsymbol{x}}\right) \tag{3.67}$$

We evaluate the partition sum

$$Z = \mathrm{Tr}\left[e^{-\beta\tilde{H}^{\mathrm{MF}}}\right] \tag{3.68}$$

$$= 2^N\left[\cosh\left(|\boldsymbol{B}^{\mathrm{even}}|\right)\cosh\left(|\boldsymbol{B}^{\mathrm{odd}}|\right)\right]^{N/2}\exp\left[V\frac{N}{2}\beta\langle\sigma^z_{\mathrm{even}}\rangle\langle\sigma^z_{\mathrm{odd}}\rangle - N\beta J\langle\sigma^x\rangle^2\right] \tag{3.69}$$

to obtain the self-consistency equations for the order-parameters

$$\phi = \frac{\langle\sigma^x_{\mathrm{even}}\rangle + \langle\sigma^x_{\mathrm{odd}}\rangle}{2} = \frac{1}{2}\tanh\left(\beta|\boldsymbol{B}^{\mathrm{odd}}|\right)\frac{B_x^{\mathrm{odd}}}{|\boldsymbol{B}^{\mathrm{odd}}|} + \frac{1}{2}\tanh\left(\beta|\boldsymbol{B}^{\mathrm{even}}|\right)\frac{B_x^{\mathrm{even}}}{|\boldsymbol{B}^{\mathrm{even}}|} \tag{3.70}$$

$$\rho = \frac{\langle\sigma^z_{\mathrm{even}}\rangle - \langle\sigma^z_{\mathrm{odd}}\rangle}{2} = \frac{1}{2}\tanh\left(\beta|\boldsymbol{B}^{\mathrm{even}}|\right)\frac{B_z^{\mathrm{even}}}{|\boldsymbol{B}^{\mathrm{even}}|} - \frac{1}{2}\tanh\left(\beta|\boldsymbol{B}^{\mathrm{odd}}|\right)\frac{B_z^{\mathrm{odd}}}{|\boldsymbol{B}^{\mathrm{odd}}|} \tag{3.71}$$

$$\rho_0 = \frac{\langle\sigma^z_{\mathrm{even}}\rangle + \langle\sigma^z_{\mathrm{odd}}\rangle}{2} = \frac{1}{2}\tanh\left(\beta|\boldsymbol{B}^{\mathrm{even}}|\right)\frac{B_z^{\mathrm{even}}}{|\boldsymbol{B}^{\mathrm{even}}|} + \frac{1}{2}\tanh\left(\beta|\boldsymbol{B}^{\mathrm{odd}}|\right)\frac{B_z^{\mathrm{odd}}}{|\boldsymbol{B}^{\mathrm{odd}}|} \tag{3.72}$$

Where ρ is the staggered magnetisation and ρ_0 is the average magnetisation in the z direction. The magnetic order parameter ϕ measures the magnetisation in x-direction and $\beta = 1/T$ is the inverse temperature. We denote the free energy per spin in the zero temperature limit $T \to 0$ as

$$f = \frac{F}{N}\bigg|_{T\to 0} = -\frac{T}{N}\log(Z)\bigg|_{T\to 0} = \frac{1}{2}V\left(\rho^2 - \rho_0^2\right) + J\phi^2 \\ - \frac{1}{2}\left(\sqrt{\left(V(\rho_0 - \rho) + V - \frac{\Delta}{2}\right)^2 + 4J^2\phi^2} + \sqrt{\left(V(\rho + \rho_0) + V - \frac{\Delta}{2}\right)^2 + 4J^2\phi^2}\right) \tag{3.73}$$

We can determine the zero-temperature phase-diagram by solving the coupled set of Eqs. $(3.70 - 3.72)$ numerically and retain only the solutions with the lowest free-energy according to Eq. (3.73). We obtain the splitting in the $(\langle\sigma^x_{\text{even}}\rangle, \langle\sigma^x_{\text{odd}}\rangle)$ components by using Eq. (3.12). We find that we can map the equilibrium phase-diagram to the phase diagram obtained by calculating the non-equilibrium steady-states (see Fig. 3.2) if we identify the ferromagnetic exchange coupling as

$$J(g,\kappa) = \frac{4g^2\omega_0}{\omega_0^2 + \kappa^2} \tag{3.74}$$

This coupling is inferred from solving for the steady-state values of the photons (see Eq. (3.9)) which is given as $g\left(\langle a\rangle + \langle a^\dagger\rangle\right) = -\frac{1}{2}g\,\langle\sigma^x_{\text{even}} + \sigma^x_{\text{odd}}\rangle\left(\frac{g}{\omega - i\kappa} + \frac{g}{\omega + i\kappa}\right) \propto J(g,\kappa)$. Allowing the interpretation that the photonic losses with rate κ weaken the atom-atom couplings.

3.5.2. Beyond mean-field effects

Our analysis is based on mean-field theory and in this section we briefly discuss effects not captured by our approach and alternative theoretical approaches used in the literature.

Several studies investigated effects beyond mean field in driven-dissipative lattice models that allow to acquire some intuition for the effect of correlations and fluctuations and for the validity of single-site mean-field studies in driven-lattice models out of equilibrium. Specifically, various numerical techniques such as variational approaches [155, 156], cluster models [148, 157], matrix product states [130], or quantum trajectories [149, 158] can help to shed light on the effects of correlations and fluctuations in the steady-state. However, most of these studies have focussed on a single short-range interaction, whereas here we investigated a combination of both short range spin-spin interactions that compete with infinite range ferromagnetic interactions.

The most dramatic modifications of the mean-field behaviour can be expected in one-dimensional systems. First, the loss processes will lead to a noise-induced effective temperature for the atomic spins [91, 159]. We thus expect fluctuations to destroy the AFM long-range ordered phases in Fig. 3.2 for a 1D spin array. Despite the absence of true long-range order in a one-dimensional system, even-odd correlations will be visible in the correlation functions and structure factors. The order parameter of the SR phases will remain stable, due to the effectively infinite range of the interaction, and dimensionality does not play a role. The comparison of mean-field calculations with numerical methods is strongly limited to low-dimensional and often to one-dimensional systems, especially when long-range correlations are to be taken into account which is why quantum simulators are proposed to model driven-lattice models [130].

Our analysis was, however, focusing on a two-dimensional setup where not only SR but also the AFM order can be stable in the presence of thermal and non-equilibrium fluctuations as domain walls cost an infinite amount of energy. For the two-dimensional spin array discussed in the present paper, we believe the qualitative features are robust, i.e. fluctuations might shift the phase transitions, induce a finite effective temperature, and further broaden the spectra but will not fully destroy the order. In particular the AFM+SR strip ending in the multi-critical point shown in Fig. 3.2 might get washed out and/or replaced by a first order transition. As an outlook, we investigate an antiferromagnetic phase transition in the presence of cavity-mediated fluctuations in App. B. However, driven-dissipative first order transitions are still not fully explored and are currently being investigated theoretically by looking at the low-frequency behaviour of the spectral gap in Liouville operators [86]. Most recently, the fluctuation dynamics in a bistable regime was observed experimentally for a driven system with nonlinear photon-photon interactions [29], we investigate genuine non-equilibrium fluctuation dynamcis theoretically in Sec. 4.5.

The appearance of two stable fixed points in the long-time limit dynamics of mean-field master equations are often a consequence of the nonlinear equations of motion [138]. Here, the actual steady-state depends on the initial conditions. As master-equations for density matrices typically have a unique steady-state [133], mean-field equations cannot predict the true stationary state of the system. Fluctuations are needed to explore the vicinity of the fixed points such that rare fluctuation events, comprised of a sequence of noise-kicks, allow the system to explore the entirety of phase space to identify the correct long-time-limit state. We resolve such a fluctuation dominated bistability regime in Chapter 4 with numerical simulations of classical Langevin equations. Moreover, bistable regions can also be washed out, when some form of spatial correlation for short-ranged models is taken into account [160, 155, 156].

Mean-field also does not capture all critical properties. It is interesting to know whether the oscillating phases shown in the phase diagram of Fig. 3.7 will survive fluctuations beyond mean field. Let us mention that in a recent experimental investigation of a super-radiance transition in a spin-1 Dicke model, oscillating phases have been observed (2017, [115]), where oscillations in the photon number are clearly identified as oscillations in the cavity output.

We are not aware of a developed technique, which can capture quantum fluctuations for large, far-from-equilibrium quantum spin systems coupled to the (potentially large) Hilbert space of one or multiple photon modes. Promising efforts in this direction invoke a fermion representation of the quantum spins on the closed-time Keldysh contour ([161, 162, 163] and references therein).

3.5.3. Validity analysis of the even-odd sublattice Ansatz

Here, we determine the linear stability of the homogeneous fixed points of Eqs. (3.75-3.79) against excitations with momentum $\boldsymbol{k}$, see e.g. References [164, 146]. In driven-dissipative lattice models with short-range interaction, orderings with incommensurate wavevectors have been observed [146, 165, 164, 166, 167]. This can happen because of an interplay of dissipation and a competition of different, momentum-dependent interactions such as in a driven spin-1/2 XYZ-model [124]. In driven-dissipative Bose-Hubbard-type lattice models (see e.g. Reference [167]) multimode photon fields are considered which have a finite momentum dependence. This is in contrast to our single-mode photon field that only couples to the zero-momentum component. The infinite-range atom-light and the antiferromagnetic spin-spin interaction suggest that the steady-states can either be uniform or that it can break the translational invariance of the system, respectively (see also Table 3.1). We thus expect and find that homogeneous mean field solutions are maximally unstable either at $(k_x, k_y) = (0, 0)$ or against excitations with $(k_x, k_y) = (\pi, \pi)$. We outline the analysis

below.
On a mean-field level, we write down the master-equation for every lattice site $\boldsymbol{n}$

$$\partial_t \langle \sigma^x_{\boldsymbol{n}}(t)\rangle = \langle \sigma^y(t)\rangle \, [\Delta - \frac{V}{2} \sum_{\langle \boldsymbol{nm}\rangle} (\langle \sigma^z_{\boldsymbol{m}}(t)\rangle + 1)] - \frac{\gamma}{2} \langle \sigma^x_{\boldsymbol{n}}(t)\rangle \tag{3.75}$$

$$\partial_t \langle \sigma^y_{\boldsymbol{n}}(t)\rangle = \langle \sigma^x_{\boldsymbol{n}}(t)\rangle \, [\frac{V}{2} \sum_{\langle \boldsymbol{nm}\rangle} (\langle \sigma^z_{\boldsymbol{m}}(t)\rangle + 1) - \Delta] - 2g[\langle a(t)\rangle + \langle a^\dagger(t)\rangle] \langle \sigma^z_{\boldsymbol{n}}(t)\rangle - \frac{\gamma}{2} \langle \sigma^y_{\boldsymbol{n}}(t)\rangle \tag{3.76}$$

$$\partial_t \langle \sigma^z_{\boldsymbol{n}}(t)\rangle = 2g[\langle a(t)\rangle + \langle a^\dagger(t)\rangle] \langle \sigma^y_{\boldsymbol{n}}(t)\rangle - \gamma(1 + \langle \sigma^z_{\boldsymbol{n}}(t)\rangle) \tag{3.77}$$

$$\partial_t \langle a(t)\rangle = -(\kappa + i\omega_0) \langle a(t)\rangle - ig \sum_{\boldsymbol{n}} \langle \sigma^x_{\boldsymbol{n}}(t)\rangle \tag{3.78}$$

$$\partial_t \langle a^\dagger(t)\rangle = -(\kappa - i\omega_0) \langle a(t)\rangle + ig \sum_{\boldsymbol{n}} \langle \sigma^x_{\boldsymbol{n}}(t)\rangle , \tag{3.79}$$

where $\boldsymbol{n}$ is a two-dimensional position vector on the square lattice. We check the validity of our even-odd sublattice approach by adding plane-wave perturbations to the uniform steady-states with the Ansatz

$$\langle \boldsymbol{\sigma_n}(t)\rangle = \langle \boldsymbol{\sigma}\rangle + \boldsymbol{\delta\sigma_n}(t), \quad \langle a(t)\rangle = \langle a\rangle + \delta a(t) \ , \tag{3.80}$$

where $\boldsymbol{\sigma} = (\langle \sigma^x\rangle, \langle \sigma^y\rangle, \langle \sigma^z\rangle)^T$ are the homogeneous solutions to Eqs. (3.75-3.79) and $\boldsymbol{k}$ contains the wave numbers of the perturbation. We Fourier transform according to

$$\boldsymbol{\delta\sigma_n(t)} = \frac{1}{N} \sum_{\boldsymbol{k}} e^{i\boldsymbol{k}\cdot\boldsymbol{n}} \boldsymbol{\delta\sigma_k}(t), \quad \boldsymbol{k} = (k_x, k_y)^T, \quad k_\ell = \frac{2\pi}{N} j, \quad j = 0, \ldots, N-1 \tag{3.81}$$

We linearize equations Eqs. (3.75-3.79) in the fluctuations $(\boldsymbol{\delta\sigma_k}(t), \delta a(t))$ and obtain a set of equations for each wave-vector $\boldsymbol{k}$

$$\partial_t \boldsymbol{\delta_k}(t) = \mathcal{D}_{\boldsymbol{k}} \boldsymbol{\delta_k}(t) \tag{3.82}$$

$$\boldsymbol{\delta_k}(t) = \left(\delta\sigma^x_{\boldsymbol{k}}(t), \delta\sigma^y_{\boldsymbol{k}}(t), \delta\sigma^z_{\boldsymbol{k}}(t), \delta a(t), \delta a^\dagger(t)\right)^T \tag{3.83}$$

with the stability matrix

$$\mathcal{D}_{\boldsymbol{k}} = \begin{pmatrix} -\frac{\gamma}{2} & \Delta - 2V(\langle \sigma^z\rangle + 1) & -V\langle \sigma^y\rangle t_{\boldsymbol{k}} & 0 & 0 \\ 2V(\langle \sigma^z\rangle + 1) - \Delta & -\frac{\gamma}{2} & V\langle \sigma^x\rangle t_{\boldsymbol{k}} - 2g(\langle a\rangle + \langle a^\dagger\rangle) & -2g\langle \sigma^z\rangle & -2g\langle \sigma^z\rangle \\ 0 & 2g(\langle a\rangle + \langle a^\dagger\rangle) & -\gamma & 2g\langle \sigma^y\rangle & 2g\langle \sigma^y\rangle \\ -ig\delta(\boldsymbol{k}) & 0 & 0 & -(\kappa + i\omega_0) & 0 \\ +ig\delta(\boldsymbol{k}) & 0 & 0 & 0 & -(\kappa - i\omega_0) \end{pmatrix} \tag{3.84}$$

here the momentum dependence is given by $t_{\boldsymbol{k}} = \cos(k_x) + \cos(k_y)$. The stability matrix has eigenvalues λ that depend on the wave number $\boldsymbol{k}$. The sign (±) of the real part of the eigenvalues determine if perturbations with momentum $\boldsymbol{k}$ decay (-) or grow (+) in time. If an eigenvalue acquires a positive real part, the uniform solution is unstable. The dynamics of the instability will be dominated by the wave vector $\boldsymbol{k}$ for which $\mathrm{Re}[\lambda]$ is at its maximum. Inspecting the matrix in Eq. (3.84), one can see that for an infinite system size, it depends continuously on the momentum $\boldsymbol{k}$ only through the Rydberg interaction which, on a mean-field level, favors ordering around $(k_x, k_y) = (\pi, \pi)$. The appearance of the delta function $\delta(\boldsymbol{k})$ shows that fluctuations in the coherent photon field only couple to uniform perturbations. In particular, there is no competition with other $\boldsymbol{k}$-dependent terms that could induce instabilities at finite momentum $\boldsymbol{k} \neq (0,0)$. In Fig. 3.12 we show where the homogeneous solution to Eqs. (3.75-3.79) (excluding the empty cavity, where $\langle \sigma^x\rangle =$

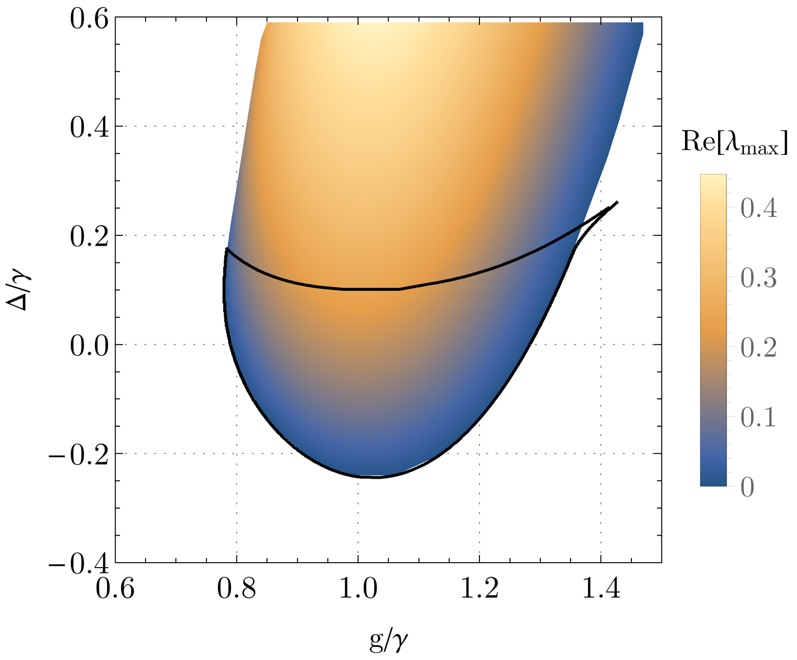

Figure 3.12.: Instability of the homogeneous solution against excitations with wavevector $(k_x, k_y) = (\pi, \pi)$, calculated from Eq. (3.84). The color scale shows the real part of the eigenvalue that is maximally unstable. Using the even-odd sublattice Ansatz we find the phase-boundary of stable anti ferromagnetic solutions (enclosed by the bold line) which are consistent with the stability analysis of the homogenous solutions. In the upper half-plane, where $\Delta > 0$, there is a region where the homogeneous solution is unstable against excitations with $(k_x, k_y) = (\pi, \pi)$ but the mean-field antiferromagnetic solutions are not stable above the bold line. The region around $(g/\gamma, \Delta/\gamma) \approx (1.4, 0.18)$ is bistable and can show steady-states of (AFM + SR) or $\mathrm{SR}_{\mathrm{UNI}}$ ordering. This plot is done for the same parameters as in the entire phase diagram that is given in Fig. 3.7

$\langle\sigma\rangle^y = 0$ and $\langle\sigma^z\rangle = -1$ and $\langle a\rangle$=0) in linear response is maximally unstable towards excitations at $(k_x, k_y) = (\pi, \pi)$. Within the even-odd sublattice Ansatz of Eqs. (3.6-3.9) we include the phase boundary of the stable (AFM + SR) solutions (solid line). Our results are fully consistent with each other. As it can be seen in Fig. 3.12, there is a region where the homogeneous solution is unstable towards excitation at $\boldsymbol{k} = (\pi, \pi)^T$ but where the corresponding antiferromagnetic solution is not a stable steady-state. The entire phase-diagram is given in Fig. 3.7.

3.5.4. Hierarchy of energy scales and problematic Rydberg decays

We now compare typical timescales associated to the Hamiltonian and Liouvillian dynamics given by Eqs. (3.1)-(3.4), using two recently performed experiments. One on a 2d Ising Hamiltonian with an interaction between Rydberg-dressed ground states, (see Eq. (3.1)) carried out by Zeiher *et al.* [50] and an experiment by Baden *et al.* [49] with cavity-assisted Raman processes to realise the Dicke superradiance transition with ultracold atoms coupled to a high-finesse optical cavity, as described with the Hamiltonian given by Eq. (3.2). The list of time and frequency scales is given in Table 3.3 and in Table 3.2, respectively. It can be seen that the Rydberg-dressed interaction V is relatively small compared to the other appearing energy scales. For an experimental realisation of

	$\gamma_{\mathrm{BB}}\beta^2/2\pi$	$\gamma_r\beta^2/2\pi$	$V/2\pi$	$\Delta^Z/2\pi$	$\kappa/2\pi$	$\Delta^B/2\pi$	$g_c/2\pi$	$\omega_0/2\pi$
kHz	0.003-0.020	0.06-0.45	0.1-1.8	27-64	100	50-100	50-150	100-300

Table 3.2.: Hierarchy of frequencies for all involved energy scales. The energy scales involving the spin-spin dynamics ($\gamma_{\mathrm{BB}}, \gamma_r, V, \Delta^Z$) are calculated from experiments by Zeiher *et al.* [50]. The energy scales ($\kappa, \Delta^B, g_c, \omega_0$) involving the spin-light and cavity dynamics are calculated from the experiments performed by Baden *et al.* [49]. Here, Δ^Z and Δ^B refer to the level splitting of the two-level atom and ω_0 is the effective cavity detuning. g_c refers to the critical atom-light coupling for the superradiance transition in the Singapore experiment. γ_{BB} and γ_r refer to black-body radiation induced decay of the Rydberg-state [168] and the decay time of the bare Rydberg state, respectively.

	$\tau_{\mathrm{BB}}/\beta^2$	τ_r/β^2	τ_V	τ_Δ^Z	τ_κ	τ_Δ^B	τ_{g_c}	τ_{ω_0}
μs	50880-361808	2200-15630	552-10472	15-36	10	6-20	10-20	3-10

Table 3.3.: Hierarchy of timescales for all involved processes calculated from table 3.2.

a phase with an even/odd asymmetry it would thus be required to increase the strength of interaction. This can be achieved by reducing the laser detuning to the bare Rydberg level. However, this will lead to higher inherited loss rates for the admixed state. Additionally, it could be possible to prepare an initial many-body state such that it is close to a state with an even/odd symmetry breaking. A scheme to prepare such states in extended Rydberg ensembles is in Ref. [169]. As indicated in Table 3.3, radiative losses set the longest timescale of the system. However, blackbody radiation induced losses can limit the coherence time in Rydberg-dressing schemes [50, 168, 170] as a single decay event can lead to avalanche-like losses of atoms from the trapping lattice. Rydberg atoms are also very sensitive to stray electric fields imposing additional restrictions on experimental setups to implement proper shielding from any other source of radiation. However, it was also pointed out [50], that such impurity Rydberg atoms could be eliminated in future experiments by using a laser quench before atom-loss occurs.

3.6. Conclusions and future directions

In this chapter we have presented research on a large array of self-interacting qubits trapped in an intra-cavity lattice interfaced with a single photon mode of an optical resonator. The point was to create a simple and yet experimentally relevant base case for a model of quantum magents with competing short- and long-range interactions in driven-dissipative systems that can be (approximately) solved.

Why do we believe this is needed? Because of a growing number of experimental platforms ranging from many-body quantum lattice models in optical cavities, superconducting circuits, photonic cavity arrays, Rydberg gases and cavities supporting multiple, degenerate modes that aim to scale up the number of atomic qubits and interface them with single- or even multimode cavity systems in an effort to realise new quantum phases resulting from competing, variable-range interaction potentials.

These systems often come with considerable complexity in their theoretical description in the face of large number of quantum spins, dynamical light fields, competing interactions with different range, motional degrees of freedom and additional external fields drive and dissipation and possibly, non-equilibrium fluctuations.

Our simple model has yielded some experimentally directly testable predictions: A regime where magnetic translation symmetry breaking and superradiance occur together, a new even-odd collective mode in the cavity spectrum, and oscillating solutions for both, the spin components and a coherent photon field.

Unfortunately, we were not able to solve even our simple model exactly; the Rydberg-mediated nearest-neighbour interaction does induce non-trivial quantum fluctuations between the spins and our non-equilibrium mean-field ansatz for the density matrix kept track of only the expectation values of the spin components on the even and odd sublattices, and the photon field, respectively. However, we have discussed possible beyond mean-field effects extensively in Sec. 3.5.2.

Modern experiments with Rydberg-dressed spin lattices in optical cavities are on track to check and refine the results we have obtained and there have been promising experimental realisations very recently (after the publication of this research) on spin-texture formation in a quantum gas coupled to an optical cavity [114] and oscillating cavity fields in a superradiant spin-1 Dicke model [115].

Chapter 4

First-Order Phase Transition in the Dicke model with collective loss

The Dicke model is the generic model for atom-light interactions of a laser-driven ensemble of two-level atoms with a single, quantized mode of radiation. In experimental realizations, the coherent exchange of excitations from the light-field and the many-body spin ensemble features dissipation due to e.g. atomic spontaneous emission and cavity photon loss. For the atoms, there are two channels of dissipation. The first is an uncorrelated decay of individual atomic excitations, spontaneous emission, and the second is a collective decay of an excitation that is shared by N atoms. In this chapter we analyse the interplay of strong collective and single-site spontaneous emission processes in the Dicke model.

In Sec. 4.3, we derive a many-body master equation for the dissipative Dicke model from the quantum Heisenberg-Langevin equations wherein it can be seen that the collective loss channel for atomic excitations induces a new non-linearity in the equations of motion that competes with the infinite range atom-atom interaction mediated by the cavity-photons. For strong collective losses, the conventional second-order phase transition from an empty to a macroscopic occupation of the cavity mode is replaced with a bistability regime, where an empty and a superradiant cavity are both stable steady-states under the same driving conditions. Close to the bicritical point, the dynamics of the system is captured by a Ginzburg-Landau potential that is derived from a power expansion of an effective slow mode.

In Sec. 4.4 we derive a non-thermal, markovian noise strength for the atom-photon system that can be derived in a Heisenberg-Langevin framework.
In Sec. 4.5 we show that, with noise, the system dynamics is described in terms of semiclassical, stochastic and nonlinear optical Bloch equations which for the infinite-range Dicke Model become exact in the large-N-limit. In the bistability regime, the noise renders the states metastable by inducing transitions between them. The absence of an effective free energy functional, however, necessitates to include fluctuation corrections with $\mathcal{O}(1/N)$ for finite $N < \infty$ to locate the non-thermal first-order phase transition between the superradiant and the empty cavity. The noise induces a genuine non-equilibrium dynamics and breaks detailed balance on a microscopic scale. However, due to the presence of an inversion symmetry, the noise trajectories are symmetry constrained and restore detailed balance on a macroscopic scale.

In Sec. 4.6 we numerically track the response of the system to a time-dependent drive of the atom-light coupling by evaluating the power law decay of hysteresis loops for finite number of atoms N. The present setup enables the possibility to study both in experiment and in theory far from equilibrium noise activation, bistability and hysteresis close to a first-order phase transition.

- This research is published as: *Dissipative Dicke model with collective atomic decay: Bistability, noise-driven activation, and the nonthermal first-order superradiance transition*
  J. Gelhausen and M. Buchhold, Phys. Rev. A **97**, 023807 (2018)
- This chapter contains the research presented in the above mentioned paper. We go beyond the published research content by including several additional sections, which are Sec. 4.3.1, Sec. 4.3.2,
  Sec. 4.3.3, Sec. 4.3.4, Sec. 4.5.2, and Sec. 4.6. We have also made several changes in the remaining sections. We have rewritten the summary of results presented at the beginning of this chapter and have rewritten parts of the introduction mainly to provide additional information and to update citations of related work that have meanwhile been published. In general, we added several new smaller paragraphs and figures mainly to provide more details and a more in-depth analysis of our results.
- Sections and paragraphs not listed above can be found almost identically in the above mentioned publication.

4.1. Introduction

Investigations of nonequilibrium phase transitions both theoretically and experimentally are set to strongly influence future research avenues especially in quantum optical systems, see also the general introduction to this thesis. We study such a driven-dissipative first-order phase transition in the paradigmatic Dicke model that provides the possibility for well-controlled approximations in the presence of a large number of cavity-emitters for both mean-field and fluctuational dynamics.

Bistability in driven quantum optical setups allows to investigate how fluctuations take a crucial role for quantum many-body dynamics that cannot be captured in a mean-field analysis. Quantum or classical fluctuations render the predicted mean-field steady-states metastable by inducing rare transitions between them [171, 172].

Bistabilities are common consequences from competing nonlinearties in the (semiclassical) dynamical equations of motion. Whether or not fluctuations wash out or collapse the bistability regime depends on the relation of the intrinsic timescales associated to noise activation and experimental observation times. For example, semiclassical bistability consistent with a mean-field prediction was observed experimentally in a superconducting resonator inductively coupled to a large number of negatively charged nitrogen vacancy center spins in diamond [173]. Here, fluctuations were strongly suppressed by the large number of atoms , $N \sim 10^{12}$, pushing fluctuation times far beyond experimental accessibility. If fluctuations can be resolved, they typically lead to a partial or full collapse of the bistability regime hinting at an underlying fluctuation induced dissipative first-order phase transition.

A prime example for an optical bistability is a single, driven cavity with an optical Kerr-nonlinearity [174]. On the level of single-operator expectation values the system shows a coexistence regime of two stable states with different photon numbers for the same driving strength. However, a full quantum treatment [175, 176] reveals that quantum fluctuations induce a driven-dissipative first-order phase transition in the thermodynamic limit of large intracavity photon numbers [86]. An experimental realization in a semiconductor microcavity analysed the time-resolved fluctuation dynamics [29].

The growing experimental access and realization of driven-dissipative non-linear systems that display such a bistability has led to a surge of interest in theoretical descriptions for out of equilibrium systems [177, 14, 89, 178, 87, 160] and signatures of first-order dissipative phase transitions and the crucial role played by fluctuations [30, 29, 179, 85, 180, 181]. For example in a driven circuit quantum electrodynamics system up to three artificial atoms made of superconducting Josephson junctions were strongly coupled to a coplanar waveguide resonator which realizes a driven version of the Jaynes-Cummings model, i.e. two-level systems stronlgy coupled to a harmonic oscillator[182, 183, 184, 173].

We consider the simple, yet paradigmatic Dicke model [185] describing N-atoms coupled to a single mode cavity. In addition to single photon and single atom loss channels, we consider a collective atomic loss channel, which enhances the decay rate if excitations are shared by many atoms. It has been introduced recently in a single-excitation framework for super- and subradiant cavity states [69] and in a non-superradiant resonance fluoresence model [186]. We extend this idea to the many-body regime, i.e. we introduce and analyze the many-body quantum master equation for the dissipative Dicke model with collective and single atom decay.

We find that if the collective loss strength exceeds a critical value, the conventional second-order phase transition from the empty to the superradiant state is replaced by a bistable regime for the dark and the bright cavity, which is absent for weak losses [187]. When the atomic emitters radiate collectively, the decay rate is actually enhanced by the number of emitters $\gamma \to \gamma N$. Collective emission of radiation is relevant for many-body states such as atomic, collective angular momentum or Dicke states where the atomic ensemble can behave like one giant atom. However, superradiance can occur even for a single photonic excitation that is shared among N atoms and is known as single-photon superradiance [55]. Sometimes even two atoms coupled to a single mode resonator are enough to experimentally observe enhanced radiation rates [76]. This illustrates quite generally Dicke's original idea [185] that the emission dynamics of a single atom can be changed by the presence of a second atom. Geometrically, this behaviour is typically expected when the atoms are closer together than the wavelength of radiation. However, even for larger atomic samples the radiation rate can be enhanced [57, 69]. In the present case the relevant geometric factor ($\alpha \ll 1$) depends on the size of the atomic cloud and the cavity parameters, see Sec. 1.2.1. The collective excitation rate is then modified as $\gamma N \to \gamma \alpha N \equiv \gamma \beta$. However, both the average energy and loss rate per particle have to remain finite in the thermodynamic limit, which implies that for $N \to \infty$, $\beta = const.$ and is set by the fixed number of atoms in an experiment. Both the collective and the individual loss channel are derived from the same Hamiltonian that couples the system degrees of freedom with the electromagnetic vacuum, see Sec. 1.2.1. The collective atomic loss channel does therefore not introduce any new characteristic time scales that would call the time-local Lindblad structure and thus the Born-Markov approximations into question that are valid when system-bath couplings are small $\gamma \ll (\omega_0, \omega_z, g)$.

Mapping the quantum dynamics to stochastic optical Bloch equations, we show that the bistable regime features noise activated transitions between the metastable states. The noise activation rates are, however, suppressed exponentially with the number of atoms, such that in the thermodynamic limit one of the metastable states becomes stable and thus the true steady state. This leads to a collapse of the bistable regime towards a sharp first-order transition.

The dynamics in the considered model can generally not be derived from the gradient of a potential, as is the case in dissipative equilibrium systems. However, in the vicinity of the bicritical point, the dynamics is expressed in terms of a single slow mode. The $(0+1)$-dimensional Langevin equation with one component can then always be derived from a potential. Moreover, fluctuations are not uniformly distributed in phase space and depend on the current state of the system. This promotes the Dicke model to a prime example to

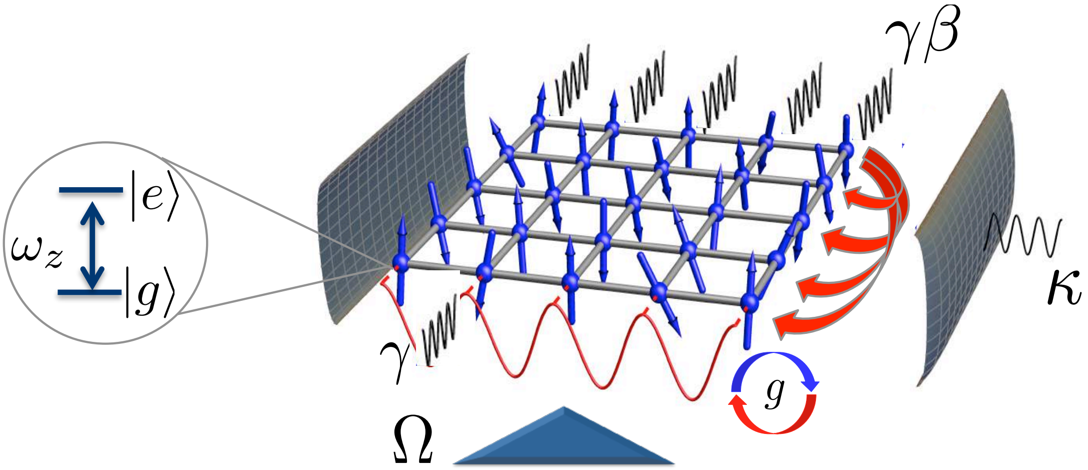

Figure 4.1.: Illustration of a model setup. An ensemble of N two-level atoms with a level splitting characterised by the frequency ω_z is driven from the side with an external laser with a Rabi-frequency Ω. The cavity photons mediate an infinite-range atom-atom coupling of strength $J(\kappa)$ (red arrows). There are three incoherent loss-processes. Photons escape cavity mirrors with rate κ, individual atoms can decay incoherently with a rate γ. The atomic ensemble can collectively emit an excitation into the surrounding vacuum modes with strength $\gamma\beta$.

study the fate of hysteresis and bistability also far from equilibrium circumstances.

4.2. Model

[1]The state of the cavity ensemble of N atoms and a single photon mode is expressed via the density matrix ρ, whose time evolution is given by the Markovian quantum master equation

$$\partial_t \rho = -i[H,\rho] + \mathcal{L}_\gamma[\rho] + \mathcal{L}_\kappa[\rho]. \tag{4.1}$$

The coherent evolution, including the cavity photon-atom coupling, is given by the Dicke Hamiltonian [185, 52]

$$H = \omega_0 a^\dagger a + \frac{\omega_z}{2}\sum_{\ell=1}^{N}\sigma_\ell^z + \frac{g}{\sqrt{N}}(a+a^\dagger)\sum_{\ell=1}^{N}\sigma_\ell^x\ . \tag{4.2}$$

Here, ω_0, ω_z is the photon energy and the atomic level splitting and g is the atom-light coupling strength. Equation (4.2) implicitly contains an external drive laser, whose time-dependence has been eliminated in a rotating frame [26].

The loss channels are described by the Lindblad terms

$$\mathcal{L}_\gamma[\rho] = \gamma(1-\beta/N)\sum_{\ell=1}^{N}\left(2\sigma_\ell^- \rho \sigma_\ell^+ - \{\sigma_\ell^+\sigma_\ell^-, \rho\}\right) \tag{4.3}$$

$$+ \gamma\beta/N(2S^-\rho S^+ - \{S^+S^-, \rho\}), \tag{4.4}$$

$$\mathcal{L}_\kappa[\rho] = \kappa(2a\rho a^\dagger - \{a^\dagger a, \rho\})\ . \tag{4.5}$$

---

[1] Model section taken verbatim from J. Gelhausen and M. Buchhold, Phys. Rev. A **97**, 023807 (2018)

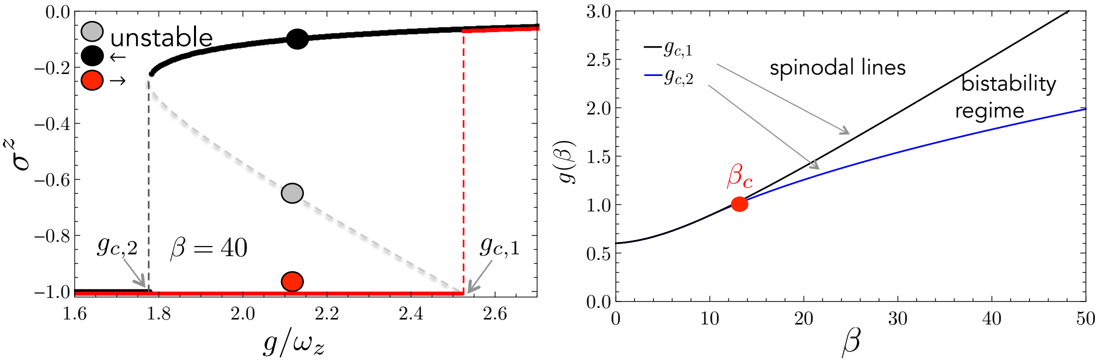

(a) (b)

Figure 4.2.: (a) Static hysteresis on mean-field shown for the σ^z component. We follow the (non)trivial steady-state solution to the mean-field equations adiabatically by (de)increasing the atom-light coupling. The jump for the "←"("→")-direction occurs at $g_{c,1} \approx 1.78$, ($g_{c,2} \approx 2.52$). The dashed line marks the repulsive fixed points inside the bistable regime. (b) Bistability regime in (g, β) space. Inside the spinodal lines marked by $g_{c,1}, g_{c,2}$ the system possesses two stable minima. One of these minima is always the empty state, see (a). Parameter set $\omega_0/\omega_z = 1.4$,$\gamma/\omega_z = 0.1 \kappa/\omega_z = 0.2$, with $\beta = 40$ in (a).

The two-level atoms are modeled by a local spin algebra $\sigma_i^+ = |e\rangle_i \langle g|, \sigma_i^z = |e\rangle_i \langle e| - |g\rangle_i \langle g|$ and $S^\pm = \sum_{\ell=1}^N \sigma_\ell^\pm$. Here (e, g) refers to the excited and ground state of an atom, respectively and $a^\dagger, a$ creates, annihilates a cavity photon. Photon loss through the cavity mirrors with rate κ is described by the Lindblad $\mathcal{L}_\kappa$. Atomic spontaneous emission into the electromagnetic vacuum outside the cavity is captured by $\mathcal{L}_\gamma$.

The atoms can either decay individually and uncorrelated (4.3) or can decay through a collective channel, resulting from the electromagnetic bath being commonly shared by all the atoms. In the context of the Dicke model, the most important collective decay channel is the spontaneous decay of a superradiant state (4.4). A sketch of a systematic experimental setup is illustrated in Fig. 4.1. Intuitively, the photonic rate of dissipation κ and the single atom loss rate γ shift the critical atom-light coupling for the superradiant phase transition towards higher pump strength to compensate for the losses [187, 26, 109, 188]. The collective noise, however, introduces an additional non-linearity, leading to a drastic modification of the phase transition in the thermodynamic limit $N \to \infty$.

4.3. Noiseless mean-field master equations and bicritical point

In this section we analyse noiseless mean-field master equations for spin and photon amplitudes (deterministic optical Bloch equations) of the dissipative Dicke model. We analyse their stationary non-equilibrium states and find classical bistability between an empty atom-cavity system and a superradiant regime for the same set of coupling parameters. Close to a bicritical point, we show that the bistable behaviour is described in terms of a Ginzbug-Landau potential of an Ising-ϕ^6 model.

In order to derive the semiclassical optical Bloch equations for the dissipative Dicke model (Eqs. (4.2)-(4.5)), which can be addressed numerically, we start with the computation of the Heisenberg-Langevin equations (HLE) for the individual spin and photon operators. Although the Dicke Hamiltonian in Eq. (4.2) preserves the total spin quantum number of the system, the single atom loss components mix sectors of different total spin $\hat{S}^2$ and the HLE have to be expressed in the local spin basis.

The HLE for any system operator O_i are obtained from a conjugate master equation, see Sec. 1.2.

$$\partial_t O_i = D_i[\boldsymbol{O}] + \xi_i^O, \tag{4.6}$$

where the deterministic relaxation D_i contains both unitary elements from the system Hamiltonian H and dissipative elements from the Lindblad $\mathcal{L}$ as

$$D_i[\boldsymbol{O}] = -i[O_i, H] + \mathcal{L}^*_\gamma[O_i] + \mathcal{L}^*_\kappa[O_i], \tag{4.7}$$

where in $\mathcal{L}^*$ compared to $\mathcal{L}$ the order of operators in the quantum jump term has been inverted, e.g. $\mathcal{L}^*_\kappa[.] = \kappa(2a^\dagger .\, a - \{a^\dagger a, .\})$.

Applying Eq. (4.6) to the photon field and the individual spin components at site i yields

$$\partial_t a = -\left(\kappa + i\omega_0\right) a - \frac{ig}{\sqrt{N}} \sum_{\ell=1}^{N} \sigma_\ell^x + \xi^a, \tag{4.8}$$

$$\partial_t \sigma_i^x = -\omega_z \sigma_i^y - \gamma \sigma_i^x + \frac{\gamma\beta}{N} \sum_{\ell \neq i} \sigma_\ell^x \sigma_i^z + \xi_i^x, \tag{4.9}$$

$$\partial_t \sigma_i^y = \omega_z \sigma_i^x - \left[\frac{2g(a^\dagger + a)}{\sqrt{N}} - \frac{\gamma\beta}{N} \sum_{\ell \neq i} \sigma_\ell^y \right] \sigma_i^z - \gamma \sigma_i^y + \xi_i^y, \tag{4.10}$$

$$\begin{aligned} \partial_t \sigma_i^z = {} & \frac{2g(a^\dagger + a)}{\sqrt{N}} \sigma_i^y - 2\gamma(1 + \sigma_i^z) + \xi_i^z \\ & - \frac{\gamma\beta}{2N} \sum_{\ell \neq i} [(\sigma_i^x + i\sigma_i^y)(\sigma_\ell^x - i\sigma_\ell^y) + hc.]. \end{aligned} \tag{4.11}$$

While incoherent atomic spontaneous emission is linear in the spins, the collective decay contribution is manifestly nonlinear and non-local, see Eq. (4.10). Note that here we have rescaled $\gamma \to 2\gamma$ in comparison to chapter 2 and 3 for notational convenience. We eliminate the gapped photon field by setting $\partial_t a = 0$ in (4.8) and solve for a. Through the presence of both co- and counter rotating terms, the photon operators always appear in the combination $(a + a^\dagger)$. As a consequence, there is no dissipative contribution $\sim g^2\kappa$ to the equations of motion. The coherent contribution $\sim g^2\omega_0$ adds a nonlinear, ferromagnetic coupling $\sim -J/N \sum_\ell \sigma_\ell^x$, with

$$J = 4g^2\omega_0/(\kappa^2 + \omega_0^2). \tag{4.12}$$

The noise fields of the atoms however inherit a contribution from the photons as $\left(\xi^a + \xi^{a^\dagger}\right)$. The adiabatic elimination is detailed in Sec. 4.4.1. The collective decay leads to another, competing nonlinearity $\sim \gamma\beta$ to the HLE, which introduces a bistable regime for parameters $\gamma\beta \approx J \approx J_c$, where J_c is the critical coupling for the superradiance transition.

We analyze the remaining set of equations for the atoms in a large N-framework, where the operators in the HLE are replaced by the quantum mechanical average over all atoms, i.e. we analyze the equations of motion for $\sigma^\alpha = \sum_\ell \langle \sigma_\ell^\alpha \rangle / N$, $\alpha = x, y, z$. Approximating the average of the double sums $\sum_{i,\ell} \langle \sigma_i^\alpha \sigma_\ell^\beta \rangle / N^2$ by the product $\sigma^\alpha \sigma^\beta$ is correct up to $\mathcal{O}(1/N)$ corrections and becomes exact in the thermodynamic limit. This is due to the infinite range nature of both the Dicke nonlinearity $\sim g$ and the collective decay $\sim \gamma\beta$.

Disregarding the noise yields the deterministic optical Bloch equations

$$\partial_t \sigma^\alpha = D^\alpha \tag{4.13}$$

with the deterministic force

$$\boldsymbol{D} = \begin{pmatrix} -\gamma\sigma^x(1-\beta\sigma^z) - \sigma^y\omega_z \\ \omega_z\sigma^x + J\sigma^x\sigma^z - \gamma\sigma^y(1-\beta\sigma^z) \\ -2\gamma(\sigma^z+1) - \gamma\beta\left((\sigma^x)^2 + (\sigma^y)^2\right) - J\sigma^x\sigma^y \end{pmatrix}, \tag{4.14}$$

including the additional nonlinearities $\sim J, \beta\gamma$ in comparison to the conventional Bloch equations [72].

We remark that $\nabla_\sigma \times \boldsymbol{D} \neq 0$ and $\nabla_\sigma \cdot \boldsymbol{D} \neq 0$, which results from the presence of unitary and dissipative dynamics and prohibits the interpretation of $\boldsymbol{D}$ as a conservative force, $\boldsymbol{D} \neq \nabla_\sigma V$ for some potential V. Here, unitary and dissipative dynamics cannot be generated by the same Hamiltonian functional. This moves the system in general away from dissipative equilibrium, where the steady states coincide with the minimums of a generalized energy landscape. This statement will be more clear in chapter 5. That said however, we will show in Sec. 4.3.2 that close to a bicritical point, the dynamics of the system is determined entirely from a single slow mode whose dynamical equation can be cast into a potential form based on a power series expansion of the slow mode. In Sec. 5.4 we show that at the critical point the noise spectrum has a constant noise intensity. Consequently, there emerges an effective equilibrium description close to the bicritical point. This behaviour has been observed for a variety of driven-dissipative systems in quantum optics, see [160] and references therein.

Solving $\boldsymbol{D} = 0$ yields the mean-field stationary states and determines the steady state values for the σ^α. The superradiance transition can be seen in all channels, i.e. the atomic $(\sigma^x, \sigma^y, \sigma^z)$ as well as the photonic channel $(a, a^\dagger)$. For the population imbalance σ^z, one finds (considering only real, stable solutions)

$$\sigma^z = \max\left\{-1, \frac{1}{\beta} + \frac{J\omega_z}{2\beta^2\gamma^2}\left(\sqrt{1 - \frac{4\beta\gamma^2(\beta\omega_z + J)}{J^2\omega_z}} - 1\right)\right\}. \tag{4.15}$$

For collective loss strengths $\beta < \beta_c$ (Eq. (4.16)), σ^z is a continuous function of the Dicke coupling g. For coupling strengths above a critical value $g \geq g_{c,1}$ (Eq. (4.17)), $\sigma^z \sim |g - g_{c,1}|^{\nu_x} - 1$ always deviates from its empty cavity value of $\sigma^z = -1$. This goes in hand with a macroscopic occupation of the cavity mode $\langle a^\dagger a\rangle \sim N|g - g_{c,1}|^{\nu_x}$, i.e. the continuous phase transition from the empty cavity to the superradiant state. Here $\nu_x = 1$ is the finite temperature photon flux critical exponent [87]. We detail the critical behaviour of the population imbalance close to the critical point in Sec. 4.3.1. The dependence of the population imbalance on the strength of the atom-light coupling for $\beta < \beta_c$ and for $\beta > \beta_c$ is illustrated in Fig. 4.3.

Above the critical loss strength, $\beta > \beta_c$, the continuous transition into the superradiant state is replaced by a discontinuous jump of σ^z and $g_{c,1}$ still indicates the instability of the empty atom-cavity system. The magnitude of the jump into the superradiant regime is a function of the distance from the bicritical point. It is calculated from the diverging derivative $1/\partial_g \sigma^z = 0$. The magnitude of the jump for $\beta > \beta_c$ is then given as $1 + \sigma^z(g_{c,2}) = \frac{\beta - \beta_c}{\beta}$.

A closer look at the optical Bloch equations reveals that there appears a second critical coupling $g_{c,2}$ such that for $g_{c,2} \leq g \leq g_{c,1}$ (4.18) both the empty as well as the superradiant state appear as attractive stationary mean-field solutions. This indicates classical

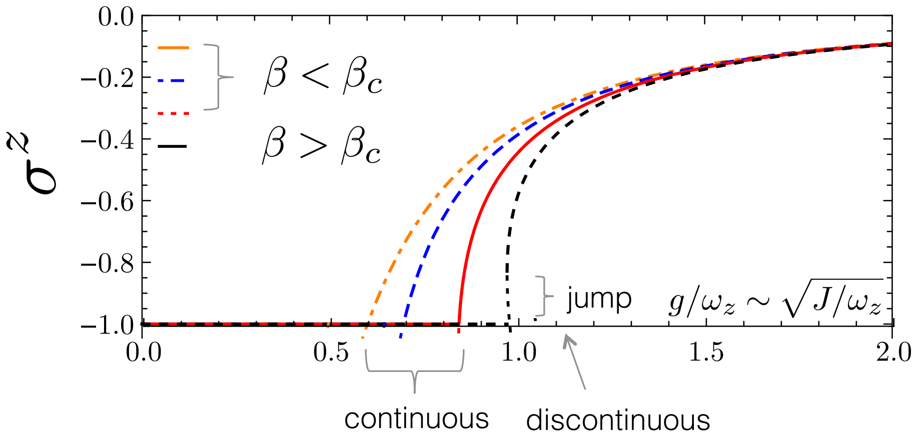

Figure 4.3.: There exists a bicritical point β_c that separates a continuous from a discontinuous superradiance transition. For $\beta < \beta_c$ the transition into the superradiant state is a continuous second-order transition, whereas for $\beta > \beta_c$ the superradiance transition is a discontinuous first-order transition.

bistability, where steady states are sensitive towards the initial configuration leading to the appearance of static hysteresis where the two mean-field solutions can coexist in a limited domain, see Fig. 4.2a. The critical couplings are

$$\beta_c = \sqrt{1 + (\omega_z/\gamma)^2}, \tag{4.16}$$

$$g_{c,1} = \frac{\sqrt{\kappa^2 + \omega_0^2}\sqrt{(1+\beta)^2\gamma^2 + \omega_z^2}}{2\sqrt{\omega_z \omega_0}}, \tag{4.17}$$

$$g_{c,2} = \sqrt{\frac{\beta\gamma\left(\sqrt{\gamma^2 + \omega_z^2} + \gamma\right)(\kappa^2 + \omega_0^2)}{2\omega_z\omega_0}}, \quad \beta \geq \beta_c. \tag{4.18}$$

The bistable regime is delimited by the spinodal lines $(g_{c,1}(\beta), g_{c,2}(\beta))$ that continuously connect at the bicritical point β_c as shown in Fig. 4.2b. Inside this regime, the empty and the superradiant cavity state, appear as attractive fixed points of $\boldsymbol{D}$.

If the bistable region in (β, g)-space is entered not through the bicritcal point $(\beta_c, g_c = g_{c,1}(\beta_c) = g_{c,2}(\beta_c))$ but from outside of the spinodal lines $(g_{c,1}, g_{c,2})$, an additional solution appears that is not continuously connected to the existing steady-state. The atomic inversion σ^z can jump at this point from the empty state to the superradiant state or vice versa with a magnitude $|\sigma^z_{Sr} - \sigma^z_0| = 1 - \frac{\beta_c}{\beta}$. At the bicritical point however, the transition from one steady-state to two steady-states is continuous, see Fig. 4.5b.

The Bloch sphere, whose surface is defined as $\sum_\alpha (\sigma^\alpha)^2 = 1$ is comprised of three three-dimensional domains Ω_0 and Ω_{Sr} corresponding to the basins of attraction of the empty and the superradiant state, respectively that are separated by a two-dimensional separatrix S defined as the surface of these domains $S = \partial\Omega_0 = \partial\Omega_{Sr}$. The two domains Ω_{Sr} are symmetry related and separated from each other through the domain Ω_0. An unstable fixed point lies on the separatrix $\sigma^\star \in S$. An analysis of the linearised dynamics around $\sigma^\star$ shows that it behaves like a saddle-point in the sense that it is characterised by two repulsive and one attractive direction. At a spinodal line, the separatrix encloses one of the attractive fixed points and forces it to vanish (saddle-node bifurcation). In a thermal system described by a free energy functional, a saddle node bifurcation occurs when a local minimum merges with a local maximum, eliminating both extrema. The

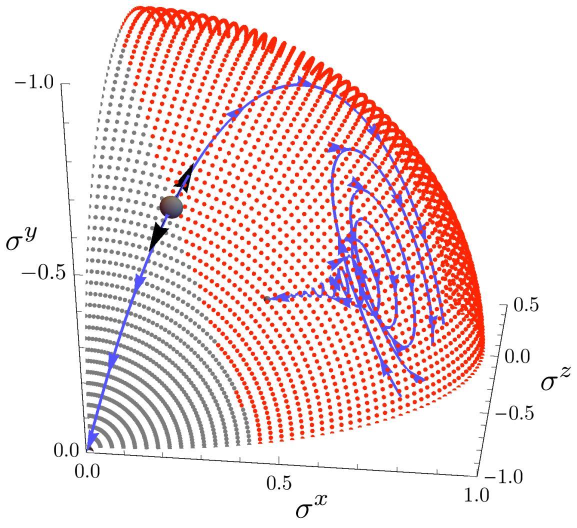

Figure 4.4.: Shown is one quadrant of the Bloch sphere in the manifold spanned by $(\sigma^x, \sigma^y, \sigma^z)$ with the empty and the superradiant fixed points. The first is located at (0,0,-1). A third, unstable fixed point $\sigma^\star$ is found on the separatrix that separates the domains of attraction of the empty (gray dots) from the domain of attraction of the superradiant fixed point (red dots). Black arrows indicate the unstable directions of the repulsive fixed point. The final state of the system is sensitive to its initial configuration as illustrated by the two deterministic, relaxational trajectories (blue) that are initialised at the repulsive fixed point with a small displacement in opposite directions along the unstable directions.

linearised dynamics around the superradiant fixed points reveal that it is characterised by an entirely real and two complex conjugated pairs of eigenvalues all with negative real part. The imaginary part leads to an oscillatory behaviour and the negative real part ensures the stability of the fixed points. Consequently, the deterministic relaxation to the superradiant fixed points is a spiraling motion in the Ω_{Sr} manifold. The empty fixed point is characterised by three real, negative eigenvalues signalizing the absence of oscillatory motions in the relaxational dynamics. Fig. 4.4 illustrates the domains $\Omega_{0,Sr}$, as well as the deterministic relaxational dynamics in the domains of attraction.

4.3.1. Classification of bicritical point

The steady-state phase diagram in the mean-field case predicts the occurence of a bistability region. We are interested in the scaling behaviour of the order parameters close to the phase-transition. In particular, we investigate the bicritical point of the system

$$\{\beta_c, g_c\} = \{\sqrt{1+\frac{\omega_z^2}{\gamma^2}}, \frac{\sqrt{\kappa^2+\omega_0^2}\sqrt{(\beta+1)^2\gamma^2+\omega_z^2}}{2\sqrt{\omega_0}\sqrt{\omega_z}}\}. \tag{4.19}$$

There are three different scenarios that can influence the fate of the critical exponent of the order parameter. These three scenarios are the coherent Dicke model that is purely Hamiltonian $(\beta,\kappa,\gamma) = (0,0,0)$ and represents the case of a closed thermal system. The second scenario is the entirely quantum and dissipative Dicke model with $(\beta = 0, \kappa > 0, \gamma > 0)$. For the case $(\beta = 0, \kappa = 0, \gamma = 0)$ and $(\beta = 0, \kappa \neq 0, \gamma = 0)$ it could be shown that the photon flux exponents which signalise a macroscopic occupation of the cavity

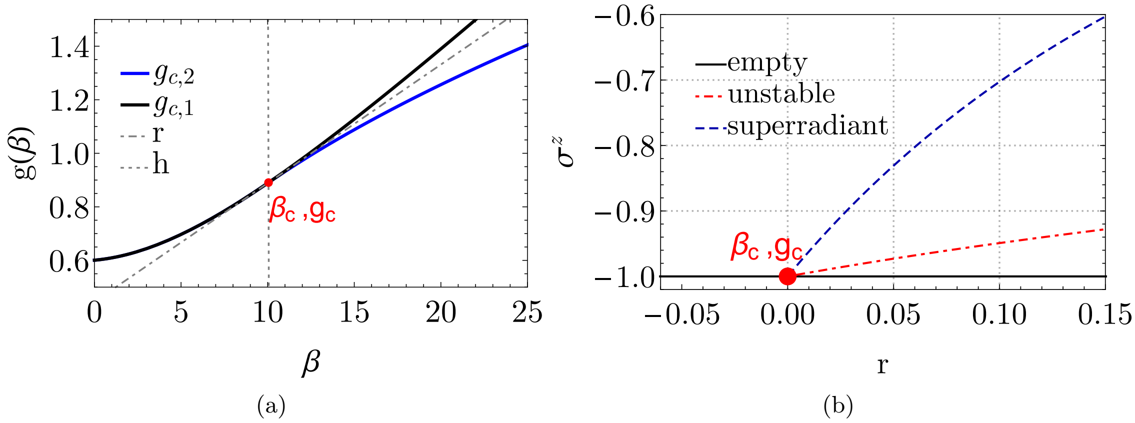

(a) (b)

Figure 4.5.: (a) Local coordinate system spanned by the $r-$ and h-axis. Along $h = 0$ and $r \to 0$ one approaches the critical point from inside the bistability regime. (b) Three solutions for the atomic inversion σ^z in the bistability regime. Corresponding to the empty atom-cavity system, to the superradiant state and an unstable solution.

mode have different exponents [47]. The purely Hamiltonian model shows a flux exponent of $\nu_x = 1/2$, whereas the dissipative model with photonic dissipation has $\nu_x = 1$. In the case of $(\beta > 0, \kappa > 0, \gamma > 0)$ we observe the following mean-field exponents

$$\lim_{\beta\to 0}[1+\sigma^z(g-g_c)] \sim (g-g_c)^{\nu_x}, \quad \nu_x = 1, \tag{4.20}$$

$$[1+\sigma^z(g-g_c)]|_{\beta=\beta_c} \sim (g-g_c)^{\nu_x}, \quad \nu_x = 1/2, \tag{4.21}$$

$$[1+\sigma^z(\beta-\beta_c)]|_{g=g_c} \sim (\beta-\beta_c)^{\nu_x}, \quad \nu_x = 1. \tag{4.22}$$

Here the notation $\sigma^z(g-g_c)$ refers to the population imbalance σ^z as a function of the distance to the critical point measured as $(g-g_c)$. To reach the bicritical point, requires to fine-tune two parameters, β and g. The different scaling regions in Eq. (4.21) and in Eq. (4.22) cross over into each other at some well-defined line in (β, g) space. We provide details for the different scaling regions in Sec. 4.3.4.

4.3.2. Emergence of dissipative equilibrium close to bicritical point

> In this section we show explicitly that the dynamics of the system close to the bicritical point is obtained from a Ginzburg-Landau potential of a ϕ^6-model with Ising inversion symmetry, see Eq. (4.31) and Eq. (4.32). ϕ is an effective slow mode that captures the low frequency relaxation dynamics to the steady state close to the bicritical point. Its dynamical equation is derived after adiabatically eliminating two massive fast modes.

At the bicritical point, all steady-state solutions converge onto each other as shown in Fig. 4.5b. Therefore, the steady-state of the system is the empty atom-cavity system characterised as $\boldsymbol{\sigma}_0 = (\sigma^x, \sigma^y, \sigma^z) = (0, 0, -1)$. Expanding the fluctuationless mean-field states around their empty state $\boldsymbol{\sigma} = \boldsymbol{\sigma_0} + \boldsymbol{\delta\sigma}$ yields the (linearised) differential equation that governs the time-evolution of fluctuations.

$$\partial_t \boldsymbol{\delta\sigma} = D(\boldsymbol{\sigma}_0)_J|_{g_c,\beta_c} \cdot \boldsymbol{\delta\sigma} + \mathcal{O}(\boldsymbol{\delta\sigma}^2). \tag{4.23}$$

The relaxation rates for deviations from the mean-field solution at the critical point are governed by the set of eigenvales $\{\lambda_i\}$ of the relaxation matrix

$$D(\boldsymbol{\sigma}_0)|_{J(g_c,\beta_c)} = \begin{pmatrix} (-\beta_c - 1)\gamma & -\omega_z & 0 \\ \omega_z - J(g_c) & (-\beta_c - 1)\gamma & 0 \\ 0 & 0 & -2\gamma \end{pmatrix}, \quad \{\lambda_i\} = \{-2\gamma, -2(\beta_c + 1)\gamma, 0\}. \tag{4.24}$$

The eigenvalues are entirely real and negative, $\lambda_i \leq 0$. Since the time-evolution of the fluctuations is given by a decomposition into the eigenmodes $\boldsymbol{\delta\sigma} = \sum_{i=1}^{3} \boldsymbol{v}_i \exp(\lambda_i t)$, fluctuations decay for $\lambda_{1,2}$ but stay constant for λ_3. At the bicritical point, one mode becomes critical, indicated by the diverging relaxation timescale $1/T_1 = \lambda_3 \to 0$ as $(g, \beta) \to (g_c, \beta_c)$. The relaxation timescale of the other two modes $\boldsymbol{v}_1$ and $\boldsymbol{v}_2$ remains finite at the bicritical point indicating an exponentially fast decay. This identifies one slow and two fast modes.

We describe the relaxation dynamics of the slow and fast modes in an orthogonal coordinate system (r, h) with its origin at the critical point (β_c, g_c) such that we express $\boldsymbol{D}(g, \beta)$ as $\boldsymbol{D}(r, h)$ where for $h = 0$ and $r > 0$ we approach the critical point from inside the bistability regime. Here, (r, h) are defined by the unitary basis transformation

$$\begin{pmatrix} \beta(r,h) \\ g(r,h) \end{pmatrix} = \frac{1}{\sqrt{m^2+1}} \begin{pmatrix} 1 & -m \\ m & 1 \end{pmatrix} \begin{pmatrix} r \\ h \end{pmatrix} + \begin{pmatrix} \beta_c \\ g_c \end{pmatrix}, \tag{4.25}$$

$$m = \partial_\beta g_c(\beta)|_{\beta_c}. \tag{4.26}$$

A visualisation of the local, orthogonal coordinate system that is spanned by (r, h) is given in Fig. 4.5a. Next, we parametrise fluctuations in terms of the eigenmodes of the linearized stability matrix that results from $\boldsymbol{D}(r, h)$ which are the fast $(\boldsymbol{v}_1(r, h), \boldsymbol{v}_2(r, h))$ and slow mode $\boldsymbol{v}_3(r, h)$ which for $(r, h) = (0, 0)$ are the eigenvectors of the relaxation matrix given in Eq. (4.24). We expand the fluctuations in these modes as

$$\delta\boldsymbol{\sigma} = \varphi \boldsymbol{v}_1 + \psi \boldsymbol{v}_2 + \phi \boldsymbol{v}_3, \tag{4.27}$$

where the time dependence is entirely in the set $\{\varphi(t), \psi(t), \phi(t)\}$. This defines the equations

$$\dot{\varphi(t)}\boldsymbol{v}_1 + \dot{\psi(t)}\boldsymbol{v}_2 + \dot{\phi}\boldsymbol{v}_3 = \boldsymbol{D}(r, h, \boldsymbol{\sigma}_0 + \varphi\boldsymbol{v}_1 + \psi\boldsymbol{v}_2 + \phi\boldsymbol{v}_3). \tag{4.28}$$

With an appropriate transformation, one obtains the time-dependence of the slow and fast modes as

$$\left(\dot{\varphi}, \dot{\psi}, \dot{\phi},\right)^T = \tilde{\boldsymbol{D}}(r, h, \varphi, \psi, \phi). \tag{4.29}$$

A numerical solution of Eq. (4.29) is depicted in Fig. 4.6.

We have identified two fast and one slow mode for the dynamics of fluctuations close to the bicritical point. The fast modes are identified by a finite mass gap due to the non-vanishing eigenvalue of the stability matrix at the bicritical point, see Eq. (4.24). Adiabatically eliminating the massive modes (φ, ψ) leads to an effective equation for the slow mode ϕ. We take Eq. (4.29) and expand $\tilde{\boldsymbol{D}}(r, h, \varphi, \psi, \phi)$ to lowest order in the fast fields (φ, ψ). However we do not know a priori how small the fields are in comparison to (r, h). The region of validity of the perturbation dynamics is limited to $h \ll r \ll 1$ around the critical point at $(r = h = 0)$. The equations are linearised

$$\begin{pmatrix} \dot{\varphi} \\ \dot{\psi} \end{pmatrix} = \begin{pmatrix} f & g \\ \tilde{f} & \tilde{g} \end{pmatrix} \begin{pmatrix} \varphi \\ \psi \end{pmatrix} + \begin{pmatrix} b_1 \\ b_2 \end{pmatrix} + \mathcal{O}(\psi^2, \varphi\psi), \tag{4.30}$$

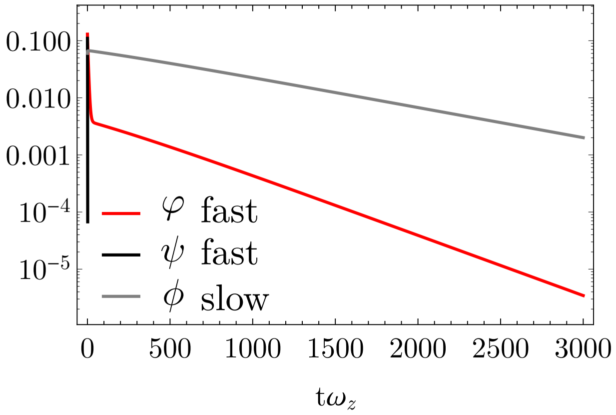

Figure 4.6.: Numerical solution to Eq. (4.29) showing the slow ϕ (grey) and the two fast modes φ (red) and ψ (black) of the relaxation dynamics close to the bicritical point ($r = 0.8$ and $h = 0.0$) for the set ($\gamma = 0.1\omega_z, \kappa = 0.2\omega_z, \omega_0 = 1.4\omega_z$). In order to map the dynamics entirely onto the slow mode ϕ, the fast modes cannot simply be ignored because they couple to the slow mode. However, they can be adiabatically eliminated in a linearised equation (4.30).

where $(f, g, \tilde{f}, \tilde{g}, b_1, b_2)$ are functions of (r, h, ϕ). Solving these for their steady-state, we receive an effective equation for the slow mode that is cast into the form of a relaxational equation,

$$\dot{\phi} = -\frac{\partial \mathcal{H}}{\partial \phi}. \tag{4.31}$$

Here $\mathcal{H}$ defines an effective potential,

$$\mathcal{H} = \frac{1}{2}a_2\phi^2 + \frac{1}{4}a_4\phi^4 + \frac{1}{6}a_6\phi^6 + \mathcal{O}(\phi^8). \tag{4.32}$$

The potential $\mathcal{H}$ obeys necessarily an Ising symmetry $\phi \to -\phi$ and can describe a frist and a second order transition depending on the set of coefficients $(a_2(r, h), a_4(r, h), a_6(r, h))$. The coefficients themselves depend on the distance to the bicritical point parametrised by r and h.

The coefficient of the ϕ^6 contribution to the potential must for all parameters (r, h) always be positive to guarantee stability of the differential equation. This coincides with our expansion results $a_6 > 0$. This is true for higher order coefficients as well such that we cut off the expansion after the a_6 term. This scenario defines a stable potential, since

$$\lim_{\phi \to \pm\infty} \mathcal{H} \to \infty. \tag{4.33}$$

4.3.3. Ginzburg-Landau potential expansion at bicritical point

> The effective potential in Eq. (4.32) in the vicinity of the bicritical point possesses the Ising inversion symmetry such that only even powers of the slow field ϕ can occur. The resulting discussion of the phases and phase transitions it describes for the set of parameters (a_2, a_4, a_6) are well-known from the Ginzburg-Landau theory of phase transitions and can be found in standard textbooks on statistical physics. In what follows, we recapitulate these results for the present model.

Depending on the set of coefficients (a_2, a_4, a_6), there is either only one, three or five extrema see Fig. 4.7b. The extrema of the potential satisfy the condition

$$\frac{\partial\mathcal{H}}{\partial\phi} = \phi(a_2 + a_4\phi^2 + a_6\phi^4) = 0. \tag{4.34}$$

There is always a solution with an extremum at $\phi = 0$. The other extrema are found at

$$\phi_{\mathrm{max}}^2 = \frac{-a_4 - \sqrt{a_4^2 - 4a_2a_6}}{2a_6}, \quad \phi_{\mathrm{min}}^2 = \frac{-a_4 + \sqrt{a_4^2 - 4a_2a_6}}{2a_6}, \tag{4.35}$$

where ϕ_{min} and ϕ_{max} denote the position of minima and maxima, respectively. If the square roots in Eq. (4.35) are imaginary, there is just a single minimum at $\phi = 0$.

At a second order phase transition, where a_2 changes from $a_2 > 0$ to $a_2 < 0$ the global minimum at $\phi = 0$ changes into a local maximum and two new, symmetry related minima that are described by ϕ_{min}^2 emerge and continuously evolve from the $\phi = 0$ state. This happens when a_2 changes its sign as $a_4 > 0$. The second order phase transition line is calculated from

$$a_2 = 0, \quad a_4 > 0. \tag{4.36}$$

A coexistence of five extrema is possible when $\phi_{\mathrm{max}}^2 \geq 0$ and $\phi_{\mathrm{min}}^2 \geq 0$ and $a_4 < 0$ and $a_2 \geq 0$. This happens when the inversion symmetry in the system is broken. Due to the stability of the potential these are ordered as $min - max - min - max - min$. The coexistence regime is delimited by two spinodal lines. The first is calculated from a sign change of a_2 from $a_2 < 0$ to $a_2 > 0$ as $a_4 < 0$. In this case there are three extrema $(\phi = 0, \phi_{\mathrm{min}}^2)$, where the local maximum at $\phi = 0$ becomes a local minimum again as two local maxima emerge continuously from $\phi = 0$ whoose evolution is described by ϕ_{max}^2. At the second spinodal line, there emerge two new minima and maxima at some $\phi \geq 0$ in addition to the global minimum at $\phi = 0$. This happens when $\phi_{\mathrm{min}}^2 = \phi_{\mathrm{max}}^2$. The two spinodal lines connect at the bicritical point. A spinodal line is thus defined at the line where a local extremum merges with a saddle point and is thus the equivalent of a saddle-node bifurcation. Spinodal lines thus delimit coexistence regimes of more than one local minima. In summary, the condition for the spinodal lines is

$$(a_2 = 0 \ \wedge \ a_4 < 0) \ \vee \ (a_2 > 0 \ \wedge \ a_4 < 0, \ \wedge \ a_4^2 - 4a_2a_6 = 0). \tag{4.37}$$

The spinodal lines calculated with Eq.(4.37) are consistent with the calculations of $g_{c,1}$ and $g_{c,2}$ in Eq. (4.17) and Eq. (4.18). Inside the coexistence regime there will be a line where all minima have the same potential value. This line defines a first-order phase transition that sets in as

$$a_2^* = \frac{3a_4^2}{16a_6}. \tag{4.38}$$

Since one minima is always located at $\phi = 0$, the potential value at this transition point is set to $\mathcal{H} = 0$. The zeros of the potential energy (except for $\phi = 0$) are derived from the conditions

$$\phi_\star^2 = \frac{-3a_4 \pm \sqrt{9a_4^2 - 48a_2a_6}}{4a_6}, \quad \mathcal{H}(\phi_\star^2) = 0, \quad \left.\frac{\partial\mathcal{H}}{\partial\phi}\right|_{\phi_\star^2} = 0 \to a_2^* = \frac{3a_4^2}{16a_6} > 0. \tag{4.39}$$

At the first-order phase transition, the minima are thus at

$$\phi_\star^2(a_2^\star) = -\frac{3a_4}{4a_6}. \tag{4.40}$$

A summary of the above relations is given in form of a phase diagram depicted in Fig. 4.7.

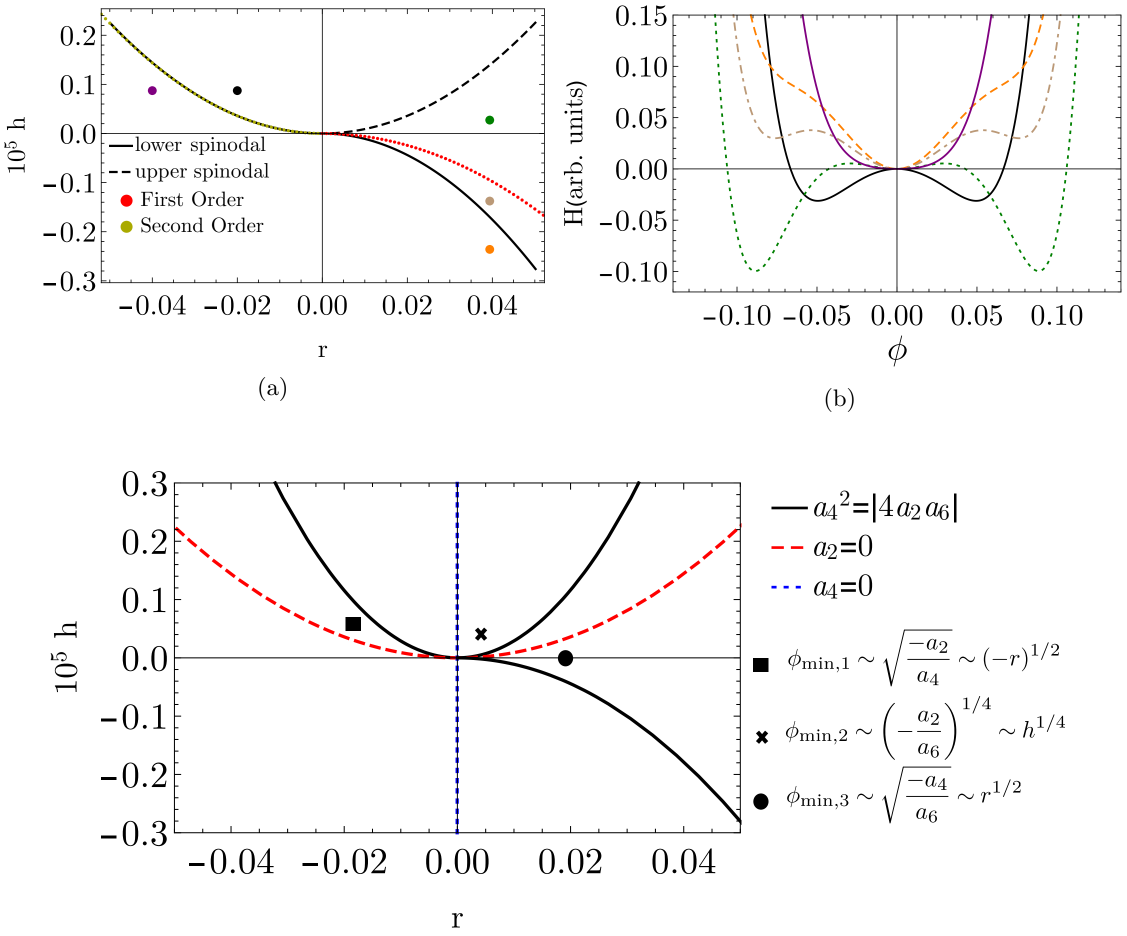

(a)

(b)

(c)

Figure 4.7.: (a) Phase diagram in (r, h) space around the bicritical point, located at $(r = 0, h = 0)$. For an orientation in (g, β) coordinates, see Fig. 4.5a. The second order phase transition (yellow, dotted) is calculated from Eq. (4.36), the first-order transition line (dotted, red) is obtained from Eq. (4.38). Spinodal lines from Eq. (4.17) and Eq. (4.18) are consistent with the expansion in Eq. (4.37). (b) Potential $\mathcal{H}$, see Eq. (4.94) for the points marked in (a).(c) Different scaling regimes of the order parameter as illustrated by the set of Eqs. (4.42)-(4.44).

4.3.4. Scaling of slow mode close to bicritical point

We can approach the bicritical point from two independent directions, parametrised by r and h. As $r \to 0$ and $h \to 0$ all minima and maxima vanish continuously at the bicritical point. By expanding the minima ϕ^2_{min} from Eq. (4.35) close to the bicritical point, one can get two different critical exponents for the order parameter scaling. One direction is on the line in (r, h)-space where $a_4 = 0$ and the other line is defined by the condition $a_2 = 0$. Close to the bicritical point, the minima are determined by

$$\phi^2_{\text{min}} = \frac{-a_4 + \sqrt{a_4^2 - 4a_2a_6}}{2a_6}. \tag{4.41}$$

The scaling of the order parameter close to the bicritical point can be understood from a series expansion of the above equation in the different regions

$$\phi_{\text{min},1} \sim \sqrt{\frac{-a_2}{a_4}} \sim (-r)^{1/2}, \quad |a_2| \ll |a_4|, \quad \text{with } a_2 < 0 \ \wedge \ a_4 > 0, \tag{4.42}$$

$$\phi_{\text{min},2} \sim \left(-\frac{a_2}{a_6}\right)^{1/4} \sim h^{1/4}, \quad |4a_2a_6| \gg a_4^2, \quad \text{with } a_2 < 0, \tag{4.43}$$

$$\phi_{\text{min},3} \sim \sqrt{\frac{-a_4}{a_6}} \sim r^{1/2}, \quad |a_2| \ll |a_4|, \quad \text{with } a_2 > 0 \ \wedge \ a_4 < 0. \tag{4.44}$$

The scaling region for $\phi_{\text{min},2}$ is separated from the two scaling regions of $\phi_{\text{min},1}$ and $\phi_{\text{min},3}$ by a crossoverline determined from the condition

$$a_4^2 = |4a_2a_6|, \tag{4.45}$$

which coincide with the condition of one of the two spinodal lines as described in Eq. (4.37).

The different scaling regions are illustrated in Fig. 4.7c. This closes the discussion of the noiseless mean-field master equations.

4.4. Derivation of Heisenberg-Langevin Noise in Born-Markov approximation

We have closed the discussion of noiseless mean-field master equations in the last section. In this section we show how to add back fluctuations to the deterministic optical Bloch equations. This is important to numerically explore the fluctuation dynamics in the bistability regime. We start by translating the quantum noise terms in the Heisenberg-Langevin equations for the atom-cavity system to a classical noise contribution, which adds to the mean-field master equations and yields stochastic optical Bloch equations. We show how to eliminate the cavity-photons in the presence of noise. As a consequence, the dynamics is entirely mapped onto the atomic sector which inherits noise contributions from the photons. Lastly, we show how the operator-valued noise kernel is translated to a classical noise kernel.

We derive the noise operators for both the atoms and the cavity photons explicitly in a Heisenberg-Langevin framework, see Eqs. (4.57-4.60). This allows a fast evaluation of a noise kernel $\chi_{i\ell}(\sigma) = \langle \xi^{O_i} \xi^{O_\ell} \rangle_{\text{bath}}$ in the Born-Markov approximation, where O_i and O_ℓ are system operators. We apply the standard Heisenberg-Langevin theory where the interaction of the system with the external bath is specified in terms of a Hamiltonian $H_{\text{sys}-\text{bath}}$ that couples the bath modes linearly to the system operators, see e.g. [72]. The two statistically independent baths for the photons and for the atoms are the continuum of radiation modes outside the cavity. We consider the system-bath Hamiltonians in the interaction picture

$$H^{\text{atoms}}_{\text{bath}-\text{sys}}(t) = \sum_{k,\ell=1}^{N} \left(\varepsilon_{k,\ell}\sigma^{+}_{\ell} b_k e^{i(\omega_z-\nu_k)t} + cc.\right), \quad H^{\text{photons}}_{\text{bath}-\text{sys}}(t) = \sum_{k} \left(\tilde{\varepsilon}_k a^{\dagger} c_k e^{i(\omega_0-\omega_k)t} + cc.\right), \tag{4.46}$$

where we have coupled all emitters $\sigma^{\pm}_{\ell}$ in $H^{\text{atoms}}_{\text{bath}-\text{sys}}(t)$ to one set of bath modes $b^{\dagger}_k b_k$ which also allows for collective emission of excitations outside of the cavity that become relevant in the superradiant regime. Here ω_0 and ω_z refer to effective frequencies for the photons and the atoms in a frame rotating at a frequency set by the external laser drive, see e.g. [26]. The Heisenberg equation of motions for the system and the bath operators can be written as

$$\partial_t a_t = -i[a_t, H_t] = -i\sum_{k} \tilde{\varepsilon}_k c_{k,t} e^{i(\omega_0-\omega_k)t}, \tag{4.47}$$

$$\partial_t b_{k,t} = -i[b_{k,t}, H_t] = -i\sum_{\ell=1}^{N} \varepsilon^{*}_{k,\ell}\sigma^{-}_{\ell,t} e^{-i(\omega_z-\nu_k)t}, \tag{4.48}$$

$$\partial_t c_{k,t} = -i[b_{k,t}, H_t] = -i\sum_{\ell=1}^{N} \tilde{\varepsilon}^{*}_{k,\ell} a_t e^{-i(\omega_z-\omega_k)t}, \tag{4.49}$$

$$\partial \sigma^{-}_{\ell',t} = -i[\sigma^{-}_{\ell',t}, H_t] = i\sum_{k} \sigma^{z}_{\ell',t} b_{k,t} e^{i(\omega_z-\nu_k)t}\varepsilon_{k,\ell}, \tag{4.50}$$

$$\partial \sigma^{z}_{\ell',t} = -i[\sigma^{z}_{\ell,t}, H_t] = \sum_{k} \left(-2i\sigma^{+}_{\ell',t} b_{k,t} e^{i(\omega_z-\nu_k)t}\varepsilon_{k,\ell'} - cc.\right). \tag{4.51}$$

Here we have used $H_t = H^{\text{atoms}}_{\text{bath}-\text{sys}}(t) + H^{\text{photons}}_{\text{bath}-\text{sys}}(t)$. We eliminate the bath degree of freedom by formal integration of their equations of motion

$$b_{k,t} = b_{k,0} - i\int_0^t dt' \sum_{\ell=1}^{N} \varepsilon^{*}_{k,\ell}\sigma^{-}_{\ell,t'} e^{-i(\omega_z-\nu_k)t'}, \quad c_{k,t} = c_{k,0} - i\int_0^t dt' \sum_{\ell=1}^{N} \tilde{\varepsilon}^{*}_{k,\ell} a_{t'} e^{-i(\omega_z-\omega_k)t'} \tag{4.52}$$

and insert Eqs. (4.52) and the conjugates into the equations of motion for the system operators given by Eqs. (4.47-4.51).

$$\partial_t a_t = \xi^{a}_t - \int_0^t dt' \sum_{k} |\tilde{\varepsilon}_k|^2 \mathcal{F}^{*}_{k,\omega_0,t,t'} a_{t'}, \tag{4.53}$$

$$\partial_t \sigma^{+}_{\ell',t} = \xi^{+}_{\ell',t} + \int_0^t dt' \sum_{\ell,k} |\varepsilon_k|^2 e^{i(\boldsymbol{k}-\boldsymbol{k_0})(\boldsymbol{r_\ell}-\boldsymbol{r_{\ell'}})} \mathcal{F}_{k,\omega_z,t,t'} \sigma^{+}_{\ell,t'}\sigma^{z}_{\ell',t}, \tag{4.54}$$

$$\partial_t \sigma^{-}_{\ell',t} = \xi^{-}_{\ell',t} + \int_0^t dt' \sum_{\ell,k} |\varepsilon_k|^2 e^{-i(\boldsymbol{k}-\boldsymbol{k_0})(\boldsymbol{r_\ell}-\boldsymbol{r_{\ell'}})} \mathcal{F}^{*}_{k,\omega_z,t,t'} \sigma^{z}_{\ell',t}\sigma^{-}_{\ell,t'}, \tag{4.55}$$

$$\partial_t \sigma^{z}_{\ell',t} = \xi^{z}_{\ell',t} - 2\left(\int_0^t dt' \sigma^{+}_{\ell',t} \sum_{\ell} |\varepsilon_k|^2 e^{i(\boldsymbol{k}-\boldsymbol{k_0})(\boldsymbol{r_\ell}-\boldsymbol{r_{\ell'}})} \mathcal{F}_{k,\omega_z,t,t'} \sigma^{-}_{\ell,t'} + cc.\right). \tag{4.56}$$

Equations (4.53)-(4.56) now contain only the dissipative and fluctuating components that arise from the interaction of the system with the external reservoir. The explicit form of the noise-operators can be read off as

$$\xi^a_t = -i\sum_k \tilde{\varepsilon}_k c_k(0) e^{-i(\omega_0-\omega_k)t}, \tag{4.57}$$

$$\xi^+_{\ell',t} = -i\sum_k b^+_k(0)\sigma^z_{\ell'}(t) e^{-i(\omega_z-\nu_k)t}\varepsilon^*_k e^{i(\boldsymbol{k}-\boldsymbol{k_0})\boldsymbol{r}_{\ell'}}, \tag{4.58}$$

$$\xi^-_{\ell',t} = i\sum_k \sigma^z_{\ell',t} b_k(0) e^{i(\omega_z-\nu_k)t}\varepsilon_k e^{-i(\boldsymbol{k}-\boldsymbol{k_0})\boldsymbol{r}_{\ell'}}, \tag{4.59}$$

$$\xi^z_{\ell',t} = \sum_k \Big(2ib^+_k(0)\sigma^-_{\ell',t}\varepsilon^*_k e^{-i(\omega_z-\nu_k)t} e^{i(\boldsymbol{k}-\boldsymbol{k_0})\boldsymbol{r}_{\ell'}} + cc.\Big), \tag{4.60}$$

within the Born-Markov approximation, the frequency independent damping constants are parametrised by the relations

$$\gamma\delta(t-t') = \sum_k |\varepsilon_k|^2 \mathcal{F}_{k,t,t'} = 2\pi|\varepsilon_{\omega_z}|^2\mathcal{D}(\omega_z)\delta(t-t'), \tag{4.61}$$

$$2\kappa\delta(t-t') = \sum_k |\tilde{\varepsilon}_k|^2 \mathcal{F}_{k,t,t'} = 2\pi|\varepsilon_{\omega_0}|^2\mathcal{D}(\omega_0)\delta(t-t'),$$

$$\mathcal{F}_{k,\omega,t,t'} = \exp[-i(\omega-\nu_k)(t-t')]. \tag{4.62}$$

Here, we have taken $\varepsilon_{k,\ell} = \varepsilon_k e^{-i(\boldsymbol{k}-\boldsymbol{k}_0)\boldsymbol{r}_\ell}$ as the cavity-shifted, spatially dependent atom-photon coupling to the bath modes b_k outside of the cavity, where $\boldsymbol{k_0}$ is the cavity wave vector. $\mathcal{D}(\omega_0)$ and $\mathcal{D}(\omega_z)$ are the density of states of the bath modes and $\varepsilon_{\omega_0}, \varepsilon_{\omega_z}$ are the microscopic system-bath coupling constants evaluated at the effective photon frequency ω_0 and the effective atom frequency ω_z.

4.4.1. Adiabatic elimination of the photons in the presence of noise

We detail the elimination of the cavity photons in the presence of photonic noise functions $(\xi^a, \xi^{a^\dagger})$ below. As a result, the local atomic components $(\sigma^x_i, \sigma^y_i, \sigma^z_i)$ at site i inherit additional noise from the photons with strength $\propto \frac{2\kappa J}{\omega_0}$, where $J = 4\frac{g^2\omega_0}{\omega_0^2+\kappa^2}$. Since the photons mediate an all-to-all coupling of the atoms for the deterministic dynamics, the noise inherited from the photons adds to the collective loss term of the atoms $\sim \gamma\beta$ in the σ^y and σ^z-channel. However, since both co- and counter-rotating terms $\sim (a + a^\dagger)\sum_\ell \sigma^x_\ell$ are present in the Dicke-Hamiltonian, the σ^x-channel does not inherit a photonic noise component. Also, there are no additional dissipative contributions that appear in the deterministic equations of motion for the atoms $\sim \kappa g^2$ due to the destructive interference of the coupling to the photons in the form of $(a + a^\dagger)$.

On the level of single operator expectation values for the system variables $\langle . \rangle \equiv \langle . \rangle_{\text{sys}}$ one can define a collective variable for the atoms σ^β as well as a collective variable for the atomic noise ξ^β and a photon noise η that appears for the macroscopic expectation value α for the photons

$$\sigma^\beta = \sum_{\ell=1}^N \langle \sigma^\beta_\ell \rangle / N, \quad \xi^\beta = \frac{1}{\sqrt{N}}\sum_\ell \langle \xi^\beta_\ell \rangle / \sqrt{N}, \tag{4.63}$$

$$\eta = \langle \xi^a \rangle / \sqrt{N}, \quad \alpha = \langle a \rangle / \sqrt{N}. \tag{4.64}$$

These averages must be taken with care. It indicates only the quantum mechanical average of system operators and not the noise average, which corresponds to the expectation value of bath operators. The first and second moments of the noise are $\langle \xi^\alpha \rangle_{\text{noise}} = 0$ and $(\langle . \rangle_{\text{noise}}$ indicating noise average, $\langle . \rangle_{\text{sys+bath}}$ average of system and bath operators). We start by considering the Heisenberg-Langevin equations given in Eq. (4.8) - (4.11) for single operator expectation values

$$\begin{aligned}\partial_t \alpha &= -\left(\kappa + i\omega_0\right)\alpha - ig\sigma^x + \eta \ , && (4.65)\\ \partial_t \sigma^y &= \omega_z \sigma^x - \left[2g(\alpha+\alpha^*) - \gamma\beta\sigma^y\right]\sigma^z - \gamma\sigma^y + \xi^y \ , && (4.66)\\ \partial_t \sigma^z &= 2g(\alpha+\alpha^*)\sigma^y - 2\gamma(1+\sigma^z) - \gamma\beta[\sigma^x\sigma^x + \sigma^y\sigma^y] + \xi^z. && (4.67)\end{aligned}$$

We eliminate the gapped ($\omega_0 \neq 0, \omega_0 \gg \kappa, \gamma, \omega_0 > \omega_z$) photon degrees of freedom ($\partial_t \alpha = 0$) to obtain their steady-state value as

$$\alpha + \alpha^* = \frac{-\eta + ig\sigma^x}{-\kappa - i\omega_0} + \frac{-\eta^* - ig\sigma^x}{-\kappa + i\omega_0}. \qquad (4.68)$$

Plugging Eq. (4.68) in Eq. (4.66) and in Eq. (4.67) leads to a redefined noise function in the $\sigma^{y(z)}$-channel

$$\begin{aligned}\tilde{\xi}^{y(z)} &= \xi^{y(z)} \mp \frac{2g}{\kappa^2+\omega_0^2}\sigma^{z(y)}\Big[\kappa(\eta+\eta^*) - i\omega_0(\eta-\eta^*)\Big] && (4.69)\\ \partial_t \sigma^y &= \omega_z\sigma^x + J\sigma^x\sigma^z + \gamma\beta\sigma^y\sigma^z - \gamma\sigma^y + \tilde{\xi}^y && (4.70)\\ \partial_t \sigma^z &= -J\sigma^x\sigma^y - 2\gamma(1+\sigma^z) - \gamma\beta[\sigma^x\sigma^x + \sigma^y\sigma^y] + \tilde{\xi}^z && (4.71)\end{aligned}$$

The covariances of the atoms now contain a noise contribution from the photon field

$$\begin{aligned}\langle \tilde{\xi}^{y(z)}\tilde{\xi}^{y(z)}\rangle_{\text{noise}} &= \langle \xi^{y(z)}\xi^{y(z)}\rangle_{\text{noise}} + \sigma^{z(y)}\sigma^{z(y)}\frac{J}{\omega_0}\left\langle \eta^*\eta + \eta\eta^*\right\rangle_{\text{noise}}, && (4.72)\\ \langle \tilde{\xi}^{y}\tilde{\xi}^{z}\rangle_{\text{noise}} &= \langle \xi^{y}\xi^{z}\rangle_{\text{noise}} - \sigma^{z}\sigma^{y}\frac{J}{\omega_0}\left\langle \eta^*\eta + \eta\eta^*\right\rangle_{\text{noise}}. && (4.73)\end{aligned}$$

Taking the bath for the photons to be in a zero temperature vacuum state, the noise correlation function is, according to Eq. (4.57)

$$\langle \eta^*\eta + \eta\eta^*\rangle = 2\kappa/N\delta(t-t'). \qquad (4.74)$$

We remark that the so-obtained variances for the atoms and photons are equivalent to the variances that would be obtained in the associated MSRDJ-path integral [189, 190, 191] for the complex fields (a_t, a_t^*) and for the real fields $(\sigma_t^x, \sigma_t^y, \sigma_t^z)$ where the photon degrees of freedom are then integrated out exactly for the zero-frequency sector. We show this explicitly in Sec. 5.1.

4.4.2. Derivation of classical noise kernel χ for stochastic optical Bloch equations

> We evaluate the operator-valued noise-kernel of the atoms $\chi_{i\ell}(\sigma) = \langle \xi^{O_i}\xi^{O_\ell}\rangle_{\text{bath}}$ and show how it can be mapped to a classical noise matrix.

The evaluation of noise correlation functions is now performed as an average over the bath degrees of freedom denoted as $\langle . \rangle_{\text{bath}}$ where the expectation value is a thermal average over a zero-temperature bath. Since the external bath is described by the vacuum and only terms $\propto b_k(0)b_k^\dagger(0)$ contribute, correlations of the form $\langle \xi^+(t)\ldots\rangle = 0$ and $\langle \ldots \xi^-(t)\rangle = 0$ vanish.

The noise-correlations for the atomic degrees of freedom can be expressed by using Eqs. (4.58-4.60) as

$$\langle \xi^i_{\ell',t'}\xi^j_{\ell,t}\rangle_{\text{bath}} = 2\gamma\delta(t-t')\Big[\delta_{\ell,\ell'} + (1-\delta_{\ell,\ell'})\alpha\Big]\tilde{\chi}^{ij}_{\ell'\ell}, \qquad (4.75)$$

$$\tilde{\chi}^{ij}_{\ell'\ell} = \begin{pmatrix} 0 & 0 & 0 \\ \sigma^z_{\ell',t}\sigma^z_{\ell,t} & 0 & -2\sigma^z_{\ell',t}\sigma^-_{\ell,t} \\ -2\sigma^+_{\ell',t}\sigma^z_{\ell,t} & 0 & 4\sigma^+_{\ell',t}\sigma^-_{\ell,t}\end{pmatrix}_{ij} \qquad (4.76)$$

where the indices $(i,j) \in (+,-,z)$ refer to the atomic variables. The entries of the matrix $\tilde{\chi}^{ij}_{\ell'\ell}$ are still dependent on the system operators σ^i_ℓ at site ℓ. With the relations $\xi^x_\ell = \xi^+_\ell + \xi^-_\ell$ and $\xi^y_\ell = -i(\xi^+_\ell - \xi^-_\ell)$ we rotate from $(+,-,z)$ into the (x,y,z) basis

$$\tilde{\chi}^{ij}_{\ell'\ell} = \begin{pmatrix} \sigma^z_{\ell'}\sigma^z_\ell & -i\sigma^z_{\ell'}\sigma^z_\ell & -\sigma^z_{\ell'}(\sigma^x_\ell - i\sigma^y_\ell) \\ i\sigma^z_{\ell'}\sigma^z_\ell & \sigma^z_{\ell'}\sigma^z_\ell & -i\sigma^z_{\ell'}(\sigma^x_{\ell'} - i\sigma^y_{\ell'}) \\ -(\sigma^x_{\ell'} + i\sigma^y_{\ell'})\sigma^z_\ell & i(\sigma^x_{\ell'} + i\sigma^y_{\ell'})\sigma^z_\ell & \tilde{\chi}^{zz}_{\ell\ell} \end{pmatrix}_{ij} , \tag{4.77}$$

with $\tilde{\chi}^{zz}_{\ell\ell'} = (\sigma^x_{\ell'}\sigma^x_\ell + \sigma^y_{\ell'}\sigma^y_\ell + i(\sigma^y_{\ell'}\sigma^x_\ell - \sigma^x_{\ell'}\sigma^y_\ell))$. For the components with $\ell = \ell'$ the local spin algebra can be used to write the correlation matrix for the local noise components as

$$\tilde{\chi}^{ij}_{\ell\ell} = \begin{pmatrix} 1 & -i & (\sigma^x_\ell - i\sigma^y_\ell) \\ i & 1 & i(\sigma^x_\ell - i\sigma^y_\ell) \\ (\sigma^x_\ell + i\sigma^y_\ell) & -i(\sigma^x_\ell + i\sigma^y_\ell) & 2(1+\sigma^z_\ell) \end{pmatrix}_{ij} . \tag{4.78}$$

Equations (4.77)-(4.78) together with Eq. (4.69) are the starting point to obtain the corresponding classical noise kernel $\chi(\sigma)$. This is consistent with the noise matrix obtained from the generalised Einstein Relations in Eq. (1.150).

Mapping the photonic and atomic noise correlations to a classical noise kernel

The general correlation matrix $\chi_{\ell\ell'}$ in Eq. (4.77) was obtained by averaging over the bath degrees of freedom and still depends on the system operators σ^α_ℓ with $\alpha = (x,y,z)$ and ℓ as the local site index. For a mapping to a classical noise correlation matrix it is necessary to erase the information on commutation relations. This is achieved by symmetrising the matrix entries $\chi^{ij}_{\ell\ell'}$ which amounts to taking their real part $\mathrm{Re}[\chi^{ij}_{\ell\ell'}]$. This procedure leads to a symmetric, real and positive definite noise kernel and is thus well-defined.

We are interested in the noise strength for the equations of motion of the collective variable $\sigma^\alpha = \sum_\ell \langle\sigma^\alpha_\ell\rangle_{\text{sys}} / N$ with the averaged noise $\tilde{\xi}^\alpha = \sum_\ell \langle\tilde{\xi}^\alpha_\ell\rangle_{\text{sys}} / \sqrt{N}$, where $\langle . \rangle_{\text{sys}}$ is a quantum mechanical average over the system variables. Here $\tilde{\xi}^\alpha$ is the modified noise function of the atoms that contains both an atomic and photonic contribution for $\alpha = (y,z)$ stemming from the elimination of the cavity degrees of freedom and is defined in Eq. (4.69). The σ^x-channel is free of a photonic contribution as discussed previously. The noise average $\langle . \rangle_{\text{noise}}$ to obtain the classical correlation matrix $\boldsymbol{\chi}$ is then defined by averaging over both bath and system degrees of freedom

$$\langle\tilde{\xi}^\alpha\tilde{\xi}^\beta\rangle_{\text{noise}} = N^{-1}\langle\sum_{\ell,m}\tilde{\xi}^\alpha_\ell\tilde{\xi}^\beta_m\rangle_{\text{sys+bath}} \tag{4.79}$$

$$= \delta(t-t')N^{-1}\sum_{\ell m}\left(\gamma\left[\delta_{\ell,m} + (1-\delta_{\ell,m})\alpha\right]\mathrm{Re}[\langle\tilde{\chi}^{\alpha\beta}_{\ell m}\rangle_{\text{sys}}] + N^{-1}\frac{2J\kappa}{\omega_0}\langle M^{\alpha\beta}_{\ell m}\rangle_{\text{sys}}\right)$$

$$= \delta(t-t')\chi^{\alpha\beta}(\boldsymbol{\sigma}), \tag{4.80}$$

where the contributions from the photons is specified as

$$\langle M^{yy}_{ij}\rangle_{\text{sys}} = \langle\sigma^z_i\rangle\langle\sigma^z_j\rangle , \quad \langle M^{zz}_{ij}\rangle_{\text{sys}} = \langle\sigma^y_i\rangle\langle\sigma^y_j\rangle , \quad \langle M^{yz}_{ij}\rangle_{\text{sys}} = \langle M^{yz}_{ij}\rangle_{\text{sys}} = -\langle\sigma^z_i\rangle\langle\sigma^y_j\rangle . \tag{4.81}$$

The noise correlation matrix $\chi^{\alpha\beta}(\boldsymbol{\sigma})$ is specified in Eq. (4.85) and contains now a noise component from the local, uncorrelated loss processes $\sim \gamma$ as well as from the collective loss processes $\sim \gamma\beta = \gamma\alpha(N-1)$, where $\beta = \mathit{const.}$ in the thermodynamic limit and a contribution from the photons $\sim 2J\kappa/\omega_0$. From Eq. (4.80) one can see that the variance of the sum of the random noise functions $\sum_\ell \langle\tilde{\xi}^\alpha_\ell\rangle_{\text{sys}}$ scales with the number of atoms N as expected for instance from the central limit theorem.

4.5. Stochastic optical Bloch equations

> We analyse the fluctuation dynamics in the bistability regime by an explicit numerical simulation of the stochastic optical Bloch equations. We find that the bistability regime collapses to a dissipative first-order phase transition that is driven by non-thermal fluctuations.

[2]Upon elimination of the cavity photons, we obtain the dynamical equation of motion of the system in a semiclassical, large N framework as stochastic optical Bloch equations

$$\partial_t \sigma^\alpha = D^\alpha + \frac{1}{\sqrt{N}}\xi^\alpha, \tag{4.82}$$

with the definitions

$$\sigma^\beta = \sum_{\ell=1}^{N} \langle \sigma_\ell^\beta \rangle /N, \quad \xi^\beta = \sum_\ell \langle \xi_\ell^\beta \rangle / \sqrt{N}. \tag{4.83}$$

The noise correlations for the atoms include the photonic contributions and are given as

$$\langle \xi^\alpha \xi^\beta \rangle_{\text{noise}} = N^{-1} \langle \sum_{\ell,m} \xi_\ell^\alpha \xi_m^\beta \rangle_{\text{sys+bath}} = \delta(t-t')\chi^{\alpha\beta}(\boldsymbol{\sigma}). \tag{4.84}$$

In the large-N limit, the covariance matrix is

$$\boldsymbol{\chi} = 2 \begin{pmatrix} \gamma\left(\beta(\sigma^z)^2 + 1\right) & \dots & \dots \\ 0 & (\tilde{\kappa} + \gamma\beta)\,(\sigma^z)^2 + \gamma & \dots \\ \sigma^x(1-\beta\sigma^z)\gamma & \sigma^y\left(\gamma - (\tilde{\kappa}+\gamma\beta)\,\sigma^z\right) & \chi_{3,3}(\sigma) \end{pmatrix}, \tag{4.85}$$

where $\chi_{3,3}(\sigma) = \tilde{\kappa}(\sigma^y)^2 + \gamma[\beta((\sigma^x)^2 + (\sigma^y)^2) + 2(\sigma^z + 1)]$, $\tilde{\kappa} = \kappa J/\omega_0$ and $\boldsymbol{\chi} = \boldsymbol{\chi}^{\mathrm{T}}$ is symmetric, real and positive semi-definite for $\sum_\alpha (\sigma^\alpha)^2 \leq 1$, i.e. as long as $\boldsymbol{\sigma}$ represents a state within the Bloch sphere. For a continuous time evolution, neither the deterministic force $\boldsymbol{D}$ nor the noise drives the system out of the Bloch sphere. The latter is ensured by $\boldsymbol{\chi}_\perp \sim ||\delta\boldsymbol{\sigma}||$, where $\boldsymbol{\chi}_\perp$ is the (local) perpendicular noise strength and $\delta\sigma$ the distance to the Bloch sphere.

Local noise terms break the translational invariance of the system. However, due to the infinite-range interactions of the Dicke system there is no spatial resolution and the description in terms of the collective variable σ^α is correct up to $\mathcal{O}(1/N)$. Locally induced, noise-driven spin flips cause energetic corrections of order $\mathcal{O}(J/N)$ such that for any finite $N < \infty$ the two fixed points can only be connected via a concatenation of $\mathcal{O}(N)$ subsequent noise kicks. Such collective events of noise kicks drive the system from the basin of attraction of one fixed point to the basin of attraction of the other. They occur on timescales set by τN where τ^{-1} is the state-dependent rate of a single spin flip set by the noise profile $\boldsymbol{\chi}(\sigma)$.

Within the bistable regime, the deterministic optical Bloch equations split the Bloch sphere into three basins of attraction, separated by a repulsive manifold, which cannot be crossed by any deterministic path, as illustrated in Fig. 4.4.

The initial Liouvillian quantum master equation given in Eqs. (4.3-4.5) however is predicted to have a unique stationary state for finite N [86]. This state would be obtained by

---

[2] The first subsection of this section is taken almost verbatim from the publication J. Gelhausen and M. Buchhold, Phys. Rev. A **97**, 023807 (2018).

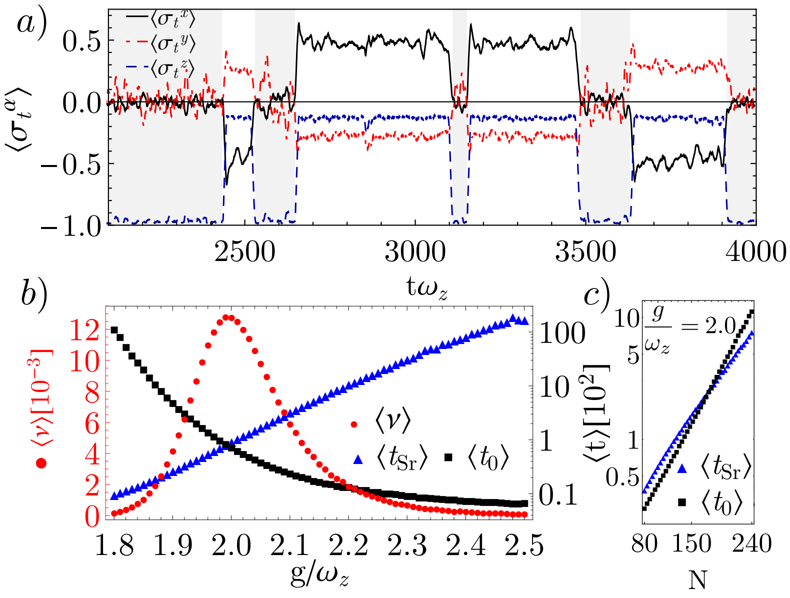

Figure 4.8.: (a) Noise-induced transitions from the empty (shaded) to the superradiant state. Each line is a moving average over a time window $(t \pm 4)\omega_z$. (b) Log-plot of mean times spent in the superradiant- $\langle t_{Sr}\rangle$ and in the empty cavity state $\langle t_0\rangle$ corresponding to vertical line in Fig. 4.10a). Circular shapes are mean transition frequencies $\langle\nu\rangle = \#\text{jumps}/t_\Sigma$ obtained from counting the total number of jumps normalised to the total simulation time t_Σ (c) Exponential sensitivity of mean occupation times to the number of atoms N.

diagonalizing the Liouvillian and by finding its right-eigenvector that corresponds to the zero-eigenvalue state. Let us remark that this procedure does not ignore the noise correlations since they can be generated from the Liouvillian through the generalised Einstein relations. In the absence of the noise function, the mean-field equations however fail to predict the unique stationary state. This lack of ergodicity, is overcome by considering the original HLE that explicitly contain the influence of the environment onto the system through the presence of noise-operators.

4.5.1. Real-time dynamics and fluctuation induced first-order phase transition

[3]In contrast to a bistable system in equilibrium, where the occupation of the states in the long-time and large system-size limit is entirely determined by a mean-field analysis of the minimum of a free energy potential, the occupation times of the metastable states out-of equilibrium can only be determined beyond mean-field by including fluctuations of $\mathcal{O}(1/N)$ in a numerical simulation for finite $N < \infty$ [20]. Simulation of Eq. (4.82) requires a careful implementation of the thermodynamic limit. Taking $N \to \infty$ first, leads the noise $\sim 1/\sqrt{N}$ to vanish and one ends up with the deterministic equations, i.e. two disconnected steady states. On the other hand, taking $t \to \infty$ first and then $N \to \infty$, for any finite N the long-time behavior is characterized by an admixture of the empty and the superradiant state. We investigate the stationary state distributions and the statistics for the occupations times in Sec. 4.5.2.

---

[3] This subsection is taken almost verbatim from the publication J. Gelhausen and M. Buchhold, Phys. Rev. A **97**, 023807 (2018).

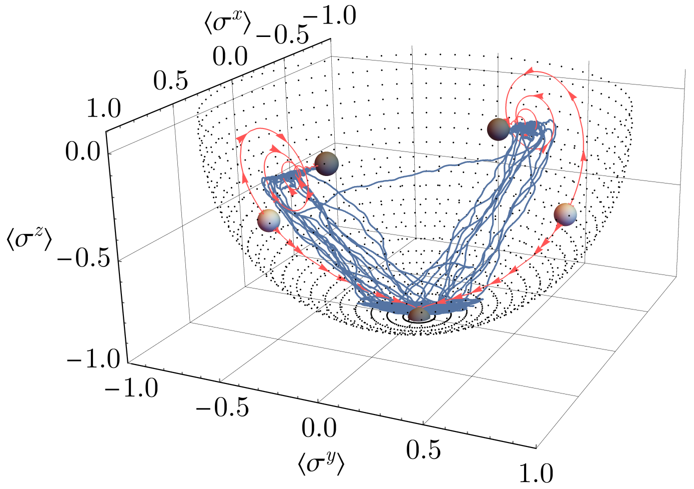

Figure 4.9.: Steady state landscape of the Bloch equations (4.82) in the bistable regime. Red lines (with arrows) departing from repulsive fixed points show deterministic motion, blue lines (no arrows) show noise-induced dynamics. There are 3 attractive (black sphere) and 2 repulsive (gray sphere) fixed points, interrelated by the Ising symmetry $(\sigma^x, \sigma^y, \sigma^z) \rightarrow (-\sigma^x, -\sigma^y, \sigma^z)$. Dotted points map out the surface of the unit Bloch sphere and serve as a guide to the eye.

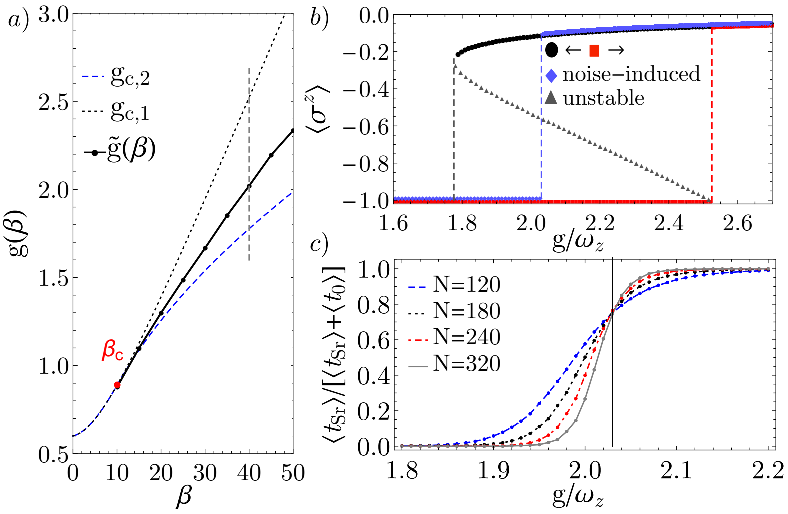

Figure 4.10.: a) Mean-field bistability region delimited by the spinodal (broken) lines and fluctuation induced first order transition (bold) line at $\tilde{g}(\beta)$. Vertical line cuts through the phase diagram as shown in b) and c). b) (Mean-field) Hysteresis inside the bistable regime obtained by adiabatically following the increasing (red), decreasing (black) atom-light coupling. c) Average amount of time spent in the superradiant state obtained from stochastic Bloch equations for different atom numbers N, see Eq. (4.82). For $N \rightarrow \infty$ it approaches a step function, revealing a first-order transition at $\tilde{g}$ (intersection), as shown in a). Parameter set $\omega_0 = 1.4\omega_z$, $\gamma = \kappa = 0.2\omega_z$, with $\beta = 40$.

The dynamics of the spin vector $\boldsymbol{\sigma}$ is obtained by interpreting Eq. (4.82) in an Itô-sense and numerically simulating the time-evolution with a two-stage stochastic Runge-Kutta algorithm [192, 193]. For a detailed description of the implementation of the algorithm, see App. A. The corresponding dynamics of $\boldsymbol{\sigma}$ including rare fluctuations between the dark and the bright cavity are visualized in Fig. 4.9 and, with temporal resolution, in Fig. 4.8a.

Tuning the atom-light coupling g through the bistable regime at fixed collective loss rate $\gamma\beta$, Fig. 4.10a, we obtain a histogram for the distribution of time intervals spent in the empty (t_0) and in the superradiant state (t_{Sr}), see Fig. 4.11. The mean occupation times $\langle t_\alpha \rangle$ in Fig. 4.8b) are obtained by summing over all intervals $\langle t_\alpha \rangle = \sum_i t_{i,\alpha} / \sum_i$ with $\alpha = \{a, Sr\}$ as seen in Fig. 4.8a). We observe an exponential dependence of $\log \langle t_{Sr} \rangle \sim g$ in the superradiant state and a strongly stretched exponential $\log \langle t_0 \rangle \sim g^{-10}$ in the empty state, Fig. 4.8b.

For any $N < \infty$, the steady state is a statistical mixture of the empty and the superradiant state and the degree of mixing is expressed via the superradiance occupation ratio $\rho_{Sr} = \langle t_{Sr} \rangle / (\langle t_{Sr} \rangle + \langle t_0 \rangle)$. It interpolates continuously between $\rho_{Sr}(g_{c,2}) = 0$ and $\rho_{Sr}(g_{c,1}) = 1$ as a function of the atom-light coupling g and varies on a scale $\Delta g \sim 1/N$, see Fig. 4.10c. In the thermodynamic limit $N \to \infty$, $\rho_{Sr} \to \Theta(g - \tilde{g})$ approaches a step-function, indicating a discontinuous jump and a first order phase transition from the empty to the superradiant state at a critical coupling $\tilde{g}(\beta)$, Fig 4.10a.

The exponential increase of the occupation times $\log\langle t_{Sr,0} \rangle \sim N$ is depicted in Fig. 4.8c. This suggests a typical Arrhenius law $\langle t_{Sr,0} \rangle = A_{Sr,0} \exp(N\psi_{Sr,0})$, which is confirmed by the classical MSRJD action [189, 190, 191] associated to the stochastical optical Bloch equations (4.82). Here, ψ_α is the non-equilibrium potential, which depends both on the path and on the relative noise strength between the two stable solutions and lacks the interpretation of a free energy functional [20]. This statement will become more clear in chapter 5. The Ising symmetry reduces the long time dynamics to that of an effective two-level system, which always fulfills detailed balance, and makes the non-equilibrium nature of the bistability hardly observable on the level of the transition rates. Lifting the degeneracy between the two superradiant states leads to three genuinely different metastable states. This three-level configuration explicitly lacks detailed balance and allows for a circulating current in the stationary state which is a clear non-equilibrium signature that is experimentally accessible, see Appendix C.

4.5.2. Statistics for the fluctuation dynamics in the bistability regime

> We collect histogram data from a numerical simulation of Eq. (4.82) to construct a probability distribution P for the atomic components $(\sigma^x, \sigma^y, \sigma^z)$ and a probability distribution $P_\downarrow(t_0)$ for the residence times $\{t_0\}$ in the empty atom-cavity state in the stationary state for finite values of N with $1 \ll N \ll \infty$. We show numerically and theoretically that the residence times are exponentially distributed. By projecting the statistics $P(\sigma^x, \sigma^y, \sigma^z)$ onto a single variable σ^α, we compare the stationary state distribution to a power series expansion of a scalar function $\Gamma(\sigma^\alpha)$ as $P(\sigma^\alpha) \sim \exp(-\Gamma(\sigma^\alpha))$.

We are interested in the statistical properties of the fluctuation dynamics such as the mean-residence times $\langle \Delta t \rangle_{0,Sr}$ in the empty (0) and the superradiant state (Sr) and their corresponding decay rates $\lambda_{0,Sr}$. A decay event triggers the transition from the empty into the superradiant state or vice versa. We obtain statistical information on the residence times by a numerical simulation of equation Eq. (4.83).

Keeping N finite and then simulating Eq. (4.82) for a long time ($t \to \infty$) generates a time sequence where the state of the system constantly changes between the empty and the superradiant cavity. The time that the system spends in either of these states (referred to as residence or occupation times) before it makes a transition into the other state is distributed randomly. We want to ascertain the probability distribution for these random time intervals in the steady state. A steady-state is now understood as the statement that for finite N and long simulation times t the ratio of the mean of the residence times stays constant $\langle t\rangle_0 / \langle t\rangle_{Sr} = const.$. For finite N there is still a parameter regime in which the residence times of both states can be of the same order of magnitude $\langle t\rangle_0 \sim \langle t\rangle_{Sr}$.

The randomly distributed residence times for both states can be described with the same probability density distribution and are distinguished by their decay rate $\lambda_{(0,Sr)}$ only. Since the system is memoryless we assume these two probability density distributions to be independent of one another. We obtain the probability density function for the distribution of residence times in either state from a collection of histogram data. The residence times are found to obey an exponential distribution as

$$\mathcal{P}_{(0,Sr)}(\Delta t) = \lambda_{(0,Sr)} \exp\left(-\lambda_{(0,Sr)}\Delta t\right). \tag{4.86}$$

This is illustrated in Fig. 4.11. Since the residence times are continuously distributed, $\mathcal{P}_{(0,Sr)}$ is a probability density and $\mathcal{P}_{(0,Sr)}(\Delta t)dt$ is the probability for observing a residence time between $[\Delta t, \Delta t + dt]$. $\lambda_{(0,Sr)}$ is an event rate and gives an indication of fluctuation induced transitions per unit time interval. From Eq. (4.86) it is clear that the mean residence time is linked to $\lambda_{0,Sr}$ as

$$\int_0^\infty d(\Delta t)\mathcal{P}_{0,Sr}(\Delta t)\Delta t = 1/\lambda_{(0,Sr)} \equiv \langle \Delta t\rangle_{0,Sr}. \tag{4.87}$$

In the following we briefly review why Eq. (4.86) generally describes the distribution of time intervals between two uncorrelated decay events. It naturally emerges for instance to describe the time differences between two decay events of an ensemble of N independently decaying radioactive atoms. The derivation that follows is therefore a standard derivation that can be found in elementary textbooks on radioactive decay or statistics, see e.g. [194].

Derivation for probability density of residence times

The probability $\omega_{(0,Sr)}$ that a rare noise-event in the time δt drives the system from the basin of attraction of one fixed point into the other is modelled as

$$\omega_{(0,Sr)}(\delta t) = \lambda_{(0,Sr)}\delta t. \tag{4.88}$$

which is valid for times much smaller than the mean residence time $\delta t \ll \langle \Delta t\rangle_{0,Sr}$ in the corresponding state. Consequently, the (survival) probability to still find the system in its initial state after time δt is then approximated as

$$P_{(0,Sr)}(\delta t) = 1 - \omega_{0,Sr}(\delta t). \tag{4.89}$$

In order to find the survival probability $P_{(0,Sr)}$ for an arbitrary length of time Δt, we consider k slices of this time interval $\delta t_k = \Delta t/k$ and then take the limit $k \to \infty$. The survival probability in this limit is then the product to survive in every time slice k and given as

$$\begin{aligned} P_{(0,Sr)}(\Delta t) &= \lim_{k\to\infty} \Pi_k[P_{0,Sr}(\delta t_k)] = \lim_{k\to\infty} \Pi_k\left[1 - \omega_{(0,Sr)}(\Delta t/k)\right] = \lim_{k\to\infty}\left(1 - \lambda_{(0,Sr)}\frac{\Delta t}{k}\right)^k \\ &= \exp\left(-\lambda_{(0,Sr)}\Delta t\right). \end{aligned} \tag{4.90}$$

$P_{(0,Sr)}(\Delta t)$ is the probability to find the system in the empty(superradiant) state after a length of time Δt where at $\Delta t = 0$ the system is initially in that same state.
However, numerically we cannot directly measure the probability $P_{(0,Sr)}(\Delta t)$ but we can measure the residence times in either state before the system decays, i.e. the lifetimes of the states. Their distribution follows Eq. (4.86) as we review in the following paragraph. The probability $W_{0,Sr}$ to surive for a time interval of Δt and to decay thereafter in a window of time dt is a combination of the two probabilities for these two events and is given as

$$W_{(0,Sr)}(\Delta t) = P_{(0,Sr)}(\Delta t) \cdot \omega_{(0,Sr)}(dt) = \exp\left(-\lambda_{(0,Sr)}\Delta t\right)\lambda_{(0,Sr)}dt. \tag{4.91}$$

The probability density for the distribution of residence times Δt is then obtained as

$$\mathcal{P}_{0,Sr}(\Delta t) = \frac{dW_{(0,Sr)}(\Delta t)}{dt}, \tag{4.92}$$

which is given by Eq. (4.86). We can use this distribution to fit the numerically obtained histograms as shown in Fig. 4.11.

From the probability density, one can calculate the probability that the system has made a transition into the only other state after a time Δt as

$$\int_0^{\Delta t} d(\Delta t)' \mathcal{P}_{0,Sr}(\Delta t') = 1 - \exp\left(-\lambda_{(0,Sr)}\Delta t\right) = 1 - P_{0,Sr}(\Delta t). \tag{4.93}$$

This result is consistent with what was expected on the basis of Eq. (4.90).

The statistics for the distribution of residence times is the same as the statistics for the distribution of time differences Δt that separate two successive decays in an ensemble of N radioactive atoms. Where λ then describes the decay rate of the ensemble of radioactive atoms. The residence time intervals of either the empty or the superradiant state are independent from one another (since the system is memoryless) and are characterised by their own decay rate λ_0 and λ_{Sr}, respectively. Therefore, each recorded time interval in the empty or the superradiant state can be considered to model the lifetime of a single atom. If we consider N of these time intervals, this corresponds to the behaviour of an ensemble of N independently decaying atoms.

Stationary state distribution of occupation times and magnetisations for finite N

To obtain $P_\downarrow$, the distribution of time intervals in the 'dark cavity' in the stationary state, we fit the distribution of residence times of the empty state according to the expected distribution in Eq. (4.86) with the mean residence times as the only fitting parameter, and observe good agreement, see Fig. 4.11a and the inset.

The probability distribution for the magnetisation can be visualized in the (σ^x, σ^y) plane, by projecting out the σ^z component as $P(\sigma^x, \sigma^y) = \int d\sigma^z P(\sigma^x, \sigma^y, \sigma^z)$. This illustrates that for finite N, the stationary state of the system is a statistical mixture of the superradiant and the empty atom-cavity system, see Fig. 4.12. The mirror symmetry constrains $P(\sigma^x, \sigma^y) = P(-\sigma^x, -\sigma^y)$. By projecting the steady-state distribution onto a single component, i.e. $P(\sigma^x) = \int d\sigma^y\ d\sigma^z\ P(\sigma^x, \sigma^y, \sigma^z) = 1/\mathcal{N} \exp(-\Gamma(x))$, where we have made an Ansatz for to parametrize the steady-state distribution with a dimensionless potential $\Gamma(x)$ of the dynamics in one spatial dimension with

$$\Gamma(\sigma_x) = \sum_{2n}^{12} \frac{1}{n}\alpha_n(\sigma^x)^n, \tag{4.94}$$

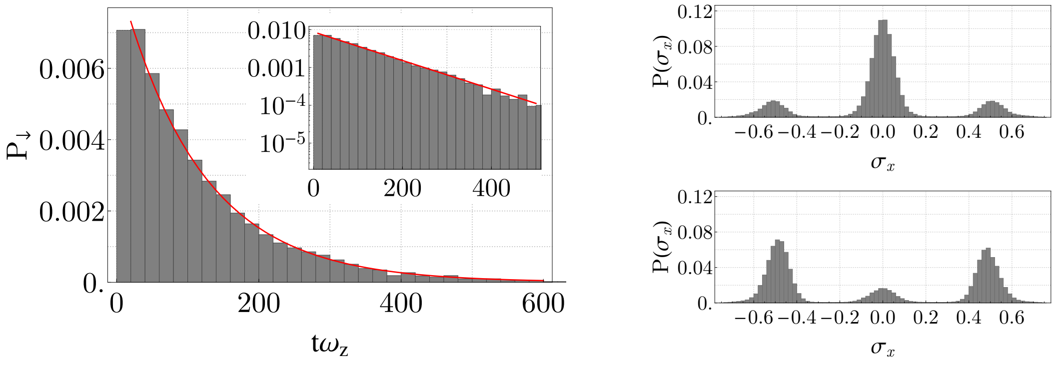

(a) (b)

Figure 4.11.: The probability distribution of time intervals in the empty state. (a) The distribution of time intervals is fitted with an exponential form $P_0(t\omega_z) = \lambda \exp(\lambda(t\omega_z))$, see Eq. (4.86). The extracted mean residence time is the inverse decay rate and obtained as $1/\lambda = \langle\tau\rangle_0 = 114.88(t\omega_z)$. Inset shows a log plot of the probability distribution. (b) Probability distribution of the of the order parameter σ_x in the long-time limit for a fixed atom-light coupling $g = 1.97\omega_z$ (top) and $g = 2.06\omega_z$ (bottom). It can clearly be seen that the steady-state can be interpreted as a mixture of both the empty and the super radiant mean-field steady-state. The Ising symmetry of the Dicke-Hamiltonian guarantees equal occupation of the two superradiant states related by $\sigma_x \to -\sigma_x$.

where $\{\alpha_n\}$ is a set of fitting parameters and $\mathcal{N}$ is the normalization. Due to the mirror symmetry, $\Gamma(\sigma^x)$ is characterized only by even powers of σ^x. in We show the potential $\Gamma(\sigma^x)$ for parameters slightly below the fluctuation induced first-order transition (see Fig. 4.10a) in Fig. 4.12b and for parameters slightly above the first-order transition in Fig. 4.12c. The form of the potential is consistent with what would have been expected from the form of a Free-Energy functional describing a thermal a first-order transition on the basis of Ginzburg-Landau theory. However, here the tuning parameter is not temperature but an external driving strength that influences the atom-light coupling. Let us note however that the dynamics of a one-component time-dependent variable with no sense of space can always be generated by some potential.

4.6. Numerical investigation of hysteresis

> We investigate the response of the system to a time-dependent sweep of the atom-light coupling. We do not compare different noise strength, but fix the number of atom-cavity emitters to $N = 200$ throughout this section.

We have shown that the bistable Dicke system far from equilibrium undergoes a first-order phase transition whose exact point $g^*(\beta)$ is determined by fluctuations in the thermodynamic limit $t \to \infty$ and $N \to \infty$. This transition line appears within the two mean-field critical points $g_{c,1}(\beta) < g^*(\beta) < g_{c,2}(\beta)$ that delimit the bistability region.

However, in an experimental realisation the first-order phase transition line is generally approached by varying the control parameter, i.e. the atom-light coupling with some time-dependence $g \to g(t)$. As this temporal variation is not infinitely slow, we expect deviations from the sharp jump behaviour at $g = g^*(\beta)$. The system can overshoot the critical point and stay in the initial metastable state past the critical point (hysteresis)

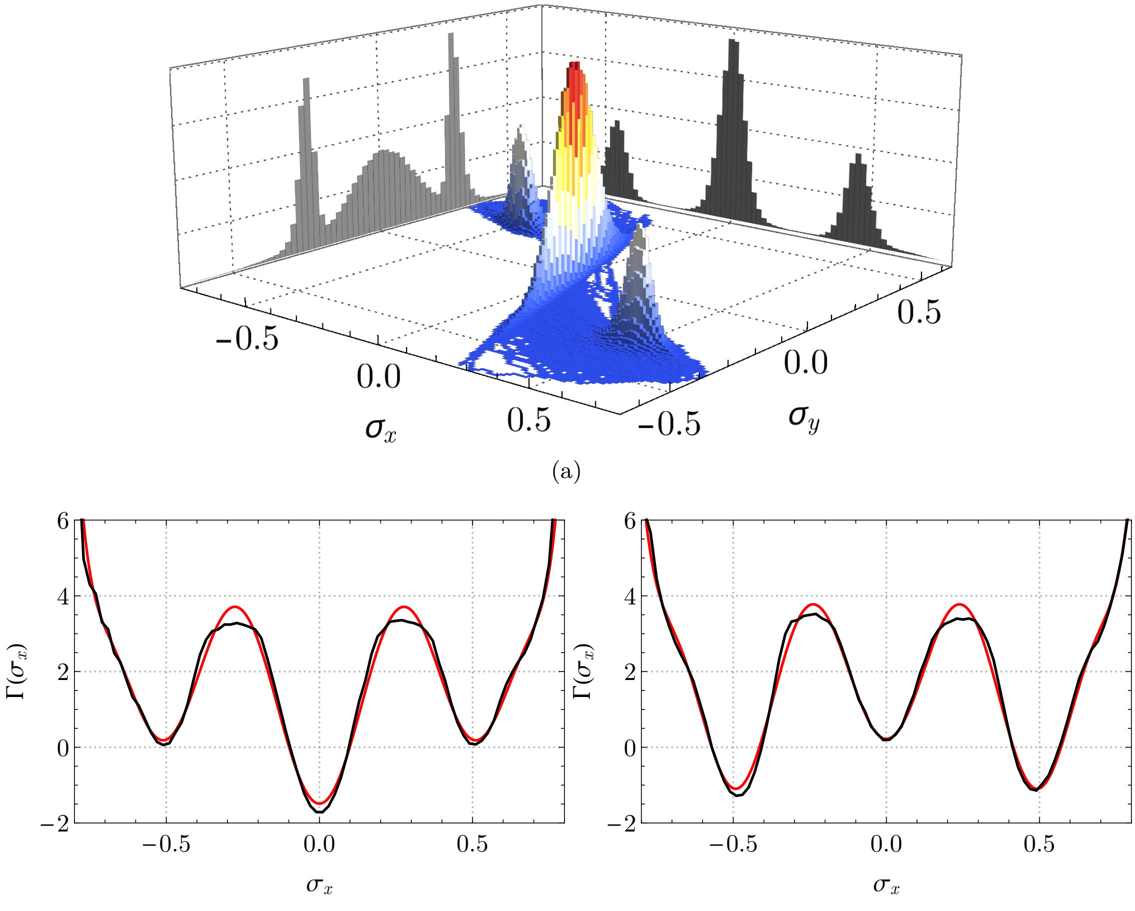

(a)

(b)

(c)

Figure 4.12.: (a) Probability Distribution $P(\sigma_x, \sigma_y)$ (colored) of the σ_x and σ_y values in the steady state for a fixed value of $g = 2.0\omega_z$ (unlabelled axis in arbitrary units). Projections on the walls show $P(\sigma_x) = \int P(\sigma_x, \sigma_y, \sigma_z) d\sigma_y d\sigma_z$ and $P(\sigma_y) = \int P(\sigma_x, \sigma_y, \sigma_z) d\sigma_x d\sigma_z$. Projections are scaled such that they are shadow images of $P(\sigma_x, \sigma_y)$. (b) and (c) show the results of fitting the distribution $P(\sigma^x)$ (black) with a dimensionless potential $\Gamma(\sigma^x)$ in the stationary state, see Eq. (4.94) (red) (b) Potential minima at the empty atom-cavity system, parameters $(g/\omega_z = 1.97, \beta = 40)$ (c) Superradiant states minimize the potential, parameters $(g/\omega_z = 2.06, \beta = 40)$.

before a rare fluctuation kicks the system to the competing metastable state at some value $g \neq g^*$. In the following, we quantify the response of the system to a linear variation of the control parameter as

$$g(t) = g_{c,2} + \dot{g}t\theta(t_s - t) - (t - 2t_s)\dot{g}\theta(t - t_s) \tag{4.95}$$

$$\dot{g} = (g_{c,1} - g_{c,2})/t_s. \tag{4.96}$$

The variation is chosen such that the control parameter varies linearly between the two spinodal line values from $g(0) = g_{c,2}$ to $g(t_s) = g_{c,1}$ and back again to $g(2t_s) = g_{c,1}$. Here $(g_{c,1} - g_{c,2})/t_s = \dot{g} = const.$ defines a sweep-velocity and t_s is a characteristic scanning time.

The response of the system to a time-dependent sweep of the control parameter is best understood as a rate competition of three timescales within the model, see [195].

- $\dot{g}$ the rate of change of the control parameter
- T_1^{-1} the local equilibration or relaxation time
- T_2^{-1} the non-local equilibration rate or "hop-over" time

The relaxation time scale T_1 determines how fast the system relaxes back to the fixed point in response to small perturbations caused by the random fluctuations. The non-local equilibration time-scale is the finite lifetime (decay time) T_2 of the empty and superradiant states due to large deviation caused by a rare fluctuation that can kick the system from one basin of attraction of the fixed point to the other basin of attraction of the fixed point. The times for a fluctuation induced hop is exponentially distributed and the timescale T_2 characterises the distribution as it is the average time it takes for a fluctuation induced switch, see Fig. 4.11.

4.6.1. Adiabaticity window for atom-light ramp with local and non-local relaxation time scales

With a variation of the control parameter, the steady-state landscape and especially the position of the superradiant fixed point changes in time. Experimentally one will observe one of three scenarios: (1) The adiabatic scenario is specified by a time window , see [195]

$$1/T_1 \gg \dot{g}(t) \gg 1/T_2. \tag{4.97}$$

The first inequality states that slow enough variation of the control parameter guarantees that the probability distribution for the occupations is dragged along to follow the moving fixed point. The second inequality states that the variation must however be fast enough such that, on average, no fluctuation-induced "hop-over" can occur. This is fulfilled, on average, if the control parameter changes faster than the mean lifetime of the corresponding state. The control parameter however cannot vary arbitrarily fast which would eventually violate the first inequality and fluctuations explore domains away from both fixed points.

If the sweeping rate $\dot{g}$ is chosen to satisfy Eq. (4.97), the system overshoots past the critical point g^* and persists in its initial state until the control parameter hits the critical points $g = g_{c,1(2)}$ and destabilizes the state. The hysteresis loop that is traced by the system as the control parameter varies between the spinodal lines is as predicted by the fluctuations-less mean-field equations. However, the variation of the control parameter affects also the mean lifetime of the state as $T_2 \to T_2(g(t))$ which eventually leads to a violation of the adiabaticity criterion in Eq. (4.97) before $g(t)$ hits the bistability boundaries. For instance, starting in the empty state, its decay-rate $1/T_2$ increases with an increasing control parameter. As a result the mean-field behaviour breaks down as fluctuations induce a premature switching approximately when $1/T_2(g(t' < t_s)) \sim \dot{g}$. This happens when the increasing decay rate finally surpasses the sweep rate $\dot{g}$ and a jump is observed before $g(t_s) = g_{c,1}$. However, non-local relaxation times in an experiment can be astronomical such that they are not accessible in an experimental setup. Hysteresis behaviour is then consistent with a mean-field prediction. This was recently observed in a cavity quantum electrodynamics system where a superconducting resonator was coupled to a large ($N \sim 10^{12}$) electronic spin [173]. Due to the large number of spins, a fluctuation induced switching between two bistable branches could not be observed on experimentally accessible time scales.

Local relaxation timescale T_1

The adiabaticity criterion in Eq. (4.97) allows a first estimate when the system overshoots its predicted first-order transition point and when this hysteretic behaviour is interrupted with a discontinuous jump. Refinements of this adiabatic window have been obtained from the condition that the hysteresis state should follow the moving steady-state, i.e. when $D(\boldsymbol{\sigma}, g) = 0$ then, as time progresses, also $D(\boldsymbol{\sigma} + \delta\boldsymbol{\sigma}, g + \delta g) = 0$, see [196] for a one component system and [197] for its generalization to a multicomponent system. Here, we briefly review their definitions of the relaxation time T_1. For a multicomponent system there are multiple relaxation time scales that can be obtained from the linearized dynamics about the steady-states $\boldsymbol{\sigma}_m$

$$\frac{d\sigma_i}{dt} = D_i(\boldsymbol{\sigma}, g) \sim \sum_{j=x,y,z} \left.\frac{\partial D_i}{\partial \sigma_j}\right|_{\boldsymbol{\sigma}=\boldsymbol{\sigma}_m} \cdot (\sigma_j - \sigma_{m,j}), \tag{4.98}$$

where we have used $D(\boldsymbol{\sigma}_m) = 0$. In the eigenvector basis $\{\tilde{\sigma}_i\}$, the relaxation times are the eigenvalues of the relaxation matrix

$$J_{ij} = (\partial D_i/\partial\tilde{\sigma}_j)|_{\tilde{\sigma}=\tilde{\sigma}_m} = 1/T_{1,i}\delta_{ij}, \tag{4.99}$$

However, the leading timescale is the dominant time scale for the relaxation dynamics

$$\frac{1}{T_1} = \min\left[\frac{1}{T_{1,i}}\right]. \tag{4.100}$$

Non-local relaxation time scale T_2

Corrections to the adiabaticity window for the non-local equilibration time were obtained in studies for multicomponent systems in dissipative equilibrium with a conservative force derived from a potential, see [197]. Here we briefly review their arguments that allows them to calculate corrections to the adiabaticity window. We take the temporal variation of the control parameter to be of the form given by Eq. (4.95) and initialise the system in the empty state $\boldsymbol{\sigma}_0$ at $t = 0$ at $g = g_{c,2}$. For fixed g the system will build a probability distribution $P_0(\boldsymbol{\sigma}) \sim \exp(-\Phi(\boldsymbol{\sigma}))$ close to the empty state. A variation of the control parameter $g(t)$ now causes the probability distribution to be dragged along the moving minimum at a rate T_{hyst}^{-1} [197]

$$T_{\text{hyst}}^{-1} \sim \left|\frac{\dot{P}}{P}\right| \sim \left|\frac{d}{dt}\log\left(P_0(\boldsymbol{\sigma})\right)\right| \sim \left|\dot{g}\frac{\partial}{\partial g}\Phi(\boldsymbol{\sigma}_0, g(t))\right| \tag{4.101}$$

This rate must be faster than the net depletion rate out of the empty state which is the difference of the depletion from $\boldsymbol{\sigma}_0 \to \boldsymbol{\sigma}_{Sr}$ and the reverse process $\boldsymbol{\sigma}_{Sr} \to \boldsymbol{\sigma}_0$. This leads to a correction for the system to show hysteresis. The sweep must be faster than the time scale given by the decay [197]

$$\dot{g} \gg \left|\frac{\partial \Phi}{\partial g}\right|^{-1} (T_{2,0} - T_{2,Sr}). \tag{4.102}$$

In general, escape times from a basin of attraction Ω associated with a fixed point $\boldsymbol{\sigma}^\star \in \Omega$ to its boundary $\partial\Omega$ are stochastic variables. The mean time it takes from any point $\boldsymbol{\sigma} \in \Omega$ to escape to the boundary is referred to as the mean first passage time (MFPT) $\tau(\sigma)$. It is defined via the adjoint of the Fokker Planck equation governing the stochastic process. An escape is a rare-event consisting of a concatenation of noise kicks building up to a large fluctuation. If initially, the system is spread out in Ω around one of the metastable states $(\boldsymbol{\sigma}_{Sr}, \boldsymbol{\sigma}_0)$ with a probability distribution $P_{0,Sr}(\boldsymbol{\sigma}) = P(\boldsymbol{\sigma}, t = 0)$ then, the timescale T_2 is estimated from

$$T_{2,Sr,(0)} = \int_\Omega P_{(0,Sr)}(\boldsymbol{\sigma}) \cdot \tau(\boldsymbol{\sigma}) d\sigma, \tag{4.103}$$

where $T_{2,0}$ is the average time the system spends in the basin of attraction of the fixed point $\boldsymbol{\sigma}_0$ and $T_{2,Sr}$ is the average time the system spends in the domain of attraction of the superradiant fixed point. Analytic expressions for escape rates κ have been derived for stochastic dynamics in potentials in one and in higher dimensions for thermal systems, [198, 199]. These celebrated results are called Kramer's rates [200]

$$1/\kappa = T_{2,Sr} \sim \tau(\boldsymbol{\sigma}_{Sr}) \tag{4.104}$$

$$\kappa = A(T, \Gamma, V) \exp\left(-\frac{\Delta V}{T}\right), \quad \Delta V \gg T. \tag{4.105}$$

The pre-factor A weakly depends on the Temperature T and on a friction coefficient Γ and on the details of the potential V such as the local curvature at the fixed points. ΔV is the height of the energy barrier that has to be overcome to escape from the domain of attraction of a fixed point. In experimental measurements of thermally activated transitions in a bistable three-dimensional optical trap, excellent agreement has been found with the predicted Kramer's rates [201].

Far from thermal equilibrium, there are typically no closed form expressions for T_2 readily available. Here, we can numerically measure the mean-lifetimes of a state and identify $\langle t_0 \rangle = T_{2,0}$ and $\langle t_{Sr} \rangle = T_{2,Sr}$.

4.6.2. Power law exponent for decaying hysteresis area

Hysteresis occurs for example in ferromagnetic materials that undergo a magnetization cycle in the presence of an externally applied field H that is swept back and forth between two field values $\pm H^\star$. This is explained by the growth of magnetic domains, i.e. areas with the same local magnetization aligning with the direction of the external field. In this case the domain wall dynamics is not reversible on the branch $H(t = 0) = 0 \to H(t^\star) = H^\star \to H(2t^\star) = 0$ which leads to a finite remaining magnetization of the sample $M(2t^\star) = M_r$, whereas initially $M(t = 0) = 0$. At $t^\star$ there is still a large number of domains oriented in the direction of the external field and as the magnetisation is a result of an average over all magnetized domains $M(2t^\star) = M_r \neq 0$.

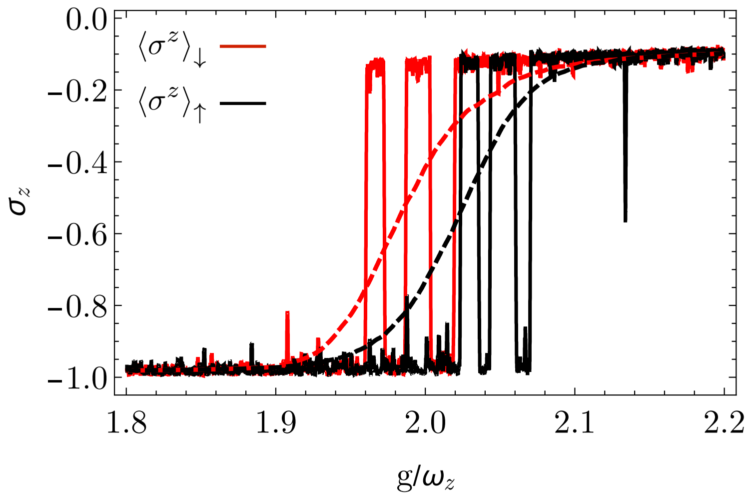

Figure 4.13.: Colored lines show single hysteresis trajectories when the power of the atom-light coupling $g(t)$ is ramped down (red) or up (black), see Eq. (4.95). Thick lines show an average over 8000 realizations of dynamic hysteresis, see Eq. (4.108). The hysteresis cycle is obtained for a fixed rampspeed $v_s/\omega_z^2 = 11.43 \cdot 10^{-5}$ in the regime given by Eq. (4.106).

As we have no equivalent of different magnetic domains in optical bistability, we cannot look at the response to a single back-to-back sweep but have to resort to an average of thousands of these sweeps that mirror the average over magnetic domains in a single back-to back sweep in a condensed matter system, see Fig. 4.13. We choose the sweep rate such that it is possible for the system to jump back and forth several times between the two metastable states in the sweeping time frame,

$$1/T_1 \gg 1/T_2 \gg \dot{g}(t). \tag{4.106}$$

For a sufficiently large number of runs, every point on the hysteresis curve is an average of the two mean-field steady-state values $\sigma_0^z = -1$ and $\sigma_{Sr}^z(g)$ which depends on g, each of them weighed by an occupation ratio

$$f_i = n_i/(n_0 + n_{Sr}), \tag{4.107}$$

where n_i counts the number of times the system was in state $i = \{0, Sr\}$ and n_0+n_{Sr} is the total number of counts or runs. For a large number of runs (typically a few thousands), the occupation ratio f_i converges to a fixed value that depends on the sweeping rate $\dot{g}$, on the value of the control parameter g and on the initial state configuration, i.e. on the sweeping direction, i.e. it defines if the atom-light coupling is increased (↑) or decreased (↓) over time. The average over several sweeps of the atom-light coupling across the bistability regime is then defined as

$$\langle\sigma^z(g,\dot{g})\rangle_{\uparrow,\downarrow} = \frac{1}{(n_0 + n_{Sr})}\left(\sum_{i=0}^{n_0}\sigma_{0,i}^z(g) + \sum_{i=0}^{n_{Sr}}\sigma_{Sr,i}^z(g)\right) = f_{0,\uparrow,\downarrow}\sigma_0^z + f_{Sr,\uparrow,\downarrow}\sigma_{Sr}^z, \tag{4.108}$$

where the second equality assumes $n_i \gg 1$, such that the occupation ratios have converged. In the ensemble average over all sweeping runs, the atomic inversion $\langle\sigma^z(g,\dot{g})\rangle_{\uparrow,\downarrow}$ now varies smoothly with the control parameter and traces out a closed loop formed by the average response to an increasing and a decreasing control parameter, see Fig. 4.13.

To quantify the amount of dynamic hysteresis, one measures the hysteresis area for several sweeping rates $\dot{g}$

$$A_{\dot{g}} = \int\limits_{g_{c,2}}^{g_{c,2}+\Delta g} |\left<\sigma^z\right>_\uparrow - \left<\sigma^z\right>_\downarrow| dg, \tag{4.109}$$

$g_{c,2}$ and $g_{c,2} + \Delta g$ defines the window where the atom-light coupling is varied. In the limit of long scanning times $t_s \to \infty$ such that $\dot{g} \to 0$, the hysteresis area disappears

$$\lim_{t_s \to \infty} A(t_s) \to 0, \tag{4.110}$$

since

$$\left<\sigma^z(g, \dot{g} \to 0)\right>_{\uparrow,\downarrow} = \frac{\left<t_0\right>\sigma_0^z + \left<t_{Sr}\right>\sigma_{Sr}^z}{\left<t_0\right> + \left<t_{Sr}\right>} = \sigma_{Sr}^z\,\rho_{Sr} + \sigma_0^z\,\rho_0 = \rho_{Sr}(1+\sigma_{Sr}^z) - 1. \tag{4.111}$$

Here we have identified the occupation ratios $(f_0(g,\dot{g}), f_{Sr}(g,\dot{g}))$ in Eq. (4.108) with the stationary state solution of a rate equation for a two-level system with the switching times $T_{2,0}(g,\dot{g})$ and $T_{2,Sr}(g,\dot{g})$,

$$\dot{f}_0 = -\frac{1}{T_{2,0}} f_0 + \frac{1}{T_{2,Sr}} f_{Sr}, \tag{4.112}$$

$$\dot{f}_{Sr} = -\frac{1}{T_{2,Sr}} f_{Sr} + \frac{1}{T_{2,0}} f_0, \quad f_0 + f_{Sr} = 1. \tag{4.113}$$

In the limit of long scanning times $t_s \to \infty$ such that $\dot{g} \to 0$, the stationary values of the rate equation are given as

$$f_0 = \rho_0 = \left<t_0\right>/(\left<t_0\right> + \left<t_{Sr}\right>), \tag{4.114}$$

$$f_{Sr} = \rho_{Sr} = \left<t_S r\right>/(\left<t_0\right> + \left<t_{Sr}\right>), \tag{4.115}$$

with the identification $\left<t_0\right> = T_{2,0}$ and $\left<t_{Sr}\right> = T_{2,Sr}$. The superradiance occupation ratio ρ_{Sr} varies smoothly from $\rho_{Sr}(g_{c,2}) = 0$ to $\rho_{Sr}(g_{c,1}) = 1$ as displayed in Fig. 4.10c.

In the opposite limit, i.e. the adiabatic scenario as specified by Eq. (4.106), the hysteresis will be static and is close to the hysteresis area dictated by the fluctuationless mean-field equations $A = A_{mf}$ that is depicted in Fig. 4.10b.

We are interested now, in the dependence of the hysteresis area on the sweeping time. We calculate hysteresis areas A for a set $\{\dot{g}\}$ and for a finite N and depict the results in Fig. 4.14a. Numerical calculations reveal a power-law dependence of the hysteresis area on the sweep rate as

$$A \propto \dot{g}^{-\nu} \propto t_s^\nu \tag{4.116}$$

where ν is the power law exponent. Numerically we find the decay exponent to be

$$\nu = -0.99 \pm 0.04 \tag{4.117}$$

The result of the fitting procedure is seen in Fig. 4.14b. Our result is in agreement with a similar system featuring an optical bistability in a single mode resonator that is influenced by quantum fluctuations [29]. The authors compared theoretical and experimental calculations and found a power law exponent of $\nu = -1$.

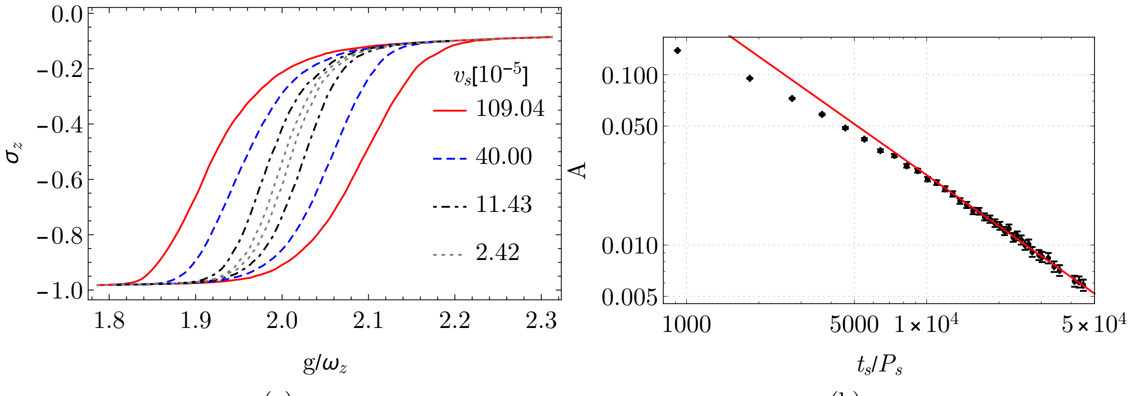

(a) (b)

Figure 4.14.: (a) Dependence of hysteresis area A on different sweeping speeds v_s for (b) Power-law decay of the hysteresis area for different sweeping speeds v_s. The data corresponds to the parameter set $N = 200$ $(\kappa/\omega_z = 0.2, \gamma/\omega_z = 0.1, \omega_0/\omega_z = 1.4, \beta = 40)$.

4.7. Conclusion and Outlook

The Dicke model with its long-range interaction and large number N of cavity-emitters, allowed us to study a fluctuation-driven first-order phase transition. The description of the system in terms of a macroscopic variable whose fluctuations are suppressed with $\mathcal{O}(1/N)$ elevates the dissipative Dicke model to a well-controlled and thus prime model candidate for studying driven-dissipative and discontinuous phase transitions in macroscopic steady-states.

The dissipative Dicke model above a critical collective loss strength features a bistability regime that separates the Bloch sphere into three basins of attraction, corresponding to the empty and the superradiant state which are connected only via rare noise activated trajectories. A bicritical point connects a continuous second-order superradiance transition with a first-order superradiance transition in the bistability regime.

The first-order phase transition can only be resolved by including fluctuation dynamics which depends on the state of the system and is therefore manifestly non-thermal. It induces a genuine non-equilibrium dynamic that breaks detailed balance on a microscopic scale. However, an inversion symmetry reduced the noise-dynamics in the Bloch-sphere to an effective two-level description that always fulfil detailed balance. The non-equilibrium character of the noise-induced transitions would be difficult to verify experimentally, since the transition rates in a two-level system can be fitted to thermal noise activation rates with an effective temperature.

In the next chapter we will review the difference between thermal and non-thermal noise activation by investigating a classical action that is associated to the stochastic optical Bloch equations.

Chapter 5

Classical Path-Integral for Stochastic Optical Bloch Equations

The time-evolution of a classical system coupled to an external environment can be described with a Langevin equation. In this chapter we review the generating functional of the Langevin equation which is the Martin-Siggia-Rose-Janssen-deDominicis (MSRJD) [189, 190, 191] path-integral. We will first review the derivation of the classical action associated with the stochastic nonlinear optical Bloch equations presented in chapter 4. The classical action allows us to investigate noise-activation rates for a state-dependent noise kernel from saddle point equations in a weak-noise limit, see Sec. 5.2. We review how to obtain from the Fokker-Planck equation the differential equation that determines the steady-state distribution in a weak-noise limit, see Sec. 5.3. Lastly, we show in Sec. 5.4 the emergence of an effective thermal equilibrium description close to the bicritical point of the bistability regime of the stochastic optical Bloch equations.

Selected parts from this chapter appeared in the publication
Dissipative Dicke model with collective atomic decay: Bistability, noise-driven activation, and the non thermal first-order superradiance transition
J. Gelhausen and M. Buchhold, Phys. Rev. A **97**, 023807 (2018)
We indicate the relevant parts in the main text.

Introduction

It is one of the main goals of this chapter to make clear and review the main difference between thermal and non-thermal noise-activation. This is achieved best in a path-integral description of classical stochastic equations where equilibrium and non-equilibrium conditions can be compared. In this chapter we review the path-integral framework for the description of the stochastic nonlinear optical Bloch equations derived in chapter 4. However, the description in terms of a MSRJD path-integral and the conclusions that can be drawn from it are generic for multidimensional nonlinear stochastic equations associated with classical nonequilibrium systems. This framework has evolved, with years of research, into a generalization of a thermodynamic theory for systems characterized by a flux equilibrium [8, 21, 202]. In this framework it is possible to identify the conditions under which the stationary state of a nonequilibrium system is described by a potential function that shares the properties of a thermodynamic potential for an equilibrium system [202, 203]. These potentials are, for instance, responsible for the stability of the fixed points of the classical, dynamical equations of motion for the nonequilibrium system. Perhaps the most straightforward way to understand the appearance of potentials in non-equilibrium systems is to identify them with the logarithm of the stationary distribution of a stochastic system weakly perturbed by some noise. As such, the potential is a construction valid only at and close to the stationary state in a weak-noise limit. The general time-evolution of classical trajectories cannot be derived from such a potential construction. In our case, we consider stochastic evolution of macroscopic quantities such as the atomic polarization with a weak noise that is proportional to $1/\sqrt{N}$ where N is the number of atoms in the cavity. The above mentioned 'potential conditions', as referred to in the literature, then place restrictions on the coefficients of the Fokker-Planck equation that allow for a straight-forward solution of the stationary state distribution, see e.g. [202].

Random perturbations in dynamical systems have been treated in the mathematical literature, in particular by Freidlin and Wentzell [20] who, among many other cases, analysed rare-fluctuations in the stationary state that are exponentially unlikely. In particular, the probability to observe the system at some point $\boldsymbol{\sigma}$ is then proportional to

$$\mathcal{P}(\boldsymbol{\sigma}) \sim \exp\left(-NW(\boldsymbol{\sigma})\right). \tag{5.1}$$

The function $W(\boldsymbol{\sigma})$ is then called a potential that can be interpreted as the analogue of a free energy for a system in thermal equilibrium. It allows one to calculate statistical quantities such as the mean residence time near a fixed point, that we have investigated numerically. However, in the weak-noise limit, it is determined from a Hamilton-Jacobi equation derived from the Fokker-Planck equation or MSRJD path-integral. In the absence of detailed balance this equation is very hard to solve and the potential form $W(\boldsymbol{\sigma})$ can, except for rare perturbative cases [204], not be given explicitly. It therefore often remains of theoretical value only. In the mathematical literature, the discussion on the existence and solvability conditions for non-equilibrium potentials appears frequently in the context of non-gradient drift fields in Langevin equations (see e.g. [205]), and in calculations of escape probabilities and noise activation rates (see e.g. [206, 207]) far from equilibrium.

In the physics community, many authors contributed to this field, however, a bulk of the research is associated to Robert Graham, who received the Max-Planck medal in 2009 [208], for his contributions to the statistical mechanics of open, stationary systems far from thermal equilibrium (and many other things). Graham was one of the first to connect solvability conditions for stationary state probability distributions of Fokker-Planck equations for general non-equilibrium processes [208, 209] with the existence or absence of detailed balance conditions. Especially in thermal equilibrium, the concept of detailed balance is fundamentally connected to the existence of thermodynamic potentials. In what follows, we can only highlight those points that are directly relevant for understanding noise-induced dynamics of the stochastic optical Bloch equations. We provide appropriate references for detailed articles throughout the chapter.

5.1. Classical action for stochastic optical Bloch equations

In this section we derive a classical Martin-Siggia-Rose-Janssen-deDominicis (MSRJD) path-integral that is equivalent to the set of stochastical optical Bloch equations, as discussed in Chapter 4. As a result, we obtain the associated classical action in the limit of a large number of atoms in the cavity after averaging over atom and cavity noise. The derivation of the classical action associated to the set of Langevin equations is a standard procedure and here we follow in particular [13] and [210].

Classical Langevin equations for atom-cavity system

The dynamical equation of motion of a system coupled to an external reservoir, has to take into account the reservoir degrees of freedom in terms of noise functions. We have seen that only a statistical average over noise realisations both in the case of a classical system (Brownian motion) and for the case of a quantum system (damped cavity) lead to a consistent implementation of fluctuation dissipation relations. As a starting point for the path integral construction, we take the Heisenberg-Langevin equations (4.8-4.11) derived in chapter 4

$$\partial_t a = D^a + \xi^a, \quad \partial_t a^\dagger = D^{a^\dagger} + \xi^{a^\dagger}, \quad \partial_t \boldsymbol{\sigma} = \boldsymbol{D} + \boldsymbol{\xi}, \tag{5.2}$$

where $\boldsymbol{\xi} = \left(\xi^x_{1,t}, \xi^y_{1,t}, \xi^z_{1,t}, \xi^x_{2,t}, \dots\right)$ are the associated atomic noise-functions that explicitly depend on the state of the system as $\boldsymbol{\xi}(\boldsymbol{\sigma})$. Moreover, we have abbreviated the notation to identify $\boldsymbol{\sigma} = (\sigma^x_{1,t}, \sigma^y_{1,t}, \sigma^z_{1,t}, \sigma^x_{2,t}, \dots)$, such that $\boldsymbol{\sigma}^\alpha_{\ell,t} = \sigma^\alpha_{\ell,t}$, where the spin components are labelled as $\alpha \in (x, y, z)$ and the index ℓ refers to a spatial index. $\boldsymbol{D} = \boldsymbol{D}(a, a^\dagger, \boldsymbol{\sigma})$ encodes deterministic dynamics and contains both dissipative and coherent, Hamiltonian contributions. The notation is understood as $\boldsymbol{D}^\alpha_\ell = D^\alpha_\ell$ being the deterministic force for the component α for the spin at site ℓ. A more detailed notation is used when clarity demands it.

Instead of operators as in the Heisenberg Langevin formalism, we work with complex fields $(a, a^\dagger, \xi^a, \xi^{a^\dagger})$ and entirely real fields $(\sigma^\alpha_{\ell,t}, \xi^\alpha_{\ell,t})$. The noise operators are represented as stochastic fields with Gaussian distributed noise. The noise correlations for the atoms are defined by

$$\langle \xi^\alpha_{\ell',t'} \xi^\beta_{\ell,t} \rangle = \int \mathcal{D}[\xi] \;\; \xi^i_{\ell',t'} \xi^j_{\ell,t} \mathcal{P}[\xi] = \gamma \delta(t-t') \Big[\delta_{\ell,\ell'} + (1 - \delta_{\ell,\ell'}) \tilde{\alpha} \Big] \chi^{\alpha\beta}_{\ell'\ell}(\sigma), \tag{5.3}$$

where $0 \leq \tilde{\alpha} \ll 1$ denotes the strength of the collective noise as defined in Eq. (1.45) and γ is the spontaneous decay rate of atomic excitations. The noise matrix $\chi^{\alpha\beta}_{\ell'\ell}(\boldsymbol{\sigma})$ depends on the state of the system $\boldsymbol{\sigma}$ and is defined in Eq. (4.77). The noise has a vanishing first moment, as $\langle \xi^\alpha_{\ell,t} \rangle = 0$ and the noise average is taken with respect to the probability distribution

$$\mathcal{P}[\boldsymbol{\xi}] = \exp\left(-\frac{1}{2} \int dt \boldsymbol{\xi} \tilde{\boldsymbol{\chi}}^{-1} \boldsymbol{\xi} \right), \quad \int \mathcal{D}[\boldsymbol{\xi}] \mathcal{P}[\boldsymbol{\xi}] = 1, \tag{5.4}$$

where the integration measure $D[\boldsymbol{\xi}]$ is chosen such that the probability distribution is properly normalised and $\tilde{\boldsymbol{\chi}}$ has to be chosen such that Eq. (5.3) holds. That said, for noise averages it is sufficient to know $\chi^{\alpha\beta}_{\ell\ell'}$ without ever having to specify $\tilde{\boldsymbol{\chi}}$. As mentioned in Chapter 4, for a mapping to a classical noise correlation matrix it is necessary to erase the information on commutation relations. This is achieved by symmetrising the matrix entries $\chi^{\alpha\beta}_{\ell\ell'}$ which amounts to taking their real part $\mathrm{Re}[\chi^{\alpha\beta}_{\ell\ell'}]$. This procedure leads to a symmetric, real and positive definite noise kernel and is thus well-defined.

Accordingly, the photonic noise function is specified by choosing

$$\langle \xi^a_t \xi^{a^\dagger}_{t'} \rangle = \int \mathcal{D}[\xi] \; \xi^a_t \xi^{a^\dagger}_{t'} \; \tilde{\mathcal{P}}[\xi] = 2\kappa \delta(t - t'), \tag{5.5}$$

$$\tilde{\mathcal{P}}[\xi] = \exp\left(-\frac{1}{2} \int dt \xi^{a^\dagger} \frac{1}{2\kappa} \xi^a \right), \tag{5.6}$$

where κ is the strength of the cavity decay for the photons.

Derivation of non-equilibrium partition function Z associated to Langevin equations

[1] In general, a statistical averaging $\langle . \rangle_\xi$ for a system observable is written as

$$\begin{aligned}\langle \mathcal{O}[\boldsymbol{\sigma}, a, a^\dagger]\rangle_\xi &= \int \mathcal{D}[\boldsymbol{\xi}]\mathcal{P}[\boldsymbol{\xi}]\tilde{\mathcal{P}}[\xi]\mathcal{O}[\boldsymbol{\sigma}_\xi, a_\xi, a^\dagger_\xi] \\ &= \int \mathcal{D}[\boldsymbol{\xi}]\mathcal{P}[\boldsymbol{\xi}]\tilde{\mathcal{P}}[\xi]\int \mathcal{D}[\boldsymbol{\sigma}, a, a^\dagger]\delta(\boldsymbol{\sigma}-\boldsymbol{\sigma_\xi})\delta(a-a_\xi)\delta(a^\dagger-a^\dagger_\xi)\mathcal{O}[\boldsymbol{\sigma}_\xi, a_\xi, a^\dagger_\xi] \\ &= \int \mathcal{D}[\boldsymbol{\xi}, \boldsymbol{\sigma}, a, a^\dagger]\mathcal{P}[\boldsymbol{\xi}]\tilde{\mathcal{P}}[\xi]J^\alpha[\boldsymbol{\sigma}]\delta(\boldsymbol{f}[\boldsymbol{\sigma}])J[a]\delta(O[a_\xi])J^\dagger[a]\delta(O[a^\dagger_\xi])\mathcal{O}[\boldsymbol{\sigma}_\xi, a_\xi, a^\dagger_\xi].\end{aligned} \tag{5.7}$$

Here, $(\boldsymbol{\sigma}_\xi, a_\xi, a^\dagger_\xi)$ are solutions to the above mentioned classical Langevin equations for a specific realisation of the corresponding noise functions and $\delta(\boldsymbol{\sigma}-\boldsymbol{\sigma}_\xi) = \prod_{\alpha,\ell=1}^N \delta(\sigma^\alpha_\ell - \sigma^\alpha_{\ell,\xi})$. In the second line we have inserted a resolution of unity

$$1 = \int \mathcal{D}[\boldsymbol{\sigma}, a, a^\dagger]\delta(\boldsymbol{\sigma}-\boldsymbol{\sigma_\xi})\delta(a-a_\xi)\delta(a^\dagger-a^\dagger_\xi), \tag{5.8}$$

where the functional delta functions satisfy

$$\int \mathcal{D}[x]Y[x]\delta(x-x_\xi) = Y[x_\xi], \tag{5.9}$$

for every test functional $Y[x]$. In the third line, we have defined

$$\delta(\boldsymbol{f}[\boldsymbol{\sigma}]) \equiv J^{-1}[\boldsymbol{\sigma}]\delta(\partial_t\boldsymbol{\sigma} - \boldsymbol{D} - \boldsymbol{\xi}) = \delta(\boldsymbol{\sigma}-\boldsymbol{\sigma}_\xi), \tag{5.10}$$

$$\delta(O[a]) \equiv J^{-1}[a]\delta(\partial_t a - D^a - \xi^a) = \delta(a - a_\xi), \tag{5.11}$$

$$\delta(O[a^\dagger]) \equiv \left(J^\dagger[(a^\dagger]\right)^{-1}\delta(\partial_t a^\dagger - D^{a^\dagger} - \xi^{a^\dagger}) = \delta(a^\dagger - a^\dagger_\xi). \tag{5.12}$$

Here, the functionals $O, \boldsymbol{f}$ are nullified by the solution to the stochastic equation of motion for a specific realisation of the noise, $O[a_\xi] = O[a^\dagger_\xi] = 0$ and $\boldsymbol{f}[\boldsymbol{\sigma}_\xi] = 0$.

The change of variables is accompanied by the Jacobian J that takes into account the change of the measure as induced by the variable transformation. In the following, we show that $J = 1$. To derive this result, we discretise time into N slices as $\Delta t N = t$. We proceed by explicitly discretising the Langevin equation (5.10) as

$$\boldsymbol{f}_j \equiv \boldsymbol{f}[\boldsymbol{\sigma}(t_j)] = \boldsymbol{f}[\boldsymbol{\sigma}_j] = \boldsymbol{f}_j = \boldsymbol{\sigma}_j - \boldsymbol{\sigma}_{j-1} - \Delta t\Big[\boldsymbol{D}(\sigma^\alpha_{j-1}) - \boldsymbol{\xi}(\sigma^\alpha_{j-1})\Big], \tag{5.13}$$

where we have discretised the temporal derivative with a retarded or Ito regularization. The Jacobian becomes an $N \times N$ matrix in the time domain, as

$$J = \Big|\det(J_{ij})\Big| \equiv \left|\det\left(\frac{\partial \boldsymbol{f}_i}{\partial \boldsymbol{\sigma}_j}\right)\right|. \tag{5.14}$$

The matrix elements in the time-domain are evaluated as

$$J_{jj} = 1, \quad J_{j,j-1} = -1 - \Delta t\Big[\boldsymbol{D}'_{j-1} - \boldsymbol{\xi}'_{j-1}\Big], \quad J_{m\ell} = 0 \;\; \text{(otherwise)}. \tag{5.15}$$

The Jacobian J becomes a lower triangular matrix with entries

$$J_{ij} = (1-\delta_{ij})\Big(-1 - \partial_{\sigma_{j-1}}\Big[\boldsymbol{D}_{j-1} - \boldsymbol{\xi}_{j-1})\Big]\Delta t\Big) + \delta_{ij} \tag{5.16}$$

---

[1] In this section we follow the conventional approach given in [13].

such that $J = \det(J_{ij}) = \prod_j J_{jj} = 1$.

We can now interpret the stochastical average in Eq. (5.7)

$$\langle \mathcal{O}[\boldsymbol{\sigma}, a, a^\dagger]\rangle_\xi = \int \mathcal{D}[\boldsymbol{\xi}]\mathcal{P}[\boldsymbol{\xi}]\tilde{\mathcal{P}}[\xi] \int \mathcal{D}[\boldsymbol{\sigma}]\mathcal{D}[a,a^\dagger]\delta(\boldsymbol{f}[\boldsymbol{\sigma}])\delta(O[a_\xi])\delta(O[a_\xi^\dagger])\mathcal{O}[\boldsymbol{\sigma}_\xi, a_\xi, a_\xi^\dagger]. \tag{5.17}$$

The integrations are performed over all field configurations $(\boldsymbol{\sigma}, a, a^\dagger)$. The presence of the functional delta functions ensures that only those trajectories contribute that solve the Langevin equations. Furthermore, each configuration is appropriately weighed by the probability distributions $\tilde{\mathcal{P}}[\xi], \mathcal{P}[\boldsymbol{\xi}]$. Taking $\mathcal{O}[\boldsymbol{\sigma}, a, a^\dagger] = 1$ one can see that the construction is indeed correctly normalised by virtue of the delta functions and the integrals over the probability measures. With the above interpretation in mind, we adopt the notation 'partition function' for $Z = 1$.

The partition function can now be written as

$$\begin{aligned} Z = \int \mathcal{D}[\boldsymbol{\xi}]\mathcal{P}[\boldsymbol{\xi}]\tilde{\mathcal{P}}[\xi] \int \mathcal{D}[\boldsymbol{\sigma}, a, a^\dagger]\ \delta\left(\partial_t a - D^a - \xi^a\right)\ \delta\left(\partial_t a^\dagger - D^{a^\dagger} - \xi^{a^\dagger}\right) \\ \prod_{\alpha=x,y,z} \prod_{\ell=1}^{N} \delta\left(\partial_t \sigma_\ell^\alpha - D_\ell^\alpha - \xi_\ell^\alpha\right). \end{aligned} \tag{5.18}$$

We rewrite the functional version of the delta function as an exponential in the following way

$$\delta(X(t)) = \int \mathcal{D}[\tilde{\sigma}_\ell^\alpha] \exp\left(-i \int dt \tilde{\sigma}_{\ell,t}^\alpha X_t\right) = \int \mathcal{D}[i\tilde{\sigma}_\ell^\alpha] \exp\left(- \int dt \tilde{\sigma}_{\ell,t}^\alpha X_t\right), \tag{5.19}$$

$$\delta(f_t)\delta(f_t^\dagger) = \int \mathcal{D}[\tilde{a}, \tilde{a}^\dagger] \exp\left(\tilde{a}(t) f_t^\dagger - \tilde{a}^\dagger(t) f_t\right). \tag{5.20}$$

Here, we require $X(t)$ to be an arbitrary real field and $f(t)$ to be an arbitrary complex field. We introduce the complex fields $(\tilde{a}, \tilde{a}^\dagger)$ and the real fields $\tilde{\sigma}_\ell^\alpha$ with $\alpha = (x, y, z)$. It will later be seen that they can be interpreted as conjugate canonical variables to the fields $(\sigma_\ell^\alpha, a, a^\dagger)$. Here, the fields $\tilde{\sigma}^\alpha$ take on real values but are integrated over the imaginary axis, as indicated by $\mathcal{D}[i\tilde{\sigma}_\ell^\alpha]$. The partition function then reads

$$\begin{aligned} Z = \int \mathcal{D}[\boldsymbol{\xi}, \boldsymbol{\sigma}, a, a^\dagger, \tilde{\boldsymbol{\sigma}}, \tilde{a}, \tilde{a}^\dagger] \prod_{\alpha=x,y,z;\ell=1}^{N} \mathcal{P}[\xi]\ \tilde{\mathcal{P}}[\boldsymbol{\xi}] \\ \times \exp\left(- \int dt \tilde{\sigma}_\ell^\alpha \left(\partial_t \sigma_\ell^\alpha - D_\ell^\alpha\right) + \int dt \tilde{\sigma}_\ell^\alpha \xi_\ell^\alpha\right) \\ \times \exp\left(\int dt \tilde{a} \left(\partial_t a - D^a\right) - \int dt \tilde{a} \xi^{a^\dagger}\right) \\ \times \exp\left(- \int dt \tilde{a}^\dagger \left(\partial_t a^\dagger - D^{a^\dagger}\right) + \int dt \tilde{a}^\dagger \xi^a\right). \end{aligned} \tag{5.21}$$

Since the noise distribution function is Gaussian, we can explicitly carry out the associated integrals to average over the noise. Since the entire action is quadratic in the (gapped) photon fields, we can eliminate the photonic variables and average over the photonic noise such that we will be left with an effective atomic action only.

Elimination of Cavity Photons

In this section we first average over the noise fields associated to the cavity photons. In the next step, we integrate out the gapped photon fields such that the dynamics is entirely given in terms of variables for the atomic degrees of freedom.

We recast the expression for the partition function given in Eq. (5.21) into the quadratic action corresponding to the photonic sector S_{Photons} and the atomic contribution S_{Atoms}

$$Z = \int \mathcal{D}[\dots] e^{iS_{\text{Photons}}} e^{-S_{\text{Atoms}}}. \tag{5.22}$$

We average over the Gaussian photonic noise components with the probability distribution $\tilde{\mathcal{P}}[\xi]$ given by Eq. (5.6) by completing the square by asymmetrically shifting the noise fields according to $\xi^a \to \xi^a - 2\kappa\tilde{a}$ and $\xi^{a^\dagger} \to \xi^{a^\dagger} + 2\kappa\tilde{a}^\dagger$ as

$$\int \tilde{\mathcal{P}}[\xi] e^{iS_{\text{Photons}}} = e^{i\langle S_{\text{Photons}}\rangle_\xi} \tag{5.23}$$

where the action of the photonic sector is given as

$$\langle S_{\text{Photons}}\rangle_\xi = \frac{1}{2}\int_\omega \boldsymbol{A}_\omega^\dagger \boldsymbol{G}_\omega^{-1} \boldsymbol{A}_\omega + \boldsymbol{A}_\omega^\dagger \boldsymbol{W}_\omega + \boldsymbol{W}_{-\omega}^T \boldsymbol{A}_\omega. \tag{5.24}$$

Notice that we have pulled out an imaginary (i) in Eq. (5.22) such that the final action will be identical to a Keldysh description of the photonic sector. For the action we have made use of the notation

$$\boldsymbol{A}_\omega^\dagger = \left(a_\omega^\dagger, a_{-\omega}, \tilde{a}_\omega^\dagger, \tilde{a}_{-\omega}\right) \tag{5.25}$$

and the abbreviation

$$\boldsymbol{W}^T_{-\omega} = \left[\frac{2ig}{\sqrt{N}}\sum_{\ell=1}^{N}\left(\tilde{\sigma}_\ell^y\sigma_\ell^z(\omega) - \tilde{\sigma}_\ell^z\sigma_\ell^y(\omega)\right), \frac{2ig}{\sqrt{N}}\sum_{\ell=1}^{N}\left(\tilde{\sigma}_\ell^y\sigma_\ell^z(\omega) - \tilde{\sigma}_\ell^z\sigma_\ell^y(\omega)\right), -\frac{g}{\sqrt{N}}\sum_{\ell=1}^{N}\sigma_\ell^x(\omega), -\frac{g}{\sqrt{N}}\sum_{\ell=1}^{N}\sigma_\ell^x(\omega)\right]. \tag{5.26}$$

Here, we have defined the expression $\tilde{\sigma}_\ell^y\sigma_\ell^z(\omega) = \int_{\omega'}\tilde{\sigma}_\ell^y(\omega')\sigma_\ell^z(-\omega-\omega')$ and the photonic Green function

$$\boldsymbol{G}_\omega^{-1} = \begin{pmatrix} 0 & (\boldsymbol{G}_{2x2}^A(\omega))^{-1} \\ (\boldsymbol{G}_{2x2}^R(\omega))^{-1} & \boldsymbol{D}_{2x2}^K(\omega) \end{pmatrix}, (\boldsymbol{G}_{2x2}^A(\omega))^{-1} = \left[(\boldsymbol{G}_{2x2}^R(\omega))^{-1}\right]^\dagger, \tag{5.27}$$

$$(\boldsymbol{G}_{2x2}^R(\omega))^{-1} = \begin{pmatrix} \omega - \omega_0 + i\kappa & 0 \\ 0 & -\omega - \omega_0 - i\kappa \end{pmatrix}, \quad \boldsymbol{D}_{2x2}^K(\omega) = \operatorname{diag}(2i\kappa, 2i\kappa). \tag{5.28}$$

consists of the inverse retarded (R) and advanced (A) Green function respectively and of the Keldysh contribution (K). We have used the Fourier transformation convention

$$a_t = \int_\omega e^{-i\omega t} a_\omega, \quad a_t^\dagger = \int_\omega e^{-i\omega t} a_{-\omega}^\dagger, \quad \sigma_t^\alpha = \int_\omega e^{-i\omega t}\sigma_\omega^\alpha, \quad \int_\omega = \int \frac{d\omega}{2\pi}. \tag{5.29}$$

The noise-averaged action $\langle S_{\text{Photons}}\rangle_\xi$ is quadratic in the (gapped) photon fields which can be integrated out completely. Shifting

$$\boldsymbol{A}_\omega \to \boldsymbol{A}_\omega - \boldsymbol{G}_\omega W_\omega, \quad \boldsymbol{A}_\omega^\dagger \to \boldsymbol{A}_\omega^\dagger - W_{-\omega}^{\mathrm{T}}\boldsymbol{G}_\omega, \tag{5.30}$$

we can integrate out the photons such that

$$\int \mathcal{D}[a, a^\dagger] \exp\left(i\left\langle S_{\text{Photons}}\right\rangle_\xi\right) = \exp\left(-\frac{i}{2}\int_\omega \boldsymbol{W}_{-\omega}^{\mathrm{T}}\boldsymbol{G}_\omega\boldsymbol{W}_\omega\right) = \exp\left(-\langle S_{\text{phot}}^{\text{fluc}}\rangle_\xi - \langle S_{\text{phot}}^{\text{det}}\rangle_\xi\right). \tag{5.31}$$

Where the individual contributions are written as

$$\langle S^{\mathrm{det}}_{\mathrm{phot}}\rangle_{\xi} = \int_{\omega} \sum_{\ell,m=1}^{N} \left(-\frac{4g^2}{N} \frac{\omega_0}{\omega_0^2 + (\kappa - i\omega)^2} \sigma^x_{\ell,\omega} \left(\tilde{\sigma}^y_m \sigma^z_{m,-\omega} - \tilde{\sigma}^z_m \sigma^y_{m,-\omega} \right) \right), \tag{5.32}$$

$$\langle S^{\mathrm{fluc}}_{\mathrm{phot}}\rangle_{\xi} = \int_{\omega} \sum_{\ell,m=1}^{N} \left(-\frac{8g^2}{N} \frac{\kappa\left((\kappa^2+\omega^2)+\omega_0^2\right)}{\left(\omega_0^2+(\kappa-i\omega)^2\right)\left(\omega_0^2+(\kappa+i\omega)^2\right)} \right.$$
$$\left. \left[\left(\tilde{\sigma}^y_\ell \sigma^z_{\ell,-\omega} - \tilde{\sigma}^z_\ell \sigma^y_{\ell,-\omega} \right) \left(\tilde{\sigma}^y_m \sigma^z_{m,\omega} - \tilde{\sigma}^z_m \sigma^y_{m,\omega} \right) \right] \right). \tag{5.33}$$

We remark that $\langle S^{\mathrm{fluc}}_{\mathrm{phot}}\rangle_{\xi}$ is quadratic in the field $\tilde{\sigma}$ and vanishes as $\kappa \to 0$ and thus represents the contribution associated to the noise fields. After integrating out the photonic components in the path-integral formalism, we can compare the contribution $\langle S^{\mathrm{det}}_{\mathrm{phot}}\rangle_{\xi}$ with the deterministic part from the Langevin equation for the cavity photons

$$\partial_t a_t = -\kappa a_t - i\omega_0 a_t - igS^x_t + \xi^a, \quad \partial_t a^\dagger_t = -\kappa a^\dagger_t + i\omega_0 a^\dagger_t + igS^x_t + \xi^{a^\dagger} \tag{5.34}$$

In the frequency domain, the solutions of the Langevin equation for the cavity photons are given as

$$a_\omega = \left(\frac{g}{\sqrt{N}} S^x_\omega + \xi^a_\omega \right) \left(\frac{1}{\omega - \omega_0 + i\kappa} \right), \quad a^\dagger_{-\omega} = \left(\frac{g}{\sqrt{N}} S^x_\omega + \xi^{a^\dagger}_{-\omega} \right) \left(\frac{1}{-\omega - \omega_0 - i\kappa} \right), \tag{5.35}$$

where $S^x = \sum_{\ell=1}^N \sigma^x_\ell$ is the collective spin operator. These expressions can be reinserted into the equations of motion for $(\partial_t \sigma^y_m + \partial_t \sigma^z_m)$ in the frequency domain to obtain

$$0 = -i\omega\sigma^y_{\omega,m} - i\omega\sigma^z_{\omega,m} - \frac{4g^2}{N} S^x_{-\omega} \left(\frac{\omega_0}{\omega_0^2 + (\kappa + i\omega)^2} \right) \left[\sigma^z_{m,\omega} - \sigma^y_{m,\omega} \right] + (\ldots). \tag{5.36}$$

Comparing Eq. (5.36) with Eq. (5.32), we see that both equations match (upon the allowed transformation $\omega \to -\omega$).

Noise Average over atomic components

Having integrated out the cavity photons, we are left with an entirely atomic action. The partition sum at this point is expressed as

$$Z = \int \mathcal{D}[\ldots] e^{-\langle S^{\mathrm{fluc}}_{\mathrm{phot}}\rangle_{\xi} - \langle S^{\mathrm{det}}_{\mathrm{phot}}\rangle_{\xi} - S_{\mathrm{Atoms}}}. \tag{5.37}$$

Here, we proceed by averaging the action over the atomic noise fields $\boldsymbol{\xi}$.

The action for the atoms reads

$$S_{\mathrm{Atoms}} = \sum_{\ell,\alpha=x,y,z} \left(\int dt \tilde{\sigma}^\alpha_\ell \left(\partial_t \sigma^\alpha_\ell - D^\alpha_\ell \right) - \int dt \tilde{\boldsymbol{\sigma}}^T_\ell \boldsymbol{\xi}_\ell + \frac{1}{2} \int dt \boldsymbol{\xi} \chi^{-1} \boldsymbol{\xi} \right) \tag{5.38}$$

where $\boldsymbol{\xi}^T_\ell = (\xi^x_\ell, \xi^y_\ell, \xi^z_\ell)$ and $\tilde{\boldsymbol{\sigma}}^\dagger_\ell = (\tilde{\sigma}^x_\ell, \tilde{\sigma}^y_\ell, \tilde{\sigma}^z_\ell)$ such that the noise-average over the atomic components is given as

$$\int \mathcal{D}[\boldsymbol{\xi}] \exp\left(-S_{\mathrm{Atoms}}\right) = \exp\left(\langle -S^{\mathrm{fluc}}_{\mathrm{atom}}\rangle_{\xi} - \langle S^{\mathrm{det}}_{\mathrm{atom}}\rangle_{\xi} \right). \tag{5.39}$$

and where the following definitions have been used

$$\langle S^{\text{fluc}}_{\text{atom}}\rangle_\xi = -\frac{1}{2}\gamma\sum_{\ell=1}^{N}\int_t \tilde{\boldsymbol{\sigma}}^\dagger_\ell \chi_\ell \tilde{\boldsymbol{\sigma}}_\ell - \frac{1}{2}\gamma\alpha\sum_{\ell,m\neq\ell}\int_t \tilde{\boldsymbol{\sigma}}^\dagger_\ell \chi_{\ell m}\tilde{\boldsymbol{\sigma}}_m \tag{5.40}$$

$$\langle S^{\text{det}}_{\text{atom}}\rangle_\xi = \sum_{\ell,\alpha=x,y,z}\int_t \tilde{\sigma}^\alpha_\ell\left(\partial_t\sigma^\alpha_\ell - D^\alpha_\ell\right). \tag{5.41}$$

Here, the strength of incoherent spontaneous decay of individual atoms is encoded in the local noise matrix χ_ℓ. Cooperative radiation processes such as the collective emission of excitation of an atomic ensemble as derived in Sec. 1.2.1 are encoded in the non-local noise matrix $\chi_{\ell m}$. The noise correlation matrices are χ_ℓ which is given by the real part of Eq. (4.78) and $\chi_{\ell m}$ which is given by the real part of Eq. (4.77). The fluctuating contribution in the atomic sector vanishes if the noise strength vanishes $\gamma \to 0$.

Noise-averaged classical action in site-decoupling mean-field Ansatz

[2]We are now in a position to put together the noise averaged action that consists of the contributions

$$S = \langle S^{\text{fluc}}_{\text{atom}}\rangle_\xi + \langle S^{\text{det}}_{\text{atom}}\rangle_\xi + \langle S^{\text{fluc}}_{\text{phot}}\rangle_\xi + \langle S^{\text{det}}_{\text{phot}}\rangle_\xi\,. \tag{5.42}$$

We invoke now a mean-field decoupling where we assume spatial independence of the individual sites ($\sigma^\alpha_\ell \to \sigma^\alpha$). This allows us to treat the system in a large N limit, leading to the transformation $S \to NS$, where N is the number of qubits. The action for the spins takes on the form ($\alpha = x, y, z$)

$$S = N\int_t\left[\tilde{\sigma}^\alpha\partial_t\sigma^\alpha - \tilde{\sigma}^\alpha D^\alpha - \frac{1}{2}\tilde{\sigma}^\alpha\chi^{\alpha\beta}\tilde{\sigma}^\beta\right] = N\int_t\left[\tilde{\sigma}^\alpha\partial_t\sigma^\alpha - \mathcal{H}\right], \tag{5.43}$$

$$Z = \int\mathcal{D}[\{\sigma^\alpha,\tilde{\sigma}^\alpha\}]\;e^{-S}. \tag{5.44}$$

The MSRJD path integral construction has led to an action that is in Hamiltonian form. Here, D^α encodes the deterministic force and captures the noiseless mean-field dynamics (repeated for convenience)

$$\boldsymbol{D} = \begin{pmatrix} -\gamma\sigma^x(1-\beta\sigma^z) - \sigma^y\omega_z \\ \omega_z\sigma^x + J\sigma^x\sigma^z - \gamma\sigma^y(1-\beta\sigma^z) \\ -2\gamma(\sigma^z+1) - \gamma\beta\left((\sigma^x)^2+(\sigma^y)^2\right) - J\sigma^x\sigma^y \end{pmatrix}, \tag{5.45}$$

and $\chi_{\alpha\beta}$ is the noise kernel for the atomic degrees of freedom in the large N-limit (repeated for convenience)

$$\boldsymbol{\chi} = 2\begin{pmatrix} \gamma\left(\beta(\sigma^z)^2+1\right) & \dots & \dots \\ 0 & (\tilde{\kappa}+\gamma\beta)(\sigma^z)^2+\gamma & \dots \\ \sigma^x(1-\beta\sigma^z)\gamma & \sigma^y\left(\gamma-(\tilde{\kappa}+\gamma\beta)\,\sigma^z\right) & \chi_{3,3}(\sigma) \end{pmatrix}, \tag{5.46}$$

where $\chi_{3,3}(\sigma) = \tilde{\kappa}(\sigma^y)^2 + \gamma[\beta((\sigma^x)^2+(\sigma^y)^2) + 2(\sigma^z+1)]$, $\tilde{\kappa} = \kappa J/\omega_0$. It is entirely real, symmetric and positive definite, i.e. all its eigenvalues satisfy $\{\lambda_\chi\} > 0$. The action still possesses the original Ising-like inversion symmetry of the Dicke-model that is expressed

---

[2] This subsection appeared in parts in the publication J. Gelhausen and M. Buchhold, Phys. Rev. A **97**, 023807 (2018) and we have used some paragraphs verbatim.

through the transformation $S[\tilde{\sigma}^x, \tilde{\sigma}^y, \tilde{\sigma}^z, \sigma^x, \sigma^y, \sigma^z] = S[-\tilde{\sigma}^x, -\tilde{\sigma}^y, \tilde{\sigma}^z, -\sigma^x, -\sigma^y, \sigma^z]$. The Hamiltonian

$$\mathcal{H} = \tilde{\sigma}^\alpha D^\alpha + \frac{1}{2}\tilde{\sigma}^\alpha \chi^{\alpha\beta}\tilde{\sigma}^\beta, \tag{5.47}$$

is the functional combining both deterministic and noise contributions. It is also known as the Freidlin-Wentzel Hamiltonian [20] where it appears in the theory of large deviations theory for systems weakly perturbed by noise. Introducing the conjugate variables $\tilde{\sigma}^\alpha$ doubles the degrees of freedom. This reflects the non-equilibrium nature of the problem. This will become clearer in the next section. We will see that σ^α governs the evolution of the order parameters whereas $\tilde{\sigma}^\alpha$ measures deviations from deterministic relaxation and are thus an indication for noise activation. This interpretation will become evident after inspecting the saddle-point equations in a weak-noise limit. Moreover, we see that the Hamiltonian treats both deterministic and noise contributions on an equal footing. The form of the Hamiltonian is generic for multidimensional stochastic equations [13].

As the action in the large-N limit scales with the number of atoms as NS both the deterministic contribution $\boldsymbol{D}$ as well as the correlation function for the noise $\boldsymbol{\chi}$, scale with the number of system constituents N. The structure of the action thus reflects its equivalence to the stochastic optical Bloch equations derived in a Langevin framework.

5.2. Noise activation in large N limit - Saddle point equations

In this section we want to confirm, without being exhaustive, three statements that we made in chapter 4 on the non-equilibrium nature of the bistability. We repeat them for convenience.

First, the mean occupation times $\langle t_0 \rangle$ and $\langle t_{Sr} \rangle$ of the empty and the superradiant state obey an Arrhenius law of the type $\langle t_{Sr,0} \rangle \sim A_{Sr,0} \exp(N\psi_{Sr,0})$, with $\psi_{Sr,0}(\sigma)$ as a non-equilibrium potential that measures the cost of fluctuations.

Second, the deterministic force $\boldsymbol{D}$, Eq. (5.45), and the noise kernel $\boldsymbol{\chi}$, Eq. (5.46), do not satisfy the necessary condition for microscopic reversibility and violate detailed balance.

Third, we comment that the combination of $(\nabla \times D \neq 0)$ and $(\nabla \cdot D \neq 0)$ is a necessary but not a sufficient criterion for out-of-equilibrium dynamics, which do not relax towards an effective thermal equilibrium.

The analysis is based on Freidlin-Wentzell theory [20] for weak noise systems, therefore applicable in the limit $N \to \infty$. Additionally we comment on the structure of the noise-induced trajectories as observed in Fig. 4.9.

Saddle-Point equations in weak-noise limit

[3] In the limit of $N \to \infty$ only the saddle points of S contribute to the dynamics and one can determine the corresponding equations of motion by variation with respect to the fields. Due to the Hamiltonian structure, the associated equations of motion demonstrate that $(\tilde{\sigma}^\alpha, \sigma^\alpha)$ are canonically conjugate variables

$$0 = \frac{1}{N}\frac{\delta S}{\delta \tilde{\sigma}^\alpha} = \partial_t \sigma^\alpha - \frac{\partial \mathcal{H}}{\partial \tilde{\sigma}^\alpha} \quad \text{and} \quad 0 = \frac{1}{N}\frac{\delta S}{\delta \sigma^\alpha} = -\partial_t \tilde{\sigma}^\alpha - \frac{\partial \mathcal{H}}{\partial \sigma^\alpha}. \tag{5.48}$$

---

[3] This subsection appeared in parts in the publication J. Gelhausen and M. Buchhold, Phys. Rev. A **97**, 023807 (2018) and we have used some paragraphs verbatim.

The Hamiltonian itself is an integral of motion on the saddle point trajectories. Taking the time derivative of the functional $\mathcal{H}$ one obtains via the chain rule

$$\partial_t \mathcal{H} = \frac{\delta \mathcal{H}}{\delta \sigma_\alpha} \partial_t \sigma_\alpha + \frac{\delta \mathcal{H}}{\delta \tilde{\sigma}_\alpha} \partial_t \tilde{\sigma}_\alpha \overset{\text{saddle point}}{=} \{\mathcal{H}, \mathcal{H}\}_{\sigma, \tilde{\sigma}} = 0, \tag{5.49}$$

where $\{,\}$ is the classical Poisson bracket. The saddle point paths are thus described by a constant functional $\mathcal{H}$. The explicit form of Eqs. (5.48) is

$$\partial_t \sigma^\alpha = D^\alpha + \chi^{\alpha\beta} \tilde{\sigma}_\beta, \tag{5.50}$$

$$\partial_t \tilde{\sigma}^\alpha = -\tilde{\sigma}_\beta \frac{\delta D_\beta}{\delta \sigma^\alpha} - \frac{1}{2} \tilde{\sigma}_\gamma \left(\frac{\delta \chi_{\gamma\delta}}{\delta \sigma^\alpha} \right) \tilde{\sigma}_\delta. \tag{5.51}$$

The saddle point equations have two solutions, one that corresponds to deterministic relaxation and another one that describes noise activation. The first solution is found by setting $\tilde{\sigma} = 0$ which also sets $\mathcal{H} = 0$. This Ansatz recovers the noiseless, deterministic Bloch equations, $\partial_t \sigma^\alpha = D^\alpha$ such that all saddle-point trajectories starting from a deterministic field configuration, $\tilde{\sigma}^\alpha = 0$, fulfill $\mathcal{H} = 0$.

Noise activated trajectories, in turn, correspond to solutions with $\tilde{\sigma}^\alpha \neq 0$, that are however still constrained to the manifold $\mathcal{H} = 0$, since noise-activated trajectories start from a deterministic fixed point that nullifies $\mathcal{H}$ and the dynamics conserves the Hamiltonian as shown above. For the second solution we make the Ansatz that the conjugated fields are a function of the order paramter field as $\tilde{\boldsymbol{\sigma}}(\boldsymbol{\sigma})$. Inserting this Ansatz into Eq. (5.51) imposes the restriction $\partial_\alpha \tilde{\sigma}_\gamma = \partial_\gamma \tilde{\sigma}_\alpha$. Which is true only if $\tilde{\boldsymbol{\sigma}} = \nabla_\sigma W(\boldsymbol{\sigma})$ can be written in the form of a potential gradient.

The scalar potential W can then be defined by the Hamilton-Jacobi equation which is a first-order non-linear, partial differential equation [211]

$$\mathcal{H}(\sigma, \nabla W) = \partial_\alpha W (D^\alpha + \frac{1}{2} \chi^{\alpha\beta} \partial_\beta W) = \langle \nabla W, D + \frac{1}{2} \chi \nabla W \rangle = 0. \tag{5.52}$$

Solving the saddle point equations non-perturbatively is equivalent to solving the Hamilton-Jacobi equation which, in general, is an impossible task [204]. We can solve it implicitly by decomposing the deterministic force $\boldsymbol{D}$ into the two orthogonal fields ∇W and $\boldsymbol{r}$ as

$$D^\alpha = -\frac{1}{2} \chi^{\alpha\beta} \partial_\beta W + r^\alpha. \tag{5.53}$$

Where we have used our freedom to allow for an additional field $\boldsymbol{r}$ that only has to obey the orthogonality condition $r^\alpha \partial_\alpha W = 0$ which demands that $\boldsymbol{r}$ encodes dynamics on equipotential surfaces of W. Plugging the Ansatz in Eq. (5.53) into the Eq. (5.52) one can verify that it solves the Hamilton-Jacobi equation formally. The first term $(-1/2\chi^{\alpha\beta}\partial_\beta W)$ is responsible for the stability of the fixed points of the deterministic force $\boldsymbol{D}$. The transversal decomposition implies in general that $\nabla W \neq -2\boldsymbol{\chi}^{-1}\boldsymbol{D}$, such that in general it is an impossible task to obtain non-perturbative analytical expressions for the non-equilibrium potential W in systems lacking detailed balance [204, 209]. The saddle-point trajectories (5.51) describing noise-activation are

$$\tilde{\sigma}^\alpha = \partial_\alpha W, \quad \partial_t \sigma^\alpha = D^\alpha + \chi^{\alpha\beta} \partial_\beta W = \frac{1}{2} \chi^{\alpha\beta} \partial_\beta W + r^\alpha = -D^\alpha + 2r^\alpha. \tag{5.54}$$

A comparison with the deterministic dynamics $\partial_t \sigma^\alpha = D^\alpha = -\frac{1}{2}\chi^{\alpha\beta}\partial_\beta W + r^\alpha$ shows that in general the noise activated trajectories are *not* the time-reversed partners of the deterministic dynamics and visit different regions in the Bloch sphere as seen in Fig. 4.9. This also means that noise-activated and relaxational dynamics do generally not have the same basin of attraction (although they share the same set of fixed points), since the field transverse to the potential (r^{α}) can move the system to different attractors. In the stationary state, the dynamics is then a succession of deterministic relaxation and noise-activation, driving the system away from stationary points. We provide more details on the decomposition of the field $\boldsymbol{D}$ at the end of this subsection.

We turn our attention to the *second* point and check violation of detailed balance. Under microscopic reversibility [209, 202] the deterministic force $\boldsymbol{D}$ and diffusive contribution $\boldsymbol{\chi}$ in general obey 'the potential conditions' [9]

$$\mathrm{rot}[\boldsymbol{\chi}^{-1}(2\boldsymbol{D} - \nabla\boldsymbol{\chi})] = 0, \tag{5.55}$$

which for our case is not satisfied. We conclude the absence of microscopic detailed balance for the dynamics generated by the stochastic optical Bloch equations.

Coming to the *third* point, for out-of-equilibrium systems in general $\boldsymbol{D}$ itself is not a gradient field and has both a non-conservative ($\boldsymbol{\nabla} \times \boldsymbol{D} \neq 0$) and a conservative contribution ($\boldsymbol{\nabla} \cdot \boldsymbol{D} \neq 0$). Whenever the generators for conservative and non-conservative dynamics do not commute, i.e. when the corresponding trajectories are not orthogonal $(-\frac{1}{2}\chi^{\alpha\beta}\partial_{\beta}W)r^{\alpha} \neq 0$, both fields $(-\frac{1}{2}\chi^{\alpha\beta}\partial_{\beta}W)$ and r^{α} contribute to both conservative and non-conservative parts of $\boldsymbol{D}$. Thus, having non-conservative and conservative dynamics is necessary to reach a non-equilibrium steady state but not sufficient. The counter example being a spin subject to a magnetic field $\boldsymbol{B} = \mu B\boldsymbol{e}_z$ and spontaneous emission.

For a system with a constant noise intensity $\chi_{\alpha\beta} = 2T\delta_{\alpha\beta}$, the trajectories of conservative and non-conservative dynamics are orthogonal, per definition for $\boldsymbol{r}$ we have $\mathrm{grad}W \cdot \boldsymbol{r} = 0$, see below Eq. (5.53). Since the deterministic dynamics is $\boldsymbol{D} = -T\mathrm{grad}\ W + \boldsymbol{r}$ and div $\boldsymbol{D} =$ div (grad W) and curl $\boldsymbol{D} =$ curl $\boldsymbol{r}$ it can be seen that conservative and non-conservative dynamics are indeed orthogonal.

The presence of non-orthogonal non-conservative and conservative forces together with the absence of detailed balance allows the conclusion that the steady-state for the stochastic optical Bloch equations in this work is firmly out-of equilibrium.

Phase space structure of saddle point equations

We will now discuss the phase space structure of the saddle point equations. The Hamiltonian equations define the dynamics in the six dimensional phase space $(\tilde{\sigma}_{\alpha}, \sigma_{\alpha})$. As the Hamiltonian is constant, the Liouville theorem guarantees the conservation of the flow in phase space. This means that the fixed points must be hyperbolic. Both deterministic and noise-activated trajectories share the same set of fixed points $\{\boldsymbol{\sigma_0}\}$ with $D(\{\boldsymbol{\sigma_0}\}) = 0$. Since all fixed points are hyperbolic, there exists one stable (M_s) and one unstable (M_u) 3-dimensional manifold for the zero-energy Hamilton $\mathcal{H} = 0$ that intersect at the set of fixed points $\{\boldsymbol{\sigma_0}\}$. The stable manifold M_s is characterized by $\tilde{\boldsymbol{\sigma}} = 0$ and $\partial_t\boldsymbol{\sigma} = \boldsymbol{D}$ and the unstable manifold M_u is characterized by $\tilde{\boldsymbol{\sigma}}(\boldsymbol{\sigma}) = \nabla W(\boldsymbol{\sigma})$ and $\partial_t\boldsymbol{\sigma} = -\boldsymbol{D} + 2\boldsymbol{r}$ (see below). A more general discussion on the phase space structure of saddle point equations can be found in [211].

In the stable manifold M_s there are two maximally attractive fixed points, the empty atom-cavity state and the superradiant state. In the space spanned by $(\sigma^x, \sigma^y, \sigma^z, \tilde{\boldsymbol{\sigma}} = 0)$ their domains of attraction are separated from each other by a two-dimensional manifold (separatrix), which hosts the unstable fixed point, see Fig. 4.9. The unstable maximum has two attractive ($= d - 1$) and one repulsive direction in the $\tilde{\boldsymbol{\sigma}}_{\alpha} = 0$ manifold. The two domains of attraction are not connected by any deterministic path. Only a noise-activated escape trajectory can connect the two stable fixed points.

[4] In the vicinity of the fixed point, the manifolds M_s and M_u are spanned by the eigenvectors of the stability matrix associated to the linearised dynamics of the saddle point Eq. (5.50) and Eq. (5.51) in the $\tilde{\boldsymbol{\sigma}} = 0$ manifold

$$\partial_t \begin{pmatrix} \delta\sigma_\alpha \\ \delta\tilde{\sigma}_\alpha \end{pmatrix} = \begin{pmatrix} D_{\alpha,\beta} & \chi_{\alpha\beta} \\ 0 & -D^T_{\alpha,\beta} \end{pmatrix} \begin{pmatrix} \delta\sigma_\beta \\ \delta\tilde{\sigma}_\beta \end{pmatrix}, \tag{5.56}$$

where we have defined $D_{\alpha,\beta} = \partial_\beta D_\alpha|_{\sigma_0}$ and $\boldsymbol{\sigma_0}$ can be either of the two attractive fixed points (empty atom-cavity or superradiant atom-cavity) or the repulsive fixed point inside the bistable regime and $\delta\boldsymbol{\sigma} = \boldsymbol{\sigma} - \boldsymbol{\sigma}_0$ measures deviations away from the stationary state. We restrict the analysis to the case of attractive fixed points. This 6×6 matrix possesses six eigenvalues. Three are given by the matrix $D_{\alpha\beta}$ which are $\mathrm{Re}[\lambda_{1,2,3}] < 0$. The corresponding eigenvectors $\boldsymbol{v}_{1,2,3}$ thus have three of their six components fixed to the manifold with $\tilde{\boldsymbol{\sigma}} = 0$. The other three eigenvalues have a positive real part and are given by $\mathrm{Re}[\lambda_{4,5,6}] = -\mathrm{Re}[\lambda_{1,2,3}] > 0$. The corresponding eigenvectors $\boldsymbol{v}_{4,5,6}$ describe activation trajectories and will thus have non zero components $\tilde{\sigma}_\alpha \neq 0$. All trajectories that depart from the fixed point can locally be written as a linear combination of the unstable eigenvectors, i.e.

$$\tilde{\boldsymbol{\sigma}}(\boldsymbol{\sigma_0})|_{t=0} = \boldsymbol{\sigma}_0 + \sum_{i=4,5,6} \alpha_i \vec{v_i} \tag{5.57}$$

These vectors locally span the manifold of activation trajectories. Since the 'energy' is conserved in the Hamiltonian dynamics, the activation trajectories will remain in the 'zero-energy' manifold $\mathcal{H} = 0$, since all fixed points lie in the $\tilde{\boldsymbol{\sigma}} = 0$ manifold which nullifies $\mathcal{H}$.

Noise-activation trajectories and interpretation of nonequilibrium cost function

[5]The saddle point action for the unstable zero-energy manifold $\mathcal{H} = 0$ reduces to

$$S^{\text{fluc}}_{[t_0,t],\sigma_0}(\boldsymbol{\sigma}) = N \int_t \tilde{\sigma}_\alpha \partial_t \sigma_\alpha = N \int_{\boldsymbol{\sigma}}^{\boldsymbol{\sigma}_0} \tilde{\sigma}_\alpha d\sigma_\alpha \tag{5.58}$$

From its form $S_{\text{fluc}}(\boldsymbol{\sigma}_0)$ can be interpreted as a function that measures the cost for a fluctuation to bring the system to the point $\boldsymbol{\sigma}$ given that it started in one of the stable fixed points $\boldsymbol{\sigma_0}$. The cost function is nullified if the system moves deterministically, i.e. fluctuationless on the $\tilde{\boldsymbol{\sigma}} = 0$ manifold. Here it is possible to attribute an interpretation to $\tilde{\boldsymbol{\sigma}}$; it measures the strength with which the system moves against or deviates from the deterministic dynamics. When the cost function is evaluated on the equations of motion, it gives the minimal cost for a fluctuation induced trajectory that corresponds to an optimal realisation of the multiplicative, stochastic noise. The optimal path is the most probable path. In the weak noise limit ($N \to \infty$) one can define a non-equilibrium potential or cost function as the minimal action acquired for a path connecting a fixed point $\boldsymbol{\sigma}_0$ to any given point $\boldsymbol{\sigma}$ on the manifold M_u as

$$\psi(\boldsymbol{\sigma}_0, \boldsymbol{\sigma}) = \min\{S^{\text{fluc}}_{[t_0,t],\sigma_0}(\sigma) : \sigma(t_0) = \sigma_0, \sigma(t) = \sigma, t_0 < t\}. \tag{5.59}$$

The result of the integration is independent of the path $(\boldsymbol{\sigma}(t), \tilde{\boldsymbol{\sigma}}(t))$ in M_u when M_u is locally defined by $\tilde{\boldsymbol{\sigma}} = \nabla W(\boldsymbol{\sigma})$. To exponential accuracy the probability p for a noise-induced trajectory is then given by $p \sim \exp(-N\psi(\boldsymbol{\sigma}_0, \boldsymbol{\sigma}))$. This explains the *first* point

---

[4] A discussion on the stability matrix for the linearised fluctuations can for example be found in [13].

[5] This subsection appeared in parts in the publication J. Gelhausen and M. Buchhold, Phys. Rev. A **97**, 023807 (2018) and we have used some paragraphs verbatim.

that the mean occupation times

$$\langle t_{Sr,0}\rangle \sim A_{Sr,0}\exp(N\psi_{Sr,0}). \tag{5.60}$$

In particular, if the dynamics is fluctuationless, i.e. on the $\tilde{\boldsymbol{\sigma}} = 0$ manifold the cost function has to vanish as the deterministic dynamics happens with probability one. For weak, but finite noise, the activation trajectory is given by $\partial_t \boldsymbol{\sigma} = -\boldsymbol{D} + 2\boldsymbol{r} + \frac{1}{\sqrt{N}}\boldsymbol{\xi}$ and spreads around the deterministic activation path as, observed in Fig. 4.9.

Comparison to a system in thermal equilibrium

As a consistency check, we take a system with a constant noise intensity T where the forces are generated entirely from a gradient, i.e. $\chi_{\alpha\beta} = T\delta_{\alpha\beta}$ and $D_\alpha = -\frac{\partial}{\partial_\alpha}V$. The Hamilton-Jacobi equation (5.52) reduces to

$$(\partial_\alpha S_{\text{fluc}})\left(-D_\alpha/T + (\partial_\alpha S_{\text{fluc}})\right) = 0, \tag{5.61}$$

which is solved by the well-known equilibrium result

$$S(\boldsymbol{\sigma}) = -\frac{1}{T}\int \partial_\alpha V d\sigma_\alpha = -\frac{V(\boldsymbol{\sigma}) - V(\boldsymbol{\sigma}_0)}{T}. \tag{5.62}$$

It tells us that the relative statistical weight for finding the system at a point $\boldsymbol{\sigma}$ is $p \sim \exp\left(-\frac{V(\boldsymbol{\sigma})-V(\boldsymbol{\sigma}_0)}{T}\right)$, The spatial probability density function for the system is therefore

$$P(\boldsymbol{\sigma}) = \frac{1}{Z}\exp\left(-\frac{V(\boldsymbol{\sigma})}{T}\right) \tag{5.63}$$

, where $Z = \int\prod_\alpha d\sigma_\alpha \exp\left(\frac{V(\boldsymbol{\sigma})}{T}\right)$ is the associated partition function. Thermally activated transitions have been measured experimentally in bistable three-dimensional optical traps with high precision and where found to be in agreement with theoretical predictions of Kramer's transition rates and its extension to multidimensional potentials, see [201] and references therein. In a system in thermal equilibrium where the forces on the system are derived from the gradient of a potential, transitions rates are of the form

$$R = R_0 \exp\left(\frac{-\Delta V}{T}\right), \tag{5.64}$$

where the pre-factor R_0 depends on details of the potential such as its local curvatures. Here $\Delta V(\boldsymbol{\sigma}) = V(\boldsymbol{\sigma}_s) - V(\boldsymbol{\sigma}_0)$ measures energy differences between the saddle point $\boldsymbol{\sigma}_s$, that separates the two basins of attractions of the fixed points from another and the stable fixed point $\boldsymbol{\sigma}_0$. In an equilibrium system noise activation is solely determined from a competition of the potential barrier height and the strength of thermal fluctuation ($\sim k_b T$). For a constant and state-independent noise-intensity, noise kicks are uniform in every direction of phase space. When the noise-intensity depends on the state of the system, it means that there are preferred directions for noise kicks that change with the position in phase space. In a thermal system, the situation is different. Noise-kicks are uniform in phase space and there is no directional preference. The most probable path for a rare-fluctuation event, that consists of a concatenation of noise kicks building towards an escape from a basin of attraction, can thus be different in a system in thermal equilibrium and in a system far from thermal equilibrium.

5.3. Weak-Noise activation in a Fokker-Planck interpretation

An equivalent description for dynamical systems with random perturbations is given by the Fokker-Planck equation for the time evolution of the probability density function function (pdf) $\mathcal{P}(\boldsymbol{\sigma}, t)$ as

$$\partial_t \mathcal{P} = \mathcal{H}\mathcal{P}. \tag{5.65}$$

It can formally be obtained from the normal ordered Hamiltonian of the MSRJD path-integral

$$\mathcal{H} = \tilde{\sigma}^\alpha D^\alpha + \frac{\epsilon}{2}\tilde{\sigma}^\alpha \chi^{\alpha\beta}\tilde{\sigma}^\beta. \tag{5.66}$$

Here, we have redefined $\frac{1}{2}\chi_{\alpha\beta} \to \frac{\epsilon}{2}\chi_{\alpha\beta}$ to make the noise strength ϵ explicit. Here, ϵ encodes the large N-limit such that $\epsilon \to 0$ as $N \to \infty$. It is formally associated with the strength of the noise, that is suppressed as $1/\sqrt{N}$. Normal ordering refers to all $\tilde{\sigma}$ being to the left of all (functions of) σ as is consistent with the Ito regularisation of the path integral. With the substitution $\tilde{\sigma}^\alpha = -\partial_\alpha$, the resulting equation reads as

$$\partial_t \mathcal{P}(\boldsymbol{\sigma}, t) = -\partial_\alpha \Big[D^\alpha \mathcal{P} - \frac{\epsilon}{2}\partial_\beta(\chi^{\alpha\beta}\mathcal{P}) \Big] \tag{5.67}$$

with the initial condition $\mathcal{P}(\boldsymbol{\sigma}, t = 0) = \boldsymbol{\delta}(\boldsymbol{\sigma} - \boldsymbol{\sigma}_{\text{initial}})$. A detailed derivation of the Fokker-Planck equation from the MSRJD path integral consistent with the above substitution rule is given in [212]. In general, it is not possible to solve for the dynamics of the probability density function. In the long-time limit however, the pdf can become quasi stationary on timescales $t_{\text{rel}} \ll t \ll \tau$ where t_{rel} is given by the relaxation dynamics of the deterministic motion and τ is the mean escape time referring to the mean time it takes for a fluctuation to move the particle to the boundary of the domain of attraction of a fixed point. As an Ansatz, we take

$$\mathcal{P}(\boldsymbol{\sigma}) = K(\boldsymbol{\sigma}) e^{-W(\boldsymbol{\sigma})/\epsilon} \tag{5.68}$$

Its form suggests that $W(\boldsymbol{\sigma})$ should be interpreted as a non-equilibrium potential function. Additionally the potential $W(\boldsymbol{\sigma})$ should be bounded from below, single-valued twice differentiable as it has to satisfy the Fokker-Planck equation. Weak noise expansions with the Ansatz in Eq. (5.68) have been intensively treated in the literature , see e.g. [213, 211]. Plugging this Ansatz into Eq. (5.67), one can collect terms with the same order of the noise strength if the noise is assumed weak. Formally, terms with a prefactor of $\mathcal{O}(1/\epsilon)$ result in a K-independent equation for the quasipotential $W(\boldsymbol{\sigma})$. The resulting equation is equivalent to a Hamilton-Jacobi equation [211]

$$D^\alpha \partial_\alpha W + \frac{1}{2}(\partial_\alpha W)\chi^{\alpha\beta}(\partial_\beta W) = \mathcal{H}(\sigma_\alpha, \tilde{\sigma}_\alpha = \partial_\alpha W) = 0. \tag{5.69}$$

The generating function $W(\boldsymbol{\sigma})$ has the total time-derivative

$$\frac{dW}{dt} = \frac{\partial W}{\partial \sigma^\alpha}\partial_t \sigma_\alpha = \tilde{\sigma}^\alpha \partial_t \sigma^\alpha \quad \to \quad W(\boldsymbol{\sigma}) = \int_t \tilde{\sigma}^\alpha \partial_t \sigma_\alpha = \int_{\boldsymbol{\sigma_0}}^{\boldsymbol{\sigma}} \tilde{\sigma}^\alpha d\sigma^\alpha, \tag{5.70}$$

where we have set the quasipotential $W(\boldsymbol{\sigma_0}) = 0$ for the fixed points $\boldsymbol{\sigma_0}$ of the deterministic equation. We can see that the generating function is equivalent to the saddle point action that was derived in the MSR path integral in Eq. (5.58). This means that we can identify the non-equilibrium potential as being equivalent to the saddle-point action for the fluctuation dynamics

$$W(\boldsymbol{\sigma}) = S_{\text{fluc}}(\boldsymbol{\sigma}). \tag{5.71}$$

Plainly speaking, the non-equilibrium function $W(\boldsymbol{\sigma})$ measures the cost of a fluctuation induced trajectory that brings the system from the fixed point $\boldsymbol{\sigma}_0$ to the point $\boldsymbol{\sigma}$ on a zero-energy manifold $\mathcal{H} = 0$ in phase space along the activation trajectory given by Eq. (5.54). However, the cost function must be bounded from below and positive such that $W \geq 0$ for all phase space trajectories. In particular, if the dynamics is fluctuationless, i.e. on the $\tilde{\boldsymbol{\sigma}} = 0$ manifold the cost function has to vanish as the deterministic dynamics happens with probability one. Writing $W(\boldsymbol{\sigma}_t)$ where $\boldsymbol{\sigma}_t$ fulfils the activation equation, one can recast

$$\frac{dW}{dt} = (\partial_\alpha W)\partial_t \sigma^\alpha = \frac{\epsilon}{2}(\partial_\alpha W)\chi^{\alpha\delta}(\partial_\delta W) \geq 0. \tag{5.72}$$

The noise matrix $\chi^{\alpha\beta}$ is positive (semi)definite and thus W can only increase in time on the activation trajectory. Intuitively, the further you move from the fixed point on the manifolds characterised by $\tilde{\boldsymbol{\sigma}} = 0$ and the longer the system stays away from the fixed point, the more expensive it should be. The probability for such trajectories is exponentially suppressed with the cost function.

So far the pdf in Eq. (5.68) is determined to exponential accuracy in the weak-noise limit only. A differential equation for the missing pre-factor $K(\boldsymbol{\sigma})$ is obtained by collecting terms of order $\mathcal{O}(\epsilon^0)$ from the Fokker-Planck equation with the Ansatz in Eq. (5.68). It can be compactly written as [206]

$$K\left[\frac{1}{2}\left(\frac{\partial^2 W}{\partial\sigma_\alpha\partial\sigma_\beta}\right)\left(\frac{\partial^2\mathcal{H}}{\partial\tilde{\sigma}_\alpha\partial\tilde{\sigma}_\beta}\right) + \left(\frac{\partial\mathcal{H}}{\partial\tilde{\sigma}_\alpha\partial\sigma_\alpha}\right)\right] + \frac{\partial K}{\partial\sigma_\alpha}\left[\frac{\partial\mathcal{H}}{\partial\tilde{\sigma}_\alpha}\right] = 0, \tag{5.73}$$

where all derivatives are evaluated at $\tilde{\sigma}^\alpha = \partial_\alpha W$.

We remark that successive construction of the pdf in terms of powers in the noise-strength ϵ is similar to the construction of tunneling wavefunctions through a potential barrier in quantum mechanics in the Wentzel-Kramer-Brillouin framework. In this case the wavefunction is determined from the Schroedinger equation and constructed by a power expansion of the small parameter $\hbar$.

5.4. Adiabatic elimination of fast modes close to bicritical point

In this section, we expand the MSRJD action around the bicritical point of the bistability regime. An analysis based on the mean-field master equations has revealed that in the vicinity of this point, there emerges an effective low-frequency deterministic dynamic that is mapped onto a single variable, see Chapter 4. The dynamics is derived from a power expansion of the single mode and can thus be derived from the gradient of the potential. Here, we take into account the noise contributions as they appear naturally in a path-integral formalism. We show that at the bicritical point, the noise has a constant intensity. This signalises the emergence of dissipative equilibrium and classifies the phase transition at the bicritical point as a thermal Ising transition.

We start with the MSRJD action, associated to the stochastic optical Bloch equations ($\alpha = x, y, z$)

$$S = N\int_t \left[\tilde{\sigma}^\alpha\partial_t\sigma^\alpha - \tilde{\sigma}^\alpha D^\alpha - \frac{1}{2}\tilde{\sigma}^\alpha\chi^{\alpha\beta}\tilde{\sigma}^\beta\right]. \tag{5.74}$$

The goal is to expand the MSRJD action around the empty steady-state close to the bicritical point (β_c, g_c). The response fields have to be expanded around $\tilde{\sigma}^\alpha = 0$ and the order parameter field instead is expanded around the empty atom-cavity system

$$\tilde{\sigma} = \tilde{\sigma}_0^\alpha + \delta\tilde{\sigma}^\alpha, \quad \sigma^\alpha = \sigma_0^\alpha + \delta\sigma^\alpha, \tag{5.75}$$

with $\boldsymbol{\sigma}_0 = (0, 0, -1)$. The fluctuations $\delta\sigma^\alpha, \delta\tilde{\sigma}^\alpha$ are expanded in the set of eigenvectors $\{\boldsymbol{v}_i\}$, where $i = (1, 2, 3)$ of the stability matrix $\boldsymbol{\nabla D}(\boldsymbol{\sigma}_0)$ where $\boldsymbol{\nabla} = (\partial_{\sigma^x}, \partial_{\sigma^y}, \partial_{\sigma^z})$ and the matrix entries $[\boldsymbol{\nabla D}(\boldsymbol{\sigma}_0)]_{\epsilon\delta} = \frac{\partial}{\partial_\delta} D^\epsilon(\boldsymbol{\sigma}_0)$. Deviations from $g = g_c, \beta = \beta_c$ are parametrised in a coordinate frame centred at the bicritical point, see Fig. 4.5a. The two eigenvectors $(\boldsymbol{v}_1, \boldsymbol{v}_2)$ are associated to the relaxation directions of the fast modes at the bicritical point. The remaining mode $\boldsymbol{v}_3$ is associated to the direction of the slow mode, see Fig. 4.6. The fluctuations are parametrised in these eigenmodes with a unitary operation as

$$\delta\boldsymbol{\sigma}^\alpha = u_{\alpha\beta}\Psi_\beta, \quad \delta\tilde{\boldsymbol{\sigma}}^\alpha = u_{\alpha\beta}\tilde{\Psi}_\beta \tag{5.76}$$

where $\Psi_\beta = (\delta\varphi, \delta\psi, \phi)$ and $\tilde{\Psi}_\beta = (\delta\tilde{\varphi}, \delta\tilde{\psi}, \tilde{\phi})$ are the vectors with the expansion coefficients that carry the time dependence of the modes. We use ϕ and ψ as variables for the fast modes and ϕ as the variable for the slow mode. The matrix $\boldsymbol{u}$ contains the normalized eigenvectors as the column entries $u_{ij} = (\boldsymbol{v}_j)_i$. For this we have orthogonalised the modes first with the Grahm Schmidt-procedure as $\boldsymbol{v}_2' = \boldsymbol{v}_2 - \frac{\langle \boldsymbol{v}_2, \boldsymbol{v}_2 \rangle}{\langle \boldsymbol{v}_3, \boldsymbol{v}_3 \rangle}\boldsymbol{v}_3$. Although the mode $\boldsymbol{v}_2'$ now contains a contribution from the slow mode, at the bicritical point this contribution vanishes as the slow mode is associated to a vanishing eigenvalue of the stability matrix that governs the time evolution close to the bicritical point. The temporal contributions transform as

$$\tilde{\sigma}^\alpha \partial_t \sigma^\alpha = \delta\tilde{\sigma}^\alpha \partial_t \delta\sigma^\alpha = u^T_{\beta\alpha} u_{\alpha\gamma} \tilde{\Psi}_\beta \partial_t \Psi_\gamma = \tilde{\Psi}_\gamma \partial_t \Psi_\gamma = \frac{1}{2}\delta\Psi^T \begin{pmatrix} 0 & -\mathbb{1}\partial_t \\ \mathbb{1}\partial_t & 0 \end{pmatrix} \delta\Psi + \tilde{\phi}\partial_t\phi. \tag{5.77}$$

We expand the action up to quadratic fluctuations in the fast modes $\delta\Psi$ as

$$S[\boldsymbol{\sigma}_0 + \delta\boldsymbol{\sigma}, \tilde{\boldsymbol{\sigma}}_0 + \delta\tilde{\boldsymbol{\sigma}}_0] = S[\delta\Psi, \phi, \tilde{\phi}] = \int dt \left(\delta\Psi^T \partial_t \delta\Psi + \tilde{\phi}\partial_t\phi + S_0 + \delta\Psi^T \nabla S + \frac{1}{2}\delta\Psi^T \nabla^2 S \delta\Psi \right), \tag{5.78}$$

where $\delta\Psi = (\delta\varphi, \delta\psi, \delta\tilde{\varphi}, \delta\tilde{\psi})$. The zeroth-order S_0, the linear Terms ∇S and the quadratic terms $\nabla^2 S$ are given as

$$(\nabla^2 S)_{\epsilon\delta} = \partial^2_{\epsilon\delta} S = \begin{pmatrix} A & B \\ B^T & C \end{pmatrix}_{\epsilon\delta}, \tag{5.79}$$

$$(\nabla S_0)_\epsilon = \partial_\epsilon S[\boldsymbol{\sigma}, \tilde{\boldsymbol{\sigma}}]|_{\delta\Psi=0, \delta\tilde{\psi}=0}, \tag{5.80}$$

$$S_0 = S[\boldsymbol{\sigma}_0 + \delta\sigma, \tilde{\boldsymbol{\sigma}}_0 + \delta\tilde{\sigma}]|_{\delta\Psi=0, \delta\tilde{\psi}=0} = S[\sigma_0 + \boldsymbol{v}_3\phi, \boldsymbol{v}_3\tilde{\phi}] = \tilde{\phi}(\cdots)\phi + \tilde{\phi}(\cdots)\tilde{\phi}, \tag{5.81}$$

and $(\epsilon, \delta) \in [\delta\varphi, \delta\psi, \tilde{\delta}\varphi, \tilde{\delta}\psi]$. In Eq. (5.81) we have not explicitly specified S_0 but have illustrated that it consists of a deterministic part $\tilde{\phi}(\ldots)\phi$ and a noise-kernel $\tilde{\phi}(\ldots)\tilde{\phi}$. Due to construction, the quadratic contribution is symmetric and in block form of 2×2 matrices where the matrix $A(\tilde{\phi} = 0) = 0$. We perform the Gaussian integral over the real fields $\delta\Psi$

to obtain an effective action for the slow fields $(\phi, \tilde{\phi})$

$$
\begin{aligned}
Z &= \int \mathcal{D}[\delta\Psi, \phi, \tilde{\psi}] \exp\Big(- \int dt S[\delta\Psi, \phi, \tilde{\phi}] \Big) \\
&= \int \mathcal{D}[\delta\Psi, \phi, \tilde{\phi}] \exp\Big(\int dt \Big[- \tilde{\phi}\partial_t \phi - \frac{1}{2} \delta\Psi^T G_\psi^{-1} \delta\Psi - \delta\Psi^T \nabla S - S_0 \Big] \Big) \\
&= \int \mathcal{D}[\phi, \tilde{\phi}] \sqrt{\frac{(2\pi)^4}{\mathrm{Det}[G_\psi^{-1}]}} \exp\Big(\int dt \frac{1}{2} \nabla S^T (G_\psi|_{\omega=0}) \nabla S - S_0 - \tilde{\phi}\partial_t\phi \Big) \\
&= \int \mathcal{D}[\phi, \tilde{\phi}] \exp\Big(S_{\text{fluc}}[\phi, \tilde{\phi}] - S_{\text{eff}}[\phi, \tilde{\phi}] \Big) ,
\end{aligned}
\tag{5.82}
$$

where we have defined the inverse Green function for the fast modes as

$$
G_\psi^{-1} = \nabla^2 S[\phi, \tilde{\phi}] + \begin{pmatrix} 0 & i\omega\mathbb{1} \\ -i\omega\mathbb{1} & 0 \end{pmatrix} . \tag{5.83}
$$

There are two contributions to the action, $S_{\text{fluc}}[\phi, \tilde{\phi}]$ associated to the quadratic fluctuations of the fast modes and $S_{\text{eff}}[\phi, \tilde{\phi}]$ which we will analyse first.

As we are looking for the steady-state in the long-time-limit, we are interested in an effective action for times much longer than the time set by the inverse mass gap of the fast modes. As the fast modes are always gapped in the vicinity of and also exactly at the bicritical point, the Green function G_ψ stays well-defined. So for long times, the temporal derivative contributions, i.e. temporal fluctuations of the slow modes are inessential and we replace $G_\psi \to G_\psi|_{\omega=0}$.
In the vicinity of the bicritical point however, the order parameter ϕ associated with the slow mode is small. This presents the opportunity to perturbatively expand the action in the powers of the fields ϕ. We remark that the action satisfies the Ising symmetry $S_{\text{eff}}[\tilde{\phi}, \phi] = S_{\text{eff}}[-\tilde{\phi}, -\phi]$ that restricts the possible terms appearing in the power expansion. We expand terms from

$$
S_{\text{eff}}[\phi, \tilde{\phi}] = \tilde{\phi}\partial_t\phi + S_0 - \frac{1}{2} \Big(\nabla S^T \; G_\psi|_{\omega=0} \, \nabla S \Big) = \tilde{\phi}\partial_t\phi - \mathcal{H}[\phi, \tilde{\phi}], \tag{5.84}
$$

where one can define a Hamiltonian as

$$
\mathcal{H}(\tilde{\phi}, \phi) = \tilde{\phi} \left(- \frac{\partial V}{\partial \phi} \right) + \tilde{\phi} \left(\alpha_0 + \sum_{n \geq 1} \alpha_{2n} \phi^{2n} \right) \tilde{\phi}, \tag{5.85}
$$

with the potential $V(\phi)$

$$
V(\phi) = \frac{1}{2} a_2 \phi^2 + \frac{1}{4} a_4 \phi^4 + \frac{1}{6} a_6 \phi^6 + O(\phi^8), \quad a_2 = \left(\frac{\partial}{\partial \tilde{\phi}} S_0 \right) \Big|_{\tilde{\phi}=0} . \tag{5.86}
$$

The expansion coefficients of the potential $V(\phi)$ match with the result obtained from the mean-field master equations, see Eq. (4.32) and Sec. 4.32. The only discrepancy is a renormalised dependence from the distance to the bicritical point that is traced back to the normalisation of fluctuations in Eq. (5.76). At this stage, it can already be seen that the noise contribution appearing in the sector in $\tilde{\phi}^2$ has a non-vanishing and constant noise intensity α_0 when $\phi \to 0$ at the bicritical point. The description of the dynamics in terms of a potential with a constant noise-intensity at and close to the bicritical point is evidence for the appearance of an effective equilibrium description. The emergence of a thermodynamic universality class in driven-dissipative phase transitions has been observed several times, see [160] and references therein, as well as [89]. This is the main result of this section and concludes the investigation of the bicritical point in the MSRJD path-integral.

Comments on $S_{\text{fluc}}[\phi, \tilde{\phi}]$

So far we have not analysed the contributions from the action $S_{\text{fluc}}[\phi, \tilde{\phi}]$ that appears in Eq. (5.82) and is associated to the quadratic fluctuations of the fast modes. We make a brief comment. By defining

$$G_{0,\psi}^{-1} = G_{\psi}^{-1}\Big|_{\phi=\tilde{\phi}=0}, \quad G_{1,\psi}^{-1} = G_{\psi}^{-1} - G_{0,\psi}^{-1}, \tag{5.87}$$

one can perturbatively expand the action $S_{\text{fluc}}[\phi, \tilde{\phi}]$ in ϕ as

$$\begin{aligned} \mathrm{Tr}[\log\left(\mathrm{G}_{\psi}^{-1}\right)] &= \mathrm{Tr}\log[\mathrm{G}_{0,\psi}^{-1}\left(\mathbb{1} + \mathrm{G}_{0,\psi}\mathrm{G}_{1,\psi}^{-1}\right)] \\ &= \mathrm{Tr}\log[\mathrm{G}_{0,\psi}^{-1}] + \mathrm{Tr}\int\frac{\mathrm{d}\omega}{2\pi}\sum_{\mathrm{n}\geq 0}(-1)^{\mathrm{n}}\frac{1}{\mathrm{n}+1}\left(\mathrm{G}_{0,\psi}\mathrm{G}_{1,\psi}^{-1}\right)^{\mathrm{n}+1}. \end{aligned} \tag{5.88}$$

from this expansion one can see that the form of the new contributions are restricted to be

$$S_{\text{fluc}}[\phi, \tilde{\phi}] = \mathcal{H}' = \tilde{\phi}\left(-\frac{\partial V'}{\partial \phi}\right) + \tilde{\phi}\left(\beta_0 + \sum_{m\geq 1}\beta_{2m}\phi^{2m}\right)\tilde{\phi} \tag{5.89}$$

where the operation Tr includes a frequency integral and a matrix trace. The Hamiltonian $\mathcal{H}'$ in Eq. (5.89) is of the same form as the Hamiltonian in Eq. (5.85) and therefore does not change the fact that there is a constant noise intensity at the bicritical point as $\phi \to 0$, which was the main result of the last section. However, we remark that care has to be taken when the Tr operation and the corresponding frequency integrals are performed since $\tilde{\sigma}$ is real but hast to be integrated over the imaginary axis as defined in Eq. (5.19).

5.5. Conclusion

In this chapter we have reviewed the non-equilibrium noise dynamics of a set of stochastic nonlinear differential equations with multiplicative noise (stochastic optical Bloch equations) in a weak-noise limit by analysing the action that governs the fluctuational dynamics within a Martin-Siggia-Rose-Janssen-de-Dominicis path integral formalism.

We have derived an effective action in the low-frequency sector close to a bicritical point that revealed that in the dynamics in this limit can be derived from an effective potential. The transition at the bicritical point happens at a constant noise intensity, signaling the emergence of the thermal Ising universality class. In general however, the equations of motion cannot be derived from a conservative force field due to the presence of both coherent and dissipative dynamics and instead of minimizing an effective free energy [214, 215, 216], the escape trajectories follow the most probable path from one stable fixed point to the other. For weak noise-systems (here, weak is meant in the sense that many noise kicks are required to leave one basin of attraction), deterministic and noise dynamics are set by a Freidlin-Wentzell Hamiltonian [20] and the role of the equilibrium free energy is taken by a nonequilibrium quasipotential [203, 217].

The current work also lays the foundation for extending the Dicke model to a true externally pumped three level system without detailed balance featuring non-vanishing probability currents in the steady-state formulated in a modern physics language. Therefore encouraging future research efforts that help to understand non-equilibrium phenomena, see more details in Appendix C.

Conclusion

In this thesis we have investigated magnetic phase transitions in driven-dissipative atomic ensembles that interact with quantum light. We believe this is needed because experiments have started to merge cavity technology and lattice-based many-body systems. The general motivation to combine these fields is to move from 'clean' condensed matter system simulations to driven non-equilibrium system that hold the promise to realise unconventional magnetic phases in systems where laser-dressing allows to engineer atom-light and atom-atom interactions both in their geometric shape and magnitude. This brings with it a considerable degree of complexity in describing competing quantum phases in non-equilibrium conditions. Throughout this thesis we have therefore been guided by the call for tractable model systems with experimentally verifiable results.

We have presented three projects that have as their basic building block an engineered, laser-driven ensemble of two-level atoms in a cavity, which is described by the Dicke model.

In a first project we have added an experimentally relevant decay channel for atomic excitations. As a result, we were able to extend the formula for the critical coupling strength for the onset of the superradiance transition in open Dicke models to the full two loss channels that take into account photonic and atomic relaxation processes. It was subsequently shown experimentally that the predicted superradiance threshold is accurately reproduced, highlighting the necessity to consider relaxation processes for cavity atoms.

In a second project we have added magnetic spin-spin interactions for intra-cavity atoms to build a blueprint for the simplest self-interacting quantum optical magnet. Although we could not solve our simple model exactly, it has yielded some experimentally testable predictions: A coexistence regime of a superradiant cavity and a canted antiferromagnetic state, a new even-odd sublattice peak in the cavity spectrum, and oscillating solutions for both, the spin components and a coherent photon field. Modern experiments with Rydberg-dressed spin lattices in optical cavities are on track to check and refine the results.

In a third project we have investigated non-thermal noise-activation in a driven-dissipative first-order phase transition in an open version of the Dicke model with a collective decay channel for cavity-atoms. Although the genuine non-equilibrium dynamic breaks detailed balance on a microscopic scale, it was restored on a macroscopic scale by a discrete Ising symmetry, making it impossible to observe the non-equilibrium nature of noise-activation if the rates would be measured experimentally.

In a last chapter we have reviewed the difference between thermal and non-thermal noise activation by investigating a classical action that is associated to the stochastic optical Bloch equations, describing the non-equilibrium dynamics of the Dicke model with collective losses.

In an outlook chapter we have put forward ideas for future projects to observe clear non-equilibrium signatures such as circulating currents in a macroscopic non-equilibrium stationary state of an open Dicke model.

Appendices

Chapter A

Numerical Implementation of Stochastic Optical Bloch Equations

The purpose of this section is to put the reader in a position to recreate the code for the numerical simulations of the dynamics of the nonequilibrium Dicke model as presented in Chapter 4 himself. As a solver for the multidimensional stochastic differential equation (SDE) with a multiplicative noise kernel, we use the three-stage stochastic Runge-Kutta algorithm [192, 193] with strong order one convergence. We start by briefly reviewing stochastic differential equations and their interpretation in Itô calculus. We review the construction of the stochastic Runge algorithm and the simple Euler-Maruyama schemes that approximate solutions to SDE. We review convergence properties of discretised approximations to stochastic differential equations.

For a clear mathematical justification of the outlined steps and an in-depth study of the simulation of stochastic Itô integrals, the reader is advised to consult the original sources. We briefly review the introductory basic concepts for stochastic differential equations that can be found in standard textbooks on stochastic calculus, see e.g. [218]. However, here we follow in parts the introductory review articles on the theoretical background of SDE [219, 220] and the article for numerical simulation of SDEs [221].

The classical set of Langevin equations that is associated to the dynamics of the nonequilibrium Dicke model is of the form

$$\partial_t \sigma_t^{\alpha,\epsilon} = D^\alpha(\boldsymbol{\sigma}_t^\epsilon) + \xi_t^\alpha. \tag{A.1}$$

The presence of the noise function ξ_t^α adds a stochastic contribution to the otherwise nonlinear set of differential equations $\partial_t \sigma_t^{\alpha,\epsilon} = D^\alpha(\boldsymbol{\sigma}_t^\epsilon)$. The noise however can be multidimensional and multiplicative, i.e. its strength depends on the state of the system. Conventional solvers for numerical simulations of differential equations e.g. the Euler- or Runge-Kutta algorithms have to be adapted to account for the stochastic nature of the evolution. Below, we aim to make the reader briefly aware of the additional complexity of SDE. A solution to Eq. (A.1) can be written in a differential form as

$$d\sigma_t^{\alpha,\epsilon} = D(\boldsymbol{\sigma}_t^\epsilon) + \epsilon^{1/2} M_{\alpha\beta}(\boldsymbol{\sigma}_t^\epsilon) dW_t^\beta \tag{A.2}$$

or in an integral form as

$$\sigma_t^{\alpha,\epsilon} = \sigma_0^{\alpha,\epsilon} + \int_0^t D^\alpha(\boldsymbol{\sigma}_s^\epsilon) ds + \epsilon^{1/2} \int_0^t M_{\alpha\beta}(\boldsymbol{\sigma}_s^\epsilon) dW_{\beta,s}, \tag{A.3}$$

where $M_{\alpha\beta} \in \mathbb{R}^{3\times 3}$ is the Cholesky decomposition of the field-dependent noise matrix

$$\langle \xi^\alpha \xi^\beta \rangle = \epsilon \chi^{\alpha\beta} \tag{A.4}$$

such that $\chi_{\alpha\beta} = M^T_{\alpha\gamma} M_{\gamma\beta}$ and $D \in \mathbb{R}^3$ is the force field for the system such that the relaxational dynamics are determined by $\partial_t \boldsymbol{\sigma}_t = D(\boldsymbol{\sigma_t})$. The ϵ superscript in σ^ϵ_t indicates the dependence of the time evolution on the particular realisation of the noise-function with strength $\epsilon > 0$. The strength of the noise is set by the atomic and photonic relaxation with (γ, κ) respectively and by the number of atoms N. Here W^β_t denotes a Wiener process, see Sec. A. Comparing Eq. (A.1) and Eq. (A.2) the white noise ξ^β_t can symbolically be identified as "$\frac{dW_\beta}{dt} = \xi_t$" However, a Wiener process $W(t)$ is nowhere differentiable. This can formally be motivated by the Markov property of the white noise function. As such it cannot depend on its history which precludes the existence of a tangent at any point in time since the Wiener process cannot store information on how a particular point was approached ,[220].

Note that $\sigma^{\alpha,\epsilon}_t$ is a random variable and depends on the specific realisation of the noise. Exact solutions can only be found in special cases however. For a numerical approximation to the solution in Eq. (A.3) it is necessary to discretise the stochastic differential equation in time. The last term is the stochastic integral, here, $M_{\alpha\beta}(\boldsymbol{\sigma}^{\alpha,\epsilon}_s)$ is integrated over Brownian motion. That is a random, discontinuous path with Brownian increments $dW_{\beta,t}$. For a definition of the stochastic integral we follow Itô calculus that defines the stochastic integral as the limit of the Riemann sum in analogy to 'ordinary' integration as

$$\int_0^T dt M(\boldsymbol{\sigma}^\epsilon_t)_{\alpha\beta} dW_{\beta,t} = \lim_{N\to\infty} \sum_{n=0}^{N-1} M_{\alpha\beta}(\boldsymbol{\sigma}^\epsilon_{t_n})(W_{\beta,t_{n+1}} - W_{\beta,t_n}) \tag{A.5}$$

where the time interval is discretised in N pieces with $t_n = n\Delta t = n\frac{T}{N}$ and $n \in \{0, 1, \ldots, N_1\}$ such that $\Delta t \to 0$ as $N \to \infty$.

Numerical approximation schemes to the true solution are, as in the case of ordinary differential equations, defined by the Taylor series expansions to the (stochastic) integrals. The accuracy of the approximation depends crucially on a proper treatment of the stochastic integral contributions. Below we show the simplest, i.e. lowest order approximation to the solution given in Eq. (A.3) that is known as the natural extension of the Euler procedure familiar from noise-free differential equations to the stochastic realm. The stochastic generalization is referred to as the Euler-Maruyama (EM) algorithm.

Euler-Maruyama (EM) Algorithm

The Euler-Maruyama algorithm is the extension of the conventional Euler algorithm into the stochastic realm. Its derivation is based on a first-order approximation to the stochastic integrals in Eq. (A.5). In the discretisation process it is necessary to approximate the integrals by a Taylor series expansion. The approximation to the deterministic part is given as

$$\int_t^{t+\Delta t} D^\alpha(\boldsymbol{\sigma}^\epsilon_s) ds \approx D^\alpha(\boldsymbol{\sigma}^\epsilon_t)\Delta t, \tag{A.6}$$

whereas the stochastic contributions coming from the Wiener increments is approximated as

$$\int_t^{t+\Delta t} ds M_{\alpha\beta}(\boldsymbol{\sigma}^\epsilon_s) dW_s \approx M_{\alpha\beta}(\boldsymbol{\sigma}^\epsilon_t)\Delta W_\beta. \tag{A.7}$$

The Euler-Maruyama approximation to Eq. (A.3) given as

$$\sigma^{\alpha,\epsilon}_{n+1} = \sigma^{\alpha,\epsilon}_n + D^\alpha(\boldsymbol{\sigma}^\epsilon_t)\Delta t + M_{\alpha\beta}(\boldsymbol{\sigma}^\epsilon_t)\Delta W_\beta + \mathcal{O}(\Delta t^{3/2}), \tag{A.8}$$

where the subscript n labels the the time step t_n. The Eq. (A.8) thus defines an iteration scheme. The quality of a numerical approximation is quantified via deviations to the exact solution . In a stochastic setting however, the meaning of convergence can be defined via the calculation of expectation values of the differences of the approximation to the exact solution.

Strong order convergence for numerical solvers of SDE

Details on convergence properties for discretised SDEs can be found in [218]. A sequence $\{\tilde{\sigma}^\alpha(t;h), 0 \leq t_n \leq T\}$ approximates the true solution $\{\sigma^{\alpha,t}, 0 \leq t \leq T\}$ at the discrete times $t_n = h \cdot n$, where $h > 0$ specifies the numerical discretisation step-width, and $n = 0, 1, \ldots N$. Convergence of the approximation to the true solution is quantified over noise averages, i.e. the behaviour of the mean square error (MSE) as the width of the time slices becomes infinitely small, i.e. $h \to 0$. A method is classified to have strong order convergence equal to γ if there is a constant C such that the MSE is bounded by

$$\langle \sigma^\alpha(t) - \tilde{\sigma}^\alpha(t;h) \rangle \leq Ch^\gamma, \quad \text{as } h \to 0, \tag{A.9}$$

for any $t = h \cdot n$. The expectation value $\langle . \rangle$ is an average over multiple noise realizations. In general, the EM-algorithm has strong order convergence with $\gamma = 1/2$, see e.g. [222]. In order to increase accuracy by a factor of 10, the discretisation needs to be increased by a factor 100. This result deviates from the deterministic case where there is no stochastic component. In this scenario, the expectation value from Eq. (A.9) can be removed and the inequality is fulfilled with $\gamma = 1$.

In order to raise the strong order of convergence back to $\gamma = 1$ for an approximation in a stochastic setting, one needs to evaluate double stochastic integrals that appear as second-order corrections in the Taylor series expansion of the stochastic integrals, see e.g. [222]. This is achieved by a multiple stage stochastic Runge-Kutta algorithm.

Three-stage stochastic Runge-Kutta algorithm

Here, we spell out in detail the algorithm that we have used for numerical simulations of the stochastic optical Bloch equations, see Eq. (4.82). It was derived by Roessler in 2009 [192].

For the multidimensional Itô SDE with a 3-dimensional driving Wiener process we employ a derivative-free order $\gamma = 1.0$ strong stochastic Runge-Kutta scheme (SRK) algorithm with three stages

$$\begin{aligned}\sigma^\alpha_{n+1} =& \sigma^\alpha_n + D^\alpha(t_n, \sigma^\alpha_n) h_n + \sum_{k=1}^{3} M^{\alpha\beta}_k(t_n, \sigma^\alpha_n) I_{(k)} \\ &+ \frac{1}{2} \sum_{k=1}^{3} \left(M^{\alpha\beta}_k(t_n, H^{(k)}_2) - M^{\alpha\beta}_k(t_n, H^{(k)}_3) \right) \sqrt{h_n},\end{aligned} \tag{A.10}$$

as derived in [192]. The first two terms generate the deterministic time-evolution. Together with the third term, which contains a single stochastic integral I_k, see Eq. (A.14) and the noise-strength $M^{\alpha\beta}(t_n, \sigma^\alpha_n)$ this algorithm is extended to treat a stochastic component and is the Euler-Maruyama algorithm that defines the first of the three evaluation stages of the algorithm. The last two terms contain the stochastic double integrals denoted as

$I_{(l,k),n}$. which appear in the stages two and three as

$$H_2^{(k)} = \sigma_n^\alpha + \sum_{\ell=1}^{3} M_l^{\alpha\beta}(t_n, \sigma_n^\alpha)\frac{I_{(l,k)}}{\sqrt{h_n}}, \tag{A.11}$$

$$H_3^{(k)} = \sigma_n^\alpha - \sum_{\ell=1}^{3} M_l^{\alpha\beta}(t_n, \sigma_n^\alpha)\frac{I_{(l,k)}}{\sqrt{h_n}}. \tag{A.12}$$

The single stochastic integral is defined and approximated as

$$I_{(i),n} = \int_{t_n}^{t_{n+1}} dW_s^i, \sim \Delta W(t_n) \tag{A.13}$$

with $\Delta W(t_n) = W(t_{n+1}) - W(t_n)$ distributed as $\Delta W(t_n) \sim N(0, \sqrt{h})$. The multiple stochastic Integrals $I_{i,j}$ for $1 \leq i, j \leq m$ with $i \neq j$ are defined as

$$I_{(i,j),n} = \int_{t_n}^{t_{n+1}} \int_{t_n}^{s} dW_u^i dW_s^j, \tag{A.14}$$

and can only be approximated as an exact simulation is not possible. An efficient simulation was suggested by Wiktorsson [193].

Iterated *Itô* integrals with the Wiktorsson algorithm

For an m-dimensional Wiener process there are m^2 two-times iterated Itô integrals. These can be simulated simultaneously by pairing the independent Wiener processes by an algorithm that was put forward by Wiktorsson [193]. The suggested algorithm converges to the exact result of the stochastic double integrals with a mean square error of order $1/n^2$ and n is the number of terms in a truncated infinite series representation of the iterated Itô integrals that was derived by Kloeden, Platen and Wright [222]. The remaining tailsum is approximated with a multivariate normal distribution. Here, we spell out the explicit steps of the Wiktorsson algorithm that were used in this thesis. In this whole section we follow of course [193].

The iterated Itô integrals can be used to define so-called Lévy stochastic area integrals

$$A_{ij}(h) = \frac{I_{ij}(h) - I_{ji}(h)}{2}, \tag{A.15}$$

where A_{ij} is the area spanned by the two-dimensional Brownian motion $\{(W_i(t), W_j(t))\}$ from 0 to h and the line connecting $\{(W_i(0), W_j(0))\}$ and $\{(W_i(h), W_j(h))\}$. From Eq. (A.15), follow the relations

$$A_{ji}(h) = -A_{ij}(h), \tag{A.16}$$

$$A_{ii}(h) = 0. \tag{A.17}$$

The stochastic area integrals obey the following relations [222]

$$I_{ij} = \frac{\Delta W_i(h)\Delta W_j(h) - h\delta_{ij}}{2} + A_{ij}(h) \tag{A.18}$$

The Lévy areas

$$A_{ij}(h) = \frac{h}{2\pi}\sum_{k=1}^{\infty}\frac{1}{k}B_{ij}(h,k) \tag{A.19}$$

$$B_{ij}(k,h) = X_{ik}\left(Y_{jk} + \sqrt{\frac{2}{h}}\Delta W_j(h)\right) - X_{jk}\left(Y_{ik} + \sqrt{\frac{2}{h}}\Delta W_i(h)\right) \tag{A.20}$$

where $\Delta W_i(h) \sim N(0,h)$,$X_{ik} \sim N(0,1)$, for $i = 1,2,3$ and $k = 1,2,\dots$ are all independent from one another. Due to the symmetry relations of the Lévy areas we are interested in the subset corresponding to $i < j$. We define

$$\tilde{A}(h) = [A_{12}(h), A_{13}(h), A_{23}(h)]^T \tag{A.21}$$

$$\tilde{B}(h,k) = [B_{12}(h), B_{13}(h), B_{23}(h)]^T \tag{A.22}$$

We split the infinite sum in Eq. (A.19) $\tilde{A}(h) = \tilde{A}^n(h) + \epsilon_n$ in two parts by defining the first contribution as

$$\tilde{A}^n(h) = \epsilon_n + \frac{h}{2\pi}\sum_{k=1}^{n}\frac{1}{k}\tilde{B}(h,k) \tag{A.23}$$

and the second contribution, the tailsum ϵ_n as

$$\epsilon_n = \frac{h}{2\pi}\sum_{k=n+1}^{\infty}\frac{1}{k}\tilde{B}(h,k) \tag{A.24}$$

It can be shown that as $(2\pi/h)a_n^{-1/2}\epsilon_n$ converges weakly to a Gaussian vector with zero mean and a covariance matrix Σ_∞.

$$\Sigma_\infty = \begin{pmatrix} \frac{2\left(\mathrm{W1}^2+W_2^2\right)}{h}+2 & \frac{2W_2W_3}{h} & -\frac{2W_1W_3}{h} \\ \frac{2W_2W_3}{h} & \frac{2\left(W_1^2+W_3^2\right)}{h}+2 & \frac{2W_1W_2}{h} \\ -\frac{2W_1W_3}{h} & \frac{2W_1W_2}{h} & \frac{2\left(W_2^2+W_3^2\right)}{h}+2 \end{pmatrix} \tag{A.25}$$

such that for $n \gg 1$,ϵ_n is approximated as

$$\epsilon_n = \frac{h}{2\pi}\sqrt{a_n}\sqrt{\Sigma_\infty}\boldsymbol{G}_n, \tag{A.26}$$

where $\boldsymbol{G}_n \sim N(0_{3\times 3}, I_3)$ is a Gaussian vector with zero mean. The matrix square root is approximated as

$$\sqrt{\Sigma_\infty} = \frac{\Sigma_\infty + 2\sqrt{1+|\Delta\boldsymbol{W}(h)|^2/h}I_3}{\sqrt{2}(1+\sqrt{1+|\Delta\boldsymbol{W}|^2/h})}. \tag{A.27}$$

The cut-off n for the simulation of the iterated Ito-integrals has to be chosen such that the MSE of the iterated Itô integrals is e smaller than the temporal discretisation error. Kloeden Platen and Wright showed that this is achieved if the MSE of the stochastic double integrals is bounded by Ch^3 for a positive constant C [218]. With the choice of

$$n \geq \left.\frac{\sqrt{5m^2(m-1)(24\pi^2)}}{Ch}\right|_{m=3} \tag{A.28}$$

it is possible to achieve a strong order one convergence. With the calculation of the Lévy areas it is possible via Eq. (A.19) to calculate the iterated Itô−integrals. The algorithm put forward by Wiktorsson [193] is the following four-step procedure.

1) Simulate $\boldsymbol{W}(h)$ from $N(0_{3\times 3}, \sqrt{h}I_{3\times 3})$
2) Approximate the Lévy areas as

$$\tilde{A}_{ij}^{(n)}(h) = \frac{h}{2\pi}\sum_{k=1}^{n}\frac{1}{k}\left(X_{ik}\left(Y_{jk}+\sqrt{\frac{2}{h}}\Delta W_j(h)\right) - X_{jk}\left(Y_{ik}+\sqrt{\frac{2}{h}}\Delta W_i(h)\right)\right) \tag{A.29}$$

where $X_{ik} \sim N(0,1)$ and $Y_{ik} \sim N(0,1)$ are independently distributed Gaussian random numbers with zero mean and $i < j$ with $(i,j) \in (1,2,3)$.

3) Add the tailsum approximation to the stochastic area integrals

$$\tilde{A}(h) = \tilde{A}^{(n)}(h) + \frac{h}{2\pi}\sqrt{a_n}\sqrt{\Sigma_\infty}\boldsymbol{G}_n \tag{A.30}$$

ans simulate $\boldsymbol{G}_n \sim N(0_{3\times3}, I_{3\times3})$.

4) Lastly, proceed to calculate the stochastic integrals

$$I_{ij}(h) = \frac{\Delta W_i(h)\Delta W_j(h) - h\delta_{ij}}{2} + \tilde{A}_{ij}(h) \tag{A.31}$$

The stochastic double integrals that appear in the three-stage stochastic Runge-Kutta algorithm in Eq. (A.10) can be simulated with the four-step process $1) - 4)$.

Properties of Wiener-Processes

In this section we review the properties of Wiener processes W_t, and we follow [221, 193] with the loose identification $W_t = \frac{d\xi}{dt}$ (see discussion above) and brownian increments dW_t in stochastic integrals. A real-valued and continuous, stochastic Wiener process satisfies the properties of a random walk

1) $W(0) = 0$
2) $W(t) - W(s) \sim N(0, t-s), \quad \forall (t \geq s \geq 0)$
3) $\{W(t_1), W(t_2 - t_1), \ldots, W(t_n) - W(t_{n-1})\}$, are independet increments$\forall t_1 < t_2 < \cdots < t_n$

this means in particular that the average $\langle . \rangle$ over multiple realizations of the brownian random walker satisfies the properties

$$\langle W(t) \rangle = 0, \quad \text{and} \quad \langle W^2(t) \rangle = t, \quad \forall t \geq 0. \tag{A.32}$$

If the Wiener process is discretised with respect to time slices Δt, these conditions lead to the properties for increments of Wiener process $W_{\beta,t} - W_{\beta,t-\Delta t}$ that satisfy the above defined relations

$$W_{\beta,0} = 0, \quad W_{\beta,t} = W_{\beta,t-\Delta t} + \sqrt{\Delta t} X_{\beta,t} \tag{A.33}$$

Here, $\boldsymbol{W}_t = (W_{t,1}, \ldots, W_{t,d})^T$ defines a $d-$dimensional Wiener process with $\beta \in [0, \ldots, d]$ whose transitions are distributed as a multivariate Gaussian $(\boldsymbol{W}_t - \boldsymbol{W}_{t-\Delta t}) \sim N(0, \Delta t \boldsymbol{I}_d)$ and $\boldsymbol{I}_d$ is the $d-$dimensional Identity matrix and $X_{\beta,t} \sim N(0,1)$. In fact, Eq. (A.8) does not involve independent but correlated Wiener processes since the noise functions in the stochastic differential equation obey the covariance relation

$$\langle \xi_t^\alpha \xi_t^\beta \rangle = \chi_{\alpha\beta}\delta(t - t'). \tag{A.34}$$

This can be implemented by modifying the discrete Wiener process as

$$\boldsymbol{W}_t = \boldsymbol{W}_s + \sqrt{\Delta t}\tilde{\boldsymbol{X}}_s \tag{A.35}$$

where the random d-dimensional vector $\tilde{\boldsymbol{X}}_s$ is distributed as $\boldsymbol{N}(0, \boldsymbol{\Sigma})$. Where $\boldsymbol{N}(\boldsymbol{0}, \boldsymbol{\Sigma})$ is the multivariate Gaussian probability distribution with $\langle \tilde{\boldsymbol{X}}_d \rangle = \boldsymbol{0}$ and $\langle \tilde{\boldsymbol{X}}_d^T \tilde{\boldsymbol{X}}_d \rangle = \boldsymbol{\Sigma}$, where the covariance matrix is defined as $\Sigma_{ij} = \langle (X_i - \mu_i)(X_j - \mu_j) \rangle$. Correlated random variables $\tilde{\boldsymbol{X}}_s$ in d-dimensions can be constructed from d draws from a one dimensional standard Gaussian probability distribution with the help of the affine transformation

$$y_i = M_{i\ell} X_\ell, \tag{A.36}$$

where now $X_\ell \sim N(0,1)$. The covariance of the new variable y_i has the desired covariance

$$\begin{aligned}
\langle y_i y_j \rangle &= \int_{-\infty}^{\infty} \Pi_{n=1}^{N} dx_n (M_{im} x_m)(M_{j\ell} x_\ell) \frac{1}{(\sqrt{2\pi})^N} e^{-\frac{1}{2}\boldsymbol{x}^T \boldsymbol{x}} && \text{(A.37)} \\
&= \int_{-\infty}^{\infty} \Pi_{n=1}^{N} d\tilde{x}_n \det(M) \frac{\exp\left(-\frac{1}{2}\tilde{x}_m M^{-1}_{m\ell} M_{\ell p} \tilde{x}_p\right)}{(\sqrt{2\pi})^N} \tilde{x}_i \tilde{x}_j && \text{(A.38)} \\
&= \int_{-\infty}^{\infty} \Pi_{n=1}^{N} d\tilde{x}_n \sqrt{\det(\Sigma)} \frac{\exp\left(-\frac{1}{2}\tilde{x}_m \Sigma^{-1}_{mp} \tilde{x}_p\right)}{(\sqrt{2\pi})^N} \tilde{x}_i \tilde{x}_j = \Sigma_{ij} && \text{(A.39)}
\end{aligned}$$

where $\det(M) = \sqrt{\det(\Sigma)} \geq 0$ due to the property of Σ being positive (semi)-definite.

The random variables $\boldsymbol{y} = \boldsymbol{M}\boldsymbol{X}$ are then distributed according to the probability distribution

$$f_Y(Y) = f_X(\boldsymbol{M}^{-1}\boldsymbol{Y}) |\det M^{-1}| = \frac{1}{(\sqrt{2\pi})^N \sqrt{\det(\Sigma)}} \exp\left(-\frac{1}{2}\boldsymbol{y}^T \Sigma^{-1} \boldsymbol{y}\right) \tag{A.40}$$

Thus, correlated Wiener processes can be constructed from uncorrelated Wiener processes with the affine transformation

$$\boldsymbol{W}_{t,\alpha} = \boldsymbol{W}_{s,\alpha} + \sqrt{\Delta t} \boldsymbol{M}_{\alpha\beta} \boldsymbol{X}_{\beta,t}, \tag{A.41}$$

where now $\boldsymbol{X}_{\beta,t} \sim \boldsymbol{N}(0, \boldsymbol{I}_d)$ such that $(\boldsymbol{W}_{t,\alpha} - \boldsymbol{W}_{s,\alpha}) \sim \boldsymbol{N}(0, \Delta t \boldsymbol{M}\boldsymbol{M}^T = \Delta t \boldsymbol{\Sigma})$. Consequently, the transition probability density for the process $(\boldsymbol{W}_{t,\alpha} - \boldsymbol{W}_{s,\alpha}) \sim \boldsymbol{N}(0, \Delta t \boldsymbol{M}\boldsymbol{M}^T = \Delta t \boldsymbol{\Sigma})$ then satisfies the relation

$$f_{\boldsymbol{W}_{t,\alpha} - \boldsymbol{W}_{s,\alpha}} = \frac{1}{\left(\sqrt{2\pi(t-s)}\right)^N \sqrt{\det(\Sigma)}} \exp\left(-\frac{1}{2(t-s)} \boldsymbol{x}^T \Sigma^{-1} \boldsymbol{x}\right) \tag{A.42}$$

Chapter B

Antiferromagnetic Phase Transition in Presence of Cavity-Mediated Fluctuations

We present preliminary work on a classical Ising Antiferromagnet on a two-dimensional square lattice with nearest-neighbour interactions driven weakly by vacuum fluctuations of a single bosonic light mode of a cavity which induces transitions between classical spin configurations.
A spin-flip occurs whenever the energetic difference of two-dimensional spin-configurations falls in a frequency window centred around the cavity resonance and bounded by the cavity decay rate. We investigate the even-odd translational symmetry breaking in the ground-state of the Hamiltonian in the presence of cavity fluctuations that induce a genuine non-equilibrium dynamics. Therefore, the occupation probabilities p_e and p_o of the even and odd lattice sites are a priori not pre-determined by the Boltzmann distribution as in thermal equilibrium. They are however fixed by a coupled, non-linear set of equations involving the transition rates that can be derived from a modern Liouvillian perturbation theory [223, 224] for weakly driven-open systems where perturbations break conservation laws associated to the unperturbed system. We compare perturbative, analytical calculations for the antiferromagnetic order parameter with a classical Monte-Carlo simulation for the stationary state of the system. We conclude our preliminary investigations by a discussion of open questions as well as a brief validity analysis. We define steps for future work.

Introduction and Model

A two-dimensional Ising Hamiltonian with tunable-range interactions has recently been realized experimentally with ultracold atoms in an optical lattice. This was achieved by realizing an effective dipole-dipole interaction between two ground-states $|\tilde{\uparrow}\rangle_i$ and $|\tilde{\uparrow}\rangle_j$ of a ground-state manifold $\{|\tilde{\uparrow}\rangle, |\downarrow\rangle\}$ of atoms at site i and j. The ground-state inherits an electrical dipole by off-resonant coupling to a highly excited Rydberg state $|r\rangle$ such that it becomes optically dressed as $|\tilde{\uparrow}\rangle = |\uparrow\rangle + \alpha\,|r\rangle$, where $\alpha \ll 1$ is the perturbatively calculated coupling constant. The Rydberg dressing induces a dipole-dipole interaction with a van-der-Waals tail $\sim 1/R^6$, where R is the separation distance of the atoms.

Here, we propose to couple the synthetic spin-lattice weakly with the vacuum mode of a cavity that drives the atom-cavity system out of equilibrium as the spin-ensemble is subject to cavity-assisted spin flips through vacuum fluctuations of the cavity. Intuitively, the photons themselves can leave the system through imperfect cavity mirrors and provide an effective cooling mechanism as they carry with them an energy ω_0 associated to the cavity frequency.

We address this problem as it raises several interesting questions.

1. Is the antiferromagnetic phase transition in the presence of cavity-assisted spin-flips within the thermal Ising universality class?
   We consider the phase transition from a paramagnet $|\uparrow,\uparrow,\dots\rangle$ to a Néel antiferromagnet $|\uparrow,\downarrow,\dots\rangle$ as a ground-state phase transition driven by an increasing dipole-dipole interaction in the Hamiltonian. The presence of cavity-assisted spin-flips could likely lead to a finite noise-intensity leading to a classical thermal phase transition. However, the non-thermal noise could potentially change the critical exponents and change the universality class of the transition.
2. Can the stationary probability distribution $P(\{\boldsymbol{s}\})$ for a spin configuration $\{\boldsymbol{s}\}$ in the long-time limit be mapped to a thermal or generalized Gibbs distribution taking into account the conserved charges of the system in addition to an effective temperature T_{eff}?
   The stationary state distribution of a Markov-chain Monte Carlo simulation for the long-time limit dynamics is determined by the cavity-assisted transition rates between classical spin configurations. Therefore, the occupation probabilities, of the even p_e and odd p_o lattice sites are not pre-determined from a Boltzmann distribution. An idea is to numerically evaluate the stationary state distribution $P(\{\boldsymbol{s}\})$ and check if it can be fitted to a thermal Boltzmann or Gibbs distribution.
3. Is the phase transition in a non-equilibrium setting a first or second order phase transition?
   In a $T = 0$ spin-mean-field calculation the Néel phase transition is a sudden, first-order transition. At finite temperatures, it is replaced by a second-order phase transition with a critical temperature determined by Onsagers exact solution of the two-dimensional Ising model.

In the remainder of this section, we touch upon the first question only.

Hamiltonian and Lindblad Perturbation

We consider a two-dimensional Ising Hamiltonian H_0 where in contrast to a conventional Ising term $\sim \sigma^z\sigma^z$, the interaction is conditioned on population in the excited state

$$H_0 = -\frac{\omega_z}{2}\sum_{\ell=1}^{N}\sigma_\ell^z + V\sum_{\langle \ell,m\rangle}\left(\frac{1+\sigma_\ell^z}{2}\right)\left(\frac{1+\sigma_m^z}{2}\right). \tag{B.1}$$

We model the two-level system with Pauli operators and define $\sigma_\ell^z = |e\rangle_\ell\langle e| - |g\rangle_\ell\langle g|$, where $|e\rangle$ refers to the excited state and $|g\rangle$ refers to the ground state. A detailed description of the setup and references to an experimental realization of the Hamiltonian is also given in section 3.2. As H_0 consists purely of σ^z-terms, the eigenstates of the system can be conveniently as $|n_i\rangle \in \{|\uparrow\downarrow\downarrow\downarrow\downarrow\rangle, |\uparrow\downarrow\downarrow\downarrow\uparrow\rangle, \dots\}$ that are atomic configurations of a spin-up and spin-down pattern with σ^z as the quantisation axis.

The Hamiltonian conserves observables built from combinations of σ^z operators as for instance the energy $C_2 = H_0$ and the total spin-z component or magnetisation $C_1 = \sum_{\ell=1}^N \sigma_i^z$ or the sublattice magnetisations $C_e = \sum_{\ell\in\text{even}}\sigma_\ell^z$ for the even and the odd sublattice $C_o = \sum_{\ell\in\text{odd}}\sigma_\ell^z$ as can be seen by

$$[H_0, C_i] = 0. \tag{B.2}$$

As such, the Hamiltonian displays purely classical, Ising-like dynamics.

However, in the presence of a weak ($g/\sqrt{N} \ll \omega_z, V$) coupling to a single light mode of the cavity, described by the Hamiltonian

$$H_1 = \frac{g}{\sqrt{N}} \sum_{\ell=1}^{N} \sigma_\ell^x (a + a^\dagger), \tag{B.3}$$

the conservation of C_1, C_e, C_o and all other quantities constructed from σ^z matrices is broken, as the cavity can mediate spin flips in the entire lattice. The cavity field is kept at $\langle a \rangle = 0$ and thus $a, a^\dagger$ describe fluctuations around the vacuum. The coupling to the cavity can be interpreted as an external drive with strength $g/\sqrt{N}$ and the cavity-induced spin flips occur on a timescale associated to the inverse energy scale of the coupling $t \gg \sqrt{N}/g$. This implies that we are interested in the limit $t \to \infty$ before taking the limit $N \to \infty$ as these two limits do not commute.

The open system dynamics is given by the markovian master equation in Liouville form

$$\dot{\rho} = \mathcal{L}\rho = \left(\mathcal{L}_0 + \mathcal{L}_\kappa + \frac{g}{\sqrt{N}} \mathcal{L}_1 \right) \rho, \tag{B.4}$$

where we have split up the total Liouville operator $\mathcal{L}$ in the unperturbed Hamiltonian part $\mathcal{L}_0$ and $\mathcal{L}_\kappa$ and the Hamiltonian perturbation $\mathcal{L}_1$

$$\mathcal{L}_0\rho = -i\Big[H_0, \rho\Big], \quad \mathcal{L}_1\rho = -i\Big[H_1, \rho\Big]. \tag{B.5}$$

We model the imperfect cavity mirrors in the standard Born-Markov approximation to account for photon losses with the Lindblad operator $\mathcal{L}_\kappa$

$$\mathcal{L}_\kappa \rho = \kappa \sum_{\ell=1}^{N} \left(a\rho a^\dagger - \frac{1}{2}(\rho a^\dagger a + a^\dagger a \rho) \right). \tag{B.6}$$

The coupling of cavity photons to the electromagnetic vacuum modes outside the cavity breaks energy conservation C_2 of the Hamiltonian as photons escaping from the cavity carry with them an energy associated to the cavity frequency.

Classical steady-state density matrix with perturbatively defined non-equilibrium occupations

The Liouville equation (B.4) defines a situation of a weakly driven and weakly open quantum system where the unperturbed system characterized by H_0 has local conservation laws associated to operators containing only σ^z-terms, such as the energy as described by C_0 and the total spin-z component or the sublattice magnetisation as described by C_1, C_e and C_o. The coupling to the cavity and to the external vacuum modes break these conservation laws and are expected to drive the system to a stationary state that can be approximately described by a (generalized) Gibbs ensemble [224],

$$\rho_0 \sim \exp\left(-\sum_i \lambda_i C_i \right) \tag{B.7}$$

where the Lagrange parameters λ_i cannot be determined from the initial state as the quantities C_i are not conserved in the presence of the Hamiltonian perturbations H_1 and the dissipative Lindblad contribution $\mathcal{L}_\kappa$. Finite expectation values of the C_i will be a consequence of a balance of drive and dissipation in the steady-state.

We follow now step by step the Liouvillian perturbation procedure outlined in [224] to derive coupled rate equations that fix the expectation values $\langle C_i \rangle$ in the stationary state. The steady-state density matrix ρ_0 is then determined from two conditions

$$\mathcal{L}_0 \rho_0 = 0, \tag{B.8}$$

$$\langle \dot{C_i} \rangle = \mathrm{Tr}\Big[\mathrm{C_i} \mathcal{L} \rho\Big] \approx \mathrm{Tr}\Big[\mathrm{C_i} \mathcal{L}_1 \mathcal{L}_0^{-1} \mathcal{L}_1 \rho_0\Big] = 0. \tag{B.9}$$

The first condition is fulfilled due to the conservation laws $[H_0, C_i] = 0$ by a density matrix ρ_0 described by a generalised Gibbs ensemble (GGE). The second condition is the first non-vanishing perturbative correction which is a second-order correction $O(g^2/N)$ in the perturbation that fixes the density matrix ρ_0 to zeroth order $\left(g/\sqrt{N}\right)^0$ in the perturbation $\mathcal{L}_1$. We have left out the steps that lead to the perturbative correction in Eq. (B.9) as they can be found in detail in [224]. As also mentioned in this paper, the second order correction is intuitive as transition rates typically come with a quadratic correction in the strength of the perturbation, as familiar for instance from Fermi's golden rule.

In two-dimensions, we will give an approximate solution for the density matrix in the steady-state when the cavity is in the vacuum mode $\langle a \rangle = 0$. We parametrise the density matrix as

$$\rho_0 = \rho_e \otimes \rho_o \otimes |0\rangle \langle 0| = \bigotimes_{i=(e,o)} \left(\sum_{s=\uparrow,\downarrow} p_{s,i} \sum_{n=1}^{\#configs} p_{n,i} \, |n, 0\rangle_i \, \langle n, 0| \right), \tag{B.10}$$

where we have assumed that the density matrix separates in a part for the even and the odd sites. Notice that the Ansatz for the density matrix is classical. Here $|n_i\rangle \in \{|\uparrow\downarrow\downarrow\downarrow\downarrow\rangle, |\uparrow\downarrow\downarrow\downarrow\uparrow\rangle, \ldots\}$ is an atomic configuration of a spin-up and spin-down pattern with σ^z as the quantisation axis. The classical state space of atomic configurations grows exponentially in the number of spins N. For our mean-field Ansatz we consider only even and odd sites with all configurational possibilities of the four neighbours which are 2^4. The index (e, o) refers to the even and the odd sides respectively. The probability for the spin on the even site to point up is given by $p_{\uparrow,e} = p_e$. The remaining configurations for the spins on the odd site is then given by the probabilities $p_{n,e}$. For example the state $|\uparrow\downarrow\downarrow\downarrow\downarrow\rangle$ has a probability of $p_{\uparrow,e} p_{n,e} = p_{,e}(1 - p_o)^4$. The probabilities are normalised with

$$\sum_{n=1}^{\#configs} p_{n,i} = (1 - p_i)^4 + 4p_e(1 - p_i)^3 + 6p_e^2(1 - p_i)^2 + 4p_e^3(1 - p_i) + p_i^4 = 1 \tag{B.11}$$

and similarly for the odd sites. The prefactors come from the Binomialcoefficient with $\binom{4}{k}$ and $k \in (0, 4)$. Such that $\mathrm{Tr}\rho = \Pi_{\mathrm{i=e,o}} \sum_{\mathrm{n=1}}^{\mathrm{\#configs}} \mathrm{p_{n,e}} = 1$. For example, the density matrix on the even sites is described as

$$\rho_e = p_e \left((1 - p_o)^4 \, |\uparrow\downarrow\downarrow\downarrow\downarrow\rangle \langle \uparrow\downarrow\downarrow\downarrow\downarrow| + p_o(1 - p_o)^3 \sum_{\text{permutations}} |\uparrow\uparrow\downarrow\downarrow\downarrow\rangle \langle \uparrow\uparrow\downarrow\downarrow\downarrow| + \ldots \right) \tag{B.12}$$

$$+ (1 - p_e) \left((1 - p_o)^4 \, |\downarrow\downarrow\downarrow\downarrow\downarrow\rangle \langle \downarrow\downarrow\downarrow\downarrow\downarrow| + p_o(1 - p_o)^3 \sum_{\text{permutations}} |\downarrow\uparrow\downarrow\downarrow\downarrow\rangle \langle \downarrow\uparrow\downarrow\downarrow\downarrow| + \ldots \right) \tag{B.13}$$

The density matrix on the odd sites is obtained by the exchange $e \leftrightarrow o$. The two conserved quantities we consider are the magnetisation on the even and the odd lattice sites respectively

$$\partial_t \langle \sigma_e^z \rangle = \mathrm{Tr}\left[\sigma_{\mathrm{e}}^z \mathcal{L}_1 \mathcal{L}_0^{-1} \mathcal{L}_1 \rho_0\right] = 0, \tag{B.14}$$

$$\partial_t \langle \sigma_o^z \rangle = \mathrm{Tr}\left[\sigma_{\mathrm{o}}^z \mathcal{L}_1 \mathcal{L}_0^{-1} \mathcal{L}_1 \rho_0\right] = 0, \tag{B.15}$$

where we have adopted the notation $\sum_{\ell \in even} \sigma_\ell^z = \sigma_e^z$ and $\sum_{\ell \in odd} \sigma_\ell^z = \sigma_o^z$. We proceed by an explicit derivation of the coupled rate equations that result from the rate equation (B.14) and Eq. (B.15)

Part 1: $\mathcal{L}_1 \tilde{\rho}_0$

In the following, we consider first a fixed single atomic configuration $|n\rangle$ in the σ^z basis and construct the corresponding density matrix

$$\tilde{\rho}_0 = |n, 0\rangle \langle n, 0| , \tag{B.16}$$

to compute the perturbatively induced spin flips with $H_1 |n, 0\rangle = \frac{g}{\sqrt{N}} \sum_\ell |\bar{n}_\ell, 1\rangle$, where $|\bar{n}_\ell\rangle = |\ldots, - \uparrow_\ell, \ldots\rangle$ has the spin at position ℓ flipped. Correspondingly, we evaluate

$$\mathcal{L}_1 \tilde{\rho}_0 = -i[H_1, \tilde{\rho}_0] = -i \frac{g}{\sqrt{N}} \sum_\ell \left(|\bar{n}_\ell, 1\rangle \langle n, 0| - |n, 0\rangle \langle \bar{n}_\ell, 1|\right). \tag{B.17}$$

Part 2: $\mathcal{L}_0^{-1} \left(\mathcal{L}_1 \tilde{\rho}_0\right)$

We proceed with an evaluation of $\mathcal{L}_0^{-1} \left(\mathcal{L}_1 \tilde{\rho}_0\right)$, where we take $\mathcal{L}_0 \equiv \mathcal{L}_0 + \mathcal{L}_\kappa$. To calculate the action of an inverted Lindblad super operator on a density matrix, we first consider the effect of $\mathcal{L}_0$ on a mixed density matrix state with zero and one photonic excitation inside the cavity in the combined atom-photon basis $|n\rangle \otimes |n_p\rangle = |n, n_p\rangle$, where the first letter n refers to a pattern of spin-up and spin-down configurations and $n_p = (0, 1)$ labels the number of photons in the cavity. The action of the inverted Lindblad can then be inferred from the matrix inversion of

$$\mathcal{L}_0 \left(\alpha_1 |n, 0\rangle \langle m, 0| + \alpha_2 |n, 0\rangle \langle m, 1| + \alpha_3 |n, 1\rangle \langle m, 0| + \alpha_4 |n, 1\rangle \langle m, 1|\right) = M\alpha, \tag{B.18}$$

where the matrix

$$M^{-1} = \begin{pmatrix} \frac{i}{E_n - E_m} & 0 & 0 & \frac{\kappa}{(E_m - E_n)(E_m - E_n + i\kappa)} \\ 0 & \frac{-i}{E_m - E_n + i\kappa/2 + \omega_0} & 0 & 0 \\ 0 & 0 & \frac{-i}{E_m - E_n + i\kappa/2 - \omega_0} & 0 \\ 0 & 0 & 0 & -\frac{i}{E_m - E_n + i\kappa} \end{pmatrix} \tag{B.19}$$

is represented in the atom-photon basis $\{|n, n_p\rangle\}$ in the order given by the set $\mathcal{B}_{nm} = \{00, 01, 10, 11\}$. The energies E_n are eigenenergies of an atomic state calculated as $H_0 |n\rangle = E_n |n\rangle$. Using Eq. (B.17) we find

$$\begin{aligned} \mathcal{L}_0^{-1} \left(\mathcal{L}_1 \tilde{\rho}_0\right) &= \mathcal{L}_0^{-1} \left(-i \frac{g}{\sqrt{N}} \sum_\ell \left(|\bar{n}_\ell, 1\rangle \langle n, 0| - |n, 0\rangle \langle \bar{n}_\ell, 1|\right)\right) \\ &= -i \frac{g}{\sqrt{N}} \sum_\ell \left(\frac{-i}{E_n - E_{\bar{n}_\ell} + i\kappa/2 - \omega_0} |\bar{n}_\ell, 1\rangle \langle n, 0| - \frac{-i}{E_{\bar{n}_\ell} - E_n + i\kappa/2 + \omega_0} |n, 0\rangle \langle \bar{n}_\ell, 1|\right) \end{aligned} \tag{B.20}$$

as our result.

Part 3: $\mathrm{Tr}\Big[\sigma_{\mathrm{o}}^{z}\mathcal{L}_1\mathcal{L}_0^{-1}\mathcal{L}_1\tilde{\rho}_0\Big]$

We now calculate the last contribution to evaluate the rate equation (B.14) and Eq. (B.15) which is given by $\mathcal{L}_1(\mathcal{L}_0^{-1}\mathcal{L}_1\tilde{\rho}_0)$. For this, consider the two contributions

$$\mathcal{L}_1\left(|\bar{n}_\ell,1\rangle\langle n,0|\right) = -i\frac{g}{\sqrt{N}}\sum_m\left(|\bar{n}_{\ell,m},0\rangle\langle n,0| + |\bar{n}_{\ell,m},2\rangle\langle n,0| - |\bar{n}_\ell,1\rangle\langle\bar{n}_m,1|\right), \quad \text{(B.21)}$$

$$\mathcal{L}_1\left(|n,0\rangle\langle\bar{n}_\ell,1|\right) = -i\frac{g}{\sqrt{N}}\sum_m\left(|\bar{n}_m,1\rangle\langle\bar{n}_\ell,1| - |n,0\rangle\langle\bar{n}_{\ell,m},0| - |n,0\rangle\langle\bar{n}_{\ell,m},2|\right), \quad \text{(B.22)}$$

where $\bar{n}_{\ell,m}$ has the spin flipped at sites ℓ and m, as $|\bar{n}_{\ell,m}\rangle = |\ldots,-\uparrow_\ell,\ldots,-\uparrow_m,\ldots\rangle$. This transforms Eq. (B.20), to

$$\begin{aligned}
&\mathcal{L}_1(\mathcal{L}_0^{-1}\mathcal{L}_1\tilde{\rho}_0) = \\
&-\left(\frac{g}{\sqrt{N}}\right)^2\sum_{\ell,m}\Bigg[\frac{-i}{E_{n_\ell}-E_{\bar{n}_\ell}+i\kappa/2-\omega_0}\left(|\bar{n}_{\ell,m},0\rangle\langle n,0| + |\bar{n}_{\ell,m},2\rangle\langle n,0| - |\bar{n}_\ell,1\rangle\langle\bar{n}_m,1|\right) \\
&-\frac{-i}{E_{\bar{n}_\ell}-E_{n_\ell}+i\kappa/2+\omega_0}\left(|\bar{n}_m,1\rangle\langle\bar{n}_\ell,1| - |n,0\rangle\langle\bar{n}_{\ell,m},0| - |n,0\rangle\langle\bar{n}_{\ell,m},2|\right)\Bigg] \qquad \text{(B.23)}
\end{aligned}$$

The trace operation eliminates all off-diagonal elements such that the only surviving terms are of the form

$$\mathrm{Tr}\Big[\sigma_i^z\mathcal{L}_1\mathcal{L}_0^{-1}\mathcal{L}_1\tilde{\rho}_0\Big] = 2\pi\frac{g^2}{N}\mathrm{Tr}\sum_\ell\Big[\delta(\Delta E_\ell,\kappa,\omega)\sigma_i^z\left(|n_\ell,0\rangle\langle n_\ell,0| - |\bar{n}_\ell,1\rangle\langle\bar{n}_\ell,1|\right)\Big]. \quad \text{(B.24)}$$

In this equation appears a transition rate

$$\delta(\Delta E_\ell,\kappa,\omega) = \frac{1}{2\pi}\left(\frac{i}{\Delta E_\ell-\omega_0+i\kappa/2} - \frac{i}{\Delta E-\omega_0-i\kappa/2}\right) = \frac{1}{\pi}\frac{\kappa/2}{(\Delta E_\ell-\omega_0)^2+(\kappa/2)^2} \quad \text{(B.25)}$$

parametrised by a Lorentzian line shape. The transition rate explicitly depends on the spin configurations of the four neighbours of the spin at site ℓ through the energy differences $\Delta E_\ell = E_{n_\ell} - E_{\bar{n}_\ell}$. The Lorentzian is centred around the cavity frequency $\omega_0 = \Delta E_\ell$ with full width at half maximum given by κ. It describes the absorption or emission of a cavity photon that leads to a flip of the spin in the lattice whenever the photon frequency matches an atomic transition frequency. The absorption or emission line is naturally broadened by the cavity loss rate κ.

Solution to the rate equation in the stationary state of the system

We now use our Ansatz from Eq. (B.10) for the density matrix ρ_e and ρ_o. This will lead to a non-linear set coupled equation for the occupation probabilities (p_e, p_o). The rate equation for the magnetisation on the even sites is written as

$$\begin{aligned}
\partial_t\langle\sigma_e^z\rangle &= \mathrm{Tr}\Big[\sigma_{\mathrm{e}}^{z}\mathcal{L}_1\mathcal{L}_0^{-1}\mathcal{L}_1\rho_{\mathrm{e}}\Big] \\
&= 2\pi\frac{g^2}{N}\mathrm{Tr}\Big[\sum_{s=\uparrow,\downarrow}p_{s,e}\sum_{n=1}^{\#configs}p_{n,e}\sum_\ell\delta(\Delta E_\ell,\kappa,\omega)\sigma_e^z\left(|n_\ell,0\rangle\langle n_\ell,0| - |\bar{n}_\ell,1\rangle\langle\bar{n}_\ell,1|\right)\Big]
\end{aligned} \quad \text{(B.26)}$$

To illustrate the evaluation of the contributions to the sum, we pick as an example the state $|\uparrow,\downarrow\downarrow\downarrow\downarrow\rangle\langle\uparrow,\downarrow\downarrow\downarrow\downarrow|$. The contribution from this configuration evaluates as

$$
\begin{aligned}
&2\pi\frac{g^2}{N}\mathrm{Tr}\Big[p_e(1-p_o)^4\left(\delta(-\omega_z)+4\delta(-\omega_z+V)\right)|\uparrow,\downarrow\downarrow\downarrow\downarrow\rangle\langle\uparrow,\downarrow\downarrow\downarrow\downarrow| \\
&-p_e(1-p_o)^4\left((-1)\delta(-\omega_z)\,|\downarrow\downarrow\downarrow\downarrow\downarrow\rangle\langle\downarrow\downarrow\downarrow\downarrow\downarrow|\right. \\
&\left.+\delta(-\omega_z+V)\,|\uparrow\uparrow\downarrow\downarrow\downarrow\rangle\langle\uparrow\uparrow\downarrow\downarrow\downarrow|+\delta(-\omega_z+V)\,|\uparrow\downarrow\uparrow\downarrow\downarrow\rangle\langle\uparrow\downarrow\uparrow\downarrow\downarrow|+\ldots\right)\Big] \\
&=4\pi\frac{g^2}{N}p_e(1-p_o)^4\delta(-\omega_z)
\end{aligned}
\tag{B.27}
$$

Combining with the other terms from Eq. (B.26) leads to

$$
\begin{aligned}
\partial_t\langle\sigma_e^z\rangle=p_e\Big[&(1-p_o)^4\delta(-\omega_z)+4(1-p_o)^3p_o\delta(-\omega_z+V)+6p_o^2(1-p_o)^2\delta(-\omega_z+2V) \\
&+4(1-p_o)p_o^3\delta(-\omega_z+3V)+p_o^4\delta(-\omega_z+4V)\Big] \\
-(1-p_e)\Big[&p_o^4\delta(\omega_z-4V)+4p_o^3(1-p_o)^1(\omega_z-3V)+6p_o^2(1-p_o)^2\delta(\omega_z-2V) \\
&+(1-p_o)^4\delta(\omega_z)+4p_o(1-p_o)^3\delta(\omega_z-V)\Big]=0
\end{aligned}
\tag{B.28}
$$

The coupled equation is generated by exchanging $e\leftrightarrow o$. The Eq. (B.28) illustrates how the dimensionality comes into play in determining the transition rates that depend on the configurations of the spins.

Comparison of Monte Carlo simulations with mean-field predictions

In general, the non-linear equations (B.28) and its counterpart with the exchanged subscripts $e\leftrightarrow o$ have homogeneous solutions where $p_e=p_o$ and solutions that break the sublattice symmetry $p_e\neq p_o$. In contrast to an equilibrium situation, the spin-up and spin-down probabilities are not set by a thermal Boltzmann distribution but in fact are determined entirely from the rate equations resulting from the the weak cavity perturbations, once again stressing the non-equilibrium character of the model.

Without the coupling to a cavity, the mean-field transition point is determined from a simple energy counting as $\Delta E=-\omega_z+4V=0$, fixing the $T=0$ transition at $V=\omega_z/4$. From a mean-field point of view, as soon as it becomes energetically favourable for a spin to flip, the transition happens in the entire lattice. The change in the magnetisation is discontinuous.
In thermal equilibrium, where the system is coupled to an external bath that is characterised by a temperature T, there exists a critical line in the space $\{\omega_z,T\}$ that separates a Néel antiferromagnetic state from a paramagnetic state. Even though there is no exact analytical solution for the critical line $T(\omega_z)$, approximate closed form expressions have been conjectured [225] which have been shown to be in good agreement with numerical Monte-Carlo simulations [226].

We investigate the phase transition from the paramagnet to the antiferromagnet as the ratio of the interaction V in comparison to the magnetic field ω_z is changed. For small $V/\omega_z\ll 1$ the system is paramagnetic with the spins aligned in the z direction of the homogeneous field. As V/ω_z increases, the system eventually undergoes a phase transition as the even-odd lattice symmetry is spontaneously broken. The behaviour of the magnetisation $\sigma^z_{e,o}(V/\omega_z)$ is illustrated in Fig. B.1. For $V = 0$ the magnetisation is set by

$$\sigma^z_e(V, \omega_z, \omega_0) = \sigma^z_0(V, \omega_z, \omega_0) = p_e + (1 - p_e)(-1) = \frac{8\omega_z\omega_0}{4\omega_z^2 + \kappa^2 + 4\omega_0^2}. \tag{B.29}$$

Corrections linear in the interaction V can be calculated analytically from an expansion of Eq. (B.28) to reproduce the slope of the magnetisation seen in Fig. . B.1.

We can compare the mean-field calculations with a numerical Monte Carlo simulation which is sensitive for example to the buildup of a diverging correlation length that is missed by the mean-field calculations. The cavity-induced transition rates $\delta(\Delta E_{ij}, \kappa, \omega_0)$ have to be used to set the transition rates from configuration i to configuration j as

$$\frac{W_{ij}}{W_{ji}} = \delta(\Delta E_{ij}, \kappa, \omega_0)/\max\Big[\delta(\Delta E_{ij}, \kappa, \omega_0)\Big], \tag{B.30}$$

where the maximum is taken with respect to all configurations and provides a normalisation for the transition probabilities. The choice of normalisation is not unique, but should not change the results for the Monte Carlo simulations. The two configurations i and j are different by a single spin flip. An update algorithm within a Markov-Chain Monte Carlo is guaranteed to produce a stationary probability distribution in the asymptotic dynamics of long times.

A comparison is seen in Fig. B.1 showing good agreement for $\omega_z/V \ll 1$ of the analytical mean-field and the numerical simulations with non-equilibrium transition probabilities given by Eq. (B.30). For moderate to strong interaction strengths, the numerical calculations show a shift of the phase transition point towards higher Rydberg-Rydberg interactions. Furthermore, the magnetisation curves on the sublattices are not monotonically growing with increasing Rydberg-Rydberg interactions but show clearly visible dips that are traced back to the non-linear transition rates $\delta(\Delta E_{ij}, \kappa, \omega_0)$. We close with a discussion of the validity of the current approach and outline further steps for future work.

Validity restrictions and future work

The results remain preliminary and provide only a first insight into the non-equilibrium dynamics of the suggested model. We discuss restrictions of the current approach together with possible next steps.

1. We assume throughout that the the spin-flips induced by the vacuum mode of the cavity connect patterns of classical product states of spin up and spin-down configurations $|n\rangle$ and $|n'\rangle$ with a rate $\delta_{|n\rangle\to|n'\rangle}$ as in Eq. (B.25). This entails that the dynamics of the system is described by a classical master equation for the diagonal elements of a density matrix. Off-diagonal elements that capture coherences or entanglement of non-classical states are explicitly excluded. Exact diagonalisation schemes for small system sizes have shown that the off-diagonal elements of the density matrix for arbitrary initial states cannot be neglected without a dephasing assumption. This restricts the validity of the current approach to systems subject to sufficiently strong decoherence leading to a dephasing of the spins. Such that the entire dynamics becomes classical. Dephasing with a rate γ is described by the

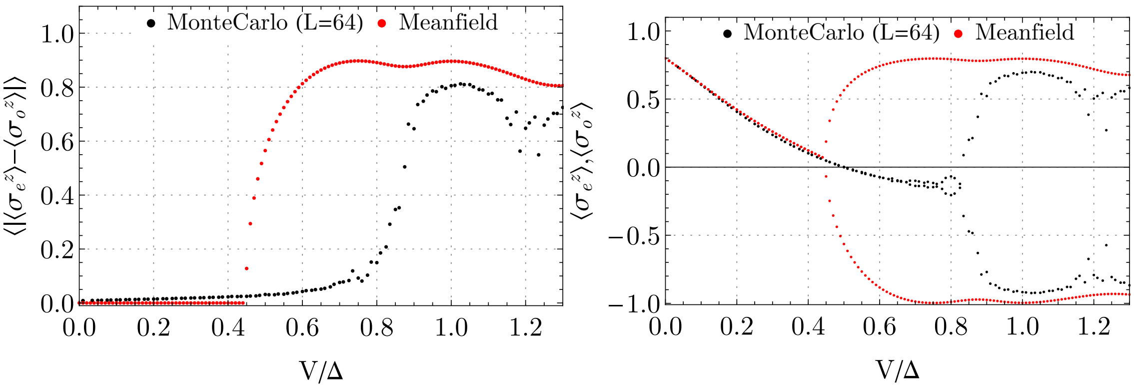

(a) (b)

Figure B.1.: Comparison of analytical mean-field calculations with Eq. (B.28) and numerical Monte Carlo simulations with non-equilibrium transition rates given by Eq. (B.30) for the antiferromagnetic phase transition of a Rydberg Hamiltonian (Eq. (B.1)) on a two-dimensional square lattice weakly interacting with vacuum fluctuations of a cavity (Eq.(B.3)). (a) Antiferromagnetic order parameter for increasing Rydberg-Rydberg interaction strength V. (b) Sublattice magnetisations $\langle\sigma_e^z\rangle$ and $\langle\sigma_o^z\rangle$ for increasing Rydberg-Rydberg interaction strength.

Lindblad

$$\mathcal{L}_z\rho = \gamma \sum_{\ell=1}^{N} \sigma_\ell^z \rho \sigma_\ell^z - \frac{1}{2}(\rho\sigma_\ell^z\sigma_\ell^z + \sigma_\ell^z\sigma_\ell^z\rho). \tag{B.31}$$

2. We want to compare the stationary probability distribution for spin configurations generated by the non-equilibrium dynamics with a thermal probability distribution. A Markov chain Monte Carlo algorithm in thermal equilibrium generates spin configurations with energy E with an (unnormalised) distribution $P(E,T) = g(E)\exp(-E/T)$, where $g(E)$ counts the number of states with a given energy E (density of states - DOS). If the DOS can be obtained numerically, the stationary state distribution can be compared to a thermal distribution with an effective temperature T_{eff}.
   Accumulation of histogram entries to determine the DOS is cost intensive for large systems due to the exponentially growing number of classical states. However, an efficient method (Wang-Landau algorithm) to directly sample the density of states $g(E)$ has been proposed [227].

3. At a critical point of a first and a second-order phase transition the numerical Monte Carlo simulation is plagued by critical slowing down of relaxation of excitations which increases the autocorrelation time of successive spin configurations. To correctly sample observables such as a magnetisation it is essential that successive samples be independent. To decrease autocorrelation times, it is therefore necessary to implement algorithms for flipping cluster of spins such as the Wolff- [228] or the Stevenson-Lang [229] algorithm.

Chapter C

Circulating Probability Currents in Stationary Non-Equilibrium States

A clear non-equilibrium signature is a circulating probability current in the stationary state which is possible only if detailed balance is broken. In chapter 4 we found that the stationary state dynamics of the driven-dissipative Dicke model in the presence of finite noise could be understood from a classical rate equation of a three level system. Importantly, the presence of a mirror symmetry constrained transition rates on a macroscopic scale to obey detailed balance. Consequently, here we explore ideas to lift this detailed balance in the presence of magnetic fields.

Presence and absence of detailed balance in classical stationary states

A truly non-equilibrium stationary state is distinct from a stationary state in equilibrium, e.g. through the presence of non-vanishing probability currents in an externally pumped system with at least three levels. A two-level system in the stationary state cannot sustain a finite current between the levels. This is understood on the level of classical rate equations for the occupation probabilities of the stationary states

$$\frac{dP_i}{dt} = \sum_j (P_j\gamma_{ji} - P_i\gamma_{ij}) = \sum_j J_{ji} = 0, \tag{C.1}$$

where γ_{ij} is the transition rate from state i to state j and P_i denotes the probability to be in state i. Thus, $P_i\gamma_{ij}$ is the probability current from i to j and

$$J_{ji} = P_j\gamma_{ji} - P_i\gamma_{ij}, \tag{C.2}$$

is the net probability current between these states. In thermal equilibrium $J_{ij} = 0$, whereas a stationary non-equilibrium state can have $J_{ij} \neq 0$. If the long time limit behaviour of the system is adequately described by the classical master equation (C.1), then the associated steady-state density matrix is

$$\rho = \sum_i P_i \left|i\right\rangle \left\langle i\right| . \tag{C.3}$$

In chapter 4 we found a bistability regime for the driven-dissipative Dicke model with collective loss within which there were three stationary states. These consisted of the empty atom-cavity system $\langle a\rangle = 0$ and the two superradiant states $\pm\langle a\rangle \neq 0$. Fluctuations rendered these states metastable and lead to transitions between them. Although detailed balance is microscopically broken as it should be since the drive, dissipation and

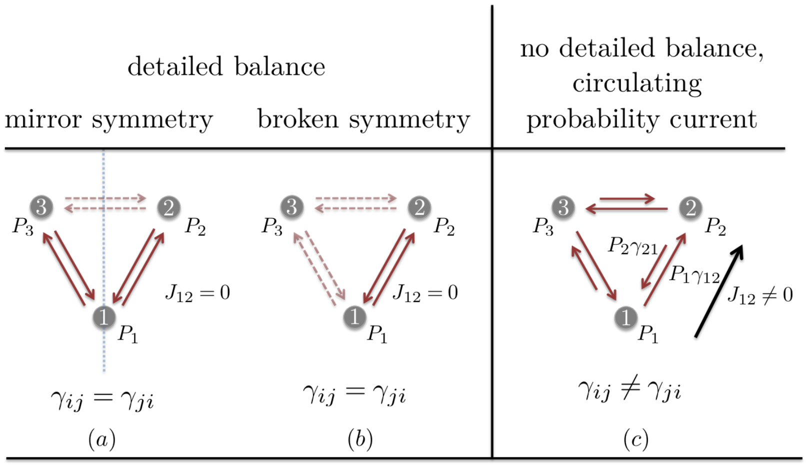

Figure C.1.: Three distinct scenarios for a stationary state of an externally pumped system with three levels as described by a classical rate equation, see Eq. (C.1). Thick arrows denote dominant transition rates, dashed arrows denote weak transition rates. (a) Detailed balance is enforced by the symmetries of the system. There is no net current between any two states. (b) The mirror symmetry is lost due to fine tuning of one external parameter such as a magnetic field that leads to a preference of one branch over the other. However, there is no net current in the system. (c) Fine-tuning of a second parameter might lead to a scenario where detailed balance is explicitly broken, allowing for non-stationary probability currents in the system. This scenario has no counterpart in an equilibrium system.

non-thermal fluctuations break time inversion symmetry for the microscopic equations of motion, it is however enforced by the Ising inversion symmetry of the model to emerge on a macroscopic scale. The three level system is thus effectively a two-level system as the transition rates from the empty to the two superradiant states are forced to be equal by symmetry.

One may wonder whether or not the non-equilibrium character of the model can be detected by experimental measurements of the transition rates for example by fitting the ratio of the rates with an effective temperature, $\beta_{\text{eff}} = 1/T_{\text{eff}}$ according to

$$-\beta_{\text{eff}}\Delta V = \log\left(\frac{\gamma_{0,Sr}}{\gamma_{Sr,0}}\right). \tag{C.4}$$

Here $\gamma_{0,Sr}$ is the transition rate from the empty (0) the the superradiant state (Sr) and ΔV would correspond to some (energetic) barrier separating the two states from another. Non-equilibrium features might be detectable by violations of the thermal fluctuation-dissipation theorem. Comparing the classical (Einstein) fluctuation dissipation theorem with predictions form linear responses (Kubo-formula) in the steady-state, one can measure deviations from thermal equilibrium and or calculate an effective noise-strength, see [230, 231].

Asymmetric transition rates in presence of a magnetic field

Ultimately, we have to break the degeneracy of the two superradiant states to realise circulating probability currents in a system with three distinct states. In this section we take the first step by adding an additional magnetic field with strength Ω to the atom-cavity system. The Hamiltonian (cavity photons integrated out) is written as

$$H = \frac{\omega_z}{2} \sum_{\ell=1}^{N} \sigma_\ell^z + \frac{\Omega}{2} \sum_{\ell=1}^{N} \sigma_\ell^x - \frac{J}{N} \sum_{\ell,m} \sigma_\ell^x \sigma_m^x. \tag{C.5}$$

The magnetic field breaks the Ising inversion symmetry of the Hamiltonian $\mathbb{Z}_2 : (\sigma_x, \sigma_y) \to (-\sigma_x, -\sigma_y)$. As a consequence, all stationary states exhibit a finite magnetisation $\langle \sigma^x \rangle \neq 0$. Including the atomic and photonic dissipative contributions, with Liouville contributions of single, as well as collective atomic decay as modelled by $\mathcal{L}^\star$, see Eqs. (4.3)-(4.5) the equation of motions are cast into the form ($\hbar = 1$)

$$\partial_t \sigma^\alpha = -i[\sigma^\alpha, H] + \mathcal{L}^*[\boldsymbol{\sigma}] = D^\alpha, \tag{C.6}$$

where the deterministic relaxation is given as

$$\boldsymbol{D} = \begin{pmatrix} \sigma^x(1-\beta\sigma^z)(-\gamma) - \sigma^y\omega_z \\ J\sigma^x\sigma^z - \Omega\sigma^z - \gamma\sigma^y(1-\beta\sigma^z) + \sigma^x\omega_z \\ -J\sigma^x\sigma^y + \Omega\sigma^y - \gamma\beta((\sigma^x)^2 + (\sigma^y)^2) - 2(\sigma^z+1)\gamma \end{pmatrix}. \tag{C.7}$$

Depending on the parameters, there are now either one, two or three fixed points for $\boldsymbol{D}$. Starting out from ($J \ll \Omega$) and increasing the exchange interaction to ($J \gg \Omega$), the number of stable fixed points changes as $1-2-3-2$, see Fig. C.2b. When the ferromagnetic exchange coupling is much weaker than the external field ($J \ll \Omega$), the stationary state of the system is unique. With the finite magnetic field of strength Ω the empty atom-cavity state $|\downarrow, \downarrow, \ldots\rangle$ is not a fixed point of the system any more and the Bloch vector $S = (\sigma^x, \sigma^y, \sigma^z)$ is tilted slightly away from z-axis leading to small, but finite magnetisations. The long-time limit behaviour of the system is now defined by a competition of the coherent mean-field that tries to align the spins parallel to the total magnetic field and the dissipation that tries to remove all excitations from the system, see also [124]. When the ferromagnetic exchange coupling is much stronger than the field $J \gg \Omega$, there appears a second solution with strong finite magnetisation in the σ^x channel, energetically split from the first by an amount proportional to the field $\sim \Omega$. The splitting vanishes asymptotically in the limit of strong interactions $\Omega/J \to 0$. A comparison of the aforementioned cases is seen in Fig. C.2a. The fixed-point landscape of $\boldsymbol{D}$ is depicted in Fig. C.3b and compared to the case where there is no magnetic field (as analysed in chapter 4), see Fig. C.3a.

Ideas to break detailed balance with forced transitions in presence of periodic drive

As seen in the previous section, the presence of a magnetic field spits the stationary states into three distinct states. However, a numerical simulation of Eq. (C.6) in the presence of finite noise ($\partial_t \sigma^\alpha = D^\alpha + 1/\sqrt{N}\xi^\alpha$) has shown that the transitions rates are exponentially stronger ($\sim \exp(f(\Omega))$) for one branch of transitions, where $f(\Omega)$ is some function of the magnetic field. This is depicted schematically in Fig. C.1.

We can however externally pump the spin system by coupling the collective spin to a time-dependent magnetic field. This pumps energy into the system and induces coherent switching between two of the three states on a Hamiltonian level. Cooling can be provided by the presence of dissipative channels. Through the replacement $\Omega \to \Omega \cos(\omega_p t)$ in Eq. (C.6) we add a periodic drive and render the Hamiltonian explicitly time-dependent.

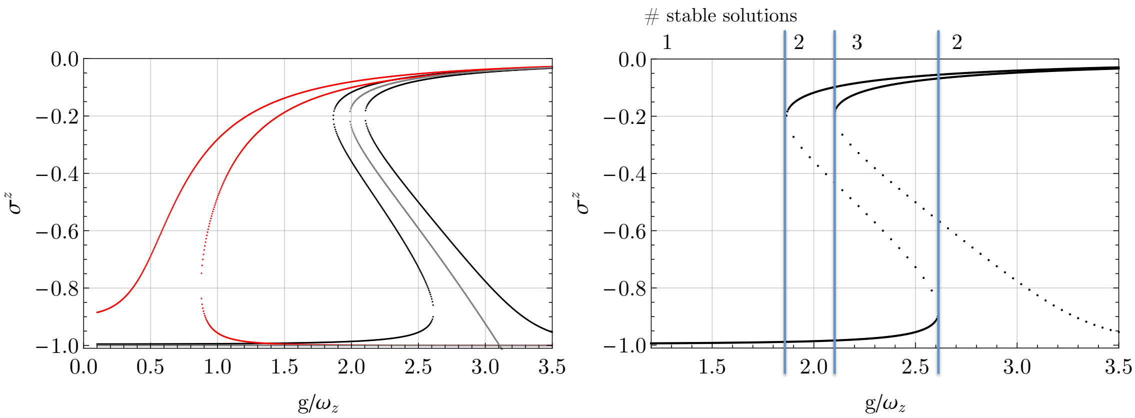

(a) (b)

Figure C.2.: Steady-state solutions for the relaxation dynamics described by Eq. (C.7) for the atomic population imbalance σ^z. (a) Shown are both stable and unstable branches. Solutions in red ($\Omega/\omega_z = 0.5, \beta = 0$) correspond to the absence of a collective loss term and show no bistability regime as the finite magnetic field Ω selects one of the two possible states. Solutions in gray ($\Omega/\omega_z = 0, \beta = 50$) correspond to solutions seen in the phase diagram in Fig. C.3a, explained in Sec. 4.3. Solutions in black ($\Omega/\omega_z = 0.5, \beta = 50$) illustrate the splitting of branches in gray in the presence of a magnetic field for the bistability regime. (b) Close up of fixed point behaviour for parameters ($\Omega/\omega_z = 0.5, \beta = 50$). Thick lines are stable, dotted lines show unstable solutions. The number of stable solutions is indicated above the figure.

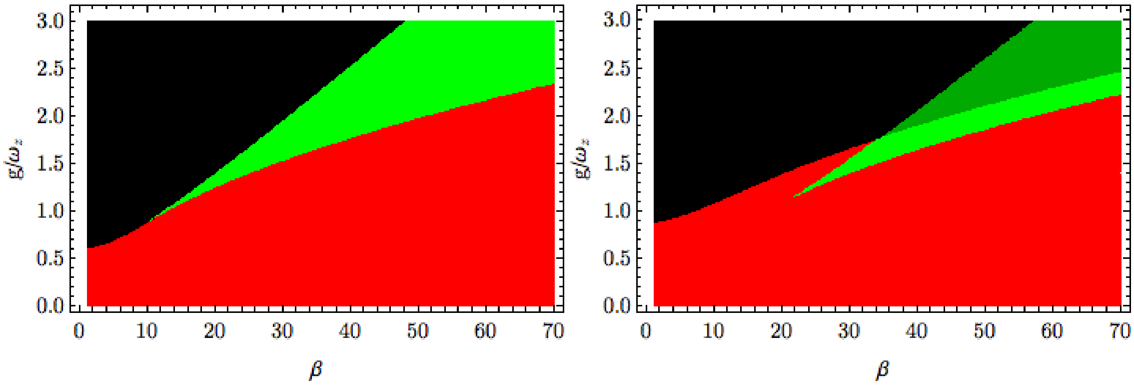

(a) (b)

Figure C.3.: Fixed point landscape corresponding to $\boldsymbol{D} = 0$, see Eq. (C.6) without (a) and with (b) additional magnetic field for the parameter set ($\omega_0/\omega_z = 1.4, \kappa/\omega_z = 0.2, \gamma/\omega_z = 0.1$). Different colours indicate a different number of stable fixed points. (a) Phase diagram as investigated in chapter 4 (shown for comparison). Shown in red are unique solutions (empty atom-cavity system), green shows a bistability regime between the empty atom-cavity and the two symmetry related superradiant states. Black areas show stability of the superradiant solutions only. (b) Steady state phase diagram with magnetic field and parameters ($\Omega/\omega_z = 0.5$). Red shows a unique steady state. Light green is a bistability regime with two stable solutions corresponding to the almost empty and a single superradiant state. Dark green shows areas with three stable stationary states which are the almost empty and two symmetry broken superradiant states. Black areas show regions with two stable states. A cut along the axis $\beta = 50$ is shown in Fig. C.2b.

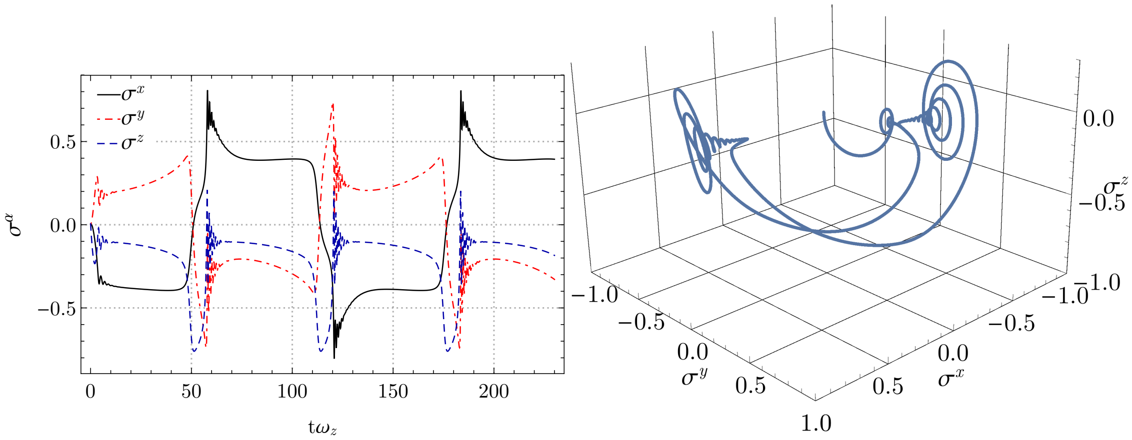

(a) (b)

Figure C.4.: Time-dependent solution of Eq. (C.6) with the replacement $\Omega \to \Omega\cos(\omega_p t)$. Independent of the initial state, the system settles onto a trajectory that connects two special points in the Bloch sphere, formerly associated with the degenerate superradiant states.(a) and (b) both show the same time-resolved dynamics in the long-time limit. (a) shows each spin-component σ^α individually and (b) shows a parametric plot of the Bloch vector $S = (\sigma^x, \sigma^y, \sigma^z)$.

The Ising symmetry is however still present under the transformation $t \to t + T/2$ where $T = 1/\omega_p$ is the time for a full oscillation. The presence of dissipation, as given by the Lindblads in Eqs. (4.3)-(4.5) ensure that independent of initial states, the dynamics of the system collapses onto a single trajectory that, as a function of time, drives the system back and forth between two strongly superradiant states without passing a fully inverted state close to the empty atom-cavity system, see Fig. C.4. The long-time limit behaviour however is not stationary and depends on the parameter values $\{\omega_z, \omega_0, \omega_p, \Omega, \kappa, \gamma\}$. Numerical simulations suggest that if the system is initialised close to the inverted state, it will also be trapped in that region. Adding back a noise contribution $1/\sqrt{N}\xi^\alpha$ realizes a scenario where the inverted state is connected to the superradiant regime by noise-induced transitions and the two superradiant states are connected by coherent pumping on a Hamiltonian level.

Discussion and conclusion

The periodic drive induces a time-dependent switching but comes at the expense of loosing clear stationary mean-field states. However, one can identify three distinct regimes in the Bloch sphere where the system spends a majority of its time, see Fig. C.4a. These regimes are associated with the former degenerate superradiant and the almost empty atom-cavity states. With a time-periodic drive, the Hamiltonian and the Liouvillian become time-periodic. Trajectories in the long time limit can then be understood in terms of Floquet eigenstates. However, the nonlinearities in the deterministic dynamic prevent a non-perturbative analysis. The explicitly driven system is then closer to the idea of directed and forced transport of a system through phase space instead of an entirely noise-driven phenomena in a stationary state. Attempts to induce non-vanishing currents by engineering additional dissipative Lindblad contributions have not been fruitful. Further work is necessary to ascertain whether non-vanishing currents can be engineered.

Bibliography

[1] Stephen Ornes. Core concept: How nonequilibrium thermodynamics speaks to the mystery of life. *Proceedings of the National Academy of Sciences*, 114(3):423–424, 2017.

[2] John Hemminger, Graham Fleming, and M Ratner. Directing matter and energy: Five challenges for science and the imagination. Technical report, DOESC (USDOE Office of Science (SC)), 2007.

[3] Graham R Fleming and Mark A Ratner. Grand challenges in basic energy sciences. *Physics Today*, 61(7):28, 2008.

[4] G. Jona-Lasinio. Understanding non-equilibrium: a challenge for the future. *Contributions to Science*, 11(2):127–130, 2015.

[5] Jonathan Lux, Jan Müller, Aditi Mitra, and Achim Rosch. Hydrodynamic long-time tails after a quantum quench. *Phys. Rev. A*, 89:053608, May 2014.

[6] Michael Buchhold and Sebastian Diehl. Kinetic theory for interacting luttinger liquids. *The European Physical Journal D*, 69(10):224, Oct 2015.

[7] Michael Buchhold and Sebastian Diehl. Nonequilibrium universality in the heating dynamics of interacting luttinger liquids. *Phys. Rev. A*, 92:013603, Jul 2015.

[8] R. Graham. Macroscopic potentials, bifurcations and noise in dissipative systems. In *Noise in nonlinear dynamical systems. volume 1. theory of continuous Fokker-Planck systems.* Cambridge University Press.

[9] R. Graham and H. Haken. Microscopic reversibility, stability and onsager relations in systems far from thermal equilibrium. *Physics Letters A*, 33(6):335 – 336, 1970.

[10] R. Graham and F. Haake. *Quantum Optics: Including Noise Reduction, Trapped Ions, Quantum Trajectories, and Decoherence.* Springer Tracts in Modern Physics, 1973.

[11] R. Graham. Von der laserschwelle zum quantenphasenuebergang. *Physik Journal*, (8):43–48, Sep 2009.

[12] Michael Cross and Henry Greenside. *Pattern Formation and Dynamics in Nonequilibrium Systems.* Cambridge University Press, 2009.

[13] Alex Kamenev. *Field Theory of Non-Equilibrium Systems.* Cambridge University Press, first edition, 2011.

[14] Lukas M Sieberer, Michael Buchhold, and Sebastian Diehl. Keldysh field theory for driven open quantum systems. *Reports on Progress in Physics*, 79(9):096001, 2016.

[15] L. M. Sieberer, A. Chiocchetta, A. Gambassi, U. C. Täuber, and S. Diehl. Thermodynamic equilibrium as a symmetry of the schwinger-keldysh action. *Phys. Rev. B*, 92:134307, Oct 2015.

[16] L. M. Sieberer, S. D. Huber, E. Altman, and S. Diehl. Dynamical critical phenomena in driven-dissipative systems. *Phys. Rev. Lett.*, 110:195301, May 2013.

[17] Lukas M. Sieberer. *Universality in Driven-Dissipative Quantum Many-Body Systems.* PhD thesis, Leopold-Franzens-Universitat Innsbruck, 2015.

[18] Jamir Marino and Sebastian Diehl. Driven markovian quantum criticality. *Phys. Rev. Lett.*, 116:070407, Feb 2016.

[19] Uwe C. Täuber and Sebastian Diehl. Perturbative field-theoretical renormalization group approach to driven-dissipative bose-einstein criticality. *Phys. Rev. X*, 4:021010, Apr 2014.

[20] M. I. Freidlin and A. D. Wentzell. *Random Perturbations.* Springer US, New York, NY, 1984.

[21] R Graham. Macroscopic potentials, bifurcations and noise in dissipative systems. In *Fluctuations and Stochastic Phenomena in Condensed Matter*, pages 1–34. Springer, 1987.

[22] A. Tomadin, S. Diehl, M. D. Lukin, P. Rabl, and P. Zoller. Reservoir engineering and dynamical phase transitions in optomechanical arrays. *Phys. Rev. A*, 86:033821, Sep 2012.

[23] Immanuel Bloch, Jean Dalibard, and Sylvain Nascimbene. Quantum simulations with ultracold quantum gases. *Nat Phys*, 8(4):267–276, 04 2012.

[24] Renate Landig, Lorenz Hruby, Nishant Dogra, Manuele Landini, Rafael Mottl, Tobias Donner, and Tilman Esslinger. Quantum phases from competing short- and long-range interactions in an optical lattice. *Nature*, 532(7600):476–479, 04 2016.

[25] J. Klinder, H. Keßler, M. Reza Bakhtiari, M. Thorwart, and A. Hemmerich. Observation of a superradiant mott insulator in the dicke-hubbard model. *Phys. Rev. Lett.*, 115:230403, Dec 2015.

[26] F. Dimer, B. Estienne, A. S. Parkins, and H. J. Carmichael. Proposed realization of the dicke-model quantum phase transition in an optical cavity qed system. *Phys. Rev. A*, 75:013804, Jan 2007.

[27] Ferdinand Brennecke, Rafael Mottl, Kristian Baumann, Renate Landig, Tobias Donner, and Tilman Esslinger. Real-time observation of fluctuations at the driven-dissipative dicke phase transition. *Proceedings of the National Academy of Sciences*, 110(29):11763–11767, 2013.

[28] K. Baumann, R. Mottl, F. Brennecke, and T. Esslinger. Exploring symmetry breaking at the dicke quantum phase transition. *Phys. Rev. Lett.*, 107:140402, Sep 2011.

[29] S. R. K. Rodriguez, W. Casteels, F. Storme, N. Carlon Zambon, I. Sagnes, L. Le Gratiet, E. Galopin, A. Lemaître, A. Amo, C. Ciuti, and J. Bloch. Probing a dissipative phase transition via dynamical optical hysteresis. *Phys. Rev. Lett.*, 118:247402, Jun 2017.

[30] Thomas Fink, Anne Schade, Sven Höfling, Christian Schneider, and Ataç Imamoglu. Signatures of a dissipative phase transition in photon correlation measurements. *Nature Physics*, 14(4):365, 2018.

[31] M. Brune, F. Schmidt-Kaler, A. Maali, J. Dreyer, E. Hagley, J. M. Raimond, and S. Haroche. Quantum rabi oscillation: A direct test of field quantization in a cavity. *Phys. Rev. Lett.*, 76:1800–1803, Mar 1996.

[32] R. J. Thompson, G. Rempe, and H. J. Kimble. Observation of normal-mode splitting for an atom in an optical cavity. *Phys. Rev. Lett.*, 68:1132, Nov 1992.

[33] Sébastien Gleyzes, Stefan Kuhr, Christine Guerlin, Julien Bernu, Samuel Deléglise, Ulrich Busk Hoff, Michel Brune, Jean-Michel Raimond, and Serge Haroche. Quantum jumps of light recording the birth and death of a photon in a cavity. *Nature*, 446:297 EP, 2007.

[34] *Cavity Quantum Electrodynamics*. Wiley-Blackwell, 2005.

[35] C. J. Hood, M. S. Chapman, T. W. Lynn, and H. J. Kimble. Real-time cavity qed with single atoms. *Phys. Rev. Lett.*, 80:4157–4160, May 1998.

[36] F. Bernardot, P. Nussenzveig, M. Brune, J. M. Raimond, and S. Haroche. Vacuum rabi splitting observed on a microscopic atomic sample in a microwave cavity. *EPL (Europhysics Letters)*, 17(1):33, 1992.

[37] Edwin T Jaynes and Frederick W Cummings. Comparison of quantum and semiclassical radiation theories with application to the beam maser. *Proceedings of the IEEE*, 51(1):89–109, 1963.

[38] Michael Tavis and Frederick W. Cummings. Exact solution for an n-molecule—radiation-field hamiltonian. *Phys. Rev.*, 170:379–384, Jun 1968.

[39] M. Gross, P. Goy, C. Fabre, S. Haroche, and J. M. Raimond. Maser oscillation and microwave superradiance in small systems of rydberg atoms. *Phys. Rev. Lett.*, 43:343–346, Jul 1979.

[40] P. Goy, J. M. Raimond, M. Gross, and S. Haroche. Observation of cavity-enhanced single-atom spontaneous emission. *Phys. Rev. Lett.*, 50:1903–1906, Jun 1983.

[41] Nobel Media AB 2014. Serge haroche - facts, 2012.

[42] Nobel Media AB 2014. Serge haroche - nobel lecture: Controlling photons in a box and exploring the quantum to classical boundary, 2012.

[43] Immanuel Bloch. Quantum gases in optical lattices. *Physics World*, 17(4):25, 2004.

[44] Zhiqiang Zhang, Chern Hui Lee, Ravi Kumar, K. J. Arnold, Stuart J. Masson, A. L. Grimsmo, A. S. Parkins, and M. D. Barrett. Dicke-model simulation via cavity-assisted raman transitions. *Phys. Rev. A*, 97:043858, Apr 2018.

[45] Alicia J Kollár, Alexander T Papageorge, Varun D Vaidya, Yudan Guo, Jonathan Keeling, and Benjamin L Lev. Supermode-density-wave-polariton condensation with a bose–einstein condensate in a multimode cavity. *Nature communications*, 8:14386, 2017.

[46] Varun D Vaidya, Yudan Guo, Ronen M Kroeze, Kyle E Ballantine, Alicia J Kollár, Jonathan Keeling, and Benjamin L Lev. Tunable-range, photon-mediated atomic interactions in multimode cavity qed. *Physical Review X*, 8(1):011002, 2018.

[47] D. Nagy, G. Szirmai, and P. Domokos. Critical exponent of a quantum-noise-driven phase transition: The open-system dicke model. *Phys. Rev. A*, 84:043637, Oct 2011.

[48] Creative commons license, attribution 4.0 international (cc by 4.0).

[49] Markus P. Baden, Kyle J. Arnold, Arne L. Grimsmo, Scott Parkins, and Murray D. Barrett. Realization of the dicke model using cavity-assisted raman transitions. *Phys. Rev. Lett.*, 113:020408, Jul 2014.

[50] Johannes Zeiher, Rick van Bijnen, Peter Schausz, Sebastian Hild, Jae-yoon Choi, Thomas Pohl, Immanuel Bloch, and Christian Gross. Many-body interferometry of a rydberg-dressed spin lattice. *Nat Phys*, advance online publication:–, 08 2016.

[51] R. H. Dicke. Coherence in spontaneous radiation processes. *Phys. Rev.*, 93:99–110, Jan 1954.

[52] Barry M. Garraway. The dicke model in quantum optics: Dicke model revisited. *Philosophical Transactions of the Royal Society of London A: Mathematical, Physical and Engineering Sciences*, 369(1939):1137–1155, 2011.

[53] Michel Gross and Serge Haroche. Superradiance: An essay on the theory of collective spontaneous emission. *Physics reports*, 93(5):301–396, 1982.

[54] Mathias Hayn. *On superradiant phase transitions in generalised Dicke models.* PhD thesis, Technische Universität Berlin, 2017.

[55] Marlan O. Scully and Anatoly A. Svidzinsky. The super of superradiance. *Science*, 325(5947):1510–1511, 2009.

[56] Jonathan Keeling. Light-matter interactions and quantum optics.

[57] Marlan O. Scully, Edward S. Fry, C. H. Raymond Ooi, and Krzysztof Wódkiewicz. Directed spontaneous emission from an extended ensemble of n atoms: Timing is everything. *Phys. Rev. Lett.*, 96:010501, Jan 2006.

[58] S Schneider and Gerard J Milburn. Entanglement in the steady state of a collective-angular-momentum (dicke) model. *Physical Review A*, 65(4):042107, 2002.

[59] Roy J. Glauber. Coherent and incoherent states of the radiation field. *Phys. Rev.*, 131:2766–2788, Sep 1963.

[60] Klaus Hepp and Elliott H. Lieb. Equilibrium statistical mechanics of matter interacting with the quantized radiation field. *Phys. Rev. A*, 8:2517–2525, Nov 1973.

[61] F. T. Hioe. Phase transitions in some generalized dicke models of superradiance. *Phys. Rev. A*, 8:1440–1445, Sep 1973.

[62] H.J.CarmichaelC.W.GardinerD.F.Walls. Higher order corrections to the dicke superradiant phase transition. *Physics Letters A*, 46:47–48, Nov 1973.

[63] K. Rzażewski, K. Wódkiewicz, and W. Żakowicz. Phase transitions, two-level atoms, and the A^2 term. *Phys. Rev. Lett.*, 35:432–434, Aug 1975.

[64] Pierre Nataf and Cristiano Ciuti. No-go theorem for superradiant quantum phase transitions in cavity qed and counter-example in circuit qed. *Nature communications*, 1:72, 2010.

[65] Kristian Baumann, Christine Guerlin, Ferdinand Brennecke, and Tilman Esslinger. Dicke quantum phase transition with a superfluid gas in an optical cavity. *Nature*, 464:1301–1306, 2010.

[66] Adam T. Black, Hilton W. Chan, and Vladan Vuletić. Observation of collective friction forces due to spatial self-organization of atoms: From rayleigh to bragg scattering. *Phys. Rev. Lett.*, 91:203001, Nov 2003.

[67] K. J. Arnold, M. P. Baden, and M. D. Barrett. Self-organization threshold scaling for thermal atoms coupled to a cavity. *Phys. Rev. Lett.*, 109:153002, Oct 2012.

[68] Peter Domokos and Helmut Ritsch. Collective cooling and self-organization of atoms in a cavity. *Phys. Rev. Lett.*, 89:253003, Dec 2002.

[69] Marlan O. Scully. Single photon subradiance: Quantum control of spontaneous emission and ultrafast readout. *Phys. Rev. Lett.*, 115:243602, Dec 2015.

[70] D. A. Steck. *Quantum and Atom Optics.* first edition, 2007.

[71] Andrew J. Daley. Quantum trajectories and open many-body quantum systems. *Advances in Physics*, 63(2):77–149, 2014.

[72] M. O. Scully and M. S. Zubairy. *Quantum Optics.* Cambridge University Press, 1997.

[73] K. J. Arnold, M. P. Baden, and M. D. Barrett. Self-organization threshold scaling for thermal atoms coupled to a cavity. *Phys. Rev. Lett.*, 109:153002, Oct 2012.

[74] Zhang Zhiqiang, Chern Hui Lee, Ravi Kumar, K. J. Arnold, Stuart J. Masson, A. S. Parkins, and M. D. Barrett. Nonequilibrium phase transition in a spin-1 dicke model. *Optica*, 4(4):424–429, Apr 2017.

[75] R. G. DeVoe and R. G. Brewer. Observation of superradiant and subradiant spontaneous emission of two trapped ions. *Phys. Rev. Lett.*, 76:2049–2052, Mar 1996.

[76] JA Mlynek, AA Abdumalikov, C Eichler, and A Wallraff. Observation of dicke superradiance for two artificial atoms in a cavity with high decay rate. *Nature communications*, 5:5186, 2014.

[77] T. Fließbach. *Statistische Physik: Lehrbuch zur Theoretischen Physik IV.* Spektrum Akademischer Verlag, 2006.

[78] PC Hohenberg and AP Krekhov. An introduction to the ginzburg–landau theory of phase transitions and nonequilibrium patterns. *Physics Reports*, 572:1–42, 2015.

[79] P. C. Hohenberg and B. I. Halperin. Theory of dynamic critical phenomena. *Rev. Mod. Phys.*, 49:435–479, Jul 1977.

[80] G. L. S. Paula and W. Figueiredo. The glauber and metropolis transition rates on the stationary states of the ising model. *Modern Physics Letters B*, 11(13):565–570, 1997.

[81] RKP Zia and B Schmittmann. Probability currents as principal characteristics in the statistical mechanics of non-equilibrium steady states. *Journal of Statistical Mechanics: Theory and Experiment*, 2007(07):P07012, 2007.

[82] RKP Zia and B Schmittmann. Towards a classification scheme for non-equilibrium steady states. *Physics Procedia*, 7:112–115, 2010.

[83] Victor V Albert and Liang Jiang. Symmetries and conserved quantities in lindblad master equations. *Physical Review A*, 89(2):022118, 2014.

[84] Bernhard Baumgartner and Heide Narnhofer. Analysis of quantum semigroups with gks–lindblad generators: Ii. general. *Journal of Physics A: Mathematical and Theoretical*, 41(39):395303, 2008.

[85] E. M. Kessler, G. Giedke, A. Imamoglu, S. F. Yelin, M. D. Lukin, and J. I. Cirac. Dissipative phase transition in a central spin system. *Phys. Rev. A*, 86:012116, Jul 2012.

[86] W. Casteels, R. Fazio, and C. Ciuti. Critical dynamical properties of a first-order dissipative phase transition. *Phys. Rev. A*, 95:012128, Jan 2017.

[87] Emanuele G. Dalla Torre, Sebastian Diehl, Mikhail D. Lukin, Subir Sachdev, and Philipp Strack. Keldysh approach for nonequilibrium phase transitions in quantum optics: Beyond the dicke model in optical cavities. *Phys. Rev. A*, 87:023831, Feb 2013.

[88] Mohammad F Maghrebi and Alexey V Gorshkov. Nonequilibrium many-body steady states via keldysh formalism. *Physical Review B*, 93(1):014307, 2016.

[89] M. Foss-Feig, P. Niroula, J. T. Young, M. Hafezi, A. V. Gorshkov, R. M. Wilson, and M. F. Maghrebi. Emergent equilibrium in many-body optical bistability. *Phys. Rev. A*, 95:043826, Apr 2017.

[90] Sebastian Diehl, Andrea Tomadin, Andrea Micheli, Rosario Fazio, and Peter Zoller. Dynamical phase transitions and instabilities in open atomic many-body systems. *Phys. Rev. Lett.*, 105:015702, Jul 2010.

[91] Emanuele G. Dalla Torre, Sebastian Diehl, Mikhail D. Lukin, Subir Sachdev, and Philipp Strack. Keldysh approach for nonequilibrium phase transitions in quantum optics: Beyond the dicke model in optical cavities. *Phys. Rev. A*, 87:023831, Feb 2013.

[92] S Schneider and Gerard J Milburn. Entanglement in the steady state of a collective-angular-momentum (dicke) model. *Physical Review A*, 65(4):042107, 2002.

[93] Andrew P. Hines, Ross H. McKenzie, and G. J. Milburn. Quantum entanglement and fixed-point bifurcations. *Phys. Rev. A*, 71:042303, Apr 2005.

[94] Paul Langevin. Sur la théorie du mouvement brownien. *Compt. Rendus*, 146:530–533, 1908.

[95] Alexander Altland and Ben Simons. *Condensed Matter Field Theory.* Cambridge University Press, 2010.

[96] M. Scully and M. Zubairy. *Quantum Optics.* Cambridge University Press, first edition, 1997.

[97] M. Orszag. *Quantum Optics: Including Noise Reduction, Trapped Ions, Quantum Trajectories, and Decoherence.* Springer International Publishing, 2016.

[98] Jens Klinder, Hans Keßler, Matthias Wolke, Ludwig Mathey, and Andreas Hemmerich. Dynamical phase transition in the open dicke model. *Proceedings of the National Academy of Sciences*, 112(11):3290–3295, 2015.

[99] A. Neuzner, M. Körber, O. Morin, S. Ritter, and G. Rempe. Interference and dynamics of light from a distance-controlled atom pair in an optical cavity. *Nat Photon*, 10(5):303–306, 05 2016.

[100] Klaus Hepp and Elliott H Lieb. On the superradiant phase transition for molecules in a quantized radiation field: the dicke maser model. *Annals of Physics*, 76(2):360 – 404, 1973.

[101] Y. K. Wang and F. T. Hioe. Phase transition in the dicke model of superradiance. *Phys. Rev. A*, 7:831–836, Mar 1973.

[102] Adam T. Black, Hilton W. Chan, and Vladan Vuletić. Observation of collective friction forces due to spatial self-organization of atoms: From rayleigh to bragg scattering. *Phys. Rev. Lett.*, 91:203001, Nov 2003.

[103] Ferdinand Brennecke, Rafael Mottl, Kristian Baumann, Renate Landig, Tobias Donner, and Tilman Esslinger. Real-time observation of fluctuations at the driven-dissipative dicke phase transition. 110(29):11763–11767, 2013.

[104] Francesco Piazza, Philipp Strack, and Wilhelm Zwerger. Bose-einstein condensation versus dicke-hepp-lieb transition in an optical cavity. *Annals of Physics*, 339:135, 2013.

[105] Manas Kulkarni, Baris Öztop, and Hakan E. Türeci. Cavity-mediated near-critical dissipative dynamics of a driven condensate. *Phys. Rev. Lett.*, 111:220408, Nov 2013.

[106] G. Kónya, G. Szirmai, and P. Domokos. Damping of quasiparticles in a bose-einstein condensate coupled to an optical cavity. *Phys. Rev. A*, 90:013623, Jul 2014.

[107] Francesco Piazza and Philipp Strack. Quantum kinetics of ultracold fermions coupled to an optical resonator. *Phys. Rev. A*, 90:043823, Oct 2014.

[108] M. J. Bhaseen, J. Mayoh, B. D. Simons, and J. Keeling. Dynamics of nonequilibrium dicke models. *Phys. Rev. A*, 85:013817, Jan 2012.

[109] Emanuele G. Dalla Torre, Yulia Shchadilova, Eli Y. Wilner, Mikhail D. Lukin, and Eugene Demler. Dicke phase transition without total spin conservation. *Phys. Rev. A*, 94:061802, Dec 2016.

[110] J. Keeling, M. J. Bhaseen, and B. D. Simons. Collective dynamics of bose-einstein condensates in optical cavities. *Phys. Rev. Lett.*, 105:043001, Jul 2010.

[111] D. Nagy, G. Szirmai, and P. Domokos. Self-organization of a bose-einstein condensate in an optical cavity. *The European Physical Journal D*, 48(1):127–137, 2008.

[112] M. J. Collett and C. W. Gardiner. Squeezing of intracavity and traveling-wave light fields produced in parametric amplification. *Phys. Rev. A*, 30:1386–1391, Sep 1984.

[113] C. W. Gardiner and M. J. Collett. Input and output in damped quantum systems: Quantum stochastic differential equations and the master equation. *Phys. Rev. A*, 31:3761–3774, Jun 1985.

[114] M. Landini, N. Dogra, K. Kroeger, L. Hruby, T. Donner, and T. Esslinger. Formation of a spin texture in a quantum gas coupled to a cavity. *Phys. Rev. Lett.*, 120:223602, May 2018.

[115] Zhang Zhiqiang, Chern Hui Lee, Ravi Kumar, KJ Arnold, Stuart J Masson, AS Parkins, and MD Barrett. Nonequilibrium phase transition in a spin-1 dicke model. *Optica*, 4(4):424–429, 2017.

[116] Immanuel Bloch, Jean Dalibard, and Wilhelm Zwerger. Many-body physics with ultracold gases. *Rev. Mod. Phys.*, 80:885–964, Jul 2008.

[117] S. Trotzky, P. Cheinet, S. Fölling, M. Feld, U. Schnorrberger, A. M. Rey, A. Polkovnikov, E. A. Demler, M. D. Lukin, and I. Bloch. Time-resolved observation and control of superexchange interactions with ultracold atoms in optical lattices. *Science*, 319(5861):295–299, 2008.

[118] Hans Peter Büchler, Eugene Demler, Mikhail Lukin, Andrea Micheli, N Prokof'ev, Guido Pupillo, and Peter Zoller. Strongly correlated 2d quantum phases with cold polar molecules: controlling the shape of the interaction potential. *Physical Review Letters*, 98(6):060404, 2007.

[119] Joseph W Britton, Brian C Sawyer, Adam C Keith, C-C Joseph Wang, James K Freericks, Hermann Uys, Michael J Biercuk, and John J Bollinger. Engineered two-dimensional ising interactions in a trapped-ion quantum simulator with hundreds of spins. *Nature*, 484(7395):489, 2012.

[120] A. W. Glaetzle, M. Dalmonte, R. Nath, I. Rousochatzakis, R. Moessner, and P. Zoller. Quantum spin-ice and dimer models with rydberg atoms. *Phys. Rev. X*, 4:041037, Nov 2014.

[121] Alexander W. Glaetzle, Marcello Dalmonte, Rejish Nath, Christian Gross, Immanuel Bloch, and Peter Zoller. Designing frustrated quantum magnets with laser-dressed rydberg atoms. *Phys. Rev. Lett.*, 114:173002, Apr 2015.

[122] Shannon Whitlock, Alexander W Glaetzle, and Peter Hannaford. Simulating quantum spin models using rydberg-excited atomic ensembles in magnetic microtrap arrays. *Journal of Physics B: Atomic, Molecular and Optical Physics*, 50(7):074001, 2017.

[123] Tony E. Lee, H. Häffner, and M. C. Cross. Antiferromagnetic phase transition in a nonequilibrium lattice of rydberg atoms. *Phys. Rev. A*, 84:031402, Sep 2011.

[124] Tony E. Lee, Sarang Gopalakrishnan, and Mikhail D. Lukin. Unconventional magnetism via optical pumping of interacting spin systems. *Phys. Rev. Lett.*, 110:257204, Jun 2013.

[125] Jia Ningyuan, Alexandros Georgakopoulos, Albert Ryou, Nathan Schine, Ariel Sommer, and Jonathan Simon. Observation and characterization of cavity rydberg polaritons. *Phys. Rev. A*, 93:041802, Apr 2016.

[126] M. Litinskaya, E. Tignone, and G. Pupillo. Cavity polaritons with rydberg blockade and long-range interactions. *arXiv:1607.08323*, 2016.

[127] Thibault Peyronel, Ofer Firstenberg, Qi-Yu Liang, Sebastian Hofferberth, Alexey V. Gorshkov, Thomas Pohl, Mikhail D. Lukin, and Vladan Vuletic. Quantum nonlinear optics with single photons enabled by strongly interacting atoms. *Nature*, 488(7409):57–60, 08 2012.

[128] D. Maxwell, D. J. Szwer, D. Paredes-Barato, H. Busche, J. D. Pritchard, A. Gauguet, K. J. Weatherill, M. P. A. Jones, and C. S. Adams. Storage and control of optical photons using rydberg polaritons. *Phys. Rev. Lett.*, 110:103001, Mar 2013.

[129] C. Tresp, P. Bienias, S. Weber, H. Gorniaczyk, I. Mirgorodskiy, H. P. Büchler, and S. Hofferberth. Dipolar dephasing of rydberg d-state polaritons. *Phys. Rev. Lett.*, 115:083602, Aug 2015.

[130] J. J. Mendoza-Arenas, S. R. Clark, S. Felicetti, G. Romero, E. Solano, D. G. Angelakis, and D. Jaksch. Beyond mean-field bistability in driven-dissipative lattices: Bunching-antibunching transition and quantum simulation. *Phys. Rev. A*, 93:023821, Feb 2016.

[131] Xi-Wang Luo, Yu-Na Zhang, Xingxiang Zhou, Guang-Can Guo, and Zheng-Wei Zhou. Dynamic phase transitions of a driven ising chain in a dissipative cavity. *Phys. Rev. A*, 94:053809, Nov 2016.

[132] Michael Hoening, Wildan Abdussalam, Michael Fleischhauer, and Thomas Pohl. Antiferromagnetic long-range order in dissipative rydberg lattices. *Phys. Rev. A*, 90:021603, Aug 2014.

[133] SG Schirmer and Xiaoting Wang. Stabilizing open quantum systems by markovian reservoir engineering. *Physical Review A*, 81(6):062306, 2010.

[134] A. Tomadin, V. Giovannetti, R. Fazio, D. Gerace, I. Carusotto, H. E. Türeci, and A. Imamoglu. Signatures of the superfluid-insulator phase transition in laser-driven dissipative nonlinear cavity arrays. *Phys. Rev. A*, 81:061801, Jun 2010.

[135] Andrea Tomadin, Sebastian Diehl, and Peter Zoller. Nonequilibrium phase diagram of a driven and dissipative many-body system. *Phys. Rev. A*, 83:013611, Jan 2011.

[136] B. Everest, M. Marcuzzi, and I. Lesanovsky. Atomic loss and gain as a resource for nonequilibrium phase transitions in optical lattices. *Phys. Rev. A*, 93:023409, Feb 2016.

[137] Felix Nissen, Sebastian Schmidt, Matteo Biondi, Gianni Blatter, Hakan E. Türeci, and Jonathan Keeling. Nonequilibrium dynamics of coupled qubit-cavity arrays. *Phys. Rev. Lett.*, 108:233603, Jun 2012.

[138] Steven H Strogatz. *Nonlinear dynamics and chaos: with applications to physics, biology, chemistry, and engineering.* CRC Press, 2018.

[139] N. Dogra, F. Brennecke, S. D. Huber, and Donner T. Phase transitions in a bose hubbard model with cavity-mediated global-range interactions. *arXiv:1604.00865*, 2016.

[140] Yu Chen, Zhenhua Yu, and Hui Zhai. Quantum phase transitions of the bose-hubbard model inside a cavity. *Phys. Rev. A*, 93:041601, Apr 2016.

[141] Yongqiang Li, Liang He, and Walter Hofstetter. Lattice-supersolid phase of strongly correlated bosons in an optical cavity. *Phys. Rev. A*, 87:051604, May 2013.

[142] Peter Domokos and Helmut Ritsch. Collective cooling and self-organization of atoms in a cavity. *Phys. Rev. Lett.*, 89:253003, Dec 2002.

[143] Emanuele G. Dalla Torre, Eugene Demler, Thierry Giamarchi, and Ehud Altman. Dynamics and universality in noise-driven dissipative systems. *Phys. Rev. B*, 85:184302, May 2012.

[144] Stefan Schütz and Giovanna Morigi. Prethermalization of atoms due to photon-mediated long-range interactions. *Phys. Rev. Lett.*, 113:203002, Nov 2014.

[145] Ching-Kit Chan, Tony E. Lee, and Sarang Gopalakrishnan. Limit-cycle phase in driven-dissipative spin systems. *Phys. Rev. A*, 91:051601, May 2015.

[146] Ryan M. Wilson, Khan W. Mahmud, Anzi Hu, Alexey V. Gorshkov, Mohammad Hafezi, and Michael Foss-Feig. Collective phases of strongly interacting cavity photons. *arXiv:1601.06857*, 2016.

[147] Francesco Piazza and Helmut Ritsch. Self-ordered limit cycles, chaos, and phase slippage with a superfluid inside an optical resonator. *Phys. Rev. Lett.*, 115:163601, Oct 2015.

[148] Jiasen Jin, Davide Rossini, Martin Leib, Michael J. Hartmann, and Rosario Fazio. Steady-state phase diagram of a driven qed-cavity array with cross-kerr nonlinearities. *Phys. Rev. A*, 90:023827, Aug 2014.

[149] Tony E. Lee, H. Häffner, and M. C. Cross. Collective quantum jumps of rydberg atoms. *Phys. Rev. Lett.*, 108:023602, Jan 2012.

[150] Jens Honer, Hendrik Weimer, Tilman Pfau, and Hans Peter Büchler. Collective many-body interaction in rydberg dressed atoms. *Phys. Rev. Lett.*, 105:160404, Oct 2010.

[151] G. Pupillo, A. Micheli, M. Boninsegni, I. Lesanovsky, and P. Zoller. Strongly correlated gases of rydberg-dressed atoms: Quantum and classical dynamics. *Phys. Rev. Lett.*, 104:223002, Jun 2010.

[152] N. Henkel, R. Nath, and T. Pohl. Three-dimensional roton excitations and supersolid formation in rydberg-excited bose-einstein condensates. *Phys. Rev. Lett.*, 104:195302, May 2010.

[153] A. W. Glaetzle, R. Nath, B. Zhao, G. Pupillo, and P. Zoller. Driven-dissipative dynamics of a strongly interacting rydberg gas. *Phys. Rev. A*, 86:043403, Oct 2012.

[154] F. Nogrette, H. Labuhn, S. Ravets, D. Barredo, L. Béguin, A. Vernier, T. Lahaye, and A. Browaeys. Single-atom trapping in holographic 2d arrays of microtraps with arbitrary geometries. *Phys. Rev. X*, 4:021034, May 2014.

[155] Hendrik Weimer. Variational principle for steady states of dissipative quantum many-body systems. *Phys. Rev. Lett.*, 114:040402, Jan 2015.

[156] Hendrik Weimer. Variational analysis of driven-dissipative rydberg gases. *Phys. Rev. A*, 91:063401, Jun 2015.

[157] Jiasen Jin, Alberto Biella, Oscar Viyuela, Leonardo Mazza, Jonathan Keeling, Rosario Fazio, and Davide Rossini. Cluster mean-field approach to the steady-state phase diagram of dissipative spin systems. *Phys. Rev. X*, 6:031011, Jul 2016.

[158] Anzi Hu, Tony E. Lee, and Charles W. Clark. Spatial correlations of one-dimensional driven-dissipative systems of rydberg atoms. *Phys. Rev. A*, 88:053627, Nov 2013.

[159] Jan Gelhausen, Michael Buchhold, and Philipp Strack. Many-body quantum optics with decaying atomic spin states. *arXiv:1605.07637*, 2016.

[160] Mohammad F. Maghrebi and Alexey V. Gorshkov. Nonequilibrium many-body steady states via keldysh formalism. *Phys. Rev. B*, 93:014307, Jan 2016.

[161] P. Schad, Yu. Makhlin, B.N. Narozhny, G. Schoen, and A. Shnirman. Majorana representation for dissipative spin systems. *Annals of Physics*, 361:401 – 422, 2015.

[162] Mehrtash Babadi, Eugene Demler, and Michael Knap. Far-from-equilibrium field theory of many-body quantum spin systems: Prethermalization and relaxation of spin spiral states in three dimensions. *Phys. Rev. X*, 5:041005, Oct 2015.

[163] Nathan Shammah, Shahnawaz Ahmed, Neill Lambert, Simone De Liberato, and Franco Nori. Open quantum systems with local and collective incoherent processes: Efficient numerical simulation using permutational invariance. *arXiv preprint arXiv:1805.05129*, 2018.

[164] Alexandre Le Boité, Giuliano Orso, and Cristiano Ciuti. Bose-hubbard model: Relation between driven-dissipative steady states and equilibrium quantum phases. *Phys. Rev. A*, 90:063821, Dec 2014.

[165] Alexandre Le Boité, Giuliano Orso, and Cristiano Ciuti. Steady-state phases and tunneling-induced instabilities in the driven dissipative bose-hubbard model. *Phys. Rev. Lett.*, 110:233601, Jun 2013.

[166] M. Schiró, C. Joshi, M. Bordyuh, R. Fazio, J. Keeling, and H. E. Türeci. Exotic attractors of the nonequilibrium rabi-hubbard model. *Phys. Rev. Lett.*, 116:143603, Apr 2016.

[167] L. J. Zou, D. Marcos, S. Diehl, S. Putz, J. Schmiedmayer, J. Majer, and P. Rabl. Implementation of the dicke lattice model in hybrid quantum system arrays. *Phys. Rev. Lett.*, 113:023603, Jul 2014.

[168] I. I. Beterov, I. I. Ryabtsev, D. B. Tretyakov, and V. M. Entin. Quasiclassical calculations of blackbody-radiation-induced depopulation rates and effective lifetimes of rydberg ns, np, and nd alkali-metal atoms with $n \leq 80$. *Phys. Rev. A*, 79:052504, May 2009.

[169] T. Pohl, E. Demler, and M. D. Lukin. Dynamical crystallization in the dipole blockade of ultracold atoms. *Phys. Rev. Lett.*, 104:043002, Jan 2010.

[170] E. A. Goldschmidt, T. Boulier, R. C. Brown, S. B. Koller, J. T. Young, A. V. Gorshkov, S. L. Rolston, and J. V. Porto. Anomalous broadening in driven dissipative rydberg systems. *Phys. Rev. Lett.*, 116:113001, Mar 2016.

[171] H. Abbaspour, G. Sallen, S. Trebaol, F. Morier-Genoud, M. T. Portella-Oberli, and B. Deveaud. Effect of a noisy driving field on a bistable polariton system. *Phys. Rev. B*, 92:165303, Oct 2015.

[172] Joseph Kerckhoff, Michael A. Armen, and Hideo Mabuchi. Remnants of semiclassical bistability in the few-photon regime of cavity qed. *Opt. Express*, 19(24):24468–24482, Nov 2011.

[173] Andreas Angerer, Stefan Putz, Dmitry O. Krimer, Thomas Astner, Matthias Zens, Ralph Glattauer, Kirill Streltsov, William J. Munro, Kae Nemoto, Stefan Rotter, Jörg Schmiedmayer, and Johannes Majer. Ultralong relaxation times in bistable hybrid quantum systems. *Science Advances*, 3(12), 2017.

[174] R. Bonifacio and L. A. Lugiato. *Introduction: What are Resonance Fluorescence, Optical Bistability, and Superfluorescence*, pages 1–9. Springer Berlin Heidelberg, Berlin, Heidelberg, 1982.

[175] P D Drummond and D F Walls. Quantum theory of optical bistability. i. nonlinear polarisability model. *Journal of Physics A: Mathematical and General*, 13(2):725, 1980.

[176] KV Kheruntsyan. Wigner function for a driven anharmonic oscillator. *Journal of Optics B: Quantum and Semiclassical Optics*, 1(2):225, 1999.

[177] Michael Buchhold, Benjamin Everest, Matteo Marcuzzi, Igor Lesanovsky, and Sebastian Diehl. Nonequilibrium effective field theory for absorbing state phase transitions in driven open quantum spin systems. *Phys. Rev. B*, 95:014308, Jan 2017.

[178] Michael Buchhold, Philipp Strack, Subir Sachdev, and Sebastian Diehl. Dicke-model quantum spin and photon glass in optical cavities: Nonequilibrium theory and experimental signatures. *Phys. Rev. A*, 87:063622, Jun 2013.

[179] W. Casteels, F. Storme, A. Le Boité, and C. Ciuti. Power laws in the dynamic hysteresis of quantum nonlinear photonic resonators. *Phys. Rev. A*, 93:033824, Mar 2016.

[180] H. J. Carmichael. Breakdown of photon blockade: A dissipative quantum phase transition in zero dimensions. *Phys. Rev. X*, 5:031028, Sep 2015.

[181] Matteo Marcuzzi, Michael Buchhold, Sebastian Diehl, and Igor Lesanovsky. Absorbing state phase transition with competing quantum and classical fluctuations. *Phys. Rev. Lett.*, 116:245701, Jun 2016.

[182] G. Rempe, R. J. Thompson, R. J. Brecha, W. D. Lee, and H. J. Kimble. Optical bistability and photon statistics in cavity quantum electrodynamics. *Phys. Rev. Lett.*, 67:1727–1730, Sep 1991.

[183] A. Baas, J. Ph. Karr, H. Eleuch, and E. Giacobino. Optical bistability in semiconductor microcavities. *Phys. Rev. A*, 69:023809, Feb 2004.

[184] L. Hruby, N. Dogra, M. Landini, and T. Esslinger. Observation of metastability in an open quantum system with long-range interactions. *arXiv:1708.02229*, 2017.

[185] R. H. Dicke. Coherence in spontaneous radiation processes. *Phys. Rev.*, 93:99–110, Jan 1954.

[186] D. F. Walls, P. D. Drummond, S. S. Hassan, and H. J. Carmichael. Non-equilibrium phase transitions in cooperative atomic systems. *Progress of Theoretical Physics Supplement*, 64:307–320, 1978.

[187] Jan Gelhausen, Michael Buchhold, and Philipp Strack. Many-body quantum optics with decaying atomic spin states: (γ, κ) dicke model. *Phys. Rev. A*, 95:063824, Jun 2017.

[188] Peter Kirton and Jonathan Keeling. Suppressing and restoring the dicke superradiance transition by dephasing and decay. *Phys. Rev. Lett.*, 118:123602, Mar 2017.

[189] P. C. Martin, E. D. Siggia, and H. A. Rose. Statistical dynamics of classical systems. *Phys. Rev. A*, 8:423–437, Jul 1973.

[190] Hans-Karl Janssen. On a lagrangean for classical field dynamics and renormalization group calculations of dynamical critical properties. *Zeitschrift für Physik B Condensed Matter*, 23(4):377–380, Dec 1976.

[191] C. De Dominicis and L. Peliti. Field-theory renormalization and critical dynamics above T_c: Helium, antiferromagnets, and liquid-gas systems. *Phys. Rev. B*, 18:353–376, Jul 1978.

[192] A. Rößler. Second order runge-kutta methods for itô stochastic differential equations. *SIAM J. Numer. Anal.*, 47:1713–1738, 2009.

[193] Magnus Wiktorsson. Joint characteristic function and simultaneous simulation of iterated itô integrals for multiple independent brownian motions. *Ann. Appl. Probab.*, 11(2):470–487, 05 2001.

[194] James Edward Turner, Darryl J Downing, and James S Bogard. *Statistical methods in radiation physics.* Wiley-VCH, 2012.

[195] R. Gilmore. Catastrophe time scales and conventions. *Phys. Rev. A*, 20:2510–2515, Dec 1979.

[196] G. S. Agarwal and Subodh R. Shenoy. Observability of hysteresis in first-order equilibrium and nonequilibrium phase transitions. *Phys. Rev. A*, 23:2719–2723, May 1981.

[197] Subodh R Shenoy and GS Agarwal. First-passage times and hysteresis in multivariable stochastic processes: The two-mode ring laser. *Physical Review A*, 29(3):1315, 1984.

[198] H A Kramers. Brownian motion in a field of force and the diffusion model of chemical reactions. 7(4):284–304, April 1940.

[199] Vladimir Ivanovič Mel'nikov. The kramers problem: Fifty years of development. *Physics Reports*, 209(1-2):1–71, 1991.

[200] Peter Hänggi, Peter Talkner, and Michal Borkovec. Reaction-rate theory: fifty years after kramers. *Rev. Mod. Phys.*, 62:251–341, Apr 1990.

[201] McCann Lowell I., Dykman Mark, and Golding Brage. Thermally activated transitions in a bistable three-dimensional optical trap. *Nature*, 402(6763):785–787, dec 1999. 10.1038/45492.

[202] R. Graham and H. Haken. Generalized thermodynamic potential for markoff systems in detailed balance and far from thermal equilibrium. *Zeitschrift für Physik A Hadrons and nuclei*, 243(3):289–302, Jun 1971.

[203] R. Graham and T. Tél. Existence of a potential for dissipative dynamical systems. *Phys. Rev. Lett.*, 52:9–12, Jan 1984.

[204] Freddy Bouchet, Krzysztof Gawedzki, and Cesare Nardini. Perturbative calculation of quasi-potential in non-equilibrium diffusions: A mean-field example. *Journal of Statistical Physics*, 163(5):1157–1210, Jun 2016.

[205] Robert S Maier and DL Stein. Transition-rate theory for nongradient drift fields. *Physical review letters*, 69(26):3691, 1992.

[206] Robert S Maier and Daniel L Stein. Limiting exit location distributions in the stochastic exit problem. *SIAM Journal on Applied Mathematics*, 57(3):752–790, 1997.

[207] Robert S Maier and Daniel L Stein. Escape problem for irreversible systems. *Physical Review E*, 48(2):931, 1993.

[208] R. Graham. Physik-preise 2009. *Physik Journal*, (8):50, Sep 2009.

[209] R. Graham. Solution of fokker planck equations with and without manifest detailed balance. *Zeitschrift für Physik B Condensed Matter*, 40(1):149–155, Mar 1980.

[210] S. Diehl. Field theory of non-equilibrium systems, 2017.

[211] R. Graham and T. Tél. On the weak-noise limit of fokker-planck models. *Journal of Statistical Physics*, 35(5):729–748, Jun 1984.

[212] Alex Kamenev and Alex Levchenko. Keldysh technique and non-linear σ-model: basic principles and applications. *Advances in Physics*, 58(3):197–319, 2009.

[213] R. Graham and A. Schenzle. Non-equilibrium potentials and stationary probability distributions of some dissipative models without manifest detailed balance. *Zeitschrift für Physik B Condensed Matter*, 52(1):61–68, Mar 1983.

[214] Henry Eyring. The activated complex in chemical reactions. *The Journal of Chemical Physics*, 3(2):107–115, 1935.

[215] R. Landauer and J. A. Swanson. Frequency factors in the thermally activated process. *Phys. Rev.*, 121:1668–1674, Mar 1961.

[216] J.S. Langer. Statistical theory of the decay of metastable states. *Annals of Physics*, 54(2):258 – 275, 1969.

[217] H.R. Jauslin. Nondifferentiable potentials for nonequilibrium steady states. *Physica A: Statistical Mechanics and its Applications*, 144(1):179 – 191, 1987.

[218] P.E. Kloeden and E. Platen. *Numerical Solution of Stochastic Differential Equations.* Applications of Mathematics. Springer-Verlag, 1992.

[219] Simon JA Malham and Anke Wiese. An introduction to sde simulation. *arXiv preprint arXiv:1004.0646*, 2010.

[220] Lawrence C. Evans. An introduction to stochastic differential equations version 1.2. 2017.

[221] Desmond J Higham. An algorithmic introduction to numerical simulation of stochastic differential equations. *SIAM review*, 43(3):525–546, 2001.

[222] P.E. Kloeden, E. Platen, and I.W. Wright. The approximation of multiple stochastic integrals. *Stochastic Analysis and Applications*, 10(4):431–441, 1992.

[223] F. Lange, Z. Lenarčič, and A. Rosch. Pumping approximately integrable systems. *Nature Communications*, 8:15767 EP, 2017.

[224] Zala Lenarčič, Florian Lange, and Achim Rosch. Perturbative approach to weakly driven many-particle systems in the presence of approximate conservation laws. *Phys. Rev. B*, 97:024302, Jan 2018.

[225] E. Müller-Hartmann and J. Zittartz. Interface free energy and transition temperature of the square-lattice ising antiferromagnet at finite magnetic field. *Zeitschrift für Physik B Condensed Matter*, 27(3):261–266, Sep 1977.

[226] DC Rapaport. Monte carlo study of the phase boundary of the ising antiferromagnet. *Physics Letters A*, 65(2):147–148, 1978.

[227] DP Landau, Shan-Ho Tsai, and M Exler. A new approach to monte carlo simulations in statistical physics: Wang-landau sampling. *American Journal of Physics*, 72(10):1294–1302, 2004.

[228] Ulli Wolff. Collective monte carlo updating for spin systems. *Phys. Rev. Lett.*, 62:361–364, Jan 1989.

[229] Robert H. Swendsen and Jian-Sheng Wang. Nonuniversal critical dynamics in monte carlo simulations. *Phys. Rev. Lett.*, 58:86–88, Jan 1987.

[230] Leticia F Cugliandolo. The effective temperature. *Journal of Physics A: Mathematical and Theoretical*, 44(48):483001, 2011.

[231] D Villamaina, A Baldassarri, A Puglisi, and A Vulpiani. The fluctuation-dissipation relation: how does one compare correlation functions and responses? *Journal of Statistical Mechanics: Theory and Experiment*, 2009(07):P07024, 2009.

Declaration and Acknowledgements

This section gives me the opportunity to say thank you to everyone who supported me during my PhD studies at the University of Cologne. I would like to begin by saying thank you to Dr. Philipp Strack with whom I started my PhD as part of his junior research group with Professor Achim Rosch. I thank him for his time, effort guidance, feedback and the interesting and well-thought out research projects he suggested and supervised.

I thank Professor Achim Rosch for his supervision, all the time he took for discussions and guidance, for his insightful and critical comments on the work that have led to this thesis. His heartfelt joy for physics is infectious and inspiring.

Especially, I would like to thank Dr. Michael Buchhold who provided professional support throughout all of my projects and always made time for scientific discussions. I admire the true excitement and joy he derives from understanding intricate phenomena and also his relentless drive to move forward his research projects to learn about and explore new problems. He has helped me grow professionally and also personally.

I would also like to thank my parents who always supported me during my entire studies. Without them it would not have been possible to pursue my research.

During my PhD time I was lucky enough to have had two opportunities for international collaborations. This allowed me to kick off my PhD with a two-month research stay in Boston, visiting Dr. Philipp Strack at Harvard University. Towards the end of my PhD, I took the chance to visit Dr. Michael Buchhold at the California Institute of Technology in Pasadena. Both research stays have been fantastic opportunities to progress with my research projects in this thesis and have also just been a wonderful time. This would not have been possible without additional financial support and therefore I am grateful for funding from the Bonn-Cologne Graduate School of Physics and Astronomy (BCGS) and would like to thank ’Quantum Matter and Materials’ for financially supporting my research visits in the USA.

I would like to thank the people who took time to proofread on selected chapters of this thesis. Their suggestions and critical comments have increased readability and at times accuracy of the presented research. Especially, these people are Ori Alberton, Dr. Michael Buchhold, Björn Ladewig, Florian Lange, Henry Legg and Emilio Torres.

I enjoyed my time at the institute for Theoretical Physics in Cologne and the work I have done during my PhD studies. Especially because of the great people from the research group of Professor Diehl, Professor Rosch and of Professor Trebst. In particular, I mention my office mates Florian Lange, Henry Legg, Dr. Stefan Maier, Emilio Torres and Yoran Tournois. Thank you all for the pleasant atmosphere and for your friendship.

Of course, it’s not all roses and I have had to endure setbacks and failures in projects like every PhD student but I can confidentially say that I would do it all again.

Erklärung

Ich versichere, dass ich die von mir vorgelegte Dissertation selbständig angefertigt, die benutzten Quellen und Hilfsmittel vollständig angegeben und die Stellen der Arbeit - einschließlich Tabellen, Karten und Abbildungen-, die anderen Werken im Wortlaut oder dem Sinn nach entnommen sind, in jedem Einzelfall als Entlehnung kenntlich gemacht habe; dass diese Dissertation noch keiner anderen Fakultät oder Universität zur Prüfung vorgelegen hat; dass sie, abgesehen von unten angegebenen Teilpublikationen, noch nicht veröffentlicht worden ist, sowie, dass ich eine solche Veröffentlichung vor Abschluss des Promotionsverfahrens nicht vornehmen werde. Die Bestimmungen der Promotionsordnung sind mir bekannt. Die von mir vorgelegte Dissertation ist von Professor Dr. Achim Rosch betreut worden.

Teilpublikationen

- *Many-body quantum optics with decaying atomic spin states: (γ, κ) Dicke model*
  J. Gelhausen and M. Buchhold and P. Strack
  Phys. Rev. A **95**, 063824, (2017)
- *Quantum-optical magnets with competing short- and long-range interactions: Rydberg-dressed spin lattice in an optical cavity*
  J. Gelhausen and M. Buchhold and A. Rosch and P. Strack
  SciPost Phys. **1**, 004 (2016)
- *Dissipative Dicke model with collective atomic decay: Bistability, noise-driven activation, and the nonthermal first-order superradiance transition*
  J. Gelhausen and M. Buchhold
  Phys. Rev. A **97**, 023807 (2018)